UNIVERSITE DE LILLE

THÈSE

Présentée en vue d'obtenir le grade de

DOCTEUR DE L'UNIVERSITE

Spécialité : Electronique, Microélectronique, Nanoélectronique et Micro-ondes

Développement d'une Station de Mesure Hyperfréquence sous Pointes Nano-Robotisée et Automatisée

Par

Cerine MOKHTARI

Soutenue le 05 décembre 2023 devant le jury d'examen

Président :	Pr. Guillaume Ducournau	Univ. Lille
Rapporteur :	Pr. Valérie Vigneras	ENSCBP-Bordeaux INP
Rapporteur :	Pr. Valérie Madrangeas	Xlim, Limoges
Examinateur :	Dr. Johannes Hoffmann	METAS, Bern
Invité :	Dr. Joao Azevedo Goncalves	STMicroelectronics, Crolles
Invité :	Dr. Djamel Allal	LNE, Paris
Directeur de thèse :	Pr. Kamel Haddadi	Univ. Lille

Thèse préparée à l'Institut d'électronique, de microélectronique et de nanotechnologie de Lille
Ecole doctorale ENGSYS 632

UNIVERSITY OF LILLE

PhD THESIS

Submitted to obtain the degree of

Doctor

In

Electronics, Microelectronics, Nanoelectronics, and Microwaves

Development of a Nano-robotics and Automated Microwave On-Wafer Probe Station

by

Cerine MOKHTARI

Oral defense at the Institute of Electronics, Microelectronics, and Nanotechnology (IEMN) in front of the examination board:

President :	Pr. Guillaume Ducournau	Univ. Lille
Reviewer :	Pr. Valérie Vigneras	ENSCBP-Bordeaux INP
Reviewer :	Pr. Valérie Madrangeas	Xlim, Limoges
Examiner :	Pr. Guillaume Ducournau	Univ. Lille
Guest :	Dr. Johannes Hoffmann	METAS, Bern
Guest :	Dr. Joao Azevedo Goncalves	STMicroelectronics, Crolles
Supervisor :	Dr. Djamel Allal	LNE, Paris

Thesis prepared at Institute of Electronics, Microelectronics, and Nanotechnology of Lille
Doctoral School ENGSYS 632

Résumé

Dans le contexte général de l'industrie européenne de la nanoélectronique, il est nécessaire de développer de nouvelles techniques et de nouveaux instruments de caractérisation sous pointes pour la validation précise et fine de circuits destinés à des applications haute fréquence (HF). Pour faire progresser la miniaturisation des dispositifs à haute fréquence, de nouvelles questions métrologiques liées à la caractérisation dimensionnelle et électrique doivent être abordées. Un instrument universel de caractérisation des dispositifs à radiofréquences (RF) consiste en un analyseur de réseau vectoriel (VNA), une station de mesure équipée d’une paire de sondes micro-ondes Ground-Signal-Ground (GSG) alignées manuellement ou automatiquement au moyen d'un microscope ou d'un système de caméra sur des substrats d'étalonnage et des dispositifs sous test (DUT). Les structures de test RF conventionnelles nécessitent des tampons (structures de contact) spécifiques pour s'adapter à la géométrie de la pointe de la sonde. Le positionnement de la sonde sur la structure de test CPW génère des erreurs de mesure de désalignement qui affectent la reproductibilité de la mesure. En outre, les dispositifs présentent des impédances extrêmes par rapport à l'impédance de référence 50 Ω du VNA, ce qui se traduit par une sensibilité et une précision de mesure médiocres.

Pour relever ce défi, une nouvelle station de mesure sous pointe entièrement automatisée et robotisée a été conçue et construite à partir de zéro. Les sondes de mesure ainsi que le porte échantillon accueillant le dispositif sous test sont montés sur des nano-positionneurs piézoélectriques du constructeur SmarAct®. La vision du contact sondes – au – composant sous test est assurée par une caméra microscope haute résolution. Un analyseur de réseau vectoriel Streamline Keysight® a été intégré à la station afin d’obtenir une solution compacte au plus près des sondes et réduire ainsi les erreurs non systématiques inhérentes aux variations de l'environnement. Enfin, un programme de pilotage des sondes et du porte échantillon automatique basé sur la reconnaissance d’image a été développé avec le logiciel LabVIEW™.

Mots clés: mesures hyperfréquences, mesures sous pointes, analyseur de réseaux vectoriel, métrologie haute fréquence, calibration, traçabilité électrique, nano-robotique, automatisation.

Abstract

In the general context of the European nanoelectronics industry, it is necessary to develop new on-wafer characterisation techniques and instruments for precise and accurate validation of circuits designed for high-frequency (HF) applications. To advance the miniaturisation of HF devices, new metrological issues related to dimensional and electrical characterization must be addressed. A universal instrument for the characterization of RF devices consists of a vector network analyzer (VNA), a measurement station equipped with a pair of ground-signal-ground (GSG) microwave probes aligned manually or automatically using a microscope or a camera system on calibration substrates and devices under test (DUT). Conventional RF test structures require contact pads to adapted to the probe tip geometry. The positioning of the probe on the CPW test structure generates misalignment measurement errors that affect the reproducibility of the measurement. In addition, nanodevices have extreme impedances compared to the VNA's characteristic impedance of 50 Ω, resulting in poor measurement sensitivity and accuracy.

To meet this challenge, a new fully automated and robotic on-wafer probing station was designed and built from scratch. The measurement probes as well as the chuck hosting the

device under test are mounted on SmarAct® piezoelectric nanopositioners. The view on the probe-to-DUT contact is provided by a high-resolution microscope camera. A Keysight® Streamline vector network analyzer was integrated into the station to obtain a compact solution close to the probes in order reduce the non-systematic errors inherent in environmental variations. Finally, a program for driving the probes and chuck, based on image recognition, was developed with the LabVIEW™ software.

Keywords: high frequency measurements, on-wafer measurements, vector network analyzer, high frequency metrology, calibration, electrical traceability, nano-robotics, automation.

Acknowledgments

The work done in this manuscript has been realised as part of the Circuits Systems Application of Microwaves (CSAM) group of the Institute of Electronics, Microelectronics and Nanotechnology (IEMN) laboratory in Lille. In particular, the project has been carried out in the RF-2S team located at the IEMN (developer) and Institute of Research on Devices software and materials for the Information and The Advanced Communication (IRCICA in French) in Lille.

First, I would like to thank Dr. Thierry MELIN and Prof. Natalie ROLLAND for welcoming me in both institutes.

This work was carried out within the framework of the joint IEMN - ST Microelectronics laboratory. I would like to thank Dr. Emmanuel DUBOIS, IEMN, and Dr. Andrea CATHELIN, ST Microelectronics, for their hospitality in the joint laboratory.

I would like to thank Prof. Valérie VIGNERAS, Ensmac (ex ENSCPRO) in Bordeaux, and Prof. Valérie MADRANGEAS, University of Limoges for doing me the honour of being the "Reviewers" of my thesis work.

I also thank Prof. Guillaume DUCOURNAU, University of Lille and Dr. Johannes HOFFMANN, Federal institute of Metrology in Switzerland for accepting to participate in the examination of this thesis.

I would like to warmly thank Prof. Kamel HADDADI, for supervising this thesis. His endless support, help and guidance allowed this work to come this far. Working under his lead made me grow as a researcher and as a human.

I thank Dr. Christophe LOYEZ for welcoming me into the CSAM team and for his kindness and generosity.

I thank Dr. Joao Azevedo GONCALVEZ, at ST Microelectronics and Dr. Djamel ALLAL, at the LNE for all the exchange we had throughout the years. It was a privilege to have their professional inputs regarding my work. I also thank Daouda SECK, PhD student at the LNE for his involvement during my PhD and for his future contribution, as he will take this work further during his PhD.

I would also like to thank the members of my team, with whom I shared three years of teamwork and hardships, Mohamed SEBBACHE, assistant engineer and Clément Lenoir, apprentice (now engineer). This work would have never been possible without their help and support.

I thank Christophe BOYAVAL, engineer at the IEMN laboratory for all the help he provided me during my PhD years. My sincere gratitude also goes to Prof. Henri HAPPY, University of Lille and part of the Doctoral school for his kindness.

I also thank all the people who contributed to this work: Gilles DAMBRINE, Gia NGOC PHUNG, Johaness HOFFMAN.

I also thank Anne-Sophie BEURET, Ahmed BEN ABDESELAM and Jean-Luc GUEUSQUIN at IRCICA for the help provided in the workplace.

I would like to thank all the people that I met during those three years, people with whom I shared precious memories: Lydia ABASSI, Ronan PETIT, Tomasz SWEBOCKI, Nawal ALSALAH, and all the PhD students of EGSYS, MADIS and SMRE.

Finally, I thank the administrative team, in particular, Nora BENBAHLOULI, Andy LEDENT, Gaëlle VANSTAEVEL, Emmanuelle GILLMANN, Laëtitia DEBAS, Thi NGUYEN and Céline GLOANEC.

"If I have seen further, it is by standing
on the shoulders of giants".

- Sir Issac Newton

To the most important people in my life,
my sister, my parents, my grand-father,
my cousin, my whole family and my fiends.

Table of content

Résumé ... 3
Acknowledgments ... 5
List of figures ... 11
List of tables ... 16
General introduction ... 18
Structure of the manuscript ... 21
1. State of the art – On-wafer probe station ... 23
Introduction ... 24
1.1 Basic probing station components ... 25
1.2 Probes to pads alignment ... 26
1.3 Manual probing stations ... 28
1.4 Semi-automated/automated probing stations ... 30
1.5 Radio-frequency (RF) probe technology ... 32
1.6 Probe mechanical layout rules ... 36
1.7 EQUIPEX ExCELSiOR Micro-probes ... 37
1.8 Automated on-wafer probing in the research field ... 39
1.9 Conclusion ... 41
1.10 References ... 42
2. Fundamental Notions ... 46
Introduction ... 47
2.1 Scattering parameters ... 48
2.1.1 1-port network or dipole ... 48
2.1.2 2-port network ... 49
2.2 Vector Network Analyzer ... 50
2.3 Error models and calibration algorithms ... 52
2.4 De-embedding ... 57
2.5 Conclusion ... 59
2.6 References ... 60
3. Development of the automated and nanorobotics probe station ... 62
Introduction ... 63
3.1 The SmarAct Technology ... 64
3.2 Mechanical properties of the positioning stages ... 66

3.2.1 SLC Linear Stages 67
3.2.2 SR Rotation Stages 68
3.2.3 MCS2 68
3.2.4 Repeatability 68
3.2.5 Sensor type 69
3.2.6 Positioner Movement 69
3.3 Positioner Properties 70
3.4 Automated and robotic probing station: hardware development 75
3.5 Positioning repeatability of the SmarAct nano-positioners with a DC probe 87
3.6 Static drift of the positioners with the Infinity probe 89
3.7 Automated and robotics probing station: Software development 93
3.8 Conclusion 98
4. On-wafer RF measurements 99
Introduction 101
4.1 On-wafer measurement uncertainties related to probes to pad alignments from manual probing station 102
4.1.1 Methodology for the determination of residual calibration error terms 102
4.1.2 Experimental set-up and validation 105
4.1.3 Standard deviation computed on microwave signals 108
4.1.4 Residual calibration error terms 109
4.1.5 Error propagation on complex impedances 110
4.2 Robotic-manual measurement for 1-port SOL calibration 113
4.2.1 Measurement protocol 115
4.2.2 Data analysis 115
4.2.3 Residual calibration error terms 116
4.2.4 Measurement uncertainty 118
4.3 Semi-automated measurements for 1-port SOL calibration 119
4.4 Approach/retract study for probe-substrate surface contact 122
4.5 Automated measurements for 1-port SOL calibration 125
4.5.1 On-wafer experimental set-up and configuration 125
4.5.2 Automated and robotics alignment 126
4.5.3 RF measurements results and data interpretation 127
4.5.4 Residual calibration error terms 135
4.5.5 Error propagation on complex impedances 137
4.6 Conclusion 141
4.7 References 142

5. Complementary studies 144
Introduction 145
5.1 Streamline VNA noise characterisation 146
5.1.1 Set-up and material 146
5.1.2 Measurement protocol 146
5.1.3 Measurement set-up 147
5.1.4 Analysis 148
5.2 Extend IQ Six-Port Demodulator RF Bandwidth by 250% Using 157
5.2.1 Fourier Based Modelling 157
5.2.2 Six-port reflectometry 157
5.2.3 The direct problem equation 160
5.2.4 Theoretical and simulation analysis 160
5.2.5 Experimental six-port junction 162
5.2.6 Measurement protocol and Modelling 164
5.2.7 Experimental results 164
5.3 Impedance Standard Substrate EM-Simulation for On-wafer GSG probing 168
5.3.1 Imaging 168
5.3.2 EM modelling 169
5.3.3 Simulation 170
5.3.4 Analysis 171
5.4 Conclusion 174
5.5 References 175
General conclusion 177
Bibliography 178

List of figures

Figure 1.1 Representation of a conventional RF on-wafer probing station. 25
Figure 1.2 A schematic of the probe's movement axis. 26
Figure 1.3 Schematic of probe tips alignments (a) no offset (b) translation offset (c) rotation offset. 26
Figure 1.4 Schematic of a tilted probe. 27
Figure 1.5 Representation of the overtravel and the skating of a probe tip. 28
Figure 1.6 (a) ISS 101-190C alignment marks (b) correct alignment of the probe tips of both ACP and Infinity type probes [7]. 28
Figure 1.7 MPS150 manual probe station from FormFactor™ [9].. 29
Figure 1.8 FormFactor™ manual probe positioners (a) RPP210 (b) RPP305 (c) EPP404 [14]. 30
Figure 1.9 FormFactor™ (a) SUMMIT200 (b) CM300xi [15] [16]....................................... 31
Figure 1.10 FormFactor™ motorized RF probe positioner RP504 [14]................................ 32
Figure 1.11 Design of an on-wafer probe based on ceramic technology [17]. 33
Figure 1.12 Evolution of the RF probing technology [16].. 33
Figure 1.13 (a) The first commercial sapphire calibration substrate CAL96 (b) the Tektronix® RF wafer probe TMP9600 (c) the WPH probe from Cascade Microtech®. (Pictures courtesy of FBH) [17]. 35
Figure 1.14 GSG probe tip technologies: (a) Picoprobe (top view, 100-nm pitch) (b) ACP (125-µm pitch) (c) Allstron (100-nm pitch) (d) Infinity Probe (125-µm pitch; all bottom view) and (e) |Z| Probe (125-µm pitch). (Pictures courtesy of FBH) [17]. 36
Figure 1.15 Some of FormFactor™ recommendations for working with Infinity probes: minimum pad size is 25 x 35 µm, minimum pad pitch is 100 µm (50 µm for fine pitch probes) [38]. 37
Figure 1.16 SEM photo of a 100 µm Infinity GSG probe from FormFactor™. 37
Figure 1.17 Schematic representation of the Nanoprober developed in [39].......................... 38
Figure 1.18 First generation of microprobes [42] [40] [43]. (a) Synoptic diagram. (b) SEM photo of the first generation microprobe. 38
Figure 1.19 (a) Resonance detection technique when three probe tips contact with the substrate [47]. (b) illustration of the RSD techniques when dealing with complicated structures [48]. (c) automated contact detection between the probe and the DUT using a PSD and a laser unit [49]. 40

Figure 2.1 Fluence chart in the case of a 1-port network. 49
Figure 2.2 Fluence chart in the case of a 2-port network. 50
Figure 2.3 Block diagram of a 2-port Vector Network Analyzer [3]...................................... 51
Figure 2.4 System Error Model for the Forward Direction [6]. 52
Figure 2.5 One-Port 3-Term Error Model. 53
Figure 2.6 12-Terms Error Model for the Forward Direction 54
Figure 2.7 12-Terms Error Model for the Reverse Direction [6]. 54
Figure 2.8 101-190 C Impedance Standard Substrate from FormFactor™. 55
Figure 2.9 ISS standards in a GSG configuration. 55
Figure 2.10 Standards used in the SOLT, TRL, and LRRM calibration algorithms with GSG probes [21]... 57

Figure 2.11 De-embedding technique for a 2-port network measurement [20]. 58

Figure 3.1 Schematic representation of the probe and the chuck axis. 67
Figure 3.2 Representation of the SmarAct Step mode. 69
Figure 3.3 Representation of the SmarAct Closed-Loop mode. 70
Figure 3.4 Representation of the SmarAct Scan mode. 70
Figure 3.5 Actual images of the SLC2430ds-22 (X), SLC2430ds-23 (Y), SLC1730ds-40 (Z) stages. 71
Figure 3.6 Displacement of the positioner as a function of time for different velocities considering the X direction and the SLC2430ds-22 stage. 71
Figure 3.7 Displacement of the positioner as a function of time for different frequencies considering the X direction and the SLC2430ds-22 stage. 72
Figure 3.8 Maximum velocity as a function of frequency considering the X direction and the SLC2430ds-22 stage. 73
Figure 3.9 Drift over time of the positioner considering the Z direction and the SLC1730ds-40 stage. 74
Figure 3.10 The Moticam CAM-1080P HDMI camera (www.micromecanique.fr). 77
Figure 3.11 The MPI OP-Z10 Zoom Microscope. In red, the 90 ° angle fixation (MPI Corporation All Rights Reserved). 77
Figure 3.12 Schematic representation of the optical bridge. 78
Figure 3.13 Optical bridge installed on the probing station. 78
Figure 3.14 The SmarAct® MCS2 controller Rack Housing system. 79
Figure 3.15 FormFactor™ Infinity GSG probe (the 150 µm and 100 µm pitch are similar in shape and size, only difference is the tip). 79
Figure 3.16 Schematic representation of the robotics and automated probing station. 80
Figure 3.17 Top view picture of the probes and the chuck with a calibration substrate (left). Side view picture pf the probes and the camera (right). 80
Figure 3.18 Side picture of the complete probing station (top). Top view picture of the complete probing station (bottom). 81
Figure 3.19 LabVIEW™ dedicated screen (left). Wincal™ dedicated screen (middle). Camera feedback dedicated screen (right). 82
Figure 3.20 SmarAct probe positioner. 82
Figure 3.21 the attachment pieces 3D printed in PLA (at IEMN). 83
Figure 3.22 the fabricated pieced in metal by Materialisel (external commercial company). . 83
Figure 3.23 1st piece attached to the Z stage, 2nd piece attaching the 1st piece to the rotation stage, 3rd piece attaching the rotation stage to the probe 84
Figure 3.24 SmarAct probe positioner with the attachment pieces and the Infinity GSG probe. 84
Figure 3.25 Actual picture of the Infinity probe mounted on the four stages positioner. 85
Figure 3.26 Schematic representation of the chuck positioner. 85
Figure 3.27 Original design of the top plate as provided by SmarAct® (quotations are in mm). 86
Figure 3.28 Design of the top plate after modifications (quotations are in mm). 86
Figure 3.29 The automated and robotics GSG probing station based on SmarAct positioners. 87
Figure 3.30 Schematic representation of the positioning repeatability process. 88

Figure 3.31 Position of the DC probe along the Z axis for 10 successive positioning. 88
Figure 3.32 Absolute positioning error of the DC probe along the Z axis for 10 successive positioning at 500 nm/s. 89
Figure 3.33 Probing station: Positioner with the DC probe and the RF cables attached on the optical table. 90
Figure 3.34 Absolute error of the static positions of the probe positioner over 30 minutes for the cable attached to the probe alone. X-axis (top). Y-axis (middle). Z-axis (bottom). 91
Figure 3.35 Absolute error of the static positions of the probe positioner over 30 minutes for the cable attached to the probe and the VNA. X-axis (top). Y-axis (middle). Z-axis (bottom). 92
Figure 3.36 Automated and robotic probe station algorithms in LabVIEW™. 94
Figure 3.37 Schematic representation of the angles between the structure, the probe tips and the frame of the camera. 95

Figure 4.1 Manual probe station in the characterisation platform at the IEMN laboratory. .. 102
Figure 4.2 12-terms error model in the forward direction represented by the error coefficients E_D, E_S, E_R, E_L, E_T, and E_X [10]. 103
Figure 4.3 Raw reflection coefficient magnitude of the short, open and load standards considering the XYZ-analysis for the 10 measurements. 105
Figure 4.4 Raw reflection coefficient phase shift of the short, open and load standards considering the XYZ-analysis for the 10 measurements. 106
Figure 4.5 Raw reflection coefficient magnitude of the short, open and load standards considering the Z-analysis for the 10 measurements. 107
Figure 4.6 Raw reflection coefficient phase shift of the short, open and load standards considering the Z-analysis for the 10 measurements. 108
Figure 4.7 Standard deviation (Std) obtained from measured complex reflection coefficient $S11M$ on the impedance standard substrate (ISS). 109
Figure 4.8 Reflection coefficient magnitude uncertainty. 110
Figure 4.9 Vector representation of the measurement uncertainty on the complex reflection coefficient S_{11}. 112
Figure 4.10 Measurement uncertainty ΔIm(Z) computed by propagation of χ-disk on the complex impedance. 112
Figure 4.11 MCS2 joystick. 114
Figure 4.12 Automated and robotics on-wafer probing station. MPI® Camera. (2) VNA. (3) nano-robotic probe station. (4) Controllers. 115
Figure 4.13 Absolute Z-position as a function of "n° of probing" (approach – retract by 70 µm) for (a) short. (b) load. (c) open. 116
Figure 4.14 Standard deviations calculated for the three error terms (a) directivity $\delta 1$. (b) reflection tracking $\tau 1$. (c) source match $\mu 1$. 117
Figure 4.15 Reflection coefficient magnitude uncertainties. (a) robotic-manual approach. (b) conventional probing. 118
Figure 4.16 Infinity GSG probe's tips aligned with the alignment structure of the ISS (on screen). 119
Figure 4.17 Standard deviations calculated for the three error terms (a) directivity $\delta 1$. (b) reflection tracking $\tau 1$. (c) source match $\mu 1$. 121
Figure 4.18 Reflection coefficient magnitude uncertainties. 121

Figure 4.19 Position of the probe along the Z-axis when approaching the probe from 100 µm above the surface with a 500 nm step increment. 122
Figure 4.20 Position of the probe along the Z-axis when approaching the probe from 50 µm above the surface with a 100 nm step increment. 123
Figure 4.21 Real part of the measured reflection coefficient when approaching from 100 µm with 500 nm step. 124
Figure 4.22 Real part of the measured reflection coefficient when approaching from 50 µm with 100 nm step. 124
Figure 4.23 Imaginary part of the measured reflection coefficient when approaching from 100 µm with 500 nm step and from 50 µm with 100 nm step. 125
Figure 4.24 "In contact – CW – 1 GHz" raw reflection coefficient $S11$ data of 10 successive measurements of the Short standard at 1 Hz and 100 Hz. 128
Figure 4.25 "In contact – CW – 1 GHz" First value of the raw reflection coefficient $S11$... 129
Figure 4.26 "In movement - CW" raw reflection coefficient $S11$ data of 10 successive measurements of the Short standard at 1 Hz, 10 Hz, and 100 Hz. 129
Figure 4.27 "In movement – CW – 1 GHz" First value of the raw reflection coefficient $S11$. 130
Figure 4.28 Cumulative Complex Standard Deviation for the different configuration. (a) In contact. (b) In movement. 130
Figure 4.29 "In contact – Sweep" and "In movement – Sweep" raw reflection coefficient $S11$ data of 10 successive measurements of the Load standard at 100 Hz. 133
Figure 4.30 Standard deviation of the error terms calculated on 10 successive measurement at 1 Hz and 100 Hz for both measurement sets. 136
Figure 4.31 Reflection coefficient magnitude uncertainty at 1 Hz and 100 Hz for both measurement sets. 137

Figure 5.1 Keysight Streamline connected to the coaxial cables. 147
Figure 5.2 Keysight PNA connected to the coaxial cables. 148
Figure 5.3 Reflection coefficient and transmission coefficient measured for a short standard directly connected to the Streamline (Top 4) and the PNA (Bottom 4) at IFBW of 100 Hz and 10 GHz 149
Figure 5.4 Reflection coefficient and transmission coefficient measured for a short standard connected via a cable to the Streamline (Top 4) and the PNA (Bottom 4) at IFBW of 100 Hz and 10 GHz. 150
Figure 5.6 Six-port reflectometry technique [16]. 158
Figure 5.7 Double reactive couplers based six-port reflectometer [16]. 159
Figure 5.8 Double six-port network analyzer [16]. 159
Figure 5.9 Typical six-port IQ demodulator / interferometer comprising a power divider, three hybrid couplers and four power detectors. 162
Figure 5.10 Simulated detected powers P_3 to P_6 as a function of the phase-shift $\Delta\phi$ between the LO and the RD signals (_ P_3 _ P_4 _ P_5 _ P_6). 162
Figure 5.11 Experimental set-up including a six-port IQ demodulator realized on microstrip technology at 2.45 GHz (1. LO signal 2. RF signal 3. Digital score). 163
Figure 5.12 The six-port IQ demodulator 163
Figure 5.13 Detected voltages as a function of the phase-shift $\Delta\phi$ at different operating frequencies. 165

Figure 5.14 Curve fitting based on the 2nd order Fourier analysis for V_1 at (a) 2.45 GHz and (b) 6 GHz. 167
Figure 5.15 101-190 C Impedance Standard Substrate. 168
Figure 5.16 SEM images of short (left), thru (middle) and load (right) structures of the 101-190 C Impedance Standard substrate. 169
Figure 5.17 Dimensions of the sheet resistance on an ISS load structure. 169
Figure 5.18 The 101-190 Impedance Standard Substrate design in CST Studio Suite. 170
Figure 5.19 Portion of the ISS consisting of a single load structure on alumina substrate. 170
Figure 5.20 Waveguide port definition. 171
Figure 5.21 The waveguide port as defined in CST®. 171
Figure 5.22 Reflection coefficient of the 50 Ω load obtained from the CST simulation. 172
Figure 5.23 Reflection coefficient obtained from measuring the load with a vector network analyser 172
Figure 5.24 Electrical field and magnetic field respectively obtained from a simulated load structure of the 101-190 C ISS. 172
Figure 5.25 SEM picture of the Infinity GSG probe with 100 µm pitch captured at IEMN laboratory. 173
Figure 5.26 CST design of a microstrip line based GSG probe with 100 µm pitch. 173

List of tables

Table 3.1 SLC Linear Stages used for the probes and the chuck. 67
Table 3.2 SR Rotation Stages used for the probes and the chuck. 68
Table 3.3 Positioner Properties. 74
Table 3.4 Specification Sheet regarding the development of the robotics and automated on-wafer probe station. 75
Table 3.5 Keysight Streamline P5008A physical properties (dimensions/weight). 76
Table 3.6 Maximum absolute error, minimum absolute error and mean absolute error for 10 positioning at two different positioner's speed. 89
Table 3.7 mean and maximum absolute error calculated for both configurations. 90
Table 3.8 Template used by the NI Vision module captured with the camera on the ISS. 96
Table 3.9 Example of the execution of the program on the alignment structure of the ISS. 97

Table 4.1 3σ standard deviations computed at 1 GHz, 10 GHz, 30 GHz and 60 GHz considering the Z-analysis. 109
Table 4.2 3σ standard deviations computed at 1 GHz, 10 GHz, 30 GHz and 60 GHz considering the XYZ-analysis. 110
Table 4.3 Impedance measurement uncertainty at 10 GHz for Z-analysis and XYZ-analysis. 113
Table 4.4 Capacitance measurement uncertainties at 10 GHz for Z-analysis and XYZ-analysis. 113
Table 4.5 3σ standard deviations computed at 1 GHz, 10 GHz, 30 GHz and 50 GHz. 117
Table 4.6 Capacitance measurement uncertainties at 10 GHz. 119
Table 4.7 Measurement configurations. 126
Table 4.8 "CW Mode" Maximum difference calculated between the highest and the lowest value for the magnitude and phase shift of the raw reflection coefficient $S11$ for the Short standard. 131
Table 4.9 "CW Mode" Maximum difference calculated between the highest and the lowest value for the magnitude and phase shift of the raw reflection coefficient $S11$ for the Load standard. 131
Table 4.10 "CW Mode" Maximum difference calculated between the highest and the lowest value for the magnitude and phase shift of the raw reflection coefficient $S11$ for the Open standard. 132
Table 4.11 "Sweep Mode" Maximum difference calculated between the highest and the lowest value for the magnitude and phase shift of the raw reflection coefficient $S11$ for the Short standard. 134
Table 4.12 "Sweep Mode" Maximum difference calculated between the highest and the lowest value for the magnitude and phase shift of the raw reflection coefficient $S11$ for the Load standard. 134
Table 4.13 "Sweep Mode" Maximum difference calculated between the highest and the lowest value for the magnitude and phase shift of the raw reflection coefficient $S11$ for the Open standard. 135
Table 4.14 3σ standard deviations computed at 10 GHz considering the "In contact – Sweep" and "In movement – Sweep" at 100 Hz and the manual measurements. 137

Table 4.15 “In contact – Sweep – 1 Hz” Measurement uncertainty and measurement capacitances uncertainties on capacitances at 10 GHz.. 138
Table 4.16 “In movement – Sweep – 1 Hz” Measurement uncertainty and measurement capacitances uncertainties on capacitances at 10 GHz.. 138
Table 4.17 “In contact – Sweep – 100 Hz” Measurement uncertainty and measurement capacitances uncertainties on capacitances at 10 GHz.. 139
Table 4.18 “In movement – Sweep – 100 Hz” Measurement uncertainty on capacitances at 10 GHz compared with manual results. 139
Table 4.19 “In movement – Sweep – 100 Hz” Measurement capacitances uncertainties on capacitances at 10 GHz compared with manual results. 140
Table 4.20 “In movement – 100 Hz” Measurement capacitances uncertainties on capacitances at 1 GHz. 140

Table 5.1 Measurement configurations. 146
Table 5.2 Measurement periods. 147
Table 5.3 Standard deviation calculated for the load without cables measurement sets. 151
Table 5.4 Standard deviation calculated for the short without cables measurement sets. 152
Table 5.5 Standard deviation calculated for the open without cables measurement sets....... 153
Table 5.6 Standard deviation calculated for the short with cables measurement sets 154
Table 5.7 Standard deviation calculated for the open with cables measurement sets............ 155
Table 5.8 Standard deviation calculated for the Load with cables measurement sets. 156
Table 5.9 Experimental set-up configuration. 163
Table 5.10 Calibration coefficients at 2.45 GHz, 6 GHz, and 500 MHz. 166
Table 5.11 Mean and maximum error on the complex impedance Z. 167
Table 5.12 Material properties of the different part of the ISS. 169
Table 5.13 Simulation parameters 171

General introduction

The ongoing technological progress in the nano-electronics field, especially the miniaturization of radio frequency (RF) devices is essential for the development of new and innovative technologies, such as 5G communications, cellular IoT, artificial intelligence and other digital devices operating at very high frequencies. To further advance this miniaturization, metrological locks related to dimensional and electrical characterisation must be addressed and lifted. One of the main challenges is the precise and accurate on-wafer measurement of the electrical properties of micro- and nano-devices, taking into account the high industrial demands in terms of measurement time; rise of the devices' frequency; probes tip size and calibration techniques.

Many national and international institutions are at the heart of this challenge. This work is funded by the Nano Plan 2022 as part of the IEMN/STMicroelectronics® joint laboratory, which is included in the European structuring process IPCEI (Important Project of Common European Interest) on microelectronics. The work is also part of the European TEMMT project (Traceability for Electrical Measurements at Millimetre-wave and Terahertz frequencies for communication and electronics technologies), which aims at establishing traceability to the SI for measuring S-parameters, power and complex permittivity of dielectric materials, at terahertz frequencies. The EURAMET joint research project is funded by the European Union's Horizon 2020 under the European Metrology Program for Innovation and Research (EMPIR). The project is running from May 2019 to April 2022, involves 16 European organizations and 3 international organizations. In addition, there is a joined effort from many international institutions' teams that are dedicating their work to the advancement of on-wafer characterization: the National Institute of Standards and Technology (NIST) in the USA, the German National Metrology Institute (PTB) in Germany, the Dutch National Metrology Institute (VSL) in the Netherlands, the National Physical Laboratory (NPL) in the UK, The Federal Institute of Metrology (METAS) in Switzerland and the National Institute of Advances Industrial Science and Technology in Japan. Therefore, there is a strong ecosystem allowing on-wafer characterisation to advance.

New instrumentation must enable the precise and accurate validation of electrical models dedicated to the design of circuits for high-frequency applications up to the millimetre-wave range. Indeed, in order to establish electrical models used in computer aided design (CAD) software, it is necessary to precisely characterize micro- and nano- devices in coplanar waveguide (CPW) technology. The conventional instrument used for the on-wafer characterization of RF devices consists of a vector network analyzer (VNA), a probe station equipped with a pair of ground-signal-ground (GSG) microwave probes. The probe station could be manual, semi-automated or automated. A vision system, typically a camera augmented with a microscope, is used to align the probes on the calibration substrates or the devices under test (DUTs). The DUT is positioned on a sample holder, called the chuck using a vacuum system. Manual on-wafer probing stations become quickly limited in the measurement of extreme impedances devices. The alignment of the probes on the contact pads is done manually by the operator. Accurately aligning the probes is hardly achievable, requires a trained operator and a long measurement time. Small misalignments of the probes lead to uncertainties that will degrade the quality of the measurement. Industrials have been using automated (or semi-automated) probe stations to tackle the precise alignment problem. However, a study of the

available stations showed that one micrometre precision is achieved at best. Such level of precision might not be adapted for extreme impedances measurements yet (capacitances of a few femto-Farad for example).

This work aims to develop an innovative new generation of on-wafer probe station and the associated instrumentation for high-frequency characterization of microwave and millimetre-wave devices. The station is

1- robotics: using nano-positioners based on piezo-electrical technology from SmarAct®. The RF probes are mounted on four nano-positioning stages: X, Y, and Z stages for translation with 1 nm resolution, and a θ stage for rotation with 25 µ° resolution. As for the chuck, it is mounted on three nano-positioning stages: X and Y in translation and φ in rotation with the same resolutions,

2- automated: the station allows two positioning modes: manual and automated. The SmarAct® positioners can be controlled manually with a manual joystick that lets the operator control and position the stages manually. The joystick also allows to change the parameters of the stages (displacement mode, speed, acceleration, frequency…). The nano-positioners can also be controlled automatically using a dedicated LabVIEW™ library to execute automatic movement sequences,

3- compact: in order to minimise measurement uncertainties inherent to instrument noise and cable torsions, we chose the Streamline VNA from Keysight®, a compact table VNA placed as close as possible to the probes via flexible and high phase stability MegaPhase-UtraPhase™ cables.

The automated and robotic probing station is developed from scratch. In the following, we will give an overview of the development timeline as well as the challenges that were encountered during the development of the instrument. At the beginning of the project, only a few elements were available: the nano-positioners, the metallic structure of the station and the mechanical drawings.

- The first months of the three-year period time were dedicated to understanding how the nano-positioners work. Several studies were conducted, especially on the displacement mode to be considered for our application.

- Parallel to that, a careful market study was done regarding the rest of the equipment needed: VNA, vision system and optical table. Once the right equipment was selected, it was delivered only a year later (budget, delivery time).

- Another challenge that was faced during the first year of the project is the development of a robust connection between the probes and the nano-positioners. Although the mechanical drawings of the pieces were available, we had to find the right materials and the right configuration to achieve the best performance. We also had to develop a fixation system for the DUT. Indeed, the chuck of the station does not to integrated a vacuum system. Hence, we designed specific 3D printed PLA fixations. Those fixations were later replaced by metallic screws, allowing a stronger fixation.

- The first instrument acquired was the Streamline VNA. During the next months of the first year, we worked on the VNA. Especially, a noise study was undertaken during the second year

in order to quantify the VNA's performance. In addition, the automated control of the VNA under LabVIEW™ Software was devemoped.

- As a complementary work, during the second year, we worked on the development of a low-cost six-port demodulator aiming at making a new measurement instrument that would be more suitable for the measurement of extreme impedances.

- The two last components were delivered at the end of the second year: the optical table and the camera-microscope. A long mechanical design process started in order to connect all the different parts of the system together. The camera is positioned over the probing station. It required the design and fabrication of an optical bridge. The bridge was designed to respect the working distance of the camera. A careful study was needed. The optical table had to be installed as well as the compressed air pump.

- The third year was dedicated to the development of a robust automation program. Each part of the program was developed and tested separately. The GSG probes need to be manipulated with great care and many safety options had to be integrated gradually. Other challenges were faced at this point: probe collision with the DUT during testing, poor DUT fixation to the chuck, complicated and time-consuming replacement of the damaged probes. In addition, many automated probing solutions were considered: RF signal detection, image recognition, DUT mapping. Each solution was studied and tested. Image recognition using a LabVIEW™ module was selected at the end. Last months were dedicated to the program optimization and final measurements.

Structure of the manuscript

In the first chapter, on-wafer probe stations are described. In particular, the main sub-systems of manual and semi-/fully automated on-wafer stations are described. Indeed, on-wafer probe stations consist mainly of a pair (or more) of Radio-frequency (RF) probes aligned on the Devices Under Test (DUTs) either with manual and mechanical positioners or with automated or semi-automated positioners using a vision system, typically a camera. The probes are connected to a Vector Network Analyzer (VNA) to determine the DUT electrical parameters, namely the S-parameters. The chapter also describes the main challenges faced considering on-wafer measurements. In particular, precise landing and alignment of the probes on the access pads of the DUTs remain still the largest source of measurement uncertainty. In addition, skating of the probes and planarization should be considered with great care. Some example of commercially available on-wafer probe stations are also presented. Finally, evolution of the RF probe technology is summarized as well as the actual academic work dedicated to enhancing on-wafer measurements done mainly through National Metrology Institutes (NMIs).

In the second chapter, we describe the RF characterization tools and methods. In particular, we define the concept of pseudo-waves (or power waves) and the related S-parameters, fundamental quantities used to characterize an RF device or system. One-port networks and two-port networks are also presented in this chapter. In addition, we describe the VNA architecture, reference measurement instrument in RF measurements. Especially, VNA calibration is described including calibration models and corresponding calibration algorithms. Finally, de-embedding procedures are presented.

The third chapter is dedicated to the development of the automated and robotic on-wafer probe station. The station is developed completely from scratch in both IEMN / IRCICA laboratories. First, we present the nano-positioning stages identified for building the nanorobotics part of this work. It is important to understand how they work in order to optimise the design correctly. A series of tests on the positioners are shown. In particular, the speed, the acceleration, the frequency, and the static drift of the positioners are considered. The chapter also describes all the components used to build the station (mechanical parts and RF instruments) as well as the challenges faced during the development. In addition, the first positioning and drift results of the station are shown. Finally, the automated calibration process is described. The program is based on image recognition and automated placement of the probes on the calibration substrate.

In the fourth chapter, we present different RF measurements results. First, a probe-to-pad repeatability study is performed considering a conventional manual on-wafer station, based on mechanical positioners. This preliminary benchmark is required as starting point to estimate the actual and overall performance. Residual error terms of 10 successive calibrations are propagated to extreme complex impedances in order to evaluate the influence of the probe-to-pad realignment on the measurement uncertainties. We show that precisely controlling the probes drastically reduces the measurement uncertainties. In a second step, we present the performance of the robotic positioners. Following the same methodology, we analyse the residual calibration error terms obtained through a manual but robotic repeatability study on the developed station. Also, an approach/retract study is shown. Using the RF signal during the probe's landing on the DUT could help to solve the skating/overtravel dilemma. Finally, automated and robotic calibration using the final version on the station is presented. We

demonstrate enhanced measurement uncertainty decrease when using image recognition during the alignment procedure.

Finally, in the fifth chapter, we present some additional studies that have been done in order to enhance the overall on-wafer measurements. Especially, a six-port IQ demodulator is designed and characterized. We show that using a Fourier based method, we can extend the operation frequency operation of the six-port junction. Also, we present VNA noise evaluation and electromagnetic (EM) simulation of the calibration substrate. The aim is to use six-port technology to bring the measurement instrumentation as close as possible to the probe, solving the impedance mismatch problem and the EM simulation to optimise the probe position of the calibration standards. Indeed, realigning on nano-positioners allow to align the probes with a few nanometres precision. EM simulation results could indicate the most optimal influencing parameters.

Chapter 1

1. State of the art – On-wafer probe station

Table of content

Introduction 24
1.1 Basic probing station components.. 25
1.2 Probes to pads alignment.. 26
1.3 Manual probing stations.. 28
1.4 Semi-automated/automated probing stations 30
1.5 Radio-frequency (RF) probe technology.. 32
1.6 Probe mechanical layout rules.. 36
1.7 EQUIPEX ExCELSiOR Micro-probes 37
1.8 Automated on-wafer probing in the research field.. 39
1.9 Conclusion.. 41
1.10 References 42

Introduction

This chapter introduces the general context related to radio-frequency (RF) on-wafer probe station. The building blocks of a conventional probing station are presented as well as commercially available probe stations. A short overview and focus on RF Ground-Signal-Ground (GSG) probes are also described.

The demand on the semiconductor industry is still very high. According to the 2020 edition of the International Roadmap for Devices and Systems™ (IRDS) report, consumer electronics grew 10% in 2019 (year over year) and achieve 13% in 2020. In 2022, it was forecasted to grow to $420B [1]. This evolution is due to the growing need for new microwave, mm-wave and THz technologies to provide faster and more reliable services, devices and security applications. Increasing the operating frequency together with demand of frequency agile solutions call for new accurate and reliable characterization techniques. In particular, *S*-parameter measurement and calibration procedures are crucial steps in the integrated circuits design and debug process [2].

An on-wafer probing station is a well-established measurement equipment in the semiconductor industry and in multiple research fields. The main usage concerns the on-wafer electrical test for RF circuits and devices. Industrial probing stations need to be fast, accurate and scalable (in terms of frequency of operation, wafer size) in order to make the time-to-market as low as possible. We can hence, find semi-automated to automated probing station in the semiconductor industry. Sophisticated probing stations with automated probers and image recognition of probe to pads alignment are nowadays used to speed up the process. Those technologies are presented in more details later in this chapter. Manual probe stations can be found mainly in research facilities. As their cost is lower than semi-automated and automated stations and measurement time is not the main issue here, it makes them a better choice for research purposes. They are, however, less accurate in terms of probe alignment. Some research facilities however, are developing new automated solutions for precise on-wafer characterisation. The VSL-Dutch Metrology Institute in Netherlands and the National Metrology Institute in Japan are currently developing these promising solutions.

1.1 Basic probing station components

Figure 1.1 shows a representation of a conventional on-wafer probing station. The on-wafer device, circuit or system to be characterized, commonly called Device Under Test (DUT), is positioned onto a rigid and planar metallic support (Chuck) and is kept in place using a vacuum pump. The chuck can be made from other material, for example insulating material depending mainly on the DUT dielectric characteristics. The RF contacting between the contact pads of the DUT, usually in coplanar waveguide (CPW) form, and the RF measurement system is done through RF cables and probes. The probes come in different types according to the application and the dimensions of the DUT. In all cases, the probes are moved and aligned on the DUT to perform the measurements. An optical camera on top of the system allows the alignment of the probes. The probes are mounted on probing arms, also called positioners. These positioners can be manual, using precision mechanical screws or they can be semi-automated or fully automated. Typically, they provide four movement stages, X and Y direction for horizontal 2D translation, Z direction for vertical translation and θ for rotation. Figure 1.2 shows a schematic of the probe's movement axis. Finally, the probes are connected to the measurement system such as Vector Network Analyzer (VNA) using RF coaxial cables and connectors. By sending input RF signals, i.e. incident waves to the DUT, reflected or/and transmitted signals, i.e. emergent waves, are measured by the VNA.

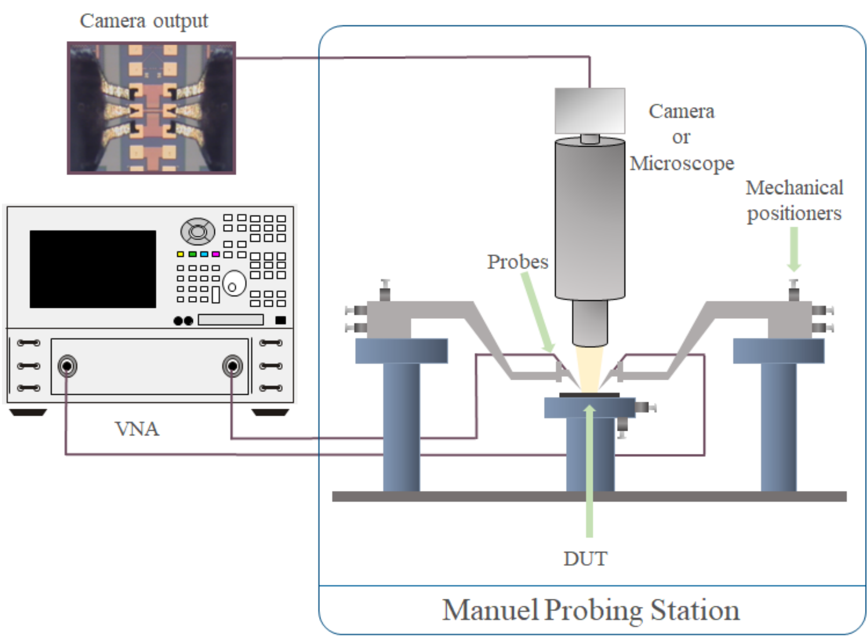

Figure 1.1 Representation of a conventional RF on-wafer probing station.

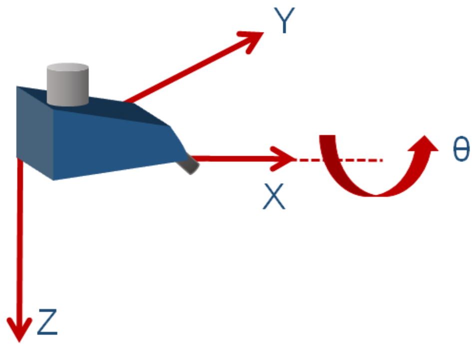

Figure 1.2 A schematic of the probe's movement axis.

1.2 Probes to pads alignment

The alignment of the probe's tips to the contact pads of the DUT is a crucial element to achieve good and accurate measurements. A proper alignment is hence necessary. Misalignments caused by tilt, rotation or translation offsets of the probe lead to non-systematic measurement errors that cannot be corrected by a calibration procedure. Figure 1.3 shows a. good alignment b. translation offset c. rotation offset. This is a common problematic faced when using manual probing stations. Such measurements are very operator dependent (hand vibrations, physical state, sight, experience…). Semi-automated and automated probing stations have tackled this issue by removing the operator from the alignment process. As it will be described in detail later, the state of the art solutions provide micrometer displacement accuracy in X, Y and Z translations, at the best.

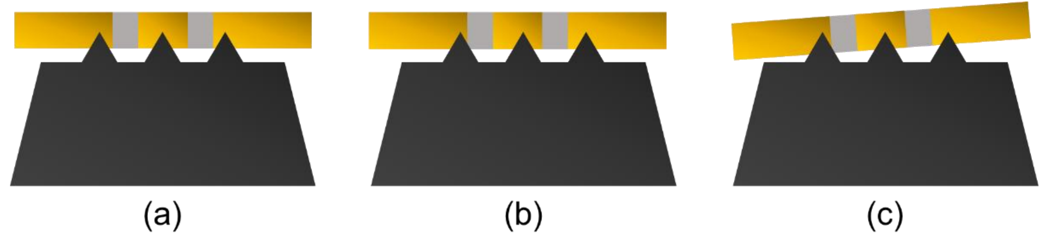

Figure 1.3 Schematic of probe tips alignments (a) no offset (b) translation offset (c) rotation offset.

This work is focused on developing a new generation of an RF on-wafer probe station oversized in terms of probe displacement accuracy, in the nanometre range (3 orders better than existing commercial solution), with ultimate objective to address extreme impedance measurements, such as sub-femto-Farad (fF) capacitance characterization. In particular, the proposed new probe station, built from scratch, is based on piezo-electric nano-positioning stages to control mechanical movements of both the chuck and probes. Indeed, improving the alignment process ensures the overall measurement accuracy and repeatability.

Limitations of manual positioning are addressed in Chapter 3. In particular, we prove that mechanical misalignment of the probe tips during the on-wafer calibration process can lead to 80% measurement uncertainty when measuring extreme impedances in the microwave range. Another issue that is usually faced is the planarization. Repeated probing causes the probe tips to wear out, hence, making them not in the same plane anymore, and increasing the measurement uncertainties. Bad planarization can also be caused by irregularities in the DUT surface or a shift in the probe's tilt (Figure 1.4). Indeed, the tilt of the probe should ensure that all probe tips are on the same plane. Prior to calibration and measurement, specific "contact pads" are available on commercial calibration substrates to check that all tips are contacting or not. All probe tips should leave a similar mark on the "contact pad"'. If not, the operator shifts the tilt of the probe until the result is satisfactory. However, this procedure can be long, time consuming and depends on the operator when done manually.

Figure 1.4 Schematic of a tilted probe.

In addition to the misalignments of the probe onto the measurement pads, other parameters can impact the overall performance, i.e. the overtravel and the skating of the probe onto the surface of the contact pads of the DUT. By definition, the overtravel is "the continued downward movement after the probe tip has made initial contact with the wafer. The skating is the lateral skate distance of the probe tip corresponding to that overtravel" [3]. Figure 1.5 shows a representation of the overtravel and the corresponding skating of the probe tip onto the measurement pad. Usually, probe manufacturers advise the users to apply some overtravel in order to ensure a good electrical contact. The amount of overtravel should be carefully monitored in order not to damage the probe tips and the pads of the DUT. Very often, calibration kit come with alignment marks that guide the user on the amount of overtravel to apply. Figure 1.6.a shows alignment marks from the Impedance Standard Substrate (ISS) 101-190C from FormFactor™ and Figure 1.6.b shows the correct alignment of the probe tips for ACP and Infinity probes from FormFactor™. The overtravel to be applied should be set before running the vector calibration. This also greatly reduces the risk of collision between two probes in the two-port calibration and measurements (when two probes are used simultaneously). The importance and the influence of skating and overtravel in accurate and planar measurements have been widely described in the literature [4], [5], [6]. Throughout this work, we keep referring to the approach advised by the industrial manufacturer of the probes.

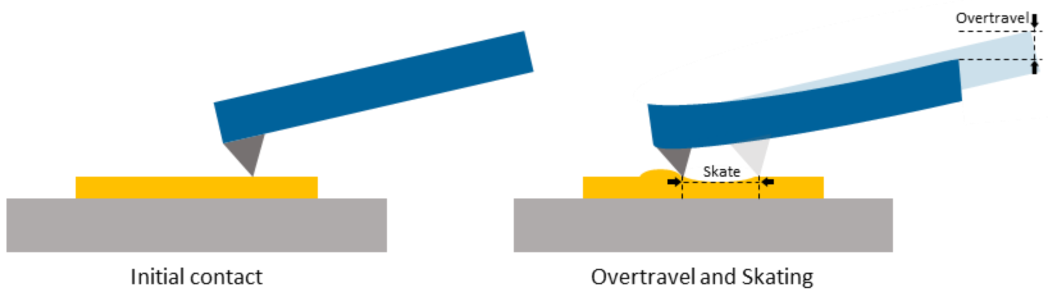

Figure 1.5 Representation of the overtravel and the skating of a probe tip.

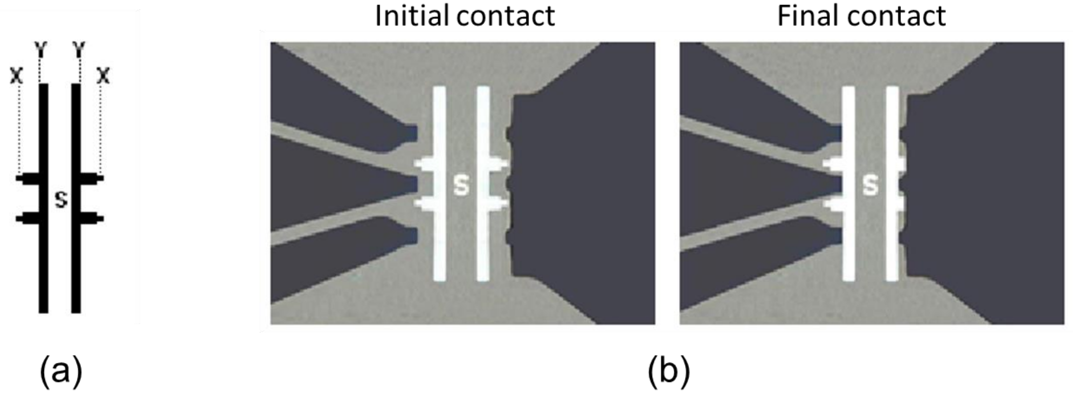

Figure 1.6 (a) ISS 101-190C alignment marks (b) correct alignment of the probe tips of both ACP and Infinity type probes [7].

1.3 Manual probing stations

Manual on-wafer GSG probe stations are used for testing RF planar devices, commonly in CPW form, after the fabrication process. As mentioned in the introduction of this chapter, a manual on-wafer probing station typically consists of an optical system such as camera augmented with a microscope for monitoring the DUT, an RF probe system (one probe or more) that can be positioned over the GSG pads of the DUT using manual and mechanical positioning stages for adjusting the position of the probes. Finally, the DUT is mounted on a chuck that can be also controlled and positioned under the probes. Manual on-wafer probing stations are often used when the number of devices to be tested is relatively small.

There are several vendors that manufacture wafer probe stations. One of the most noteworthy is FormFactor™ (previously Cascade Mirotech®). It provides precision and test solution for the microelectronic industry. FormFactor™ offers a wide range of on-wafer probing stations including manual, semi-automated and automated stations. We present some examples of commercially available probe stations from FormFactor™. Some of the other wafer probe stations manufacturers are KLA-Tencor, Advantest®, Onto Innovation® and Electro Scientific Industries (ESI®). Those vendors provide test and measurement solutions for the semiconductor and microelectronic industries especially for high-volume production testing. The choice of the probe station depends mainly on the applications targeted. The technology including frequency of operation, wafer size, measurement environment (air, temperature), and expected measurement accuracy play a role in this choice.

As it is impossible to detail every existing wafer probe station, we consider representative solutions to give a clear and general picture. Figure 1.7 shows the Cascade MPS150, 150mm

multi-probe test, high speed, high accuracy system. It is used to test a wide range of integrated circuits (ICs) such as memory chips and microprocessors. The MPS150 is highly flexible, mouldable and configurable. The basic configuration includes different functionalities such as RF Basic, mm-wave Basic, failure analysis or high power. It can be easily re-configured or upgraded for new requirements or applications. It also allows quick and easy measurement instruments' integration. The MPS150 is a stable solution as it offers solid station frame and vibration attenuation. It is known to incorporate best-known methods and hence allows highly arcuate measurement results. It is designed to be very user-friendly and is also available for education purpose, under the denomination "Education Kit". Indeed, it ensures simple microscope operation, quick and ergonomic change of the wafer under test and it minimises training efforts. Finally, the travel range of the chuck is 150 mm x 150 mm (6 in. x 6 in.) in X and Y directions together with a resolution of 5 µm. The maximum diameter of the wafer is 150 mm. More details can be found in [8].

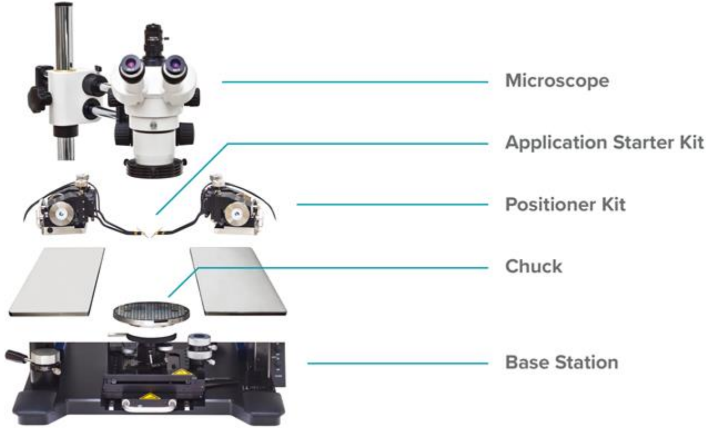

Figure 1.7 MPS150 manual probe station from FormFactor™ [9].

FormFactor™ also propose the 200 mm systems. Among them, there is the Summit, a manual/semi-automated probe system. As the MPS150, it offers high flexibility and ease of use. Its semi-automated version enables high productivity and powerful automation tools thanks to the eVue™ imaging system. These features will be discussed more in the following section. In the 200 mm systems, we can also note the PM8 manual probe system, the EPS200RF manual probe system for RF test up to 67 GHz or the EPS200MMW for testing up to THz and load-pull. More details can be found in [10] [11] [12].

In the last paragraph, we focus specifically on the manual probe positioners available on the stations cited above. They are a crucial part of the probe station, whether they are manual or automated. The positioners hold the probes in place and align them over the pads of the DUT during testing and measurement operations. We can identify three main type of manual positioners: DC probe positioners, RF probe positioners and vacuum/cryogenic probe positioners. Each type offers multiple advantages, each product having different dimensions, travel range, resolution, applications and other features. As the core of this work is directed towards accurate positioning for RF applications, we can mention that the typical resolution for the RF probe positioners is around one µm (>1 µm as announced by the manufacturer). Figure 1.8 illustrates some of the manual RF probe positioners from FormFactor™.

These manual probe positioners are designed to be highly precise, allowing users to position probes with a high level of accuracy and repeatability. Nevertheless, as suggested by their

commercial denomination, manual probe positioners require manual operations, which can be slower and less precise than their automated counterparts. It may be an issue for applications where high-speed testing or very precise positioning is required. In this work, we demonstrate that manual positioners become quickly problematic for the characterization of RF extreme impedances [13]. This kind of positioners is also very operator skill dependent. The measurement accuracy and repeatability depend also on the dexterity and experience of the operator. It is even more problematic when multiple operators are involved in the measurements or when the operator is not well trained.

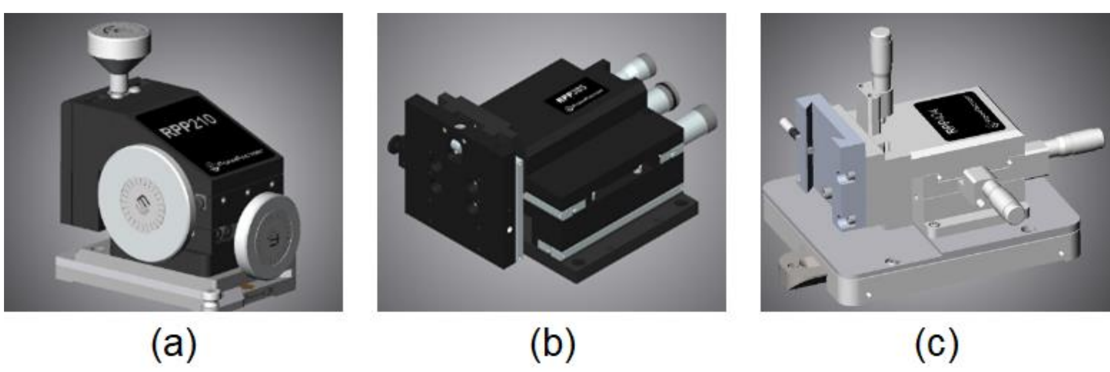

Figure 1.8 FormFactor™ manual probe positioners (a) RPP210 (b) RPP305 (c) EPP404 [14].

1.4 Semi-automated/automated probing stations

Semi-automated and automated probe stations unlike the manual one, are equipped with automation features that enable some or all the aspects of the testing process to be carried out automatically, such as the alignment of the probes over the pads of the DUT. This can reduce the amount of manual work required and improve the measurement accuracy and repeatability. The difference between semi-automated and automated is the degree of automation that is embedded in the station. For example, the semi-automated stations still require manual intervention in the initial alignment of the probes. Automated stations on the other hand, are built with a high level of automation and do not need any manual adjustments. In short, they are capable of carrying out the entire testing process without any intervention from the operator. They are usually used in high-volume manufacturing environments where efficiency and time saving are prioritized.

Formfactor™ offers a large choice of semi-automated and fully automated probe stations, each one more or less adapted for a certain application. We will give some examples with the most important features. In the 200 mm systems, we can cite the SUMMIT200, represented in Figure 1.9.a, an advanced semi-/fully automated probe station. The SUMMIT200 has been designed for high accuracy and high-speed measurements on single or volume wafer. Some of the applications targeted by the station are ultra-low noise, DC, RF, mm-wave and THz frequency operation. It is equipped with PureLine (spectral noise cancelling), AutoGuard and MicroChamber (low-leakage and low-capacitance measurements) technologies in order to achieve high accuracy measurements. It also allows accurate RF/mm-wave measurements and calibration with integrated tools such as WinCal XE™. As its name states, it has a 200 mm stage and automated wafer handling. Finally, it comes with eVue™ digital imaging system, allowing enhanced optical visualization and wafer navigation and with Velox Probe station

Control Software to perform autonomous testing (alignment and mapping over multiple temperatures). More details can be found in [15].

Figure 1.9.b represents the CM300xi, a 300 mm semi-/fully automated probe system. Like the SUMMIT200, it is equipped with the constructor's latest technologies to enable accurate and repeatable measurements. The CM300xi probe station tackles challenges brought by complex measurement environments. Some of the applications cover DC, AC and RF/microwave device characterization and design debug. It also enables automated tests and thermal measurements. More details can be found in [16].

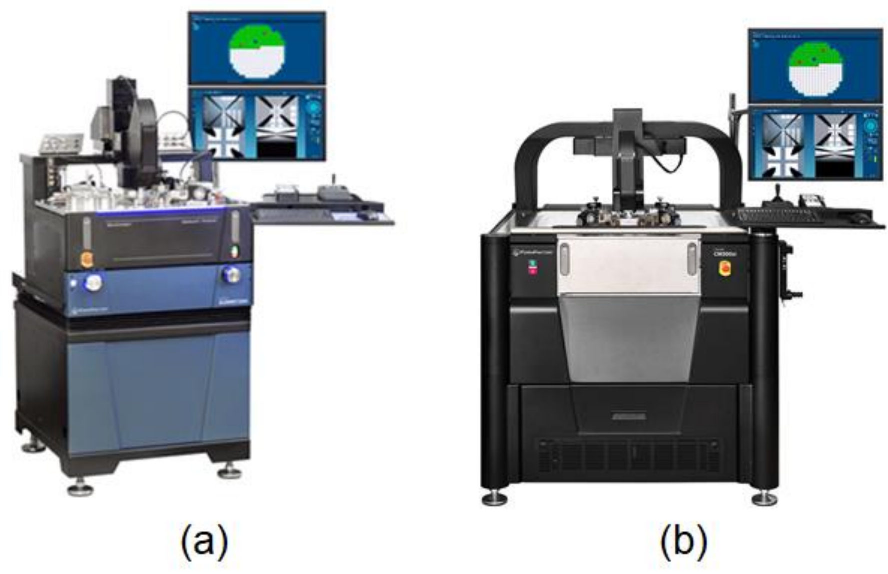

Figure 1.9 FormFactor™ (a) SUMMIT200 (b) CM300xi [15] [16].

As for the manual station, the key element of the probing station is the nature of the probe positioners. We can identify two type of automated or also called motorized probe positioners developed by FormFactor™. For example, the motorized RF probe positioner RP504 for autonomous RF, mm-wave and THz measurements is represented in Figure 1.10. It is compatible with multiple probes and probe stations. Its resolution is around 1 µm (>1 µm as announced by the manufacturer). It enables fully autonomous and hand free measurements over multiple temperatures. The second type is the motorized HexNano probe Positioners for autonomous Silicon Photonics measurements. FormFactor™ offers a completely integrated solution to measure photonic devices without further development. More details can be found in [14].

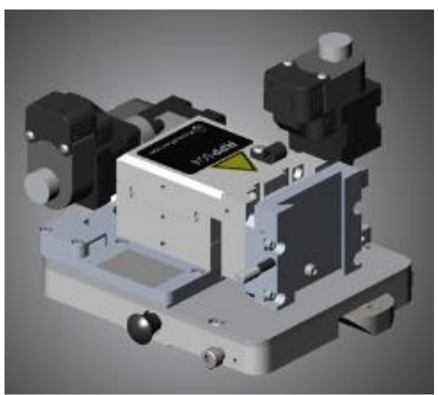

Figure 1.10 FormFactor™ motorized RF probe positioner RP504 [14].

1.5 Radio-frequency (RF) probe technology

RF GSG wafer probes are used to measure the electrical properties of RF devices integrated onto CPW test structures, the so-called on wafer characterization. They allow relatively precise RF characterisation of the electrical RF characteristics to ensure that the device meets the required specifications. They are also used for design verification and quality control. RF wafer probes can also help identify the cause of failures in ICs and improve the design and the manufacturing process to prevent similar failure from occurring again.

Over the last three to four decades, RF probe technology witnessed an impressive progress. Today's technologies allow measurements up to 1.1 THz. RF wafer probes manufacturers are constantly improving their technologies and including new features that cover a wide range of applications: impedance matching, multiport, differential and mixed-signal measurement up to 110 GHz, temperature beyond 500 °C and down to 4 K, high-power measurements up to 60 W in continuous-wave mode and THz and photonic applications.

In [17], the authors presented a complete review of the evolution of the RF wafer probe technology. Based on [17], we present a brief history and cite the main advances through the years.

The first notable study using RF probes up to 4 GHz was demonstrated in [18], where the probes featured a 50-Ω microstrip line with a short wire tip that connected the device under test (DUT) pads through a hole in the probe substrate. In [19], this concept was investigated further where the aim was to achieve repeatable measurements above 4 GHz. Soon, the development of the 50-Ω planar transmission line probe, allowed a significant breakthrough in the on-wafer RF probe technology. It allowed bringing the 50-Ω environment very close to the DUT pads. In addition, the probe contacts were realized small as gold balls, allowing a reliable and repeatable contact. Other specifications (probe planarization and shifting the measurement reference plane to the tips of the probe) also became the "common rules" for decades regarding the RF probe technology. In particular, moving the probe design from microstrip to coplanar waveguide (CPW) simplified the fabrication process (Figure 1.11). Rapidly, Tektronix® made the first RF probe considered as a real product for the RF semiconductor industry.

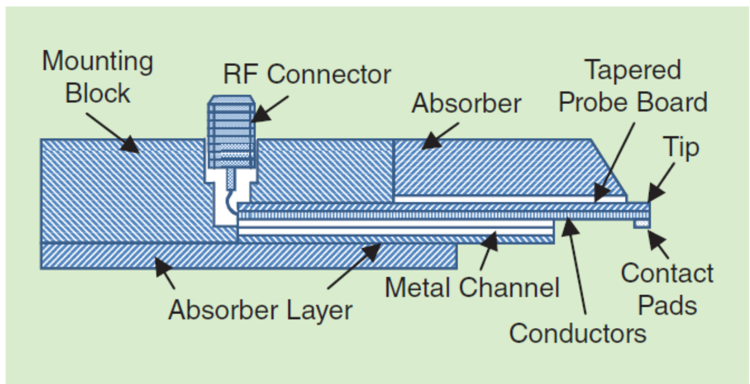

Figure 1.11 Design of an on-wafer probe based on ceramic technology [17].

In Figure 1.12, authors in [17] show the evolution of probe technologies over the years. We can observe an exponential increase in frequency capabilities of RF probes, the development of new probe technologies and a list of probe manufactures. The figure may not show the exact dates and has not been updated. Still, it draws an overall picture of the evolution of probe technology.

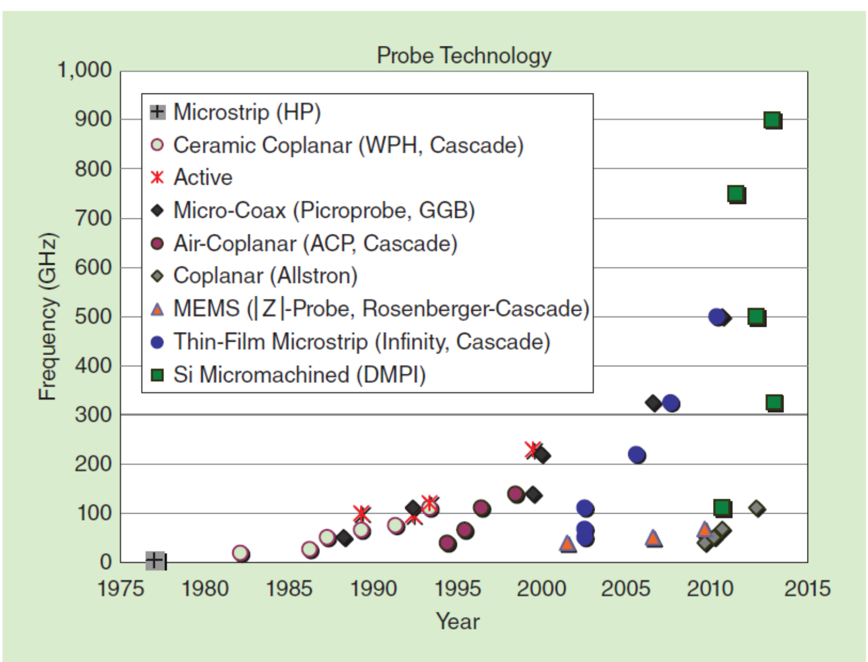

Figure 1.12 Evolution of the RF probing technology [16].

In the 1980s, Tektronix® developed the first RF probe model TMP9600 and the sapphire calibration substrate CAL96 (Figure 1.13) [20], [21]. Later, they were followed by Cascade Microtech®, which became the main supplier of RF probes to the industry after Tektronix® stepped out of the probe business in the early 1990s. In order to meet the needs of the rapidly developing monolithic microwave integrated circuits (MMICs), the frequency range of the WPH probe quickly expanded to 26 GHz in 1987 [22] and to 50 GHz in 1991 [23]. In 1988, Cascade Microtech® introduced a series of 26.5 GHz replaceable-tip probes (RTPs), improving ease of use in volume-production applications by allowing a quick replacement of the ceramic tip [24]. Despite their contribution to the microwave technology in the 1980s and 1990s,

ceramic CPW line probes remained fragile and expensive, which led to their inevitable replacement by alternative technologies as shown in Figure 1.13.

In 1988, GGB Industries® patented the RF probes based on micro-coaxial cables (Picoprobe) [25], which offered several technical benefits: extended lifespan and cheaper cost, easy and quick repair for damaged probes, improved insertion loss and simplified manufacturing process. In 1993, GGB introduced a W-band probe at the IEEE Microwave Theory and Techniques Society International Microwave Symposium (IMS) [26]. Over the years, they improved their technology, achieving frequencies of 220 GHz in 1999 [27], 325 GHz in 2006 and 500 GHz in 2012 [28], [29].

In 1994, Cascade® presented their 40 GHz air-coplanar probe (ACP) [30]. Couple of years later, ACP probes had reached frequencies of 110 GHz (1-mm connector model) and 140 GHz (waveguide based model) [31], effectively replacing the WPH product line. Many engineers still prefer the ACPs for probing on gold pads (soft and non-destructive touch).

In 2000, Rosenberger introduced a new concept for RF probes for PCB applications [32]. The next year, in 2001, Rosenberger in partnership with Karl Suess KG (later SUSS MicroTec), scaled down the probe geometry to the wafer-level requirements. The same year, they introduced the new RF probe |Z|-Probe [33], covering the 40 GHz range. The |Z|-probe featured: a direct transition from the coaxial connector to the air-isolated coplanar contact line, transition within the probe body minimizing possible discontinuities, coplanar contacts made using ultraviolet lithography and electroplating process (UV-LIGA) providing accurate shape and a constant air gap. The coplanar contacts were made from Nickel (Ni), allowing optimal contact performance on both Aluminum (Al) and gold (Au) contact pads.

In 2002, Cascade Microtech® launched a new wafer probe bases on thin-film technology [34]. This new Infinity Probe demonstrated higher contact consistency and very low probe-to-probe crosstalk. Infinity Probes were available for 40, 50, 67 and 110 GHz frequencies. In 2005 and 2007, the waveguide probes for 220 and 325 GHz frequencies were introduced respectively [35], [36]. After several design interactions, Cascade began offering an Infinity probe for the 500 GHz band in late 2009 as a custom product. Recently, they introduced the InfinityXT Probe with improved tip life and durability [37].

Between 2009 and 2011, two new companies entered the probing market: DMPI focused on micromachined probes for the emerging sub-THz market, while Allstron, Inc. from Taiwan offered affordable probes for application below 110 GHz to reduce testing costs. Allstron's probes conventionally use a microcoaxial cable and air-isolated coplanar waveguide (CPW) contact structure (similar to ACP), but with a tip designed for probing on Al pads with small passivation windows.

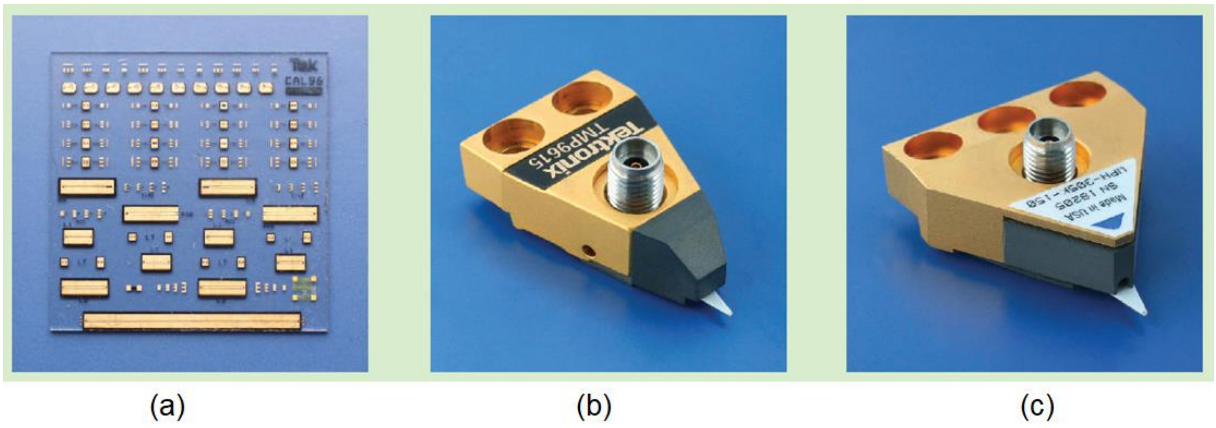

Figure 1.13 (a) The first commercial sapphire calibration substrate CAL96 (b) the Tektronix® RF wafer probe TMP9600 (c) the WPH probe from Cascade Microtech®. (Pictures courtesy of FBH) [17].

A conventional RF probe consists of four main components: a test instrumentation interface (waveguide or coaxial), a transition connecting the test interface to a microcoaxial cable, a transition connecting the microcoaxial cable to a planar waveguide (CPW or microstrip), a coplanar interface connecting the probe to the pads of the DUT.

There are various technologies for designing and attaching probe tips to the probe (Figure 1.14). Picoprobe® and GGB® use the signal conductor of the microcoaxial cable to shape the signal tip, and the ground blades are soldered from both sides of the cable. ACP, Cascade Microtech®, and Allstron Probes use an air-isolated CPW tip that is attached to the microcoaxial cable. Infinity Probe from Cascade Microtech® uses a flexible polyamide microstrip line that ends with CPW tips, which is attached to the microcoaxial cable. The |Z|-Probe from Rosenberger-Cascade Microtech® uses direct transmission from the coaxial connector to the air-isolated CPW contacts, without a micro-coaxial cable. The 500 GHz Infinity Probe uses direct transmission from the rectangular waveguide to a polyamide microstrip line. DMPI uses a direct transition from rectangular waveguide to a micromachined silicon CPW contact structure.

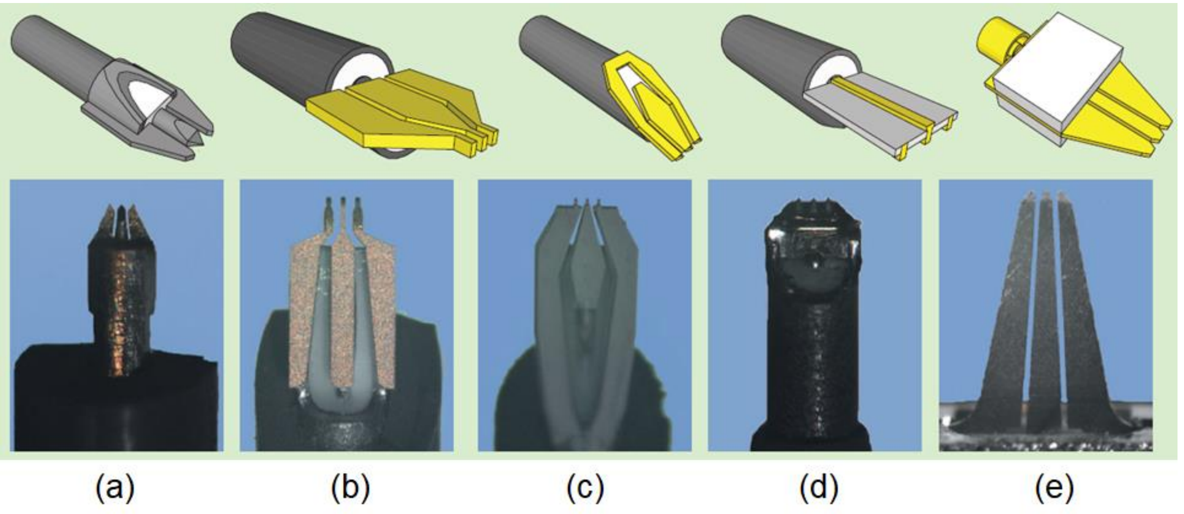

Figure 1.14 GSG probe tip technologies: (a) Picoprobe® (top view, 100-nm pitch) (b) ACP (125-µm pitch) (c) Allstron (100-nm pitch) (d) Infinity Probe (125-µm pitch; all bottom view) and (e) |Z| Probe (125-µm pitch). (Pictures courtesy of FBH) [17].

1.6 Probe mechanical layout rules

Working with on-wafer probes require a good understanding of the probes mechanical layout. We work with Infinity GSG probes from FormFactor™. There are two important probe mechanical parameters to keep in mind when using the Infinity probes: the contact dimensions and the substrate extension past the contact. Figure 1.15 shows a Scanning Electron Microscope (SEM) photo of an $100\ \mu m$ Infinity probes. The typical contact size for the Infinity probes is $12 \times 12\ \mu m$. Knowing the contact size is important as the passivation window must be large enough in order to allow the entire contact to touch the pad. The minimum pad size when manually placing the probes is $25 \times 35\ \mu m$, and the recommended minimum size for either manual or semi-/fully-automated probe placement is $50 \times 50\ \mu m$. If narrow pitch probes are used ($50/75\ \mu m$ pitch probes), the minimum pad size should be $30 \times 50\ \mu m$. However, the recommended combination is $100 \times 100\ \mu m$ pads with a $150\ \mu m$ pitch. The substrate extension is typically $100\ \mu m$ past the contact center. As stated before, the probes skate when a good electrical contact is achieved. For every $50\ \mu m$ of overtravel, the probes will skate laterally $25\ \mu m$. Therefore, there must be enough space between two probes to allow skating. Figure 1.16 shows some of the recommendation rules from FormFactor™ [38].

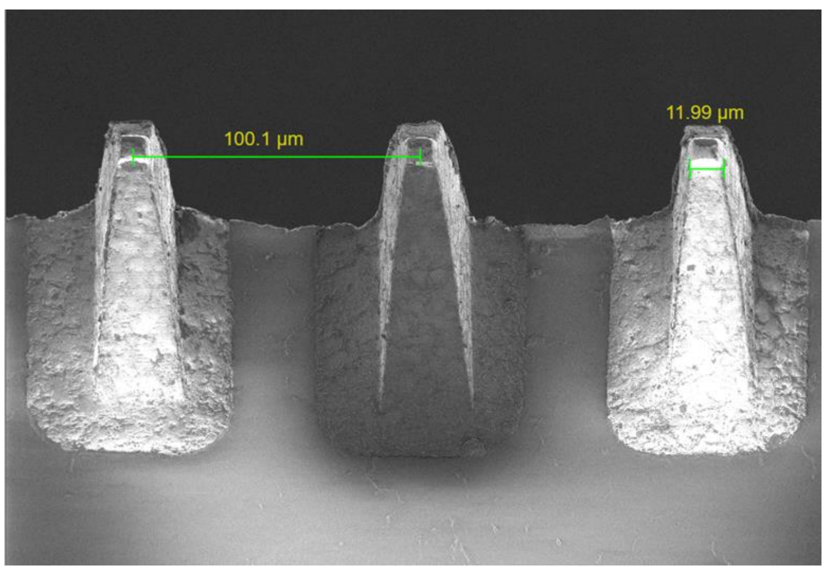

Figure 1.15 SEM photo of a 100 µm Infinity GSG probe from FormFactor^{TM}.

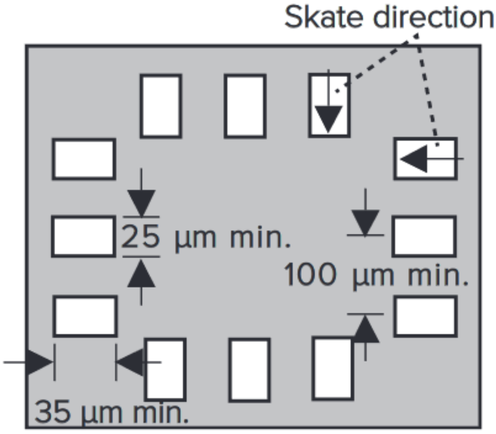

Figure 1.16 Some of FormFactor^{TM} recommendations for working with Infinity probes: minimum pad size is 25 x 35 µm, minimum pad pitch is 100 µm (50 µm for fine pitch probes) [38].

1.7 EQUIPEX ExCELSiOR Micro-probes

Another challenge in making on-wafer measurement with RF probes is the mismatch between extreme impedance devices and the CPW access pads. Indeed, the CPW pads are the electrical transition between the nano-devices and the probes. Considering the size of the contact pads, parasitic effect become important and lead to mediocre measurement of RF nano-devices. In previous thesis work among our team [39], performed within the National EQUIPEX ExCELSiOR (www.excelsior-ncc.eu) project and European project 14Ind02 PlanarCal (Microwave measurements for planar circuits and components), including European NMIS METAS (Switzerland), NPL (United Kingdom), PTB (Germany), VSL (Netherlands), a robtotic on-wafer probe station has been developed at the IEMN laboratory. Two generation of miniaturized RF probes have also been developed [40] [41]. The miniaturized probes, designed to support a few mN forces, were mounted on nano-positioners in order to precisely control their movement and their positioning over the DUTs. Finally, the traditional optical microscope

has been replaced by an SEM (Figure 1.17). As an example of the miniaturized probes, Figure 1.18 shows the first generation of microprobes. The microprobes are integrated on specific PCBs. The PCB is connected to the Nanoprober via a U.FL – SMA cable, allowing a frequency range of a few GHz.

The work realized in [39] proved that the development of nanoprobes is essential to accurately characterize nano-devices. However, the solution requires the integration of the solution in a SEM, that is not compatible with an industrial context. In this work, we extend this solution to be integrated into commercial environment. Therefore, we use commercially available probes coupled with precise nano-positioners in order to increase the measurement repeatability and accuracy of the overall on-wafer RF probing process.

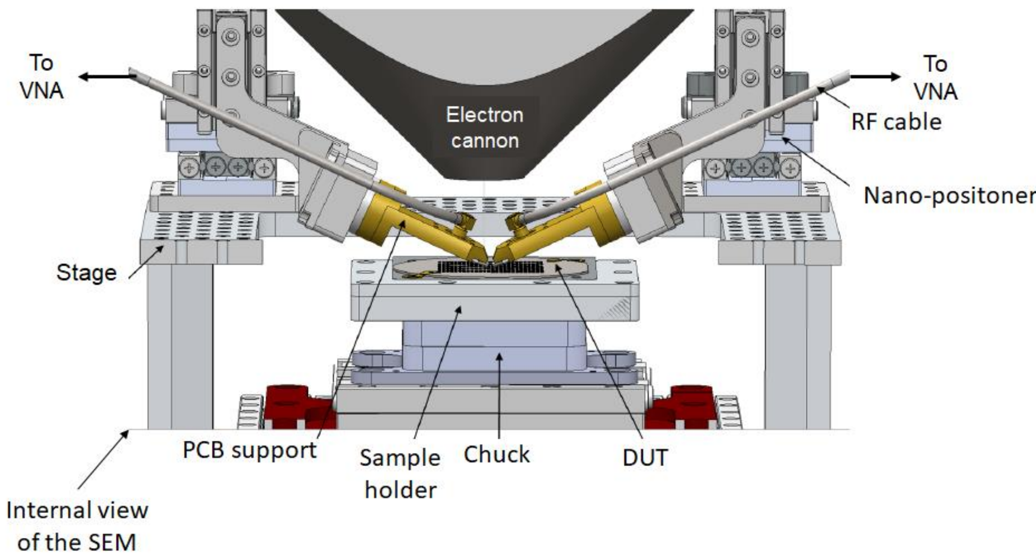

Figure 1.17 Schematic representation of the Nanoprober developed in [39].

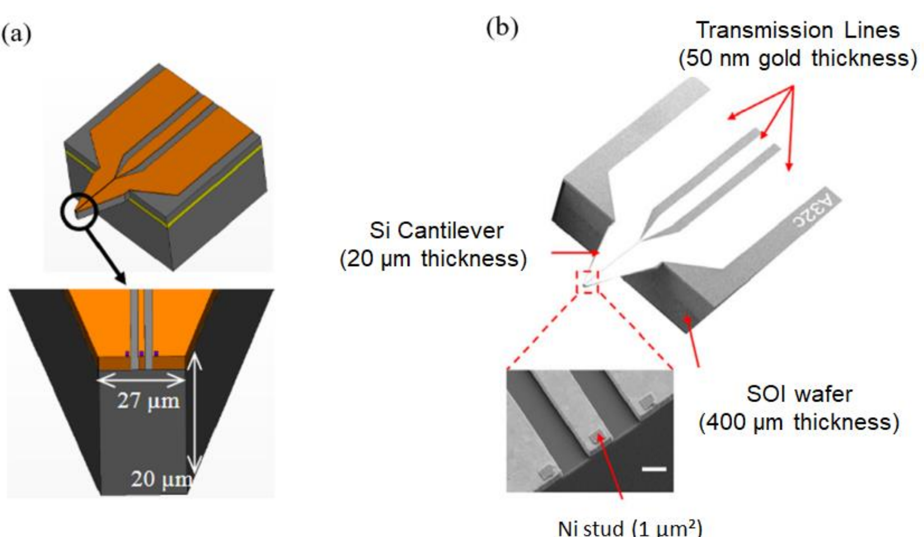

Figure 1.18 First generation of microprobes [42] [40] [43]. (a) Synoptic diagram. (b) SEM photo of the first generation microprobe.

1.8 Automated on-wafer probing in the research field

Many groups, in particular National Metrology Institutes (NMIs) are developing new and more accurate automated probing techniques for on-wafer measurements. In this section, we highlight the main contributions.

In the National Institute of Advanced Industrial Science and Technology (AIST), Ibaraki, Japan, Ryo Sakamaki and Masashiro Horibe have been working on automated on-wafer process for many years now. In [44] and [45], they introduced source of on-wafer measurements uncertainties. They demonstrated lower uncertainties regarding the probe positioning on verification devices when working with automatic probers. Later, in [46], Ryo Sakamaki and Masashiro Horibe presented a fully automated probe station that relies on the RF signal detection in order to determine the distance between the probes and align them correctly. In addition, authors designed an original Impedance Standard Substrate (ISS) with a 50-Ω transmission line and alignment patterns to define the origin coordinates of the probes. The proposed technique showed improvements in the measurement repeatability when evaluating the 50-Ω matched transmission line. In [47] and [6], authors presented an automated method for precise adjustment of the probe-tilt. The method is based on detecting the resonance created when two or three of the probe tips make contact with the substrate "In the case of a GSG probe, an inductance should exist between each ground and signal probe tip when all the GSG probe tips are in good contact with the filled-conductor pad. Therefore, no resonance should be observed in this case. In contrast, a capacitance should exist between the signal and floating ground probe tip when one of the probe tips is not in contact with the conductor" [6]. An adjustment algorithm base on the RF Signal Detection RSD technique was also implemented in order to improve the measurement repeatability. The proposed technique improved the alignment of the probe parallel to the substrate (probe-tilt angle). In [48], authors tackled the limitations of the RSD technique (devices with complicated structures) by relying on machine learning algorithm. The algorithm is based on the Local Outlier Factor (LOF) in order to detect changes in the structure. The technique was tested and compared to a conventional automatic probing technique. As a result, the difference in the probe position was approximatively 1 µm, hence, proving the validity of the machine-learning based technique.

Other researchers contributed to the development of new techniques in order to face the on-wafer measurements and repeatability. At VSL-Dutch Metrology Institute, Netherlands, Faisal Ali Mubarak and his team worked on automated solutions to address accurate on-wafer probing in the mm-wave and sub-mm-wave frequency regimes. In [49], authors proposed an automated solution to detect contact between the probe and the Device Under Test (DUT) using a photo sensitive detector (PSD) and a laser unit and in [50], authors used a vision based multi-target tracking technique for automatic probes alignment. At the ElectroScience Laboratory, The Ohio State University, researchers have been working on non-contact probes for on-wafer characterization [51] [52] [53] [54] [55] [56]. In [51] and [52], authors presented the development of a new approach for on-wafer measurements in the mm-wave and the THz frequency bands. The method is based on "radiative coupling of Network Analyzer's test ports into coplanar environment of monolithic device (DUT) through integrated planar THz antennas" [51]. Later, in [53] and [54], they introduced the use of automated stages to do the positioning of the probes. The non-contact nature of the system allow to use two automated axis only as opposite to the conventional three or four axis. Authors demonstrated that using automated and computer control into the system enables fast and repeatable measurements.

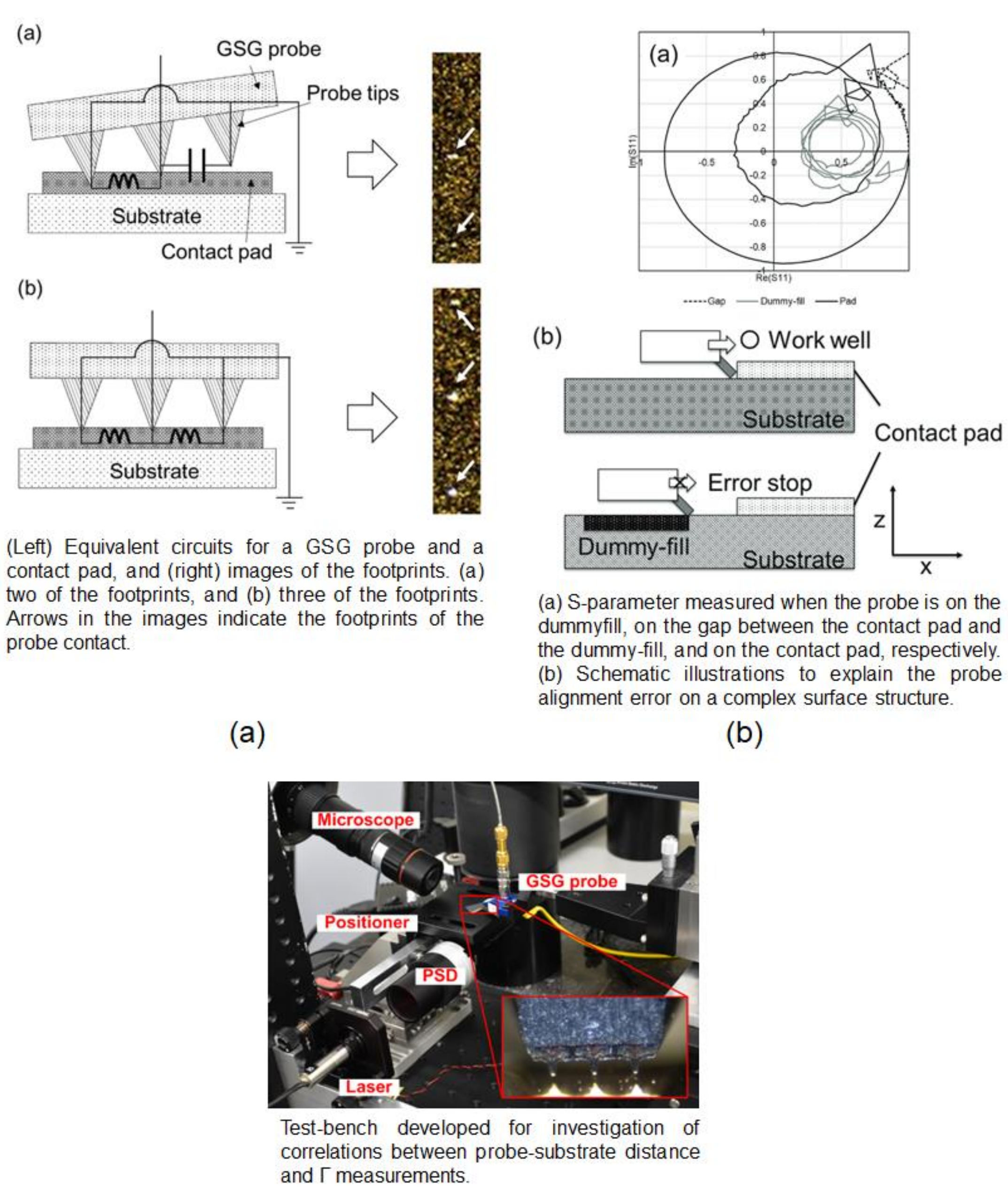

Figure 1.19 (a) Resonance detection technique when three probe tips contact with the substrate [47]. (b) illustration of the RSD techniques when dealing with complicated structures [48]. (c) automated contact detection between the probe and the DUT using a PSD and a laser unit [49].

1.9 Conclusion

With the continuous advancements in technology, automated on-wafer probing techniques play a vital role in the semi-conductor industry, providing reliable and efficient means of conducting high-precision electrical measurements. Over the years, those stations gained more interest from researchers as well as industrials. This chapter provided an overview of on-wafer probe stations and their basic sub-systems. The probe alignment on the calibrations structures and the measurement pads were also discussed. The chapter presented some manual, semi-automated and fully-automated probe stations that can be found on the market nowadays. The evolution of the RF probe technology over the years was also discussed, highlighting the advancements made in the field. Furthermore, the chapter explored the use of automated techniques designed for on-wafer probing in research, which has proven to be an effective mean in order to tackle the dilemma of precise and repeatable on-wafer calibration and measurements. Despite the complexity of such techniques and the level of control it calls for, the benefits of automation cannot be overstated. The next chapter summarizes the theoretical basics and mathematical notions regarding RF measurements as well as RF measurement instruments used in this field.

1.10 References

[1] ‘2022IRDS_ES.pdf’. Accessed: Apr. 17, 2023. [Online]. Available: https://irds.ieee.org/images/files/pdf/2022/2022IRDS_ES.pdf

[2] A. Rumiantsev, ‘On-Wafer calibration techniques enabling accurate characterization of high-performance silicon devices at the mm-wave range and beyond’, 2014.

[3] ‘Infinity Probe Mechanical Layout Rules.pdf’. Accessed: Apr. 17, 2023. [Online]. Available: https://www.formfactor.com/download/infinity-probe-mechanical-layout-rules/?wpdmdl=1850&refresh=643d3e91e14761681735313

[4] K. Daffe, J. Marzouk, C. Boyaval, G. Dambrine, K. Hadaddi, and S. Arscott, ‘A comparison of pad metallization in miniaturized microfabricated silicon microcantilever-based wafer probes for low contact force low skate on-wafer measurements’, *J. Micromechanics Microengineering*, vol. 32, no. 1, p. 015007, Jan. 2022, doi: 10.1088/1361-6439/ac3cd7.

[5] R. Sakamaki and M. Horibe, ‘Uncertainty Analysis Method Including Influence of Probe Alignment on On-Wafer Calibration Process’, *IEEE Trans. Instrum. Meas.*, vol. 68, no. 6, pp. 1748–1755, Jun. 2019, doi: 10.1109/TIM.2019.2907733.

[6] R. Sakamaki and M. Horibe, ‘Precision Adjustment of Probe-Tilt Angle With RF Signal Detection Technique’, *IEEE Trans. Instrum. Meas.*, vol. 69, no. 10, pp. 8500–8505, Oct. 2020, doi: 10.1109/TIM.2020.2991601.

[7] ‘iss-map-101-190.pdf’. Accessed: Apr. 17, 2023. [Online]. Available: https://www.formfactor.com/download/iss-map-101-190/?wpdmdl=3159&refresh=643815fcd07041681397244

[8] ‘mps150-data-sheet.pdf’. Accessed: Apr. 17, 2023. [Online]. Available: https://www.formfactor.com/download/mps150-data-sheet/?wpdmdl=3221&refresh=643d38df261911681733855

[9] ‘MPS150’, FormFactor, Inc. Accessed: Apr. 17, 2023. [Online]. Available: https://www.formfactor.com/product/probe-systems/150-mm-systems/mps150/

[10] ‘pm8-product-highlights.pdf’. Accessed: Apr. 17, 2023. [Online]. Available: https://www.formfactor.com/download/pm8-product-highlights/?wpdmdl=3387&refresh=643d3955683ee1681733973

[11] ‘eps200rf-product-flyer.pdf’. Accessed: Apr. 17, 2023. [Online]. Available: https://www.formfactor.com/download/eps200rf-product-flyer/?wpdmdl=3307&refresh=643d398a672aa1681734026

[12] ‘summit-data-sheet.pdf’. Accessed: Apr. 17, 2023. [Online]. Available: https://www.formfactor.com/download/summit-data-sheet/?wpdmdl=3326&refresh=643d4a351a3e81681738293

[13] C. Mokhtari, M. Sebbache, V. Avramovic, C. Boyaval, G. Dambrine, and K. Haddadi, ‘Impact of GSG Probe to Pads Contact Repeatability for On-Wafer RF Measurements’, in *2021 IEEE 7th International Conference on Smart Instrumentation, Measurement and Applications (ICSIMA)*, Aug. 2021, pp. 241–246. doi: 10.1109/ICSIMA50015.2021.9526303.

[14] ‘probe-positioners-brochure.pdf’. Accessed: Apr. 17, 2023. [Online]. Available: https://www.formfactor.com/download/probe-positioners-brochure/?wpdmdl=20350&refresh=643d3a2edf4211681734190

[15] ‘SUMMIT200’, FormFactor, Inc. Accessed: Apr. 17, 2023. [Online]. Available: https://www.formfactor.com/product/probe-systems/200-mm-systems/summit200/

[16] ‘CM300xi’, FormFactor, Inc. Accessed: Apr. 17, 2023. [Online]. Available: https://www.formfactor.com/product/probe-systems/300-mm-systems/cm300xi/

[17] A. Rumiantsev and R. Doerner, ‘RF Probe Technology: History and Selected Topics’, *Microw. Mag. IEEE*, vol. 14, pp. 46–58, Nov. 2013, doi: 10.1109/MMM.2013.2280241.

[18] R. Van Tuyl, C. Liechti, R. Lee, and E. Gowen, ‘4-GHz frequency division with GaAs MESFET ICs’, in *1977 IEEE International Solid-State Circuits Conference. Digest of Technical Papers*, Feb. 1977, pp. 198–199. doi: 10.1109/ISSCC.1977.1155641.

[19] E. Strid and K. R. Gleason, ‘A microstrip probe for microwave measurements on GaAs FET and IC wafers’, in *IEEE Gallium Arsenide Integrated Circuit Symp.*, Las Vegas, NV, 1980, p. Paper 31.

[16]26W-7064 TEK CAL96 Calibration Substrate. Specifications, Ordering Information, CAL96 Calibration Substrate, Tektronix Inc., Beaverton, OR, 1989.

[17] 47W-7833-1 TEK TMP9600 Series. Specifications, Ordering Information, TMP9600 Series Microwave Probes-DC to 40 GHz, Tektronix Inc., Beaverton, OR, 1990.

[18] E. Strid, “26 GHz wafer probing for MMIC development and manufacture,” Microwave J., vol. 29, pp. 71–82, Aug. 1986.

[19] K. E. Jones, E. W. Strid, and K. R. Gleason, “mm-wave wafer probes span 0 to 50 GHz,” Microwave J., vol. 30, pp. 177–183, Apr. 1987.

[20] Manufacturing Economies Provided by Replaceable-Tip Microwave Probes, Cascade Microtech MicroProbe, Beaverton, OR, Oct. 1988.

[21] G. Boll and H. Boll, “Integrated circuit probing apparatus,” U. S. Patent 4 871 964, Oct. 3, 1989.

[26] S. M. J. Liu and G. G. Boll, ‘A new probe for W-band on-wafer measurements’, in *1993 IEEE MTT-S International Microwave Symposium Digest*, Jun. 1993, pp. 1335–1338 vol.3. doi: 10.1109/MWSYM.1993.277123.

[23] T. Gaier, L. Samoska, C. Oleson, and G. Boll, “On-wafer testing of circuits through 220 GHz,” in Proc. Ultrafast Optics Electronics Conf., Snowmass, CO, 1999, pp. 20–26

[28] A. K. Fung, D. Dawson, L. Samoska, K. Lee, C. Oleson, and G. Boll, ‘On-Wafer Vector Network Analyzer Measurements in the 220-325 GHz Frequency Band’, in *2006 IEEE MTT-S International Microwave Symposium Digest*, Jun. 2006, pp. 1931–1934. doi: 10.1109/MWSYM.2006.249811.

[29] A. Fung *et al.*, ‘On-Wafer S-Parameter Measurements in the 325–508 GHz Band’, *IEEE Trans. Terahertz Sci. Technol.*, vol. 2, no. 2, pp. 186–192, Mar. 2012, doi: 10.1109/TTHZ.2011.2182369.

[30] E. M. Godshalk, J. Burr, and J. Williams, ‘An Air Coplanar Wafer Probe’, in *43rd ARFTG Conference Digest*, May 1994, pp. 70–75. doi: 10.1109/ARFTG.1994.327060.

[27] Agilent 8510 System Solutions 5965-8837E, Agilent Technologies, Inc., Santa Rosa, CA, 2000.

[32] M. Wollitzer, B. Rosenberger, and W. Strasser, ‘Novel Concept for a Modular Millimeterwave Probe Tip’, in *55th ARFTG Conference Digest*, Jun. 2000, pp. 1–3. doi: 10.1109/ARFTG.2000.327415.

[33] M. Wollitzer, S. Thies, and S. Schott, ‘New Probing Technology Now Enables Impedance Controlled On-Wafer Probing’, in *2001 31st European Microwave Conference*, Sep. 2001, pp. 1–4. doi: 10.1109/EUMA.2001.339187.

[34] A. M. E. SafWat, M. Andrews, L. Hayden, K. R. Gleason, and E. Strid, ‘A probe technology for 110+ ghz integrated circuits with aluminum pads’, in *59th ARFTG Conference Digest, Spring 2002.*, Jun. 2002, pp. 60–66. doi: 10.1109/ARFTGS.2002.1214682.

[35] R. L. Campbell, M. Andrews, T. Lesher, and C. Wai, ‘220 GHz wafer probe membrane tips and waveguide-to-coax transitions’, in *2005 European Microwave Conference*, Oct. 2005, p. 4 pp. – 1006. doi: 10.1109/EUMC.2005.1610098.

[36] R. Campbell, M. Andrews, L. Samoska, and A. Fung, ‘Membrane Tip Probes for On-Wafer Measurements in the 220 to 325 GHz Band’.

[37] ‘InfinityXT Probe’, FormFactor, Inc. Accessed: Apr. 17, 2023. [Online]. Available: https://www.formfactor.com/product/probes/infinity/infinityxt-probe/

[38] ‘Infinity Probe Mechanical Layout Rules’.

[39] K. Daffe, ‘Caractérisation Hyperfréquence Sous Pointes de Nano Dispositifs : Métrologie et Instrumentation’, 2018.

[40] J. Marzouk *et al.*, ‘MEMS probes for on-wafer RF microwave characterization of future microelectronics: design, fabrication and characterization’, *J. Micromechanics Microengineering*, vol. 25, no. 7, p. 075024, Jul. 2015, doi: 10.1088/0960-1317/25/7/075024.

[41] J. Marzouk *et al.*, ‘Miniaturized Microcantilever-based RF Microwave Probes Using MEMS Technologies’, *Procedia Eng.*, vol. 87, pp. 692–695, Dec. 2014, doi: 10.1016/j.proeng.2014.11.631.

[42] K. Daffe, ‘Caractérisation Hyperfréquence Sous Pointes de Nano Dispositifs : Métrologie et Instrumentation’, 2018.

[43] J. Marzouk *et al.*, ‘Optimization of a microelectromechanical systems (MEMS) approach for miniaturized microcantilever-based RF microwave probes’, *Sens. Actuators Phys.*, vol. 238, Dec. 2015, doi: 10.1016/j.sna.2015.10.043.

[44] R. Sakamaki and M. Horibe, ‘Development of verification process for on-wafer measurement at millimeter-wave frequency’, in *2016 Conference on Precision Electromagnetic Measurements (CPEM 2016)*, Jul. 2016, pp. 1–2. doi: 10.1109/CPEM.2016.7540617.

[45] R. Sakamaki and M. Horibe, ‘Evaluation of verification devices with precise probe measurement system in NMIJ’, in *2016 URSI Asia-Pacific Radio Science Conference (URSI AP-RASC)*, Aug. 2016, pp. 481–482. doi: 10.1109/URSIAP-RASC.2016.7601235.

[46] R. Sakamaki and M. Horibe, ‘Realization of Accurate On-Wafer Measurement Using Precision Probing Technique at Millimeter-Wave Frequency’, *IEEE Trans. Instrum. Meas.*, vol. 67, no. 8, pp. 1940–1945, Aug. 2018, doi: 10.1109/TIM.2018.2806058.

[47] R. Sakamaki and M. Horibe, ‘Proposal of a Precision Probe-Tilt Adjustment with the RF Signal Detection Technique’, in *2018 Conference on Precision Electromagnetic Measurements (CPEM 2018)*, Jul. 2018, pp. 1–2. doi: 10.1109/CPEM.2018.8500884.

[48] R. Sakamaki and M. Horibe, ‘Automatic probing system with machine learning algorithm’, in *2021 96th ARFTG Microwave Measurement Conference (ARFTG)*, Jan. 2021, pp. 1–4. doi: 10.1109/ARFTG49670.2021.9425064.

[49] F. Mubarak, C. D. Martino, R. Toskovic, G. Rietveld, and M. Spirito, ‘Automated Contacting of On-Wafer Devices for RF Testing’, in *2020 Conference on Precision Electromagnetic Measurements (CPEM)*, Aug. 2020, pp. 1–2. doi: 10.1109/CPEM49742.2020.9191800.

[50] H. Li, F. T. von Kleist-Retzow, O. C. Haenssler, S. Fatikow, and X. Zhang, ‘Multi-target tracking for automated RF on-wafer probing based on template matching’, in *2019 International Conference on Manipulation, Automation and Robotics at Small Scales (MARSS)*, Jul. 2019, pp. 1–6. doi: 10.1109/MARSS.2019.8860983.

[51] C. Caglayan, G. C. Trichopoulos, and K. Sertel, ‘On-wafer device characterization with non-contact probes in the THz band’, in *2013 IEEE Antennas and Propagation Society International Symposium (APSURSI)*, Jul. 2013, pp. 1134–1135. doi: 10.1109/APS.2013.6711227.

[52] C. Caglayan, G. C. Trichopoulos, and K. Sertel, ‘Non-contact probes for device and integrated circuit characterization in the THz and mmW bands’, in *2014 IEEE MTT-S International Microwave Symposium (IMS2014)*, Jun. 2014, pp. 1–3. doi: 10.1109/MWSYM.2014.6848606.

[53] C. Caglayan, G. C. Trichopoulos, and K. Sertel, ‘Accuracy and repeatability of automated non-contact probes for on-wafer characterization’, in *84th ARFTG Microwave Measurement Conference*, Dec. 2014, pp. 1–2. doi: 10.1109/ARFTG.2014.7013406.

[54] C. Caglayan and K. Sertel, ‘Non-contact differential-mode on-wafer device characterization in the mmW and THz bands’, in *2016 IEEE MTT-S International Microwave Symposium (IMS)*, May 2016, pp. 1–3. doi: 10.1109/MWSYM.2016.7540146.

[55] C. Caglayan and K. Sertel, ‘Experimental Analysis of Repeatability and Calibration Residuals in On-Wafer Non-Contact Probing’, *IEEE Trans. Microw. Theory Tech.*, vol. 65, no. 6, pp. 2185–2191, Jun. 2017, doi: 10.1109/TMTT.2017.2649498.

[56] K. Sertel, ‘Automated Performance of On-Wafer Calibration and Characterization Using Non-Contact Probes’, in *2019 92nd ARFTG Microwave Measurement Conference (ARFTG)*, Jan. 2019, pp. 1–4. doi: 10.1109/ARFTG.2019.8637236.

Chapter 2

2. Fundamental Notions

Table of content

Introduction 47
2.1 Scattering parameters 48
2.1.1 1-port network or dipole 48
2.1.2 2-port network 49
2.2 Vector Network Analyzer 50
2.3 Error models and calibration algorithms 52
2.4 De-embedding 57
2.5 Conclusion 59
2.6 References 60

Introduction

In this chapter, we start by presenting the fundamental mathematical tools involved in radiofrequency (RF) small-signal modelling and characterisation. In particular, the concept of multi-port networks and associated scattering parameters (S-parameters) is detailed. These are the basic concepts behind RF systems and understanding them is essential for analysing such systems. Then, we will introduce the Vector Network Analyzer (VNA), reference instrument used to determine calibrated S-parameters of multi-port networks. We explore the architecture of the VNA and how it can be used to characterize RF devices. Finally, we will introduce the error models for vector network calibration and some of the commonly used calibration algorithms.

2.1 Scattering parameters

The microwave frequency range expands from 300 MHz to 30 GHZ and the millimetre-wave frequency range from 30 GHz to 300 GHz. At those frequencies, the propagation phenomena are represented by variation of voltages and currents along transmission lines. However, the impedance matrix (Z), the admittance matrix (Y) and the hybrid matrix (H), that are usually used to describe the currents and voltages, cannot be determined by direct measurements of voltages and currents. Consequently, it is preferable to substitute pseudo-waves related to the concept of power, which are easily measurable at microwave and millimetre-wave frequencies. Hence, we can define the scattering parameter matrix [*S*]. The pseudo-waves are mathematical quantities that are defined with respect to a reference impedance Z_{ref}. Generally, the reference is set to 50 Ω. The following section was written using information provided in [1].

2.1.1 1-port network or two terminal device

Figure 2.1 represents the flow chart in the case of a 1-port network. The incident pseudo-wave a_1 and the reflected pseudo-wave b_1 are defined as follow [2]:

$$a_1 = \frac{\sqrt{Re(Z_{ref})}}{2|Z_{ref}|}(V_1 + Z_{ref}I_1) \tag{2.1}$$

$$b_1 = \frac{\sqrt{Re(Z_{ref})}}{2|Z_{ref}|}(V_1 - Z_{ref}I_1) \tag{2.2}$$

where the index 1 is referring to the measurement plane (port) and is defined by the voltage V_1, the current I_1 and the reference impedance Z_{ref}.

The reference impedance of microwave measurement systems is $Z_{ref} =$ 50 Ω, a purely real standard value established in the United States in the 1930s. This value was chosen as the best compromise in terms of maximum power transfer, maximum breakdown voltage, minimum losses, and dimensional constraints in coaxial lines.

The complex reflection coefficient S_{11} of a 1-port network or two terminal device is defined as:

$$S_{11} = \frac{b_1}{a_1} \tag{2.3}$$

The reflection coefficient of a 1-port network can also be expressed using its complex impedance and the reference impedance as follow:

$$S_{11} = \frac{Z - Z_{ref}}{Z + Z_{ref}} = \frac{Z-50}{Z+50} \tag{2.4}$$

The incident power $P_{INC,1}$ and the reflected power $P_{REF,1}$, at the dipole input are calculated from the pseudo-waves as follow:

$$P_{INC,1} = \frac{1}{2}|a_1|^2 \tag{2.5}$$

$$P_{REF,1} = \frac{1}{2}|b_1|^2 \quad (2.6)$$

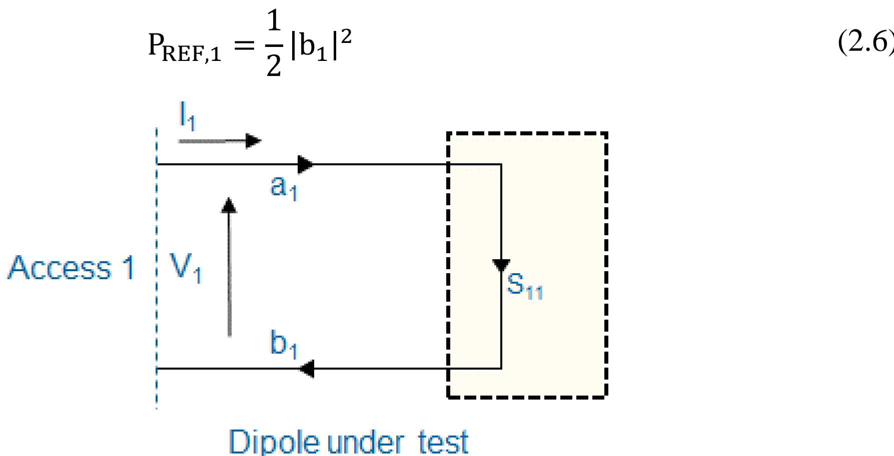

Figure 2.1 Flow chart in the case of a 1-port network.

2.1.2 2-port network

Figure 2.2 represents the Flow chart in the case of a 2-port network. The incident pseudo-wave a_i (i = 1, 2) and the reflected pseudo-wave b_i (i = 1, 2) are defined as follow:

$$a_i = \frac{\sqrt{Re(Z_{ref}^i)}}{2|Z_{ref}|}(V_i + Z_{ref}^i I_i) \quad (2.7)$$

$$b_i = \frac{\sqrt{Re(Z_{ref}^i)}}{2|Z_{ref}|}(V_i - Z_{ref}^i I_i) \quad (2.8)$$

where the index 1 and the index 2 are referring to the measurement planes and are defined by the voltages V_i $(i = 1, 2)$, the currents I_i (i = 1, 2) and the reference impedances Z_{ref}^i $(i = 1, 2)$.

The S-parameters S_{ij} (i = 1, 2 and j = 1, 2) of a 2-port network under test are described by the complex matrix [S]. The relationship between the pseudo-wave a_i $(i = 1, 2)$ and b_i (i = 1, 2) and the parameters S_{ij} (i = 1, 2 and j = 1, 2) is given by:

$$\begin{bmatrix} b_1 \\ b_2 \end{bmatrix} = \begin{bmatrix} S_{11} & S_{12} \\ S_{21} & S_{22} \end{bmatrix} \cdot \begin{bmatrix} a_1 \\ a_2 \end{bmatrix} \quad (2.9)$$

The linear relationships between the input and output signals are given by:

$$b_1 = S_{11}a_1 + S_{12}a_2 \quad (2.10)$$

$$b_2 = S_{21}a_1 + S_{22}a_2 \quad (2.11)$$

$S_{11} = b_1/a_1$ $(a_2 = 0)$ is the reflection coefficient at the input of the 2-port network.

$S_{21} = b_2/a_1$ $(a_2 = 0)$ is the transmission from the input to the output of the 2-port network.

$S_{22} = b_2/a_2$ $(a_1 = 0)$ is the reflection coefficient at the output of the 2-port network.

$S_{12} = b_1/a_2$ $(a_1 = 0)$ is the transmission from the output to the input of the 2-port network.

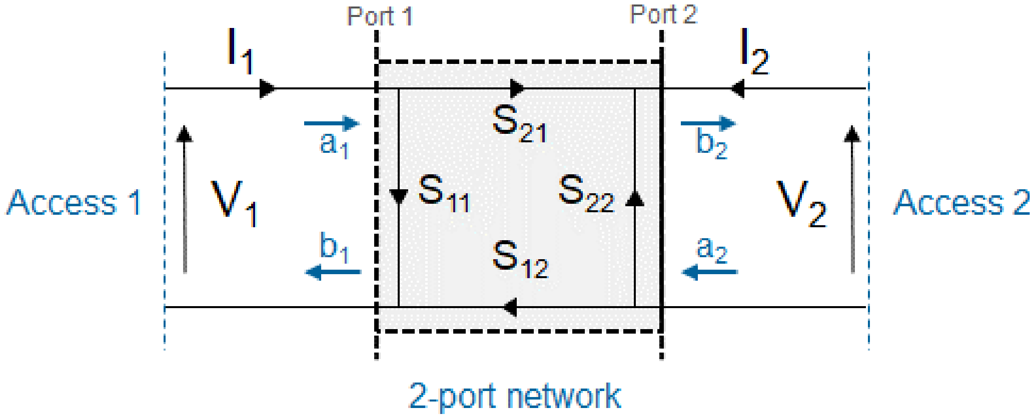

Figure 2.2 Fluence chart in the case of a 2-port network.

The *S*-parameters of a 1-port or 2-port network are frequency dependent. It is possible to measure the four parameters at each frequency point in terms of magnitude and phase-shift using a VNA.

2.2 Vector Network Analyzer

VNAs are precision instruments used to measure the electrical properties of circuits and networks in the RF spectrum. They can be used to analyse a wide range of circuits, from simple devices such as filters and amplifiers to complex modules used in communications satellites. As examples of how VNAs are used in RF engineering, we can cite: performance characterization of RF components, such as antennas, filters, and amplifiers; design and optimisation of RF systems, such as radar systems and communication networks; troubleshooting of RF problems such as signal loss or interference; calibration of RF measurement equipments. In [1] and [3], authors provided a clear and concise explanation of how the VNA works. We used their document as a reference when writing this section.

A VNA measures the amplitude and phase of wave quantities and uses these values to calculate complex reflection coefficient S_{11} for a two terminal device or complex S-parameters S_{ij} $(i = 1, 2 \text{ and } j = 1, 2)$ for a 2-port network.

Figure 2.3 shows the block diagram of a 2-port VNA. The block diagram contains four main parts:

- The test set uses a reflectometer to separate the incident and reflected waves at the test port. The waves are then injected to either the reference channel or the measurement channel. Electronic attenuators can be used in order to vary the test port output power.
- The RF synthesizer produces the RF signal. The source switch is used to connect the RF signal to one of the test ports, which then operates as an active port.
- Each test set has two separate receivers, one for the measurement channel, called the ‘measurement receiver’ and one for the reference channel, called the ‘reference receiver’. They both consist of an RF signal section and a digital signal processing stage. The output of the stage is raw measurement data in complex numerical values.
- A computer is used to perform system error correction, display measurement data, and provide a user interface.

Figure 2.3 illustrates the principle of sampling different microwave signals based on reflectometry. To measure all four *S*-parameters without having to disconnect the DUT, the

source can be directed to port 1 (or port 2) for the measurement of parameters S_{11} and S_{21} (or S_{12} and S_{22}) using a switch. The architecture of the network analyzer can also include multiple microwave sources to avoid using switches and increase the measurement accuracy. The injected power is controlled using an attenuator, allowing the adjustment of the power during testing to match the DUT characteristics. The power provided by the source is split using a power divider. One part is directed to the reference path, and the other part is directed to the DUT. Signal A and signal B are taken respectively from the reflected and the transmitted signals from the couplers. These RF signal are translated around an intermediate frequency using a mixer and a local oscillator. They are then sampled, digitized, and processed.

However, VNA's components present imperfections that appear during the measurement of *S*-parameters. Therefore, it is necessary to take these imperfections into account in order to correct the measurements. This is the purpose of vector calibration, which will be presented below.

We can distinguish two types of measurement errors [4] [5]:

- Random errors are inherent to the unpredictable fluctuation in the measurement environment (humidity, temperature) and the measurement system itself. These errors cannot be corrected by software. However, we can reduce the impact of random errors by controlling the environment fluctuations, reducing the bandwidth of the intermediate frequency (IF) and by averaging multiple measurements.
- Systematic errors are characteristics of the measurement system and are reproducible. A dedicated electrical model can be used to express the measured *S*-parameters by the VNA in terms of the actual *S*-parameters of the DUT and complex error terms. These error terms are determined by a vector calibration procedure also called "calibration" [6].

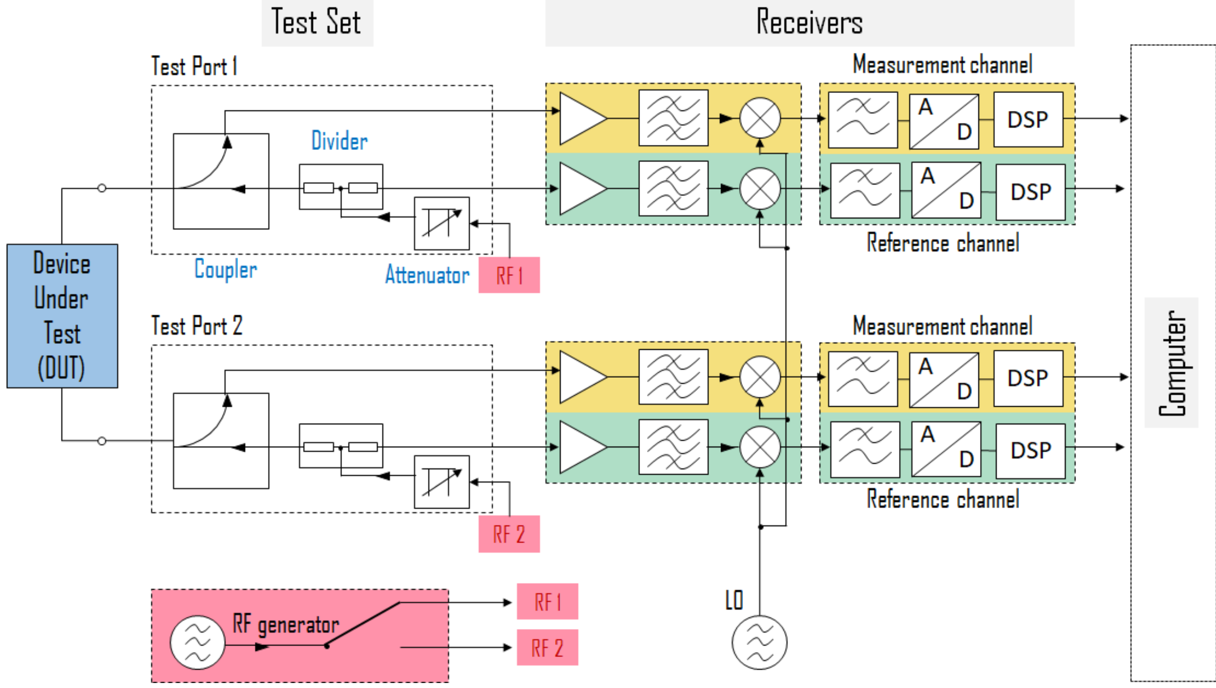

Figure 2.3 Block diagram of a 2-port Vector Network Analyzer [3].

2.3 Error models and calibration algorithms

Several works covered calibration procedures [7], [8], [9], [10], [11].The system error coefficients of VNA are determined by measuring calibration standards with known reflection and transmission properties. These standards are commonly open, short, load, and through (referred to as “thru”) standards. These standards have well-defined reflection and transmission coefficients. The VNA measures the reflection and transmission coefficients of the calibration standards. Then, these measurements are used to calculate the system error coefficients. The measured raw reflection and transmission coefficients of the DUT are then corrected with the previously determined error coefficients. This removes the effects of systematic errors from the DUT measurements, allowing for quantitative characterization.

The system error model is derived from a generic VNA block diagram, approximating the VNA as a linear network [6] [12]. Figure 2.4 is the forward portion of the system error model where:

- e_{00} is the directivity
- $e_{10}e_{01}$ is the reflection tracking
- e_{11} is the port-1 match
- e_{30} is the leakage
- $e_{10}e_{32}$ is the transmission tracking
- e_{22} is the port-2 match

The directivity is caused by the leakage of the coupler used in the VNA. This error is also increased by the mismatch between the cable and the connectors between the coupler to the DUT. The reflection and transmission tracking errors are caused by the reflectometer and mixers. It is also caused by the imbalance in the cable lengths between the two ports of the VNA. The match error is the ratio between the reflected power and the incident power at the DUT port. It is not necessarily the same as the ‘raw’ port match. The leakage error is caused by the leakage of the local oscillator (LO) signal through the mixers. It is not the same as the leakage of the switch, which is assumed to be negligible in this model [6].

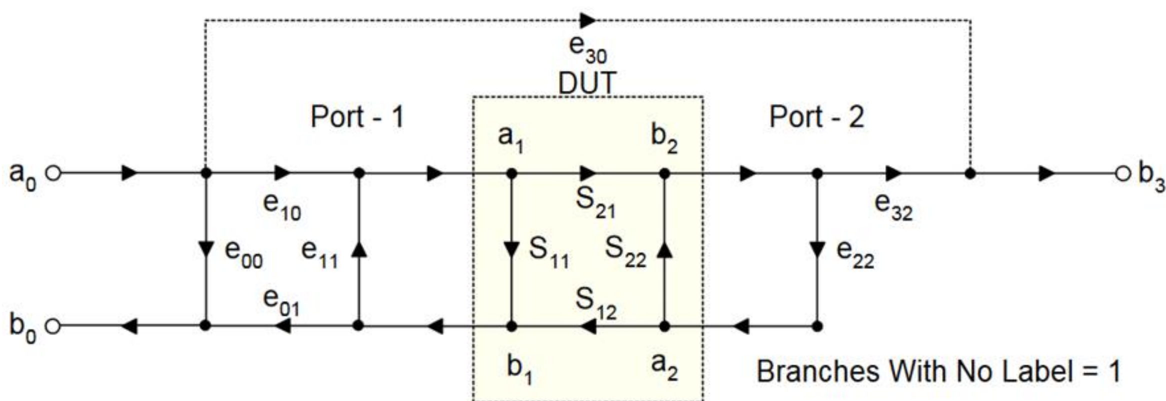

Figure 2.4 System Error Model for the Forward Direction [6].

To understand the two-port model, we start by presenting the one-port model also called the 3-Term Error Model. In Figure 2.5, the model is simplified for a one-port measurement to three error terms: directivity, port match, and tracking errors. The measured reflection coefficient and the actual reflection coefficient can be written as follow respectively using the S. J. Mason rules [13], [14]:

$$S_{11_M} = \frac{b_0}{a_0} = \frac{e_{00}\text{-}\Delta_e S_{11}}{1\text{-}e_{11}S_{11}} \tag{2.12}$$

$$S_{11} = \frac{S_{11_M}\text{-}e_{00}}{S_{11_M}e_{11}\text{-}\Delta_e} \tag{2.13}$$

$$\Delta_e = e_{00}e_{11}\text{-}(e_{10}e_{01}) \tag{2.14}$$

where S_{11_M} is the measured reflection coefficient and S_{11} is the actual reflection coefficient.

From the error model, and using three different known standards, we can write three linear equations containing three actual reflection coefficients, three measured reflection coefficients, and the three error terms:

$$e_{00} + S_{11_1}S_{11_{M1}}e_{11}\text{-}S_{11_1}\Delta_e = S_{11_{M1}} \tag{2.15}$$

$$e_{00} + S_{11_2}S_{11_{M2}}e_{11}\text{-}S_{11_2}\Delta_e = S_{11_{M2}} \tag{2.16}$$

$$e_{00} + S_{11_3}S_{11_{M3}}e_{11}\text{-}S_{11_3}\Delta_e = S_{11_{M3}} \tag{2.17}$$

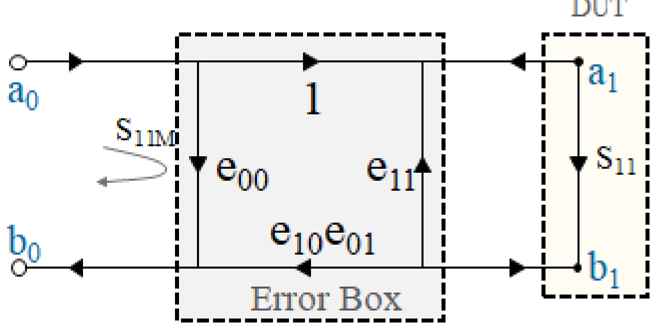

Figure 2.5 One-Port 3-Term Error Model.

The three error terms can be obtained by measuring three known standards, typically a short, on open, and a load. Hence, it becomes possible to solve the three equations for the three error terms. Finally, using the calculated error terms, the equations can be inverted in order to find the actual reflection coefficient of the measured DUT.

The two-port can be modelled in the same way. A fictitious error box is placed between the 2-port network DUT and each measurement port. This error box contains the six error terms for the forward direction. Similarly, a six term model is used for the reverse direction. From Figure 2.6, the measured reflection and transmission coefficients for the forward direction can be obtained as a function of the four actual S-parameters of the DUT and the six forward error terms:

$$S_{11_M} = \frac{b_0}{a_0} = e_{00} + (e_{10}e_{01})\frac{S_{11}\text{-}e_{22}\Delta_S}{1\text{-}e_{11}S_{11}\text{-}e_{22}S_{22} + e_{11}e_{22}\Delta_S} \tag{2.18}$$

$$S_{21_M} = \frac{b_3}{a_0} = e_{30} + (e_{10}e_{32})\frac{S_{21}}{1\text{-}e_{11}S_{11}\text{-}e_{22}S_{22} + e_{11}e_{22}\Delta_S} \tag{2.19}$$

$$\Delta_S = S_{11}S_{22}\text{-}S_{21}S_{12} \tag{2.20}$$

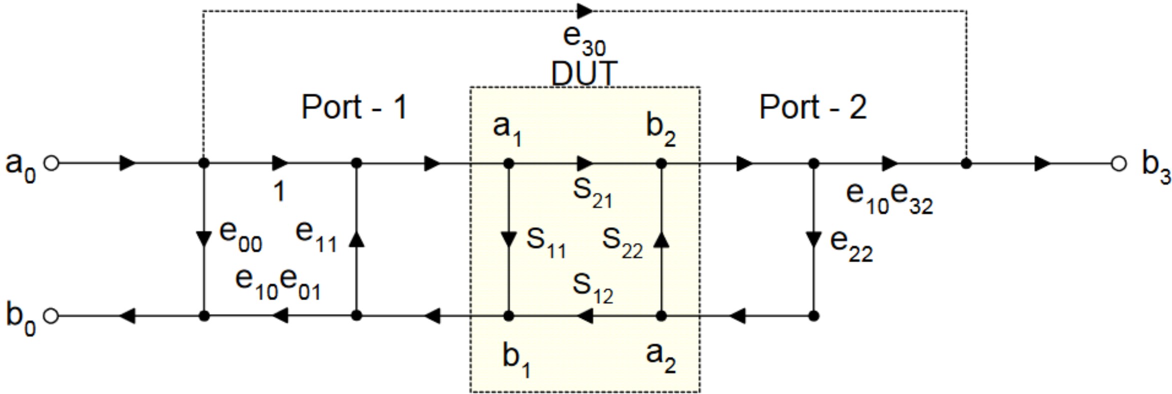

Figure 2.6 12-Terms Error Model for the Forward Direction

In the same way, solving for the reverse model in Figure 2.7, we obtain the reflection and the transmission coefficients as a function of the four actual S-parameters of the DUT and the six reverse error terms:

$$S_{22M} = \frac{b'_3}{a'_3} = e'_{33} + (e'_{23}e'_{32})\frac{S_{22}\text{-}e'_{11}\Delta_S}{1\text{-}e'_{11}S_{11}\text{-}e'_{22}S_{22} + e'_{11}e'_{22}\Delta_S} \tag{2.21}$$

$$S_{12M} = \frac{b'_0}{a'_3} = e'_{03} + (e'_{23}e'_{01})\frac{S_{12}}{1\text{-}e'_{11}S_{11}\text{-}e'_{22}S_{22} + e'_{11}e'_{22}\Delta_S} \tag{2.22}$$

$$\Delta_S = S_{11}S_{22}\text{-}S_{21}S_{12} \tag{2.23}$$

The forward and the reverse equations can be combined in order to give four equations containing the four actual S-parameters of the DUT and the 12 error terms of the model. When the 12 error terms are known, the four equations are solved for the actual *S*-parameters of the DUT. More details are presented in [6], [15], [16], [17], [18], [19].

Other error models have been developed to calibrate VNAs. They are derived from the 12-term error model. We can cite the 8-Term Error model and the 16-Term Error model. In the 8-term model, we assume that the crosstalk leakage term is zero, or that it can be determined in a separate calibration step. We also assume that the switch is perfect and does not change the port match of the network analyzer. In the 16-term model, we make no assumption about leakage.

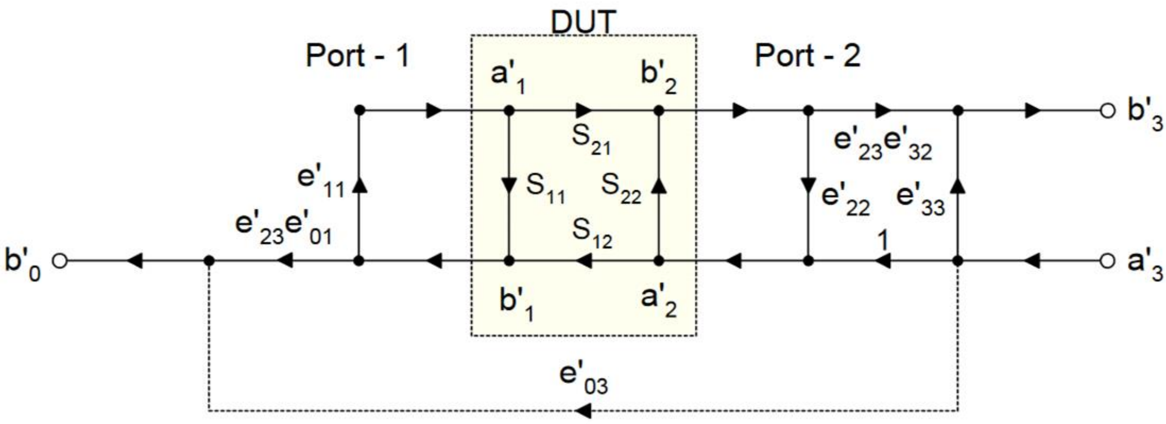

Figure 2.7 12-Terms Error Model for the Reverse Direction [6].

In the following, we briefly present some of the commonly used calibration algorithms. First, it is important to recall that this work focus on on-wafer calibration and measurements. In order to perform an on-wafer calibration, we typically use an Impedance Standard Substrates (ISS). Figure 2.8 shows the 101-190 C ISS Map from FormFactor™ that is used throughout this work. Each ISS is compatible with specific probe pitches and for specific frequency ranges. The 101-190 C ISS is compatible with GSG probes from 100 µm to 250 µm probe pitch. It provides thru, short, load and open structures as well as alignment structures to guide the user to define the overtravel of the probes. It contains also different lengths of transmission lines for verification. Figure 2.9 shows the four ISS standards used with a GSG probe.

As mentioned previously, there are many calibration algorithms based on the 12, 8 or 16-term error model. We will present the most used ones, i.e. Short-Open-Load-Thru (SOLT), Thru-Reflect-Line (TRL), and Line-Reflect-Reflect-Match (LRRM) [20], [21]. Figure 2.10 illustrates the standards used for each calibration algorithm with GSG probes.

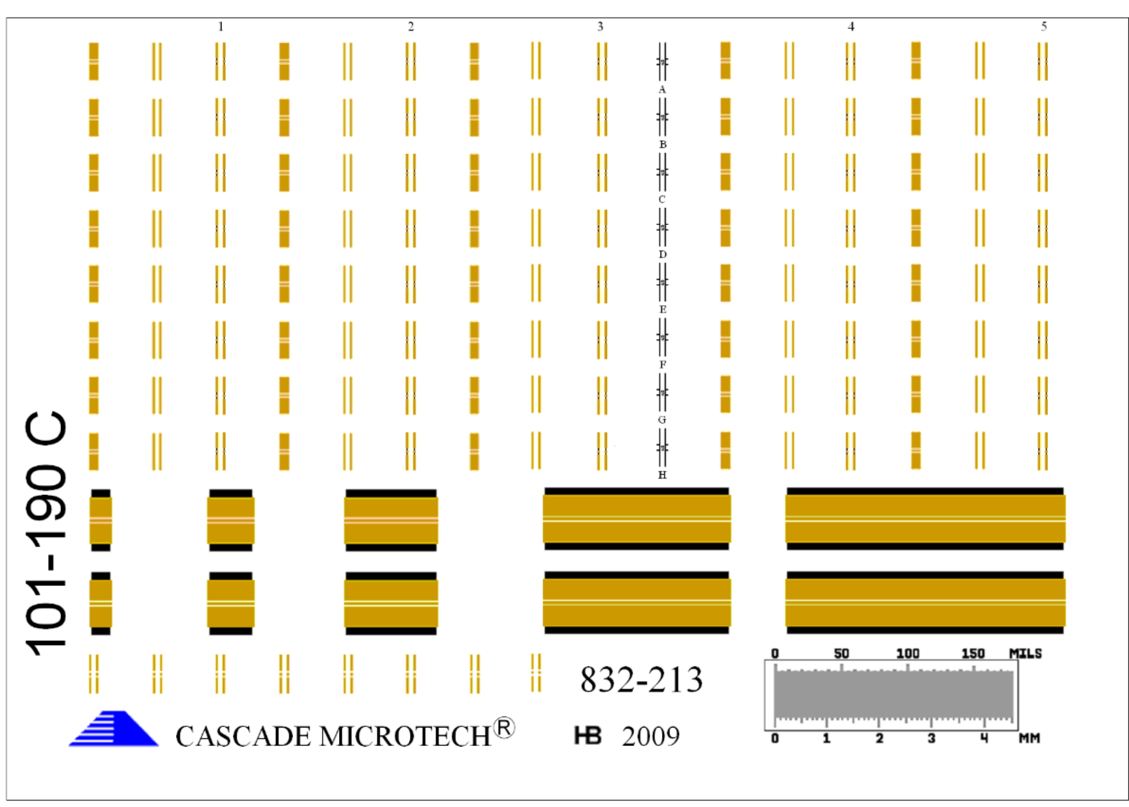

Figure 2.8 101-190 C Impedance Standard Substrate from FormFactor™.

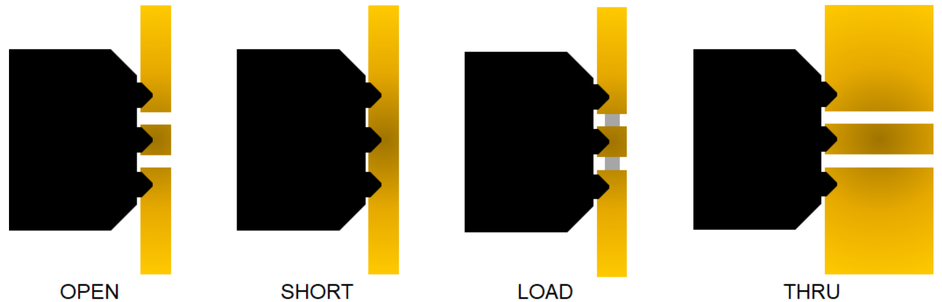

Figure 2.9 ISS standards in a GSG configuration.

The Short-Open-Load-thru (SOLT) algorithm

The SOLT method in based on the 12-term error model. It uses the properties of two fictional and directive couplers. To solve the calibration problem, we need to solve the 12 equations system as presented earlier. To solve the system, four calibration standards are needed. The SOLT method is widely used for on-wafer calibration and is robust as long as all four standards are perfectly known. It is also relatively sensitive to the probe placement on the different standards.

The Thru-Reflect-Line (TRL) algorithm

The TRL method is based on the 8-term error model. Three calibration standards are needed: two different length lines ("Thru" and "Line") and a highly reflective standard ("Short" or "Open"). It requires a minimal knowledge of the electrical behaviour of the standards. The reference place is considered as the middle of the Thru standard. It is considered to be symmetrical. However, the validity of the method is dependent of the symmetrical behaviour of the intern switch of the VNA.

The Line-Reflect-Reflect-Match (LRRM) algorithm

The LRRM method requires the same four standards as the SOLT method but requires less information about the standards. It can give better results than SOLT and is less sensitive to small errors in probe placement. The reference place of the LRRM is set at the middle of the Line. The reflect does not need known Open or Short but must its impedance must be equal at both port-1 and port-2. Match standard could have known resistance and unknown inductance. Its inductance is obtained using the Open standard.

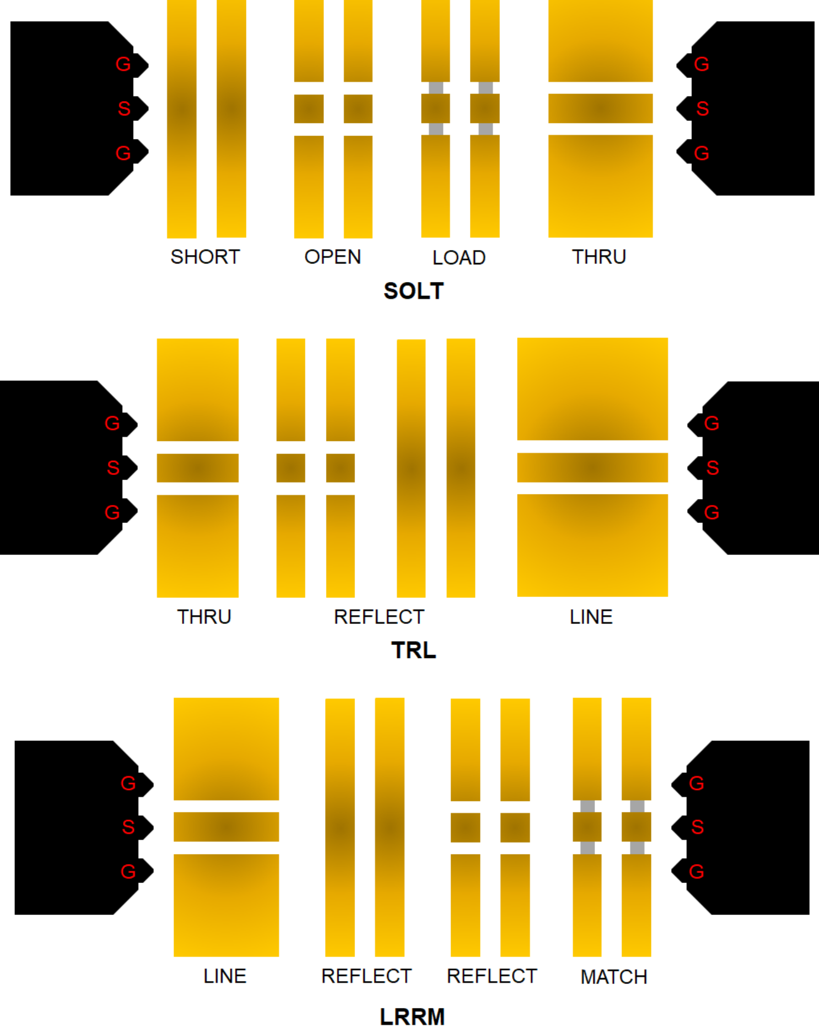

Figure 2.10 Standards used in the SOLT, TRL, and LRRM calibration algorithms with GSG probes [21].

2.4 De-embedding

In some cases, in addition to on-wafer vector calibration, an additional de-embedding procedure is required. This latter consists of shifting the reference plane at the probes'tip to a another reference plane, located closer to the DUT (Figure 2.11). It is necessary when the DUT accesses are smaller than the probe's tips and do not allow a direct contact. Hence, in the de-embedding procedure, the parasitic contributions of the CPW access are subtracted from the global measurement. As equivalent electrical model for the DUT's access needs to be developed carefully. There are several de-embedding methods for on-wafer measurements [22], [23], [24]. Those methods often use Open and Short-Open approaches. Both techniques consider a two terminal device model in which the parasitic effects of the DUT's access are modelled by resistances, inductances, and capacitances placed either in series or in parallel or both. The Open technique is the simplest one. It uses one "Open" test structure. This techniques allows to subtract the capacitive effect of the CPW DUT's access only [25]. The Open-Short techniques are more complex and allow a better extraction of the parasitic effects. It takes into account the series and parallel effects. This method is commonly used to characterize on-wafer electronic devices up to 110 GHz. Indeed, beyond 110 GHz, the Open-Short technique becomes less precise due to the rising frequency [26].

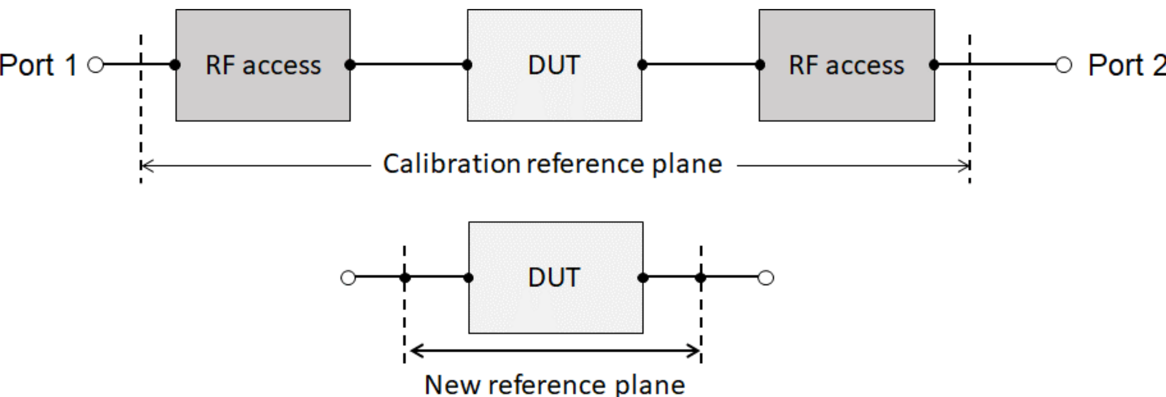

Figure 2.11 De-embedding technique for a 2-port network measurement [20].

2.5 Conclusion

In this chapter, we discussed the fundamental notions in RF technology. We presented the definition of 1-port and 2-port network respectively using the concept of S-parameters. A brief definition of the VNA was also included in this chapter. Finally, calibration and de-embedding were presented as being essential steps to obtain calibrated measurements. Understanding these concepts is crucial in order to proceed with our work, related to the development of a robotic and automated on-wafer probe station.

2.6 References

[1] K. Haddadi, "Mesure hyperfréquence des propriétés électromagnétiques de matériaux : 300 MHz à 300 GHz", *Mes. Tests Électroniques*, Dec. 2016, doi: 10.51257/a-v1-r1117.

[2] R. B. Marks and D. F. Williams, "A general waveguide circuit theory", *J. Res. Natl. Inst. Stand. Technol.*, vol. 97, no. 5, p. 533, Sep. 1992, doi: 10.6028/jres.097.024.

[3] "Fundamentals of Vector Network Analysis Primer", Published by Rohde & Schwarz USA, Inc.

[4] D. Rytting, "An Analysis of Vector Measurement Accuracy Enhancement Techniques", *Hewlett-Packard RF & Microwave Measurement Symposium and Exhibition* (1987)

[5] D. Rytting, "Appendix to an Analysis of Vector Measurement Accuracy Enhancement Techniques', *Hewlett-Packard RF & Microwave Measurement Symposium and Exhibition* (1987).

[6] D. Rytting, "Network Analyzer Error Models and Calibration Methods", White Paper (1998).

[7] G. F. Engen and C. A. Hoer, "Thru-Reflect-Line: An Improved Technique for Calibrating the Dual Six-Port Automatic Network Analyzer," in *IEEE Transactions on Microwave Theory and Techniques*, vol. 27, no. 12, pp. 987-993, Dec. 1979, doi: 10.1109/TMTT.1979.1129778.

[8] H.-J. Eul and B. Schiek, "A generalized theory and new calibration procedures for network analyzer self-calibration", *IEEE Trans. Microw. Theory Tech.*, vol. 39, no. 4, pp. 724–731, Apr. 1991, doi: 10.1109/22.76439.

[9] R. B. Marks, "Formulations of the Basic Vector Network Analyzer Error Model including Switch-Terms", in *50th ARFTG Conference Digest*, Dec. 1997, pp. 115–126. doi: 10.1109/ARFTG.1997.327265.

[10] "Latest Advances in VNA Accuracy Enhancements Microwave Journal". https://www.microwavejournal.com/articles/784-latest-advances-in-vna-accuracy-enhancements (accessed Sep. 05, 2023).

[11] "Keysight Technologies® Specifying calibration standards and kits for Keysight Vector Network Analyzers", Application Note (2014). [Online]. Available: https://web.ece.ucsb.edu/Faculty/rodwell/Classes/ECE218a/documentation/cal_kit_discussion.pdf

[12] M. Zeier, J. Hoffmann, J. Ruefenacht, and M. Wollensack, "Contemporary evaluation of measurement uncertainties in vector network analysis", *Tm - Tech. Mess.*, vol. 84, no. 5, pp. 348–358, May 2017, doi: 10.1515/teme-2016-0061.

[13] S. J. Mason, "Feedback Theory-Some Properties of Signal Flow Graphs", *Proc. IRE*, vol. 41, no. 9, pp. 1144–1156, Sep. 1953, doi: 10.1109/JRPROC.1953.274449.

[14] S. J. Mason, "Feedback Theory-Further Properties of Signal Flow Graphs", *Proc. IRE*, vol. 44, no. 7, pp. 920–926, Jul. 1956, doi: 10.1109/JRPROC.1956.275147.

[15] H. M. Cronson and L. Susman, "A Dual Six-Port Automatic Network Analyzer", in *1980 IEEE MTT-S International Microwave symposium Digest*, May 1980, pp. 434–436. doi: 10.1109/MWSYM.1980.1124312.

[16] R. B. Marks, "A multiline method of network analyzer calibration", *IEEE Trans. Microw. Theory Tech.*, vol. 39, no. 7, pp. 1205–1215, Jul. 1991, doi: 10.1109/22.85388.

[17] M. Potéreau *et al.*, "Meander type transmission line design for on-wafer TRL calibration", in *2016 46th European Microwave Conference (EuMC)*, Oct. 2016, pp. 381–384. doi: 10.1109/EuMC.2016.7824358.

[18] A. Rumiantsev, H. Heuermann, and S. Schott, "A robust broadband calibration method for wafer-level characterization of multiport devices", in *2007 69th ARFTG Conference*, Jun. 2007, pp. 1–5. doi: 10.1109/ARFTG.2007.5456344.

[19] A. Rumiantsev, P. Sakalas, N. Derrier, D. Celi, and M. Schroter, "Influence of probe tip calibration on measurement accuracy of small-signal parameters of advanced BiCMOS HBTs", in *2011 IEEE Bipolar/BiCMOS Circuits and Technology Meeting*, Oct. 2011, pp. 203–206. doi: 10.1109/BCTM.2011.6082782.

[20] K. Daffe, "Caractérisation Hyperfréquence Sous Pointes de Nano Dispositifs : Métrologie et Instrumentation", 2018.

[21] X. Shang, J. Ding, N. Ridler, C. Buck, and M. Geen, "Calibration Techniques for Millimetre-wave On-wafer S-parameter Measurements".

[22] M. Deng, "Contribution à la caractérisation et la modélisation jusqu'à 325 GHz de transistors HBT des technologies BiCMOS", 2014.

[23] M. C. A. M. Koolen, J. A. M. Geelen, and M. P. J. G. Versleijen, "An improved de-embedding technique for on-wafer high-frequency characterization", in *Proceedings of the 1991 Bipolar Circuits and Technology Meeting*, Sep. 1991, pp. 188–191. doi: 10.1109/BIPOL.1991.160985.

[24] E. P. Vandamme, D. M. M.-P. Schreurs, and G. Van Dinther, "Improved three-step de-embedding method to accurately account for the influence of pad parasitics in silicon on-wafer RF test-structures", *IEEE Trans. Electron Devices*, vol. 48, no. 4, pp. 737–742, Apr. 2001, doi: 10.1109/16.915712.

[25] P. J. Van Wijnen, "A new straightforward calibration and correction procedure for on wafer high frequency s parameter measurements (45mhz-18ghz)", presented at the Proceedings of the Bipolar Circuits and Technology Meeting, 1987.

[26] M. Deng *et al.*, "Benefits and validation of 4-dummies de-embedding method for characterization of SiGe HBT in G-band", in *2013 European Microwave Integrated Circuit Conference*, Oct. 2013, pp. 388–391.

Chapter 3

3. Development of the automated and nanorobotics probe station

Table of content

Introduction 63
3.1 The SmarAct Technology 64
3.2 Mechanical properties of the positioning stages 66
3.2.1 SLC Linear Stages 67
3.2.2 SR Rotation Stages 68
3.2.3 MCS2 68
3.2.4 Repeatability 68
3.2.5 Sensor type 69
3.2.6 Positioner Movement 69
3.3 Positioner Properties 70
3.4 Automated and robotic probing station: hardware development 75
3.5 Positioning repeatability of the SmarAct nano-positioners with a DC probe 87
3.6 Static drift of the positioners with the Infinity probe 89
3.7 Automated and robotics probing station: Software development 93
3.8 Conclusion 98

Introduction

In the last years, advancements in micro- and nanotechnology have changed and revolutionized the way we interact and manipulate electronic devices at the smallest scales. As these technologies continue to evolve, the need for precise and efficient positioning systems has become urgent. To tackle the issue, the piezo-electric nano-positioning stages have emerged as leading solution in the realm of nanotechnology instrumentation.

In the frame of this work, we benefit from the experience gained by the research team on the development of nano-robotics and fully automated solutions for microwave multiscale sensing. In particular, in 2024, the project 'Vacuum Scanning Microwave Microscopy for quantitative characterization of sub-10 nm and atto-Farad scale capacitors and memories – VACSMM" funded by the agencies ANR and DFG has pioneered the collaboration between the University of Oldenburg, Germany and IEMN. In few words, University of Oldenburg has introduced the SmarAct® technology, that offers piezo-based nanoscale high accuracy and control over centimetre movements. These systems are combined with microwave technology developed by IEMN to develop fully automated and nanorobotics RF instrumentations.

In this chapter, we dive into detail of the SmarAct® technology, exploring the SmarAct® product catalogue as well as the principles and operational mechanics of their positioners. The information and figures regarding the SmarAct® technology and the SmarAct positioners were sourced directly from their website.

An important aspect of this study is the determination of the crucial parameters that govern the behaviour of the SmarAct® positioners, which are important in achieving the desired level of accuracy and repeatability in positioning tasks. In this chapter, we investigate those parameters and how they affect the precision of the positioners.

Building upon this fundamental understanding, we introduce the development of the automated and robotic on-wafer probing station using commercial GSG probes. First, the hardware development is focused on the design of a probe station that seamlessly integrates the capabilities of the SmarAct positioners, providing a compact and adaptable platform for advanced and precise RF measurements. In a second step, the software allows achieving robotics control and automation of the positioners as well as for other sensors integrated in the platform. With LabVIEW™ programming environment as our tool of choice, we create intuitive interfaces and efficient algorithms that harness the full potential of the SmarAct® positioners within the context of on-wafer probing.

3.1 The SmarAct Technology

SmarAct® is a leading technology company specialized in the development of innovative high-precision positioning technology, metrology and automation technology. The company was founded in 2005 in Oldenburg, Germany. SmarAct® has an ever-growing product portfolio grouped in three main units: Metrology, Motion and Automation. In the Motion unit, SmarAct® focuses on the development and production of high-precision and compact products for nano-positioning that meet the user's demands while being easy to handle. The positioners in the Motion units can be divided into four classes:

- SMARSLIDE: based on piezoelectric positioning stages with a large positioning range (few mm to over a meter). They can also be used under extreme environmental conditions for specific applications
- SMARSHIFT: based on fast and highly accurate electromagnetic positioning stages
- SMARFLEX: scanners based on compliant structures that offers high resolution and dynamic capabilities
- SMARBOTIC: complex positioning systems and robots that provide multiple degrees of freedom

In the Metrology unit, the company offers components and solutions for measurement of position displacement with a high-resolution. It also offers tools for the characterization of component as well as failure analysis. The measurement systems are as follow:

- PICOSC ALE *Interferometer*: compact laser interferometer with a picometer resolution
- METIRIO: miniaturized optical encoders, compatible with demanding environmental conditions

On the other hand, the component characterisation solutions are as follow:

- PICOSCALE *Vibrometer*: to detect in-plane and out-of-plane vibrations with picometer resolution
- SMARPROBE: nano-probing platforms to push the boundaries of technical feasibility in failure analysis on wafers, ASICS and MEMS

As described, the SmarAct® catalogue is large and diverse. Each product has its own technology and characteristics. In this work, we used positioners from the Motion unit. Specifically, Stick-Slip Piezo Drives from the SMARSLIDE class. Stages from this class guarantee a low thermal drift and high resonance frequencies through high degree of miniaturisation and perfect material selection. In addition, the stages are compatible with vacuum and cryogenic application down to 10^{-11} mbar. They are also available as non-magnetic version for specific applications. Moreover, the SMARSLIDE technology is based on compact and versatile closed loop positioners that are self-clamping and backslash-free since the movable parts of the stages are permanently coupled to the piezo drives via friction elements. Finally, they are customizable according to the client's requirements. Different stages specialized are available: Linear stages, High Load stages designed vertically for heavy loads, Rotation stages, and Goniometer stages to create multi-dimensional Euler positioning systems, Micro-Grippers and so on.

The SMARSLIDE stages use the Stick-Slip Piezo Drive technology. The stages feature a patented drive system that combines macroscopic travel with nanometre resolution, high

velocities of several millimetres per second. In order to understand how the stages operate, in the following, we explain the principle of the Stick-Slip piezo drive:

- The piezo actuator is securely fixed to the stationary base of the stage. The slide of the guideway is connected to the actuator through a friction element that remains permanently attached to the actuator

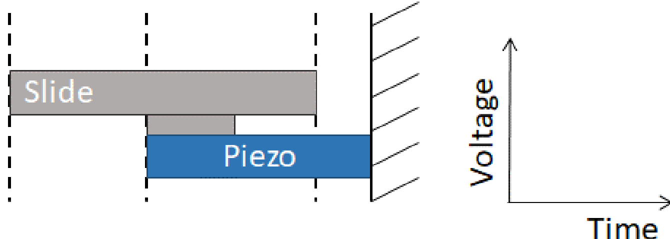

- The length of the piezo actuator adjusts proportionally to the applied voltage. By gradually increasing the voltage while controlling it, the piezo actuator expands or contracts accordingly. As a result, the slide follows the movement of the friction element. This is called the stick-phase

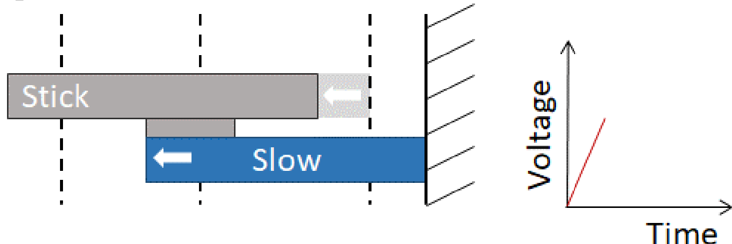

- When there is a sudden change in the applied voltage (increase or decrease), the piezo actuator contracts or expands rapidly within a short timeframe. Consequently, the friction element moves swiftly. However, the slide does not follow the motion of the friction element. This is called the slip phase. By repeating the sequence of stick and slip phases, it is possible to achieve macroscopic travel of the slide. This operation mode is referred to as the step mode.

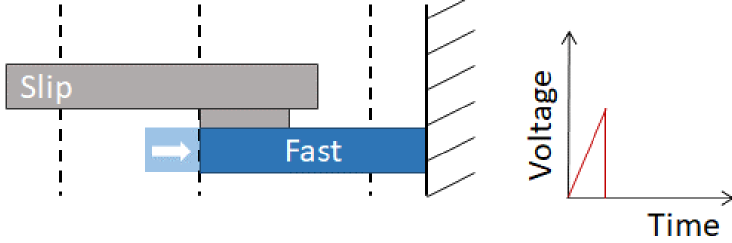

- In the stick-phase, the slide can be moved with sub-nanometer resolution by gradually extending or contraction the piezo actuator. This is called the scanning mode.

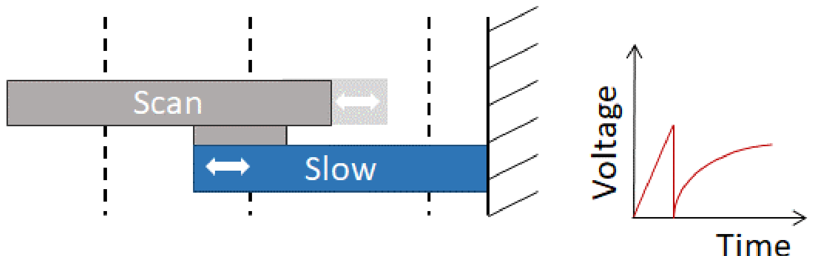

In the following, we dive into more details about the Linear Stages. Indeed, those are the stages used in the development of our automated and robotics probing station. The linear stages come in different series:

- Cryogenic Linear Stages
- SLC Series: are based of linear slides witch crossed roller bearings a characterized by their high rigidity and straightness
- CLS Series: with exchangeable drive units
- CLL Series: suitable for applications where long travel ranges are required
- DLS Series: combine stick-slip drives and piezo scanners
- SL Series: perfect when absolute miniaturization is required

In addition, SmarAct® provide high-precision rotation stages based on different drive technologies. They can be easily combined with each other or with other SmarAct positioners to form setups that are more complex. The rotation stages allow continuous and mechanically unlimited rotation. We can find the MR Series, based on electromagnetics and the standard SR series. The latest offer different sizes and shapes depending on the desired application. In the next section, we focus on the SLC (linear stages) Series for the linear stages and SR Series of the rotation stages. We will present the characteristics of each one of the models that we used in our work.

3.2 Mechanical properties of the positioning stages

First, we start by reminding the components of an automated probe station and the parts that are mounted on the SLC and the SR positioners. Indeed, in Chapter 1, we presented the automated probing station that consists of a chuck to carry the device under test (DUT), automated positioners that carry the radiofrequency probes, an optical system and a VNA. The parts we are interested in are the chuck and the probe positioners. In our station, the chuck is mounted on three positioning stages, two SLC linear stages and one SR rotation stage. The probes are mounted on four positioning stages, three SLC linear stages and one SR rotation stage. Hence, the chuck can achieve 3 degrees of freedom in the X axis, the Y axis and the φ axis. While the probes can achieve 4 degrees of freedom in the X axis, the Y axis, the Z axis and the θ. Figure 3.1 shows a schematic representation of the probe and the chuck axis as described previously.

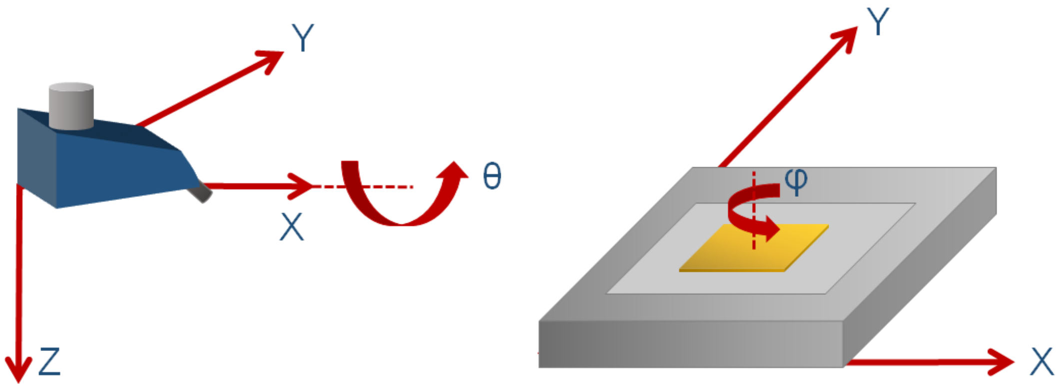

Figure 3.1 Schematic representation of the probe and the chuck axis.

3.2.1 SLC Linear Stages

The linear SMARSLIDE stages of the SLC series are built on linear slides with crossed roller bearing. The SLC stages offer compactness, high rigidity and straightness. They are suited for applications where the positioning system requires stability and high accuracy. They can be used in high and ultra-high vacuum environments. The SLC linear stage are available in two series, the SLC-17 and the SLC-24. The two differ primarily in width and height. Both series can integrate a position sensor for closed-loop operations. Table 3.1 summarizes the SLC linear stages used for both the probes and the chuck.

Table 3.1 SLC Linear Stages used for the probes and the chuck.

	Probe		Chuck	
Axis	X-Y	Z	X	Y
Reference	SL-2430	SLC-1730	SLC-24150	SLC-2475
Mechanical				
Scan Range [µm]	> 1.3	> 1.3	> 1.3	> 1.3
Travel [mm]	16	21	103	49
Dimensions [mm]	30 x 24 x 10.5	30 x 17 x 8.5	150 x 24 x 10.5	75 x 24 x 10.5
Weight [g]	36	20	180	90
Open-loop				
Velocity [mm/s]	> 20	> 20	> 20	> 20
Resolution MCS2 [nm]	< 1	< 1	< 1	< 1
Closed-loop				
Sensor Resolution MCS2 [nm]	1 (S)	1 (S)	1 (S)	1 (S)
Unidirectional Repeatability MCS2 [nm]	± 40 (S)	± 40 (S)	± 40 (S)	± 40 (S)

3.2.2 SR Rotation Stages

As described previously, the rotation stages allow a continuous and unlimited rotation of the system. However, they can be mechanically limited if necessary to avoid collisions or tearing of cables. Here, we will use the SR series only with two different sizes. Table 3.2 summarises the SR rotation stages used for both the probes and the chuck.

Table 3.2 SR Rotation Stages used for the probes and the chuck.

	Probe	Chuck
Axis	θ	ϕ
Reference	SR-2013	SR-4513
Mechanical		
Travel [°]	∞	∞
Dimensions [mm]	25.5 x 20 x 10.2	45 x 45 x 12.5
Weight [g]	11	89
Open-loop		
Angular Velocity [°/s]	> 45	> 30
Resolution MCS2 [μ°]	> 4	> 2
Closed-loop		
Sensor Resolution MCS2 [μ°]	25 (S)	15 (L, S)

3.2.3 MCS2

The MCS2 is a control system used to control the positioning stages. It is designed to provide high-precision control over the stages, making it a perfect choice for nano-positiong and micro-positioning. It is capable of controlling multiple axes simultaneously. It integrates multiple modules in order to provide adapted and pre-configured control system. Some of the features are: sensor data reading for closed-loop position control, communication interface, hand control module and so on. The MCS2 has different housing variants. The Integrated Handheld is equipped with the main controller module including a communication interface and a human-machine interface module. The Rack Housing in a modular system consisting of six slots. It contains the main controller module, a communication interface, and a backplane. Each slot can host a module carrier with three-channels, allowing for a total of six main controllers to be installed making it possible to control up to 18 positioning stages. The Table top Housing includes the main controller module with a communication interface in its standard configuration. Finally, the Hand Control Module can be connected to both the rack and the Table top Housing for external manual control.

3.2.4 Repeatability

The repeatability refers to the ability of the positioner to consistently reach a target position. It can be either from a single direction (uni-directional) or from multiple directions (bi-directional). In the case of bi-directional repeatability, the dominant factor is often the reversal error of the system. The uni-directional repeatability is obtained by the determination of the standard deviation of the positioning error at each target position across the entire range of motion of the system. The reverse error is defined as the difference between the measured mean positioning error when approaching a specific target position from different directions.

3.2.5 Sensor type

In Table 3.1 and Table 3.2 we can see the indication (S) or (L) next to the repeatability value of the positioners. Those correspond to the type of the sensor that the positioner is using. The sensors can be either optical or inductive. They are integrated into the positioning stages for closed-loop position control. This allow the definition of the desired travel distance or the target position and the velocity of the stage. The S and L sensor are optical sensors with a single reference mark and a 1 nm resolution (S) and 4 nm resolution (L). SmarAct® has other types of sensors that will not be discussed further in this document.

3.2.6 Positioner Movement

SmarAct® provides the software packages required to control the different positioning stages. The SmarAct® controller is compatible with many programing languages. Here, we focus on LabVIEW™ as RF-2S team has a long experience in the development of automated RF solutions based on LabVIEW™. One of the most important aspect while programing the positioners is the choice of the movement type as this will change the behaviour of the positioner stages completely. Hence, it is important to understand the different positioning movement modes. Whether it is under LabVIEW™, the MCS2 controller software or the hand control module, we always find the same movement types:

- Absolute Closed-Loop mode
- Relative Closer-Loop mode
- Absolute Scan mode
- Relative Scan mode
- Step mode

The Step mode is the standard or the basic movement type and the easiest to implement. It does not allow any control or feedback regarding the position of the stages. Hence, its effectiveness is limited. The controller sends the stage a command that specifies the number of steps the stage needs to achieve. The frequency and the amplitude of the impulsions need to be known too. Figure 3.2 shows a representation of the Step mode.

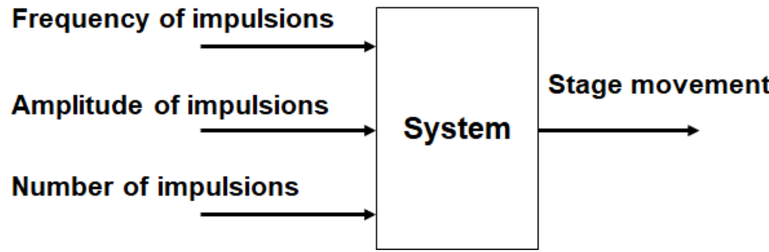

Figure 3.2 Representation of the SmarAct Step mode.

The Closed-Loop mode uses the feedback from the stage sensor in order to obtain precise movements. It considers the desired travel to achieve as a reference or a target. It uses the step mode while the control system regulates in real time the movements in order to obtain a quantifiable displacement. Figure 3.3 shows a representation of the Closed-Loop mode.

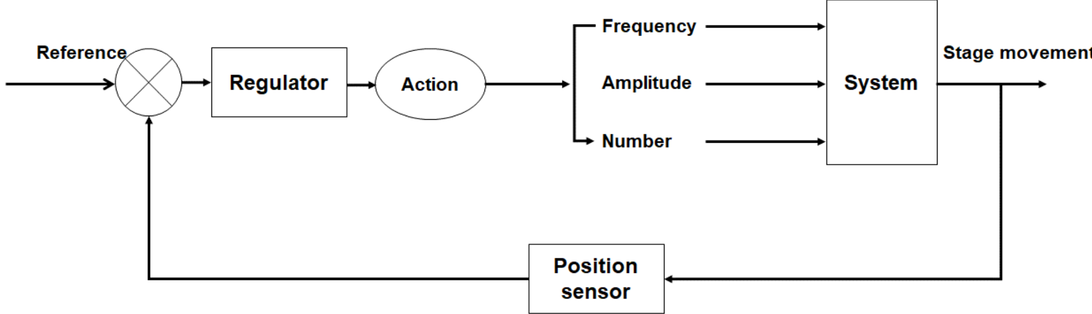

Figure 3.3 Representation of the SmarAct Closed-Loop mode.

As described in the SmarAct® technology section, the Scan mode allows controlling the extension of the piezo-element, enabling precise movements. However, no step is performed; thus, the maximum travel is very limited. Figure 3.4 shows a representation of the Scan mode.

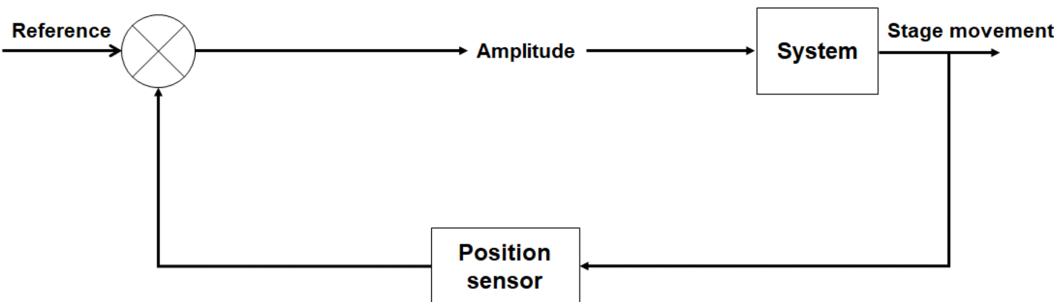

Figure 3.4 Representation of the SmarAct Scan mode.

In the following, we explain the difference between the "absolute" and the "relative" options. It is important to note that only a mode with a controllers can benefit from the two options. Hence, the Step mode is not concerned. When a movement request is made to the positioners, it can be:

- Absolute: when a movement request is done with the "absolute" option, the value requested is considered as a target position to reach. For example, if we indicate 100 µm, the positioner will reach that position considering the middle of the stage as its zero reference (by default. This parameter can be changed)
- Relative: when a movement request is done with the "relative" option, the value requested is considered a "step". If we indicate 100 µm, this distance will be added to the actual positon of the stage.

3.3 Positioner Properties

Several parameters can influence the precision and the behaviour of the positioners. We can achieve the desired outcome by modifying and adjusting these parameters. Two key parameters that are particularly important for the SmarAct® positioners are the maximum velocity (or speed) and the acceleration. In this study, we will examine and analyse these two parameters. We use the following stages: X direction SLC2430ds-22, Y direction SLC2430ds-23, Z direction SLC1730ds-40.

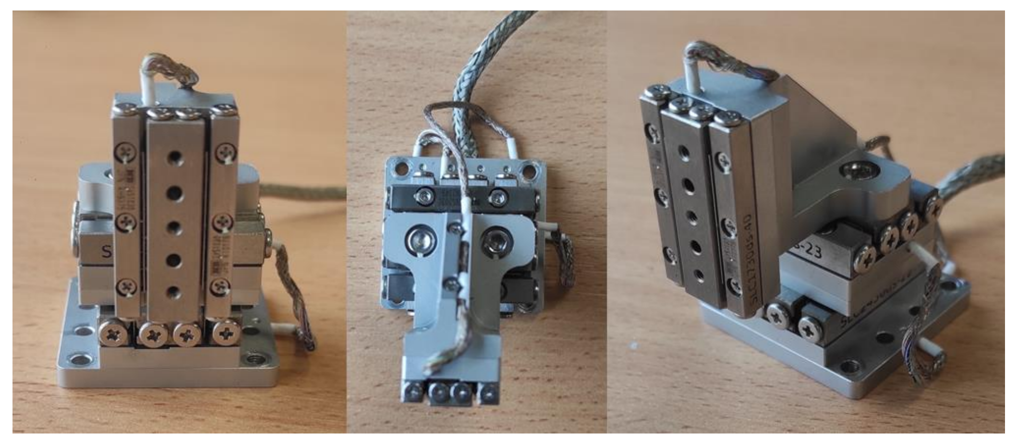

Figure 3.5 Actual images of the SLC2430ds-22 (X), SLC2430ds-23 (Y), SLC1730ds-40 (Z) stages.

By default, the MCS2 controller set the velocity to “0”. That means that the controller does not impose any restriction on the stage. Thus, the only limit is defined by the physical and mechanical performances of the positioner. Here, we still ignore the velocity that the controller imposes by default. In order to determine this value, we will impose different velocities to the positioner. We consider a target position of 3 mm, the positioner is in closed-loop and we monitor the position in real time. Figure 3.6 shows the displacement of the positioner as a function of time for different velocities. We observe that over 20 mm/s, the curves overlap. We can conclude that the physical limit of the positioner is reached. We can obtain the velocity limitation of the positioner by calculation the slope of one of the four curves. Thus, the maximum velocity as limited by the MCS2 controller is approximatively 17 mm/s. Using the positions, the velocity and the time, we can obtain the maximum acceleration, here 181.137 mm/s².

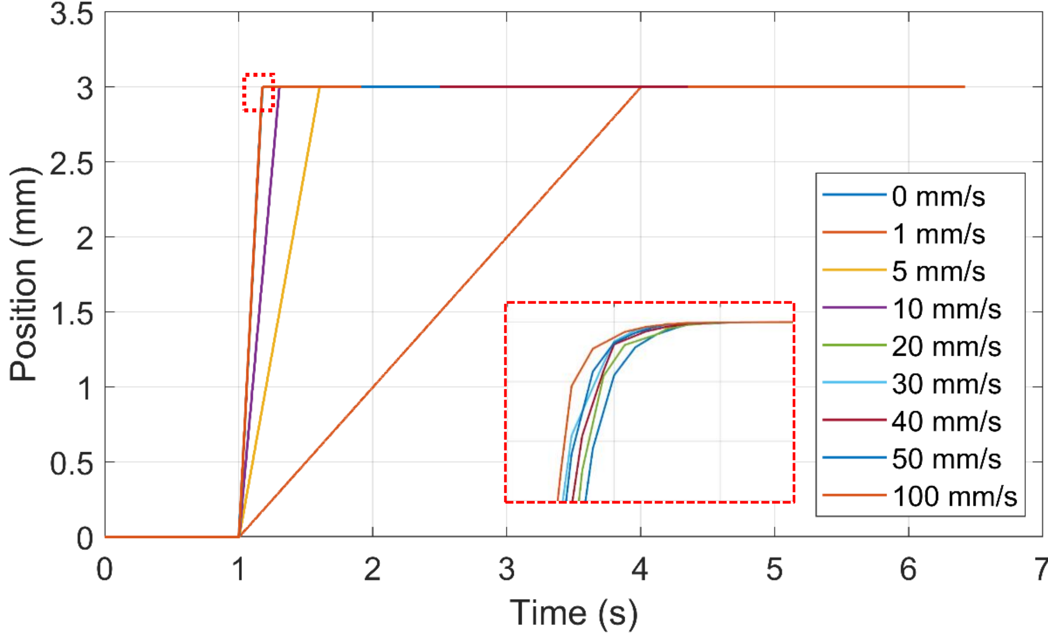

Figure 3.6 Displacement of the positioner as a function of time for different velocities considering the X direction and the SLC2430ds-22 stage.

Other parameter regulate the behaviour of the positioner: frequency of the voltage impulsions. In particular, two modes named step frequency and closed-loop frequency can be considered. Here, we focus on the closed-loop frequency. This parameter acts directly on the speed of execution of the positioner and affects the velocity and the acceleration. Here again, we impose different frequencies to the positioner. We consider a target position of 3 mm, the positioner is in closed-loop and we monitor the position in real time. Figure 3.7 shows the displacement of the positioner as a function of time for different frequencies. We observe that when the frequency of the steps increases, the positioner is faster to reach the target position. By extracting the maximum velocity for each frequency using the position over time curves in Figure 3.7, we obtain a linear relationship between the frequency and the velocity and by extension, the acceleration. This is shown in Figure 3.8. Therefore, the maximum velocity of 17 mm/s that we obtained earlier corresponds to a frequency of 5000 Hz. The positioner can go up to 70 mm/s at 20 kHz. However, the frequency will not only act on the velocity, but also on the thermal stability of the MCS2 controller. In order to avoid any overheating problem of the controller, a maximum frequency of 5000 Hz is considered in this work.

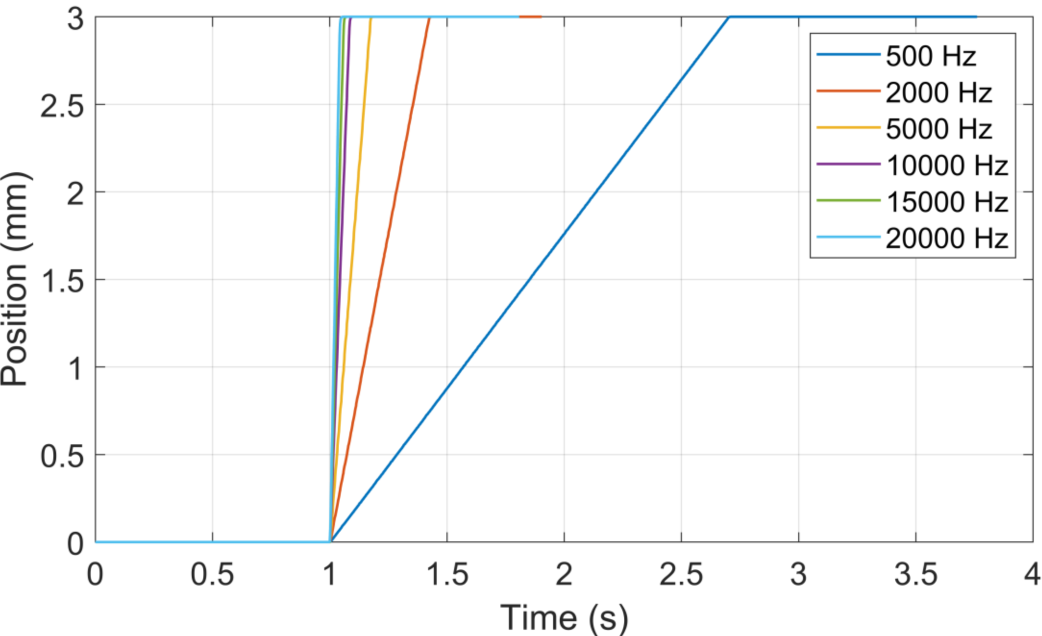

Figure 3.7 Displacement of the positioner as a function of time for different frequencies considering the X direction and the SLC2430ds-22 stage.

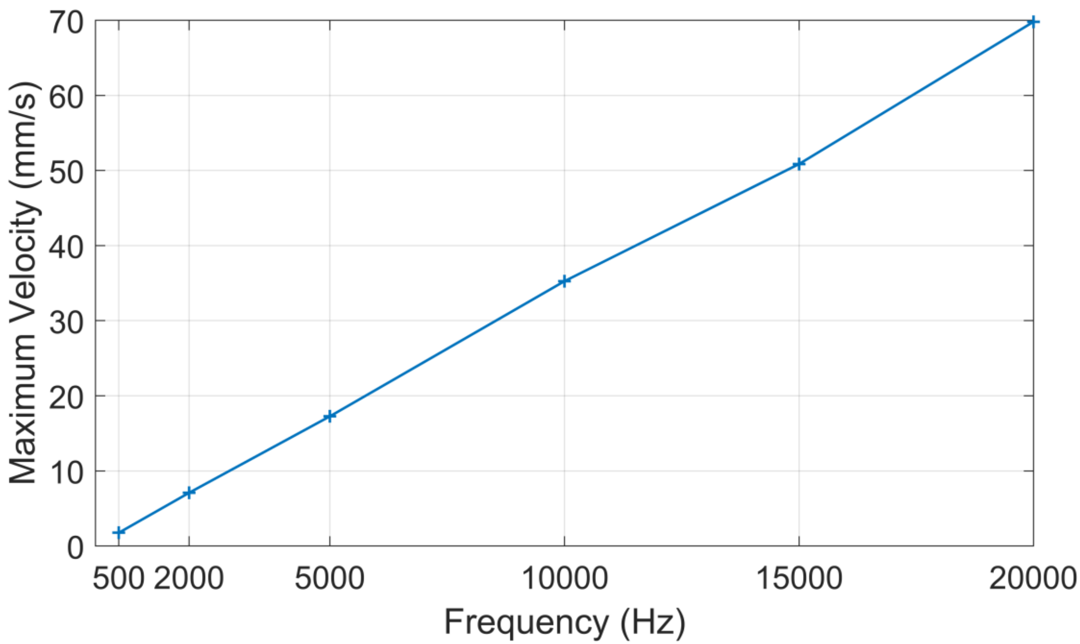

Figure 3.8 Maximum velocity as a function of frequency considering the X direction and the SLC2430ds-22 stage.

Another interesting aspect of the positioner to quantify is its static accuracy. Here, we check if the controller is able to maintain a fixed position with precision. Two control modes are tested. The controller is either:

- Stopped: and ceases any operation on the piezo-electrical part,

or

- Holding: where the positioner continuously controls the position by making slight modifications on the piezo-electrical part to maintain the target position imposed.

In order to observe the position error over time, we monitor the Z stage. Indeed, the vertical Z stage is directly subject to the gravitational force pulling the piezo-electrical part down. The "closed-loop" (CL) corresponds to an active control of the position and the positioner is "holding". The "open-loop" (OL) corresponds to no active control of the position and the positioner is "stopped". Also, we monitor the stages when free of charge not loaded (NL) and when loaded (LO) with an additional weight. Therefore, four configurations are tested: Closed-Loop Not Loaded (CL NL), Closed-Loop Loaded (CL LO), Open-Loop Not Loaded (OL NL), and Open-Loop Loaded (OP LO). Figure 3.9 shows the drift over 30 min for the four configurations.

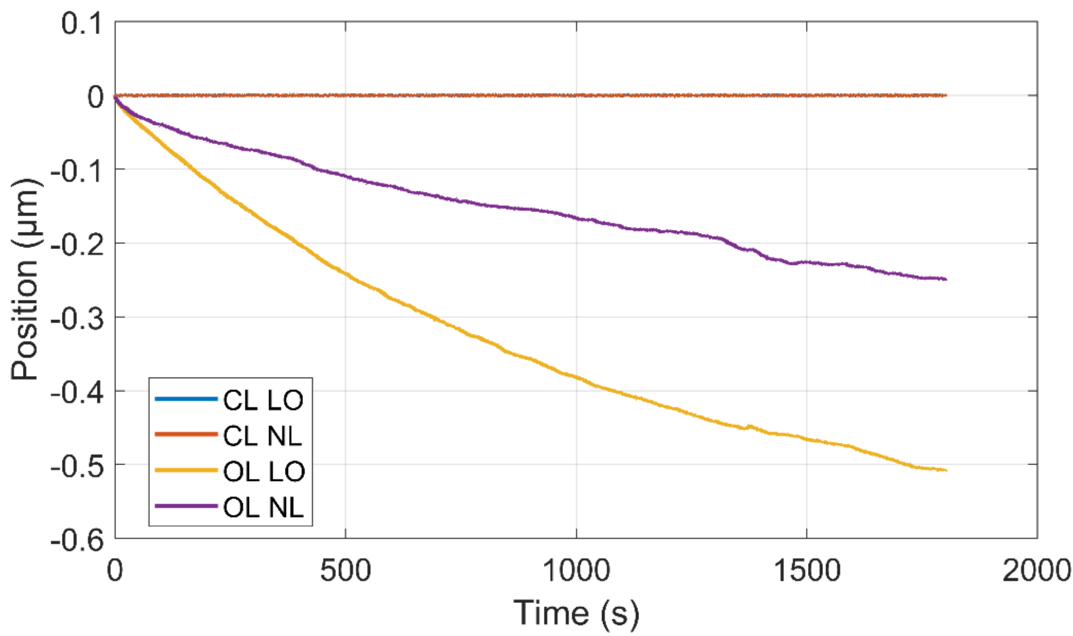

Figure 3.9 Drift over time of the positioner considering the Z direction and the SLC1730ds-40 stage.

According to Figure 3.9 we see that when the positioner is operating in the closed-loop mode (holding) there is no drift. The positioner is controlling the position in real time even when the stage is loaded with an additional weight. In the open-loop (stopped) however, we observe a significant drift: 0.25 µm when the stage is not loaded and 0.5 µm when the stage is loaded. We conclude that a real time position correction is necessary in order to keep a fixed position and avoid any drift related issues.

Table 3.3 shows some additional properties of the positioners.

Table 3.3 Positioner Properties.

Max Closed-Loop Frequency	The maximum frequency driving the stick-slip piezo-stage for closed-loop movement commands. The maximum allowed depends on the positioner and the environment. Valid range is 50 … 20000 Hz.
Default Max Closed Loop Frequency	The default value at device start up for the maximum closed-loop frequency. The default frequency is 5000 Hz.
Step frequency	The frequency that open-loop steps are performed with. The default frequency is 1000 Hz. The valid range is 1 … 20000 Hz. Used.
Step Amplitude	The amplitude that the open-loop steps are performed with. The step amplitude is 16-bit value from 1 … 65535n where 65535 corresponds to 100 V. The default amplitude is 100 V.
Control Quantum	0.0015259 V
Position Quantum	53.41 pm

3.4 Automated and robotic probing station: hardware development

The aim of this work is the development of a nanorobotics and automated probe station for on-wafer GSG measurements. The station is developed completely from scratch. Therefore, the hardware development constitutes the longest and more complex part of this work. Indeed, it involved interfacing different elements of different nature that are not designed to work together. A considerable effort was put into developing an operational on-wafer probing station in the given time. Table 3.4 shows the specification sheet followed in order to develop the robotic and automated on-wafer probe station.

Table 3.4 Specification Sheet regarding the development of the robotics and automated on-wafer probe station.

Context	The miniaturization of RF devices is essential for the development of new technologies, but it requires advances in the metrological characterization, especially, accurate S-parameters measurements. One of the main challenges is the precise and accurate on-wafer measurement of the electrical properties of micro- and nano-devices
Objective	Development of a new generation of on-wafer probe station that is robotic and automated
Instrument specifications	- Automatic alignment of GSG probes on DUTs - Accurate and repeatable positioning - Low noise instrumentation - Compact solution - Easily integrable in industrial environment
Environmental specifications	- Controlled vibrations (early goal) - Controlled temperature and humidity (end goal)
Instrument design	- SolidWorks® mechanical design of different parts of the station: probe attachment pieces, camera bridge - Fabrication of the different elements at IEMN and external commercial companies
Instrument implementation	Link the different elements efficiently
Software development	- Brainstorming on the technique to use - Explore each proposed idea and test its viability - Final program architecture - Develop each part of the program alone followed by tests and validation - Complete program
Testing	- Implementation of the automation program - Testing with no sensitive instruments (probes, DUTs) - Validation and test on the complete system

In the following, we present the different part or “Sub-systems” that compose the station as well as the challenges faced with each element. The station is built up with:

- Newport™ M-VIS3036-SG2-325A optical table: 750 x 900 x 59 mm with pneumatic isolators. It allows a horizontal isolation at 5 Hz and 10 Hz of 90% and 98% respectively and a vertical isolation at 5 Hz and 10 Hz of 90% and 98% respectively. We chose pneumatic isolators in order to have a good removal of building vibrations.

Acquiring the optical table took more than a year. Two main reasons are behind this delay. First, a market evaluation had to be done in order to choose the most suitable table for our application. Criteria were efficiency, size, integrability, and budget. We opted for a medium sized table to fit the dedicated space. The integration of pneumatic isolators required an air pump as the building is not equipped with an air system. Finally, the purchase was done only when the budget was available. The optical table is a key element of the station as it highly reduces the influence of the building vibrations. Working with nano-positioners makes sense only if the vibrations are small enough to allow a sub-micrometric accuracy.

- Keysight® 5008A Streamline Series USB Vector Network Analyzer: compact 2-port VNA 100 kHz – 53 GHz. We chose the Streamline because it offers a compact solution. Indeed, with its small physical dimensions and weight (Table 3.5), it is possible to integrate it directly on the optical table and as close as possible to the probes. This also allow having short cables, reducing the system's measurement uncertainties. In addition, the Streamline is completely automatable via Keysight® software Command Expert or LabVIEW™. The last is the best solution as our system is using LabVIEW™ for the automation part.

Here again, we were confronted to purchase delays (budget, delivery time). Once the equipment available, time was spent understanding how it works and most importantly how to connect it to other software: LabVIEW™ (as explained before) and Wincal™. Wincal™ is the calibration software by FormFactor™. It allows on-wafer calibration using multiple calibration algorithms. Specific manipulations are necessary to connect the VNA to the software.

Table 3.5 Keysight® Streamline P5008A physical properties (dimensions/weight).

Dimensions / Weight	Keysight Streamline P5008A
Width	176 mm (6.93 in.)
Height	48 mm (1.89 in.)
Depth	333 mm (13.11 in.)
Weight	2.02 g (4.45 lbs)

- MegaPhase UltraPhase™ Cable Cables: 30 cm flexible cable up to 67 GHz with 6.9 dB/m attenuation. We chose the most flexible and lighter cables possible in order to apply the least tension on the positioners. The cables are also very short, which reduces measurement uncertainties.
- Moticam CAM-1080P HDMI camera: 2 MP resolution, 60 fps 1080 p, HDMI, USB with dedicated software for calibration and measurements. The Moticam camera is easy to use and easy to install. The software provided allows calibration for dimensional measurements according to the zoom used (Figure 3.10).

Figure 3.10 The Moticam CAM-1080P HDMI camera (www.micromecanique.fr).

- MPI OP-Z10 Zoom Microscope: optical factor 0.85x – 8.5x (10:1), down to 2.5 µm resolution, 90 mm working distance. The working distance is perfect for same probes and DUTs manipulation. The zoom also includes a manual fine focus block. It is mounted on a 90 ° angle fixation block to rotate the zoom and proceed to more complex probe/DUT manipulation that required more space (Figure 3.11).

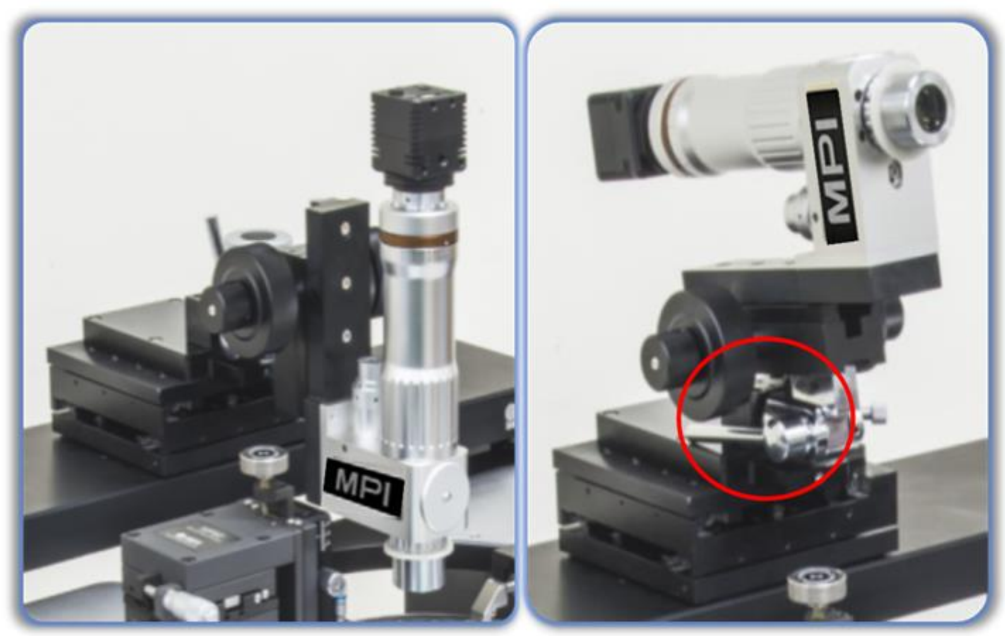

Figure 3.11 The MPI OP-Z10 Zoom Microscope. In red, the 90 ° angle fixation (MPI Corporation All Rights Reserved).

Before acquiring the MPI camera, we considered other more sophisticated cameras available on the market. However, we had to compromise between functionalities, performance and access to the software. Indeed, we finally chose a manual camera that allows good performances. As the system is in early development, the MPI camera is sufficient. Future updates might integrate an automated camera.

Due to the architecture of the camera, it was impossible to integrate it directly to the system. A "camera bridge" was designed and fabricated at the IEMN. The bridge had to be strong enough to support the weight of the whole camera. Also, it had to respect the working distance of the Zoom Microscope. The 90 mm distance between the lens of the zoom and the surface of the DUT was taken into account in the design of the bridge. Figure 3.12 shows a schematic representation of the optical bridge. The adjustment brick shown was added later to fix the final height of the bridge. Figure 3.13 shows the final version of the optical bridge installed in the station.

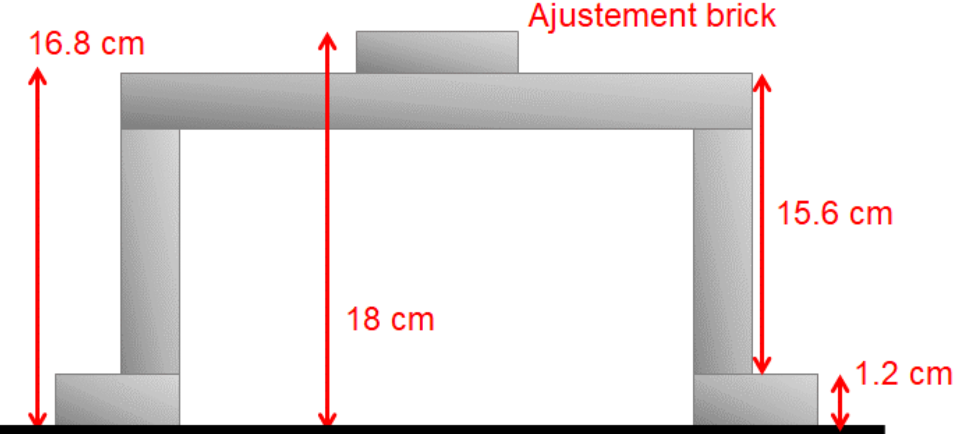

Figure 3.12 Schematic representation of the optical bridge.

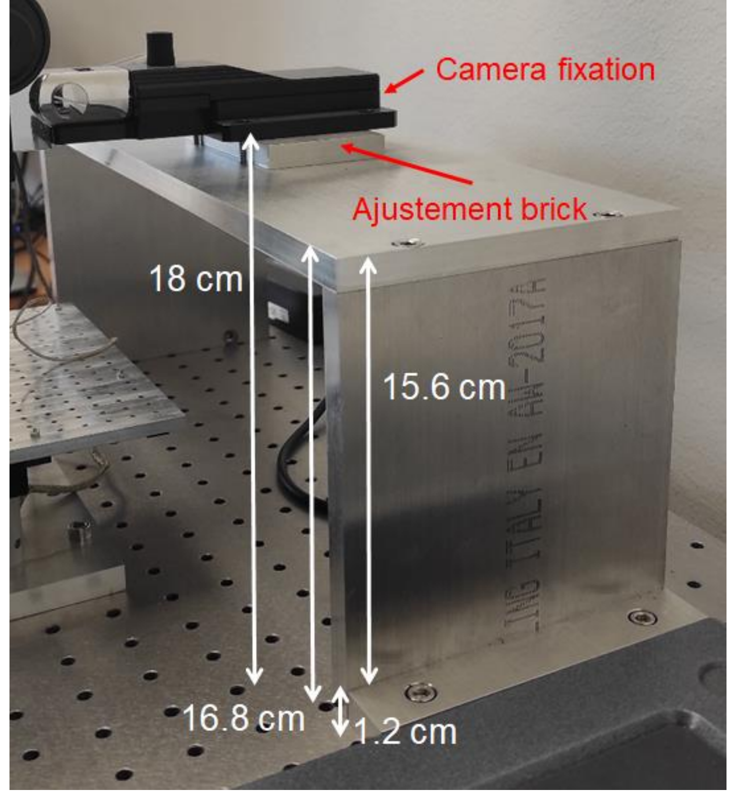

Figure 3.13 Optical bridge installed on the probing station.

- SmarAct® MCS2 controller: Rack Housing system with six slots (18 stages), closed loop control (Figure 3.14). As explained previously regarding the MCS2 controllers, each slot

controls up to three stages. The probes are mounted on four stages each and the chuck on three stages, making it a total of 11 stages. Therefore, we chose the rack housing. Extra slots are available and will allow the station to host more probes, DC probes for example for DC polarisation of active DUTs.

Figure 3.14 The SmarAct® MCS2 controller Rack Housing system.

- SmarAct® positioning stages: three linear stages and one rotation stage for the probe, 2 linear stages and one rotation stage for the chuck (Table 3.1, Table 3.2).
- FormFactor™ Infinity GSG probes with 100 µm pitch (Figure 3.15). The station is configured for the commercially available Infinity GSG probes making the station suitable for industrial application. Challenge faced with the Infinity probe was to find a mechanical solution to adapt the probe to the positioners. Details regarding this matter will be explained later.

Figure 3.15 FormFactor™ Infinity GSG probe (the 150 µm and 100 µm pitch are similar in shape and size, only difference is the tip).

Figure 3.16 shows a complete schematic representation of the robotics and automated probing station for on-wafer GSG measurement based on SmarAct positioners.

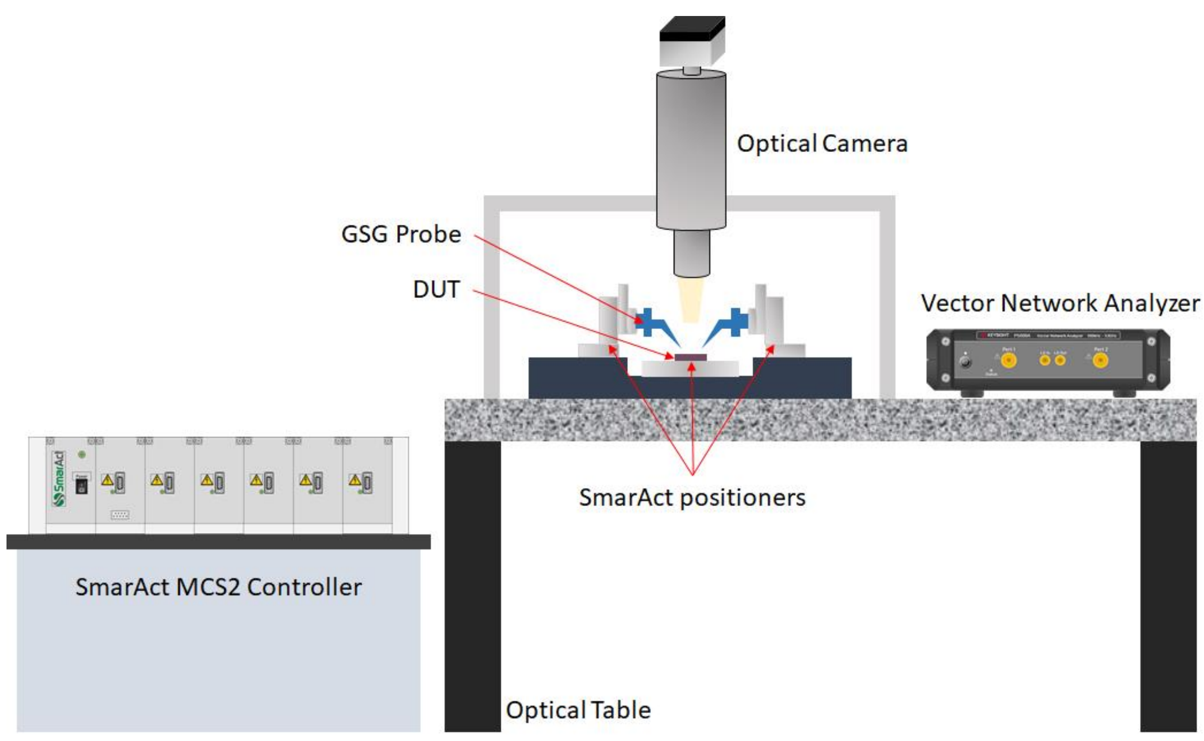

Figure 3.16 Schematic representation of the robotics and automated probing station.

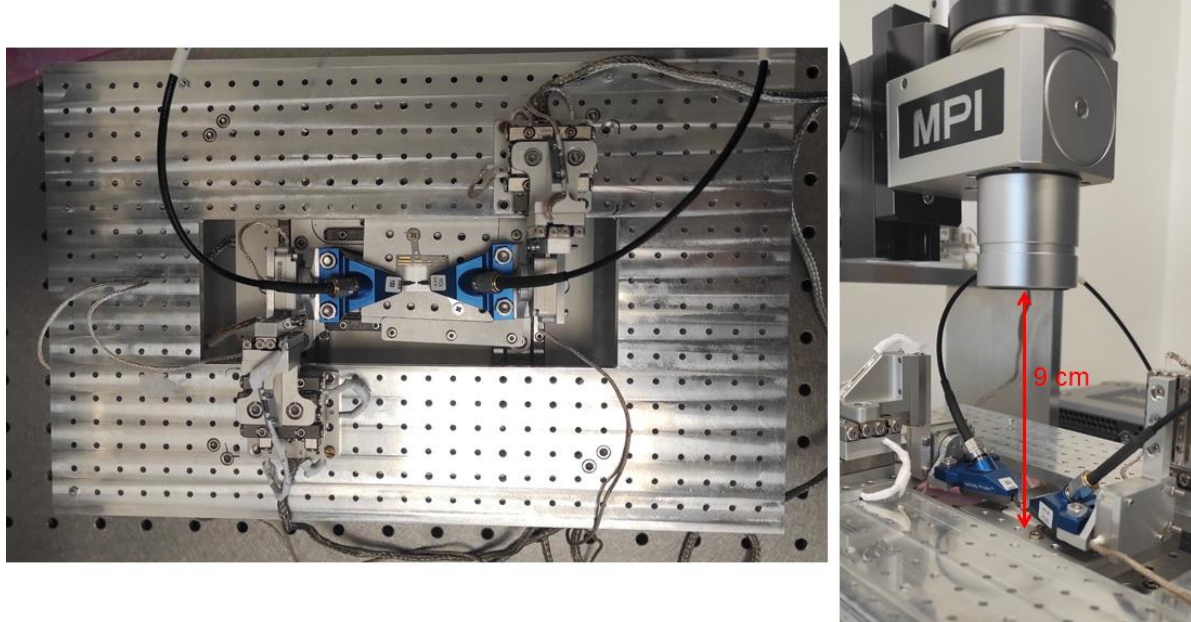

Figure 3.17 Top view picture of the probes and the chuck with a calibration substrate (left). Side view picture pf the probes and the camera (right).

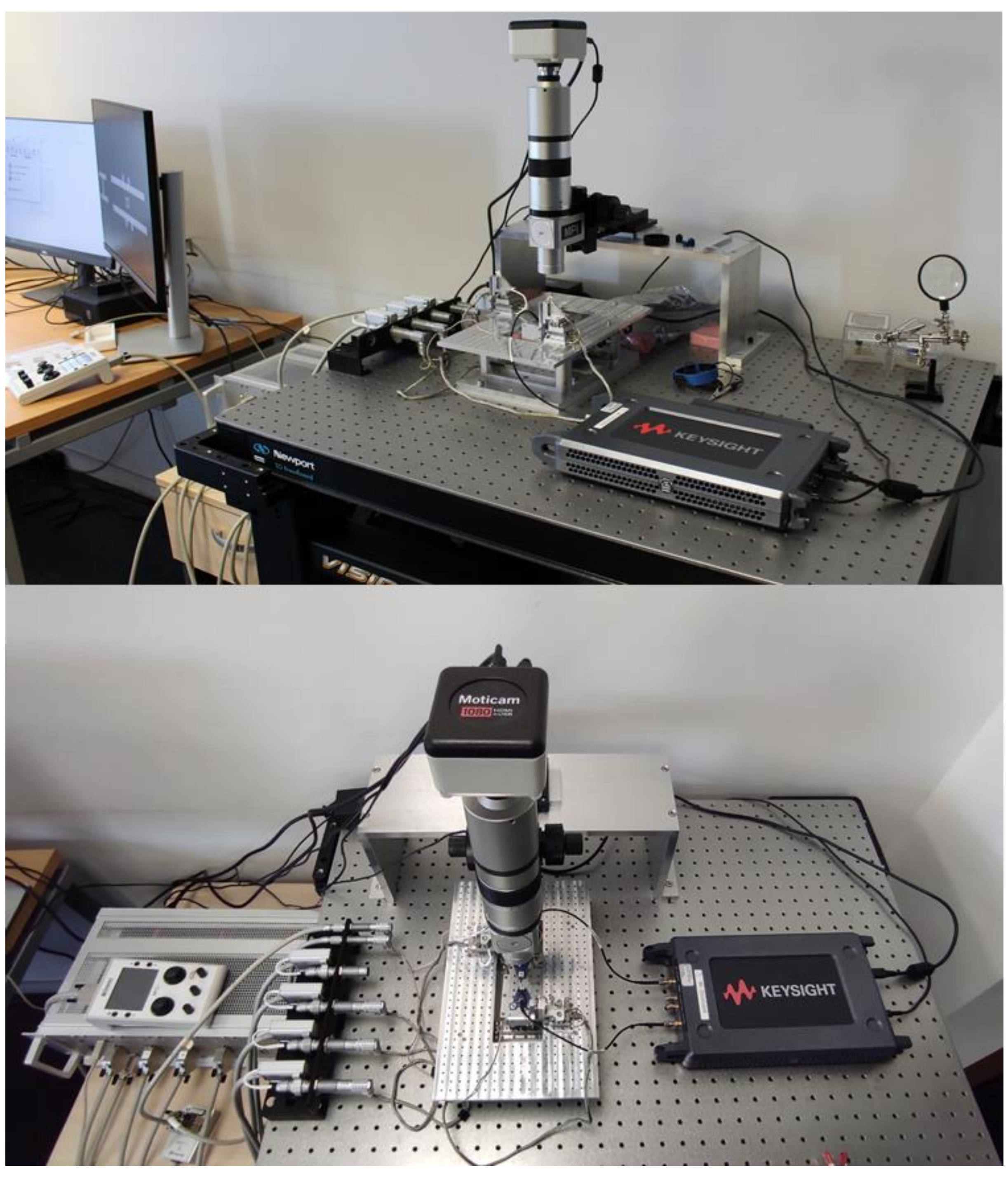

Figure 3.18 Side picture of the complete probing station (top). Top view picture of the complete probing station (bottom).

Figure 3.19 LabVIEW™ dedicated screen (left). Wincal™ dedicated screen (middle). Camera feedback dedicated screen (right).

In the following, we show how the RF probes were attached onto the positioners. Considering the geometry of the Infinity GSG probes, attachment pieces were designed using SolidWorks® and fabricated to fix and secure the probes. In addition, metallic attaches were added to the chuck in order to fix the DUT. From now on and in order to simplify the designation, we refer to the four positioning stages holding the probe as “the probe positioner” and to the three positioning stages of the chuck as the “chuck positioner”.

Figure 3.20 shows the three linear stages of the probe positioner. As we can see, the positioner is not adapted to hold a GSG probe as it is. Special attachment pieces were designed and fabricated in order to attach the probe. Figure 3.21 shows the attachment pieces 3D printed in PLA (at IEMN). Figure 3.22 shows the fabricated pieced in metal by Materialise (an external commercial company).

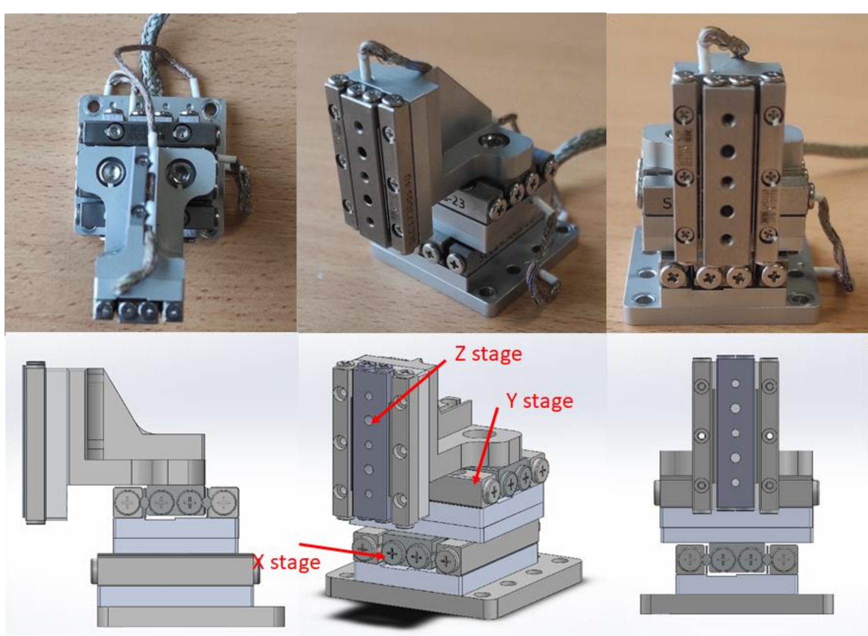

Figure 3.20 SmarAct probe positioner.

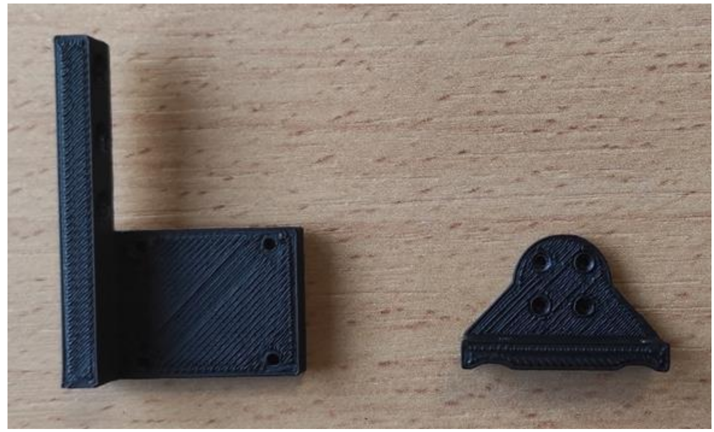

Figure 3.21 the attachment pieces 3D printed in PLA (at IEMN).

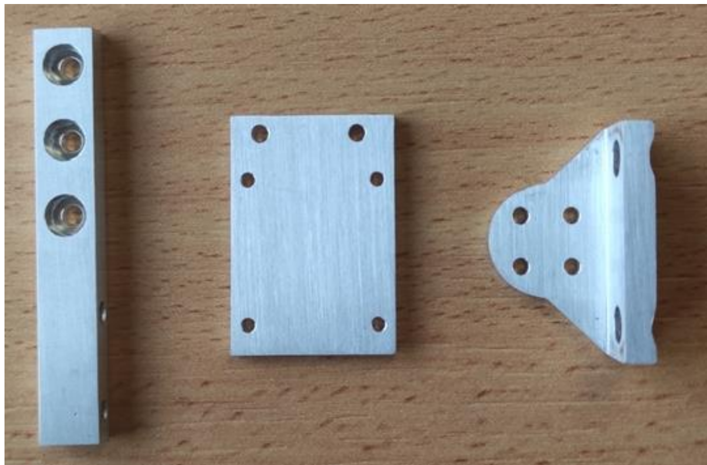

Figure 3.22 The fabricated pieced in Al6061 by Materialise (external commercial company).

There are three pieces. The first one is fixed along the Z stage on the probe positioner and holds the rest of the pieces as well as the probe. Thus, this piece needs to be secured correctly in order to maintain the probe. The second piece is fixed to the first piece from one side and to the rotation stage on the other side. The third and last piece is fixed to the rotation stage. The GSG probe will be fixed to the third piece. All pieces need to be fixed tightly to ensure the stability of the system. Figure 3.23 illustrates the attachment pieces.

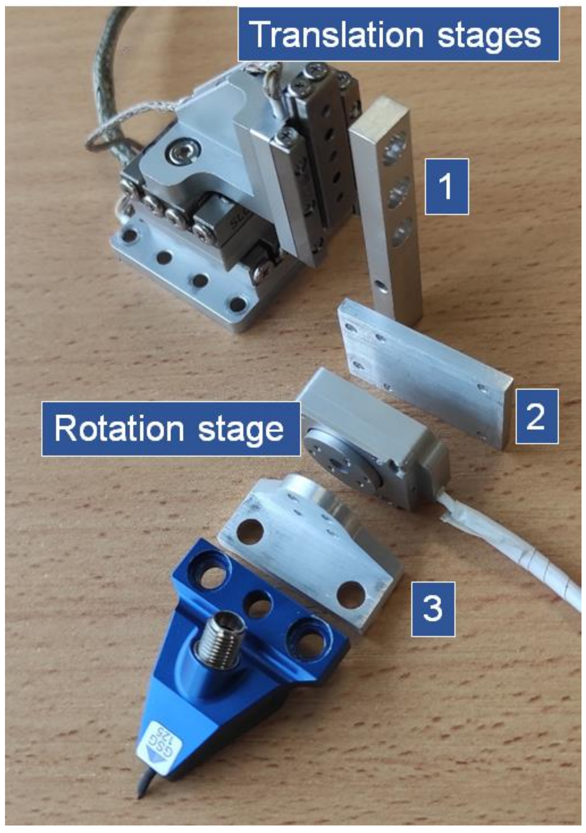

Figure 3.23 1st piece attached to the Z stage, 2nd piece attaching the 1st piece to the rotation stage, 3rd piece attaching the rotation stage to the probe

Figure 3.24 shows a schematic representation of the Infinity GSG probe attached to the positioner. Figure 3.25 shows the actual probe mounted on the positioner. Finally, the positioner is fixed on the station from its base. In total, two probe positioners are present on the station.

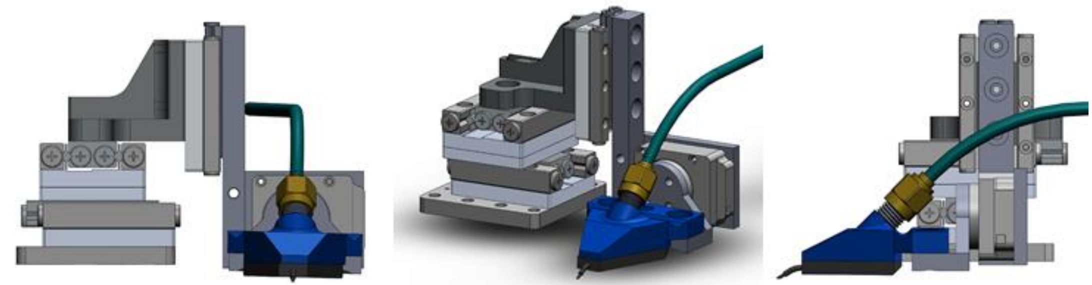

Figure 3.24 SmarAct probe positioner with the attachment pieces and the Infinity GSG probe.

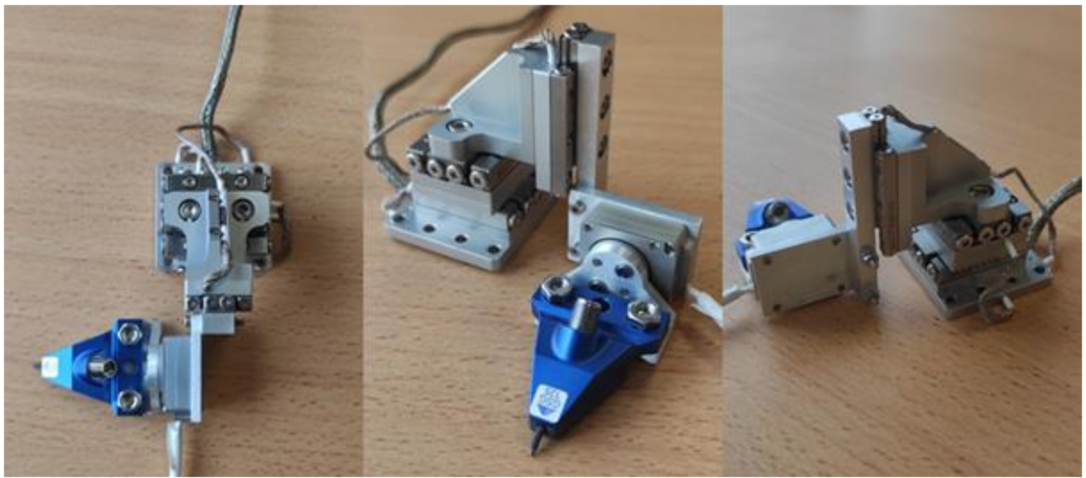

Figure 3.25 Actual picture of the Infinity probe mounted on the four stages positioner.

Figure 3.26 shows the three stages of the chuck positioner. The chuck is mounted on the rotation stage on the top. The dark grey part of the chuck can slide and detach from the rest in order to insert devices under test easily. The yellow metallic fixations allow the devices under test to be fixed tightly for measurements, as there is no vacuum system. The whole positioner will is fixed to the station from its base.

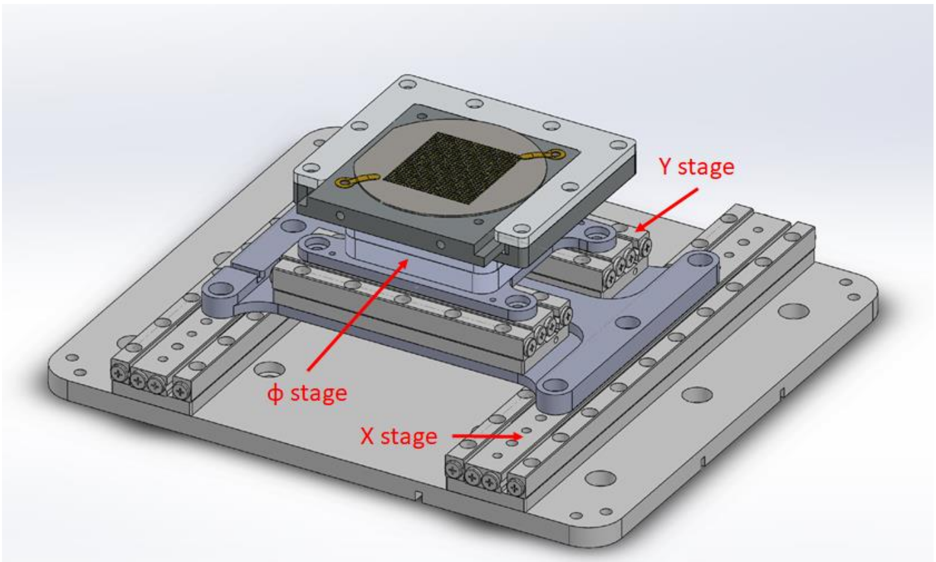

Figure 3.26 Schematic representation of the chuck positioner.

The last piece of the station to be designed is the top plate that carries the probe positioners. Figure 3.27 shows the original design provided by SmarAct®. Unfortunately, the inside hole was not wide enough to allow the probes to move freely and without a risk of collision with the hole edges. Therefore, we designed another top plate that allows better movement for the probes. The design is shown in Figure 3.28, and was designed using SolidWorks® software and fabricated at the IEMN laboratory. It also enables the probes and the chuck to cover an entire DUT that would be placed on the chuck, which the previous version of the plate did not allow for.

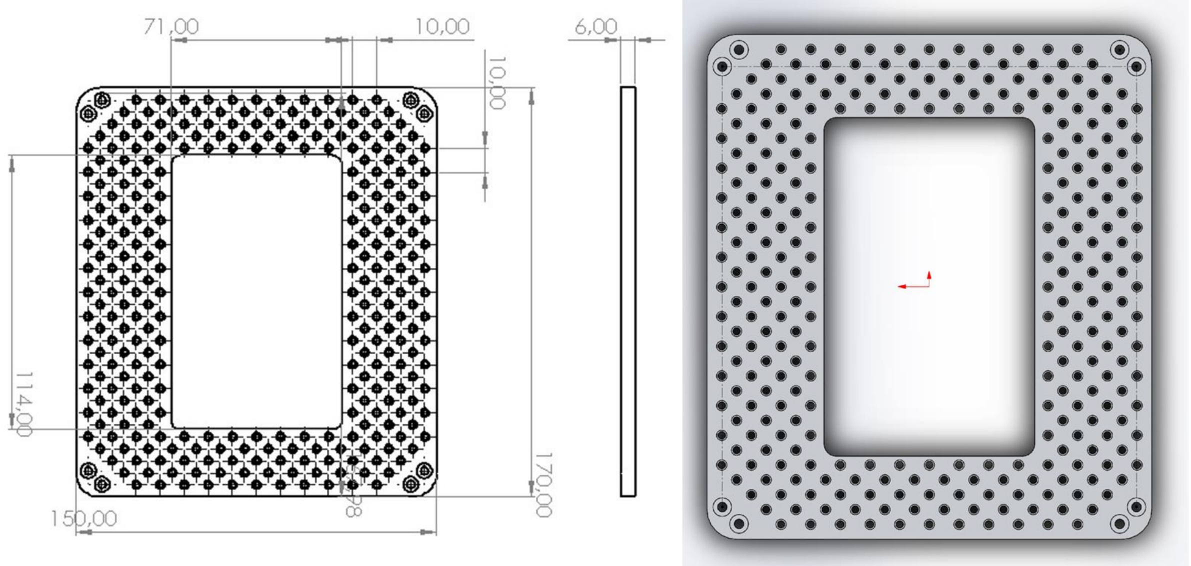

Figure 3.27 Original design of the top plate as provided by SmarAct® (quotations are in mm).

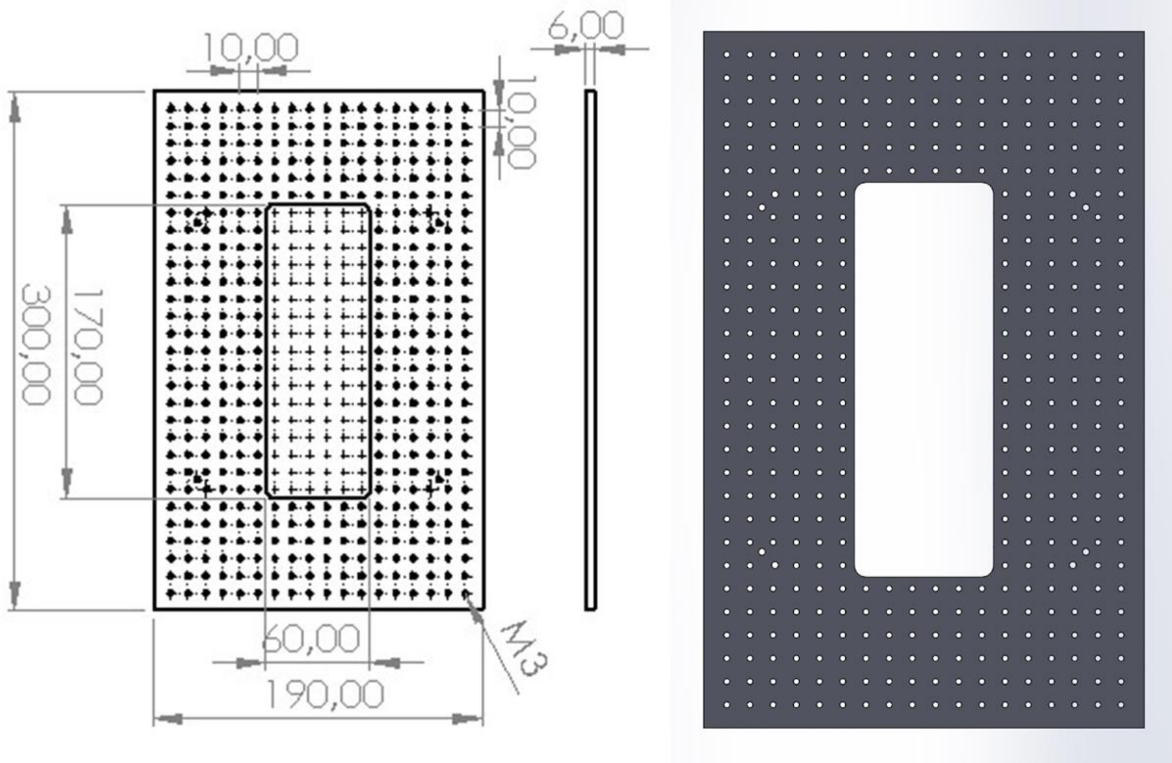

Figure 3.28 Design of the top plate after modifications (quotations are in mm).

Figure 3.29 shows the automated and robotics GSG probing station based on the SmarAct positioning stages. The station is fixed from its base to an optical table. The optical camera is positioned and centered over the station. The RF cables were chosen light enough and flexible enough so that they do not apply to much pressure on the probe positioner. Indeed, the maximal lift force of the positioners (SLC series) is 1.5 N.

It is important to note that the station was designed and developed from scratch. The RF-2S team is actually working on mechanical modifications in order to improve the performance of

the station. For example, the cables should be supported and fixed to minimise cable torsion leading to measurement uncertainties.

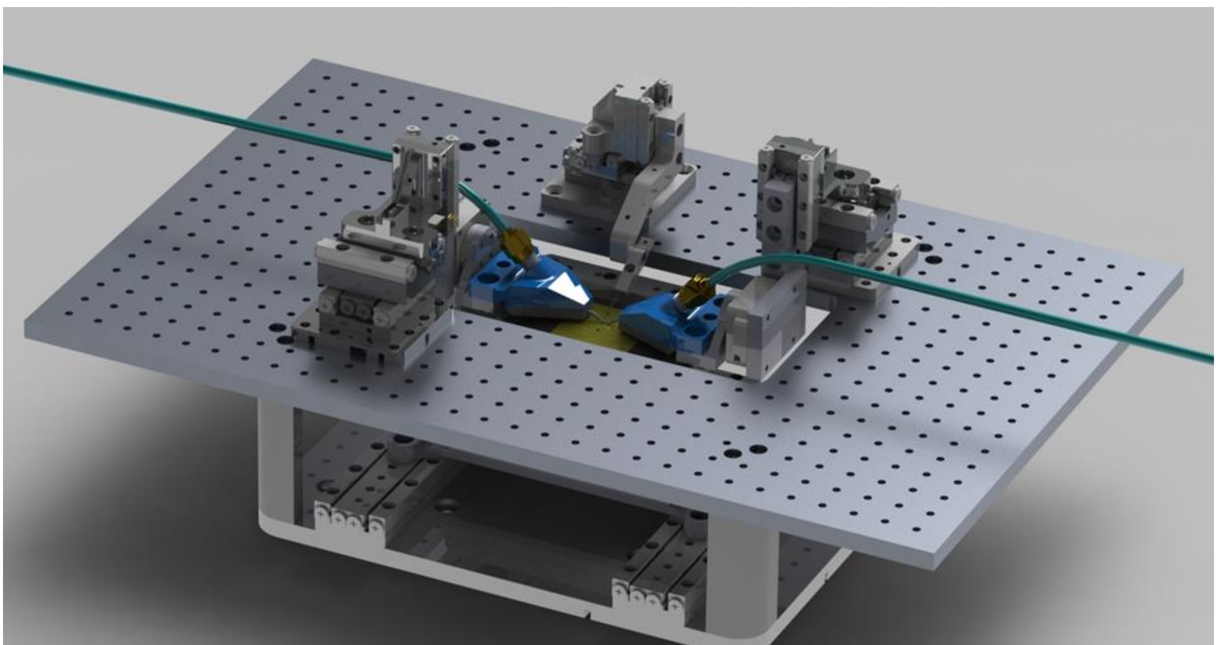

Figure 3.29 The automated and robotics GSG probing station based on SmarAct positioners.

3.5 Positioning repeatability of the SmarAct nano-positioners with a DC probe

One of the early steps in the development of the automated and robotic on-wafer probing station is to quantify the mechanical performance of the system. To this end, a DC probe was mounted on one of the nano-positioners. Manually, the DC probe was brought in contact with a gold substrate. The contact position is saved into the program. Then, the probe is raised by $100\ \mu m$ above the surface. The retract position is also saved into the program. The alignment of the probe along the X and the Y axis are fixed then locked for the rest of the experiment. 10 successive and automated repositioning of the DC probe on the gold substrate are made and the movements along the Z axis are monitored. Figure 3.30 schematizes the experiment.

Figure 3.31 shows the 10 successive positions of the DC probe on the gold substrate as well as the target position. It shows that the reached position oscillates randomly around the target position. Those oscillations are attributed mainly to environmental vibrations that were not cancelled by the optical table.

Figure 3.32 illustrates the absolute positioning error of the DC probe along the Z axis for 10 successive positioning at $500\ nm/s$. Table 3.6 gives the maximum absolute error, the minimum absolute error and the mean absolute error calculated for 10 positioning as defined by (4.24), where z is the reference contact position and z_i is the ith position ($i = 10$). Retract distance was $100\ \mu m$ and the nano-positioner was moving at (a) $500\ nm/s$ and (b) $1\ \mu m/s$.

$$AbsError = |z - z_i| \quad (4.24)$$

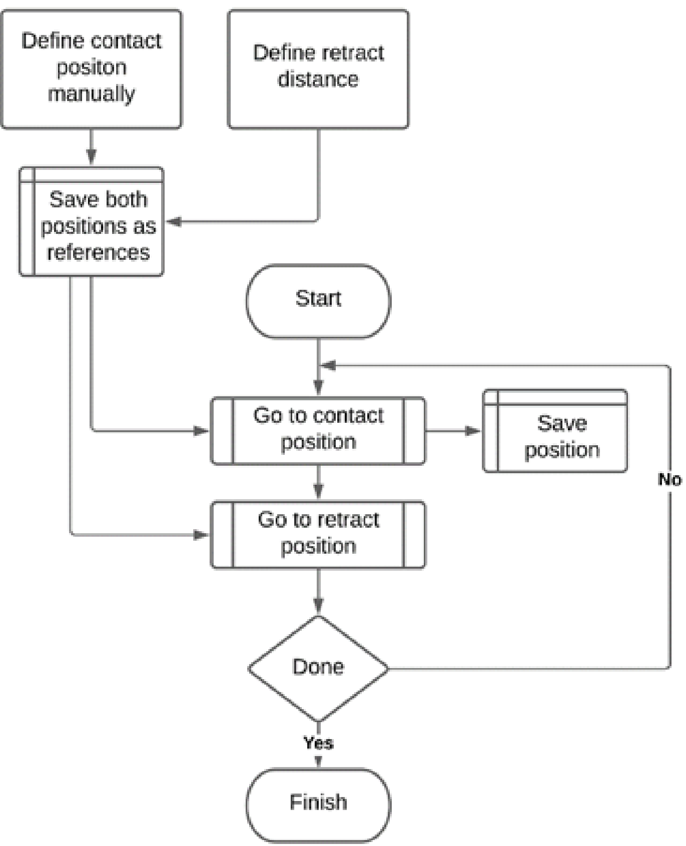

Figure 3.30 Schematic representation of the positioning repeatability process.

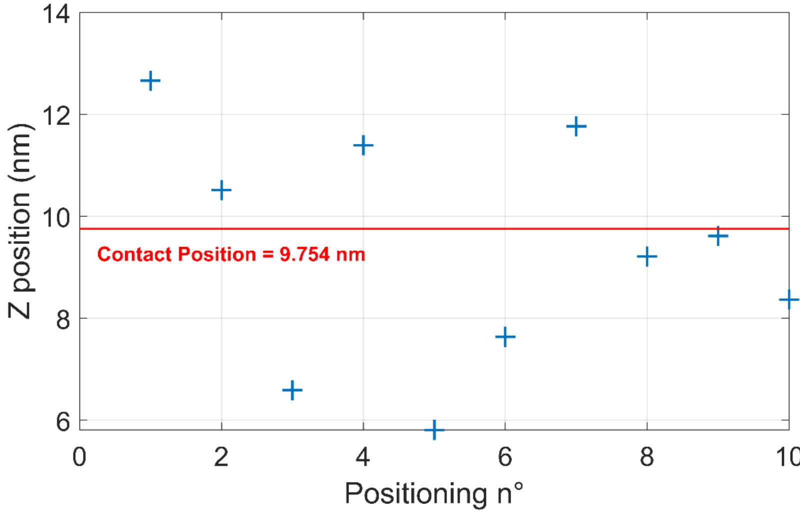

Figure 3.31 Position of the DC probe along the Z axis for 10 successive positioning.

From Figure 3.32 and Table 3.6, we can see that after 10 repositioning of the DC probe, the absolute error is kept relatively small. The maximum error is around $4\,nm$ and $6\,nm$ at $500\,nm/s$ and $1\mu m/s$ respectively. We observe that when moving at a reduced speed, the positioner is more accurate. It is important to note that even though the probing station is set on an optical table, the environment is still not completely controlled.

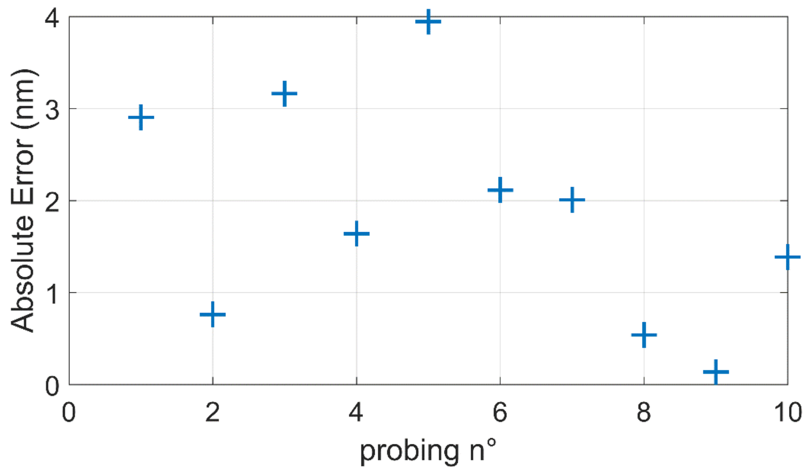

Figure 3.32 Absolute positioning error of the DC probe along the Z axis for 10 successive positioning at 500 nm/s.

Table 3.6 Maximum absolute error, minimum absolute error and mean absolute error for 10 positioning at two different positioner's speed.

Speed	max AbsError [nm]	min AbsError [nm]	mean AbsError [nm]
500 nm/s	3.944	0.138	1.8606
1 µm/s	5.514	0.191	2.432

3.6 Static drift of the positioners with the Infinity probe

Previously, we showed the static drift of the Z-axis of the positioners in closed and open loop when loaded with extra weight and not. Here, we present a similar study. However, the station is used in its final version. Meaning, the positioners are on the optical table and vibrations are cancelled. Also, the Infinity probes are mounted on their positioner.

The aim of this study is to evaluate the static precision of the positioner, especially when the RF cable is attached to the probe and the VNA from both ends, which applies an additional tension to the positioner. Hence, we want to compare the precision of the positioner when the cable is connected to both the probe and VNA and when it is connected to the probe only. The positioners have been given a static position, and put on "holding" mode (real time closed-loop position correction). The position on the X, Y, and Z axis were monitored over 30 minutes for the two configurations: probe alone, probe with cables attached.

Figure 3.33 shows the positioner and the probe we used. Positioner type is the same as used previously (SLC2430ds (X), SLC2430ds (Y), SLC1730ds (Z)).

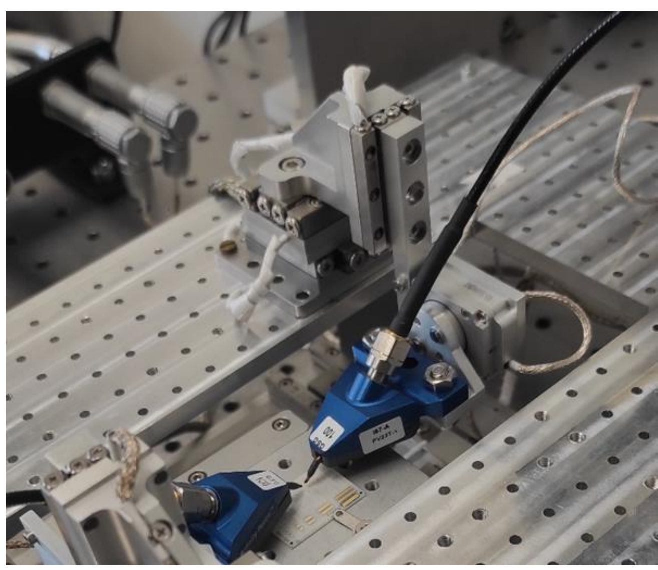

Figure 3.33 Probing station: Positioner with the DC probe and the RF cables attached on the optical table.

Figure 3.34 shows the absolute error of the static positions of the probe positioners over 30 minutes of monitoring for the three axis (stages) for the cable attached to the probe only. Figure 3.35 shows absolute error of the static positions of the probe positioners over 30 minutes of monitoring for the three axis (stages) for the cable attached to both the probe and VNA. We observe that the absolute error is relatively small, a few nanometres only for both cases. The positioner maintains a precise and accurate position over 30 minutes. The remaining oscillations are due to the vibrations that were nor completely cancelled by the optical table. Table 3.7 shows the mean and maximum absolute error calculated for both configurations. For the X and Y axis, the errors calculated when the cable is attached to the probe only are slightly smaller than when it is attached at both ends. For the Z axis however, the error is bigger when the cable is free on one side. This could be explained by the fact that when the cable is exercising a constant tension, the positioner is working harder to maintain the position and hence have a better overall performance. In addition, we can see that the error on the X axis are bigger that on the Y axis. This is due to the direction of the cable. Indeed, it is more pulling on the X-axis, introducing slightly more errors.

Table 3.7 mean and maximum absolute error calculated for both configurations.

[nm]	X		Y		Z	
Abs Error	Probe	Probe + cable	Probe	Probe + cable	Probe	Probe + cable
Mean	0.5167	0.8631	0.3004	0.7743	1.0623	0.4149
max	2.206	2.7300	1.6590	2.3820	2.9630	1.7560

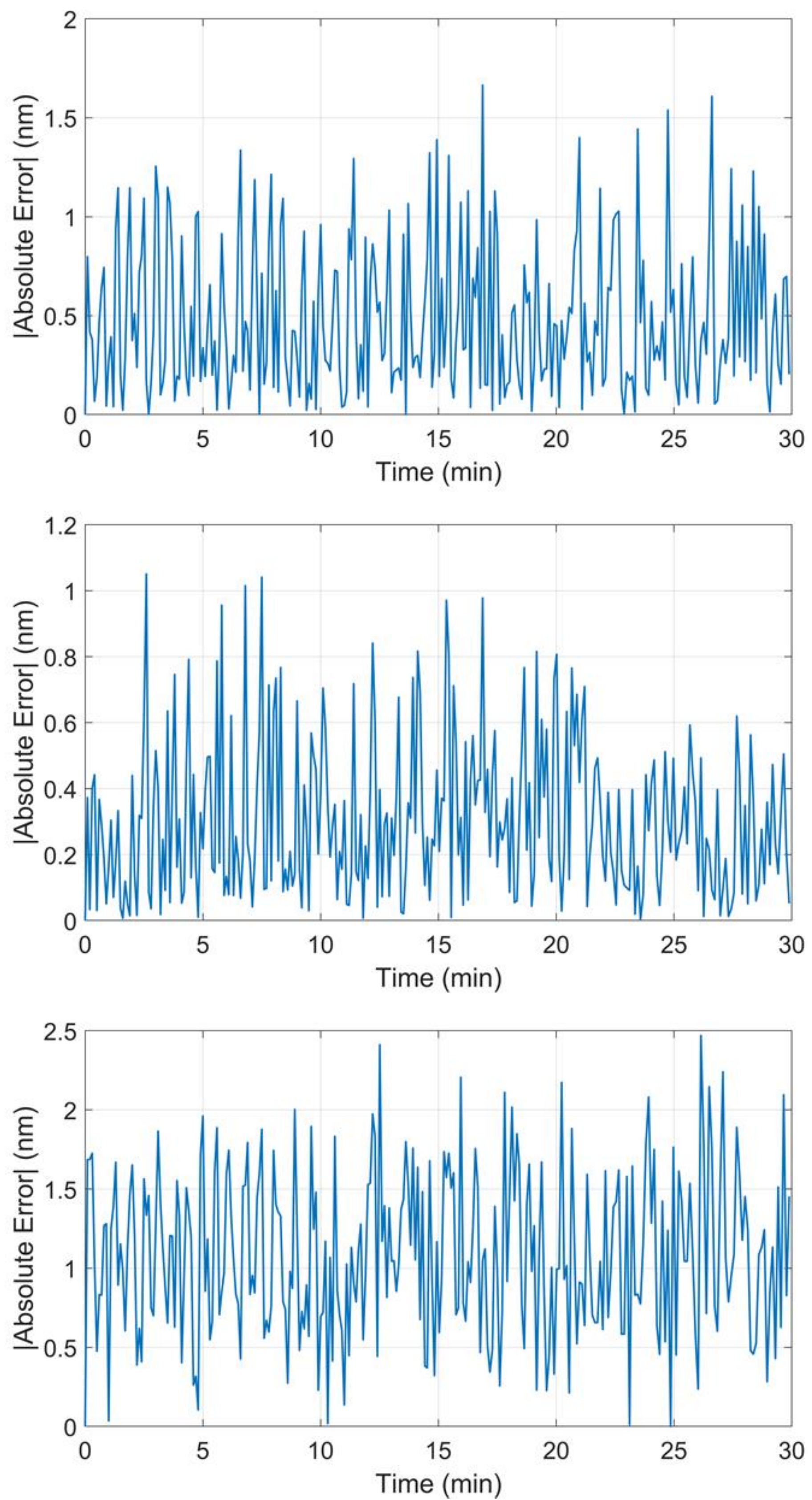

Figure 3.34 Absolute error of the static positions of the probe positioner over 30 minutes for the cable attached to the probe alone. X-axis (top). Y-axis (middle). Z-axis (bottom).

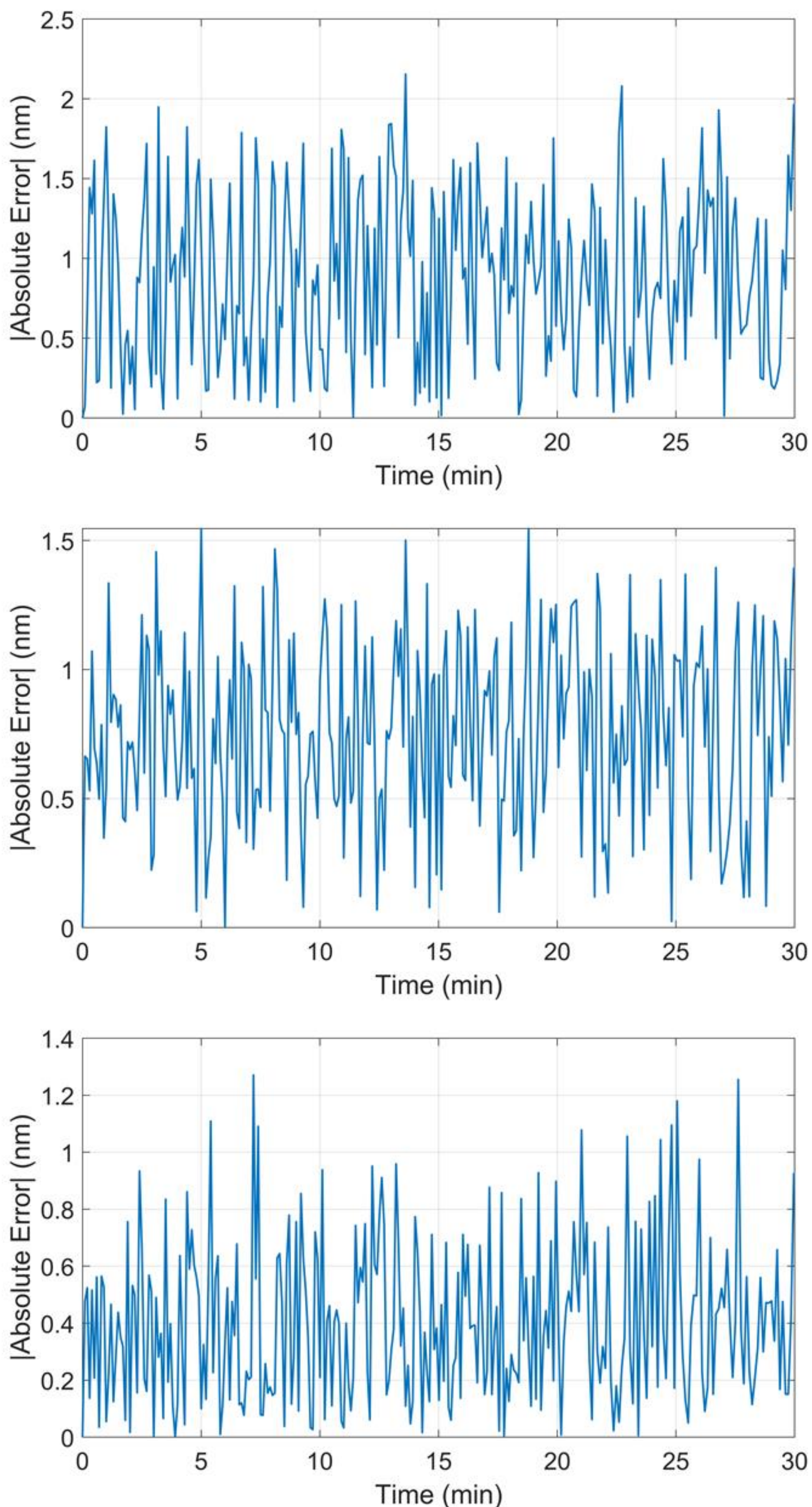

Figure 3.35 Absolute error of the static positions of the probe positioner over 30 minutes for the cable attached to the probe and the VNA. X-axis (top). Y-axis (middle). Z-axis (bottom).

3.7 Automated and robotics probing station: Software development

SmarAct provides Software Development Kits (SDKs) for seamless and rapid integration of the positioning systems in the working place. These SDKs include detailed documentations of all functions and procedures allowing easy and smooth implementation. They include C/C++, Python® and LabVIEW™.

In this work, we rely on LabVIEW™ programming. It allows the centralisation of the whole automation process: image recognition, positioners' movements according to the image information and VNA settings and measurement data acquisition once the positioners are in place. Figure 3.36 represents a simplification of the automated and robotics probe station algorithm in LabVIEW™. The pattern detection bloc consists of the camera module and the AI Vision module. The first one connects the camera to LabVIEW™ and contains the camera parameters and settings. The second one is a LabVIEW module and contains all the templates and settings for image recognition. The positioners control bloc consists of the MCS2 Settings module and the MCS2 controller. The first one contains the settings of all the positioners connected to the MCS2 controller. The second one enables the positioners to move and align according to the execution of the program. Lastly, the VNA block consists of the VNA Settings module that contains the VNA settings and the VNA module that executes the commands sent by the program such as triggering the measurement or saving the measured data. The execution of the program for a 2-port calibration on the 101-190 C Impedance Standard Substrate (ISS) regarding the positioners behaviour is as follows:

- Phase 1: using the feedback of the camera and AI Vision Module, the alignment marks of the ISS are detected. Especially, the center of the alignment mark is located as well as the angle between the structure and the frame of the camera. In addition, the tips of the two probes are detected, their centers and the angle between the parallel that links the three tips and the parallel of the camera frame. Figure 3.37 shows a schematic representation of the angles between the test structure, the probe tips and the frame of the camera.
- Phase 2: the probes are aligned with the alignment marks according to the coordinates obtained in the 1st phase. Using the positioners of the probes and the chuck, the probes and the ISS are aligned in such way that the probes' tips are perfectly centred with the structure and the angle between the tips and the structure is 0. To complete the phase, the probes are lowered until establishing a good contact*. The position of the probes along the X and Y axis are saved and locked.
- Phase 3: the operator choses one of the four calibration standards. The AI Vision Module will recognise the calibration standards and locate its center and angle similarly to the alignment mark in 1st phase.
- Phase 4: the standard is centred according to the probes using the positioners of the chuck only. Once the alignment is completed, the probes are lowered and the measurement can be launched. The probes are raised at the end of the measurement. Phase 3 and phase 4 are repeated for each calibration standard.

** In order to define the contact position, once the probes come in initial contact, we apply an additional overtravel until the probes' tips are perfectly aligned with the alignment structure as advices by the constructor of the ISS. This overtravel corresponds to 20 µm in our case. The first contact is detected automatically when the probes begin to skate. This value has been defined manually and implemented in the program.*

*** VNA measurements are done in parallel and measurement data are saved.*

Table 3.8 shows the different patterns used by the NI Vision module to recognise the different standards of the ISS as well as the tips of the GSG probes. Images were captured by the camera using the same parameters (brightness, contrast). Those parameters are locked in the camera software. Indeed, we discovered that the camera automatically readjusts those parameters to give the best image. However, when the brightness or the contrast are changed, the patterns captured do not work anymore with the same accuracy. Therefore, we fixed those values definitely. Table 3.9 shows an example of the program execution on the alignment structure of the ISS.

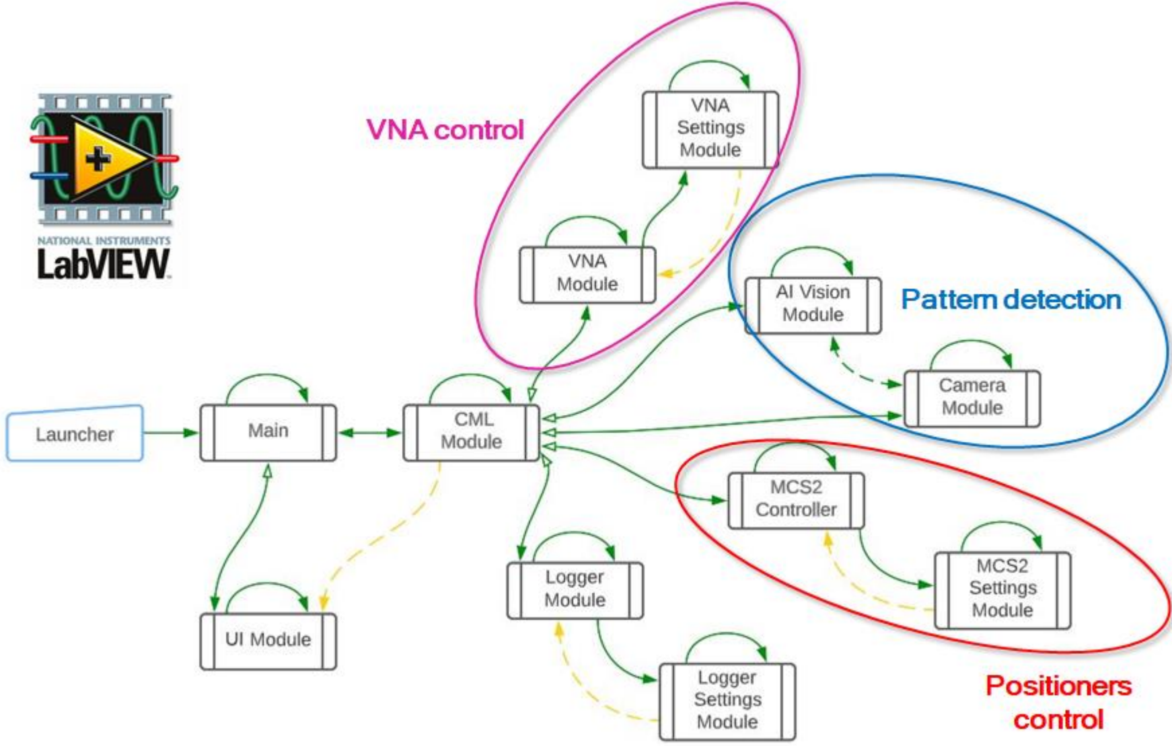

Figure 3.36 Automated and robotic probe station algorithms in LabVIEW^{TM}.

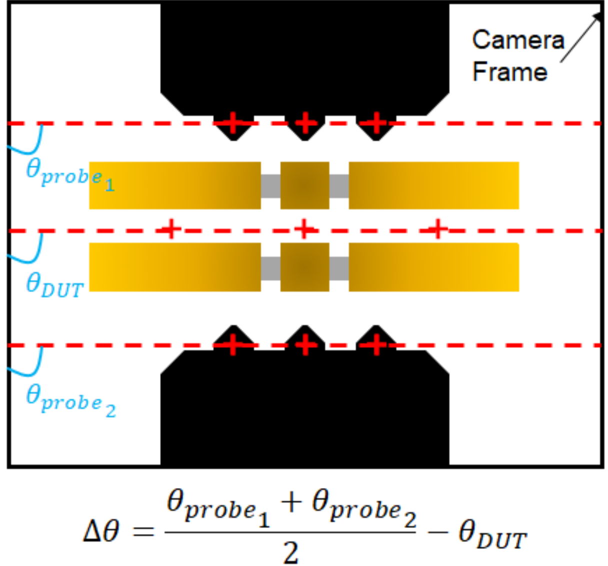

$$\Delta\theta = \frac{\theta_{probe_1} + \theta_{probe_2}}{2} - \theta_{DUT}$$

Figure 3.37 Schematic representation of the angles between the structure, the probe tips and the frame of the camera.

Table 3.8 Template used by the NI Vision module captured with the camera on the ISS.

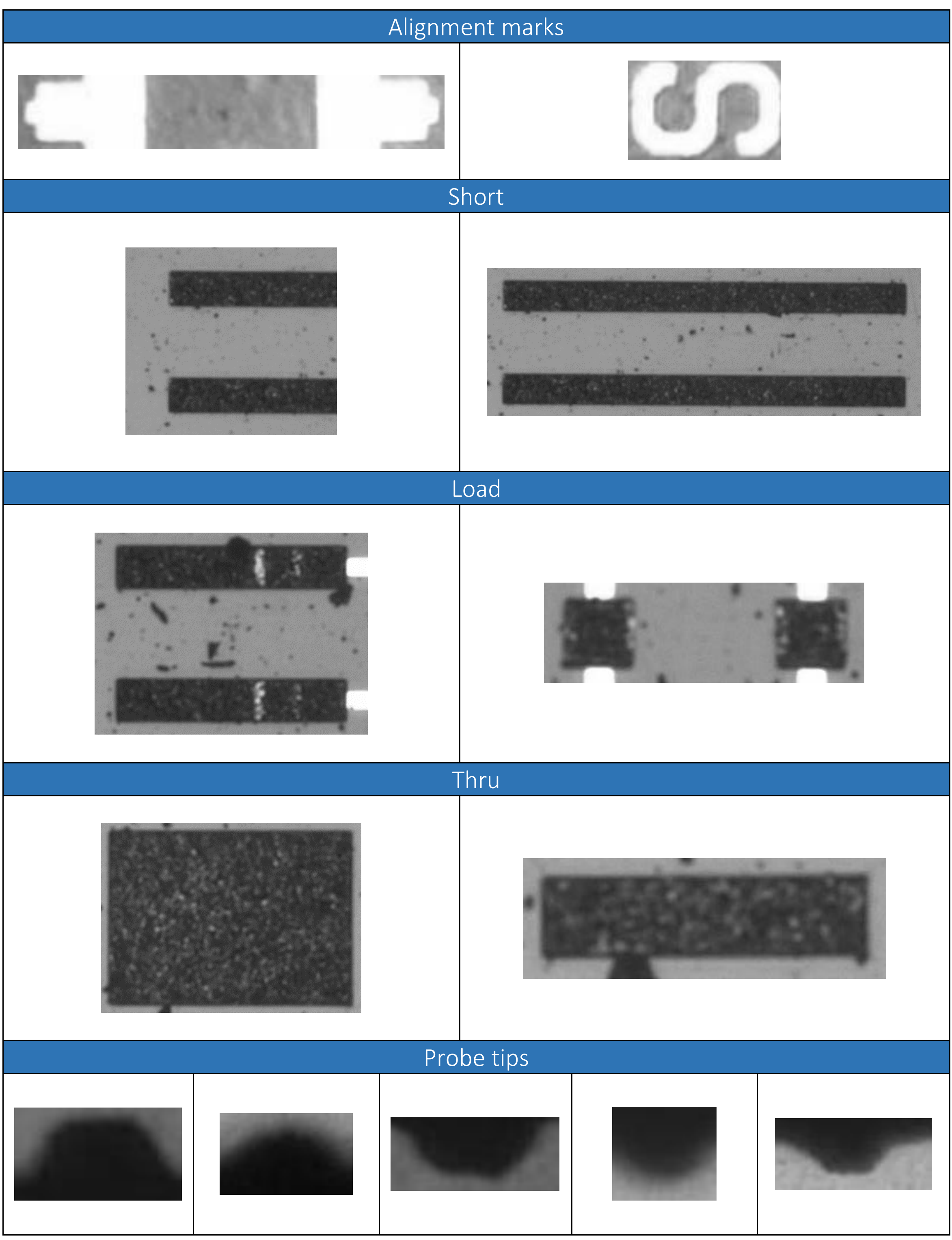

Table 3.9 Example of the execution of the program on the alignment structure of the ISS.

The alignment structure and the tips of the probes are detected and marked in red.	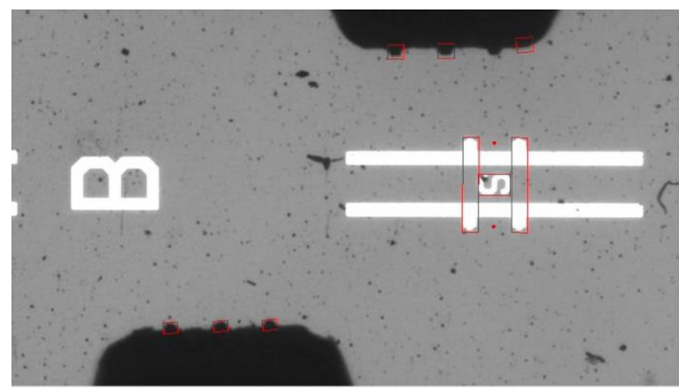
The alignment structure is centred with the two probes using the nano-positioners along the X, Y, Z, and θ axis.	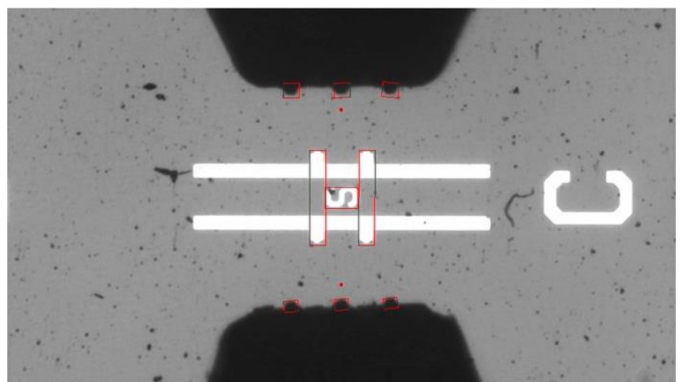
The probes are brought closed to each other until the tips reach the first edge of the structure. This distance has been tested many times and saved as a fixed value. Positions are saved and the X, Y, θ are locked.	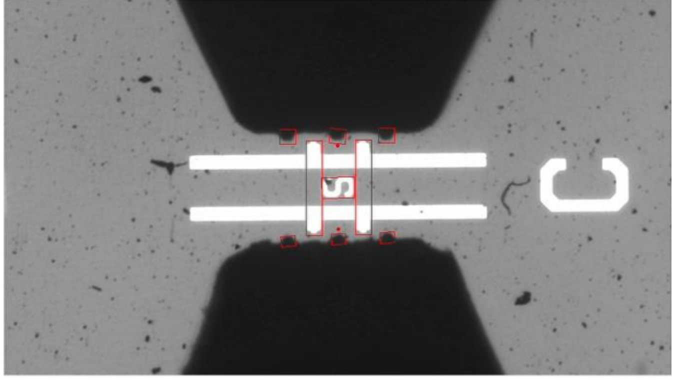
The probes go down until the first contact is established. The overtravel is then applied. The probes are raised again at the end. Here we can see the detection of third tips was lost. This is due to imperfections on the probe edge that can be detected as tips. At this stage, this does not affect the program.	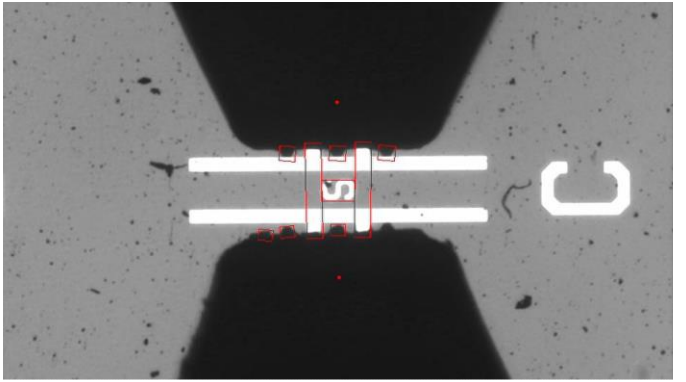

3.8 Conclusion

Throughout this chapter, we explored the SmarAct technology and determined the key positioner parameters. The insights gained provide a robust framework for optimizing SmarAct positioners and allow achieving nanoscale accuracy with confidence. The positioners were successfully implemented into the on-wafer probe station allowing accurate GSG measurements. LabVIEW™ programming offered an automated solution based on image recognition and a full control of the instrumentation present in the probing station. In the next chapter, we investigate the performance and limitations of the station trough on-wafer calibrations and measurements.

Chapter 4

4. On-wafer RF measurements

Table of content

Introduction 101
4.1 On-wafer measurement uncertainties related to probes to pad alignments from manual probing station 102
4.1.1 Methodology for the determination of residual calibration error terms 102
4.1.1.1 On-wafer experimental set-up and configuration 102
4.1.1.2 Vector calibration 103
4.1.1.3 Determination of the residual calibration error terms 104
4.1.2 Experimental set-up and validation 105
4.1.3 Standard deviation computed on microwave signals 108
4.1.4 Residual calibration error terms 109
4.1.5 Error propagation on complex impedances 110
4.2 Robotic-manual measurement for 1-port SOL calibration 113
4.2.1 Measurement protocol 115
4.2.2 Data analysis 115
4.2.3 Residual calibration error terms 116
4.2.4 Measurement uncertainty 118
4.3 Semi-automated measurements for 1-port SOL calibration 119
4.4 Approach/retract study for probe-substrate surface contact 122
4.5 Automated measurements for 1-port SOL calibration 125
4.5.1 On-wafer experimental set-up and configuration 125
4.5.2 Automated and robotics alignment 126

4.5.3 RF measurements results and data interpretation 127
4.5.3.1 CW Mode 127
4.5.3.2 Sweep Mode 132
4.5.4 Residual calibration error terms 135
4.5.5 Error propagation on complex impedances 137
4.6 Conclusion 141
4.7 References 142

Introduction

Fine control and improvement of the probe tips-to-pads for on-wafer measurement is required to address accurate characterization of microwave and mm-wave extreme impedance devices foreseen in future RF semi-conductor industry [1]. In particular, there is an urgent need to assess the traceability and the variability of agile micro- and nano-devices expected in future 5G applications and beyond [2], [3].

In chapter one, we presented a typical on-wafer probe station which consists of a VNA, a probe station with a pair of microwave GSG probes aligned manually or automatically through a microscope or a camera system onto calibration substrate and test devices [4]. In chapter two, we presented the errors related to the instrumentation such as drift, stability, and contact repeatability. Those errors degrade the measurement accuracy, especially as the frequency is raised [5], [6], [7], [8]. In particular, measurements are sensitive to X, Y, Z, and ϴ positioning of the GSG probe contacts with respect to calibration standards and devices pads [9].

In this effort, we propose a general framework including comparison between conventional and proposed RF instrumentations, measurement and analysis methodologies, targeting "best case uncertainty" on-wafer measurement. Indeed, "worst case uncertainty" is a terminology commonly found in technical documents of commercial VNAs. In this context, measurement errors are provided to situate the overall measurement performance. These errors take into account several parameters and are often over-estimated. In other words, such errors are not reached in practice. Our investigation is more challenging by providing to the user the "most accurate" quantitative data that can be expected for a particular measurement configuration. Obviously, there are still residual sources of uncertainties, but we believe that the approach proposed can be further enhanced in the future, in particular by close collaboration with European NMIs.

In this chapter, we first consider measurements performed on a conventional manual probe station. The measurement uncertainties inherent to misalignment of the probes onto the calibration structure are quantified. Those uncertainties are then propagated theoretically to a wide range of impedances. These results are instructive as they suggest that conventional measurement systems using manual positioning stages induce large measurement uncertainties for accurately characterize extreme impedances, proving the need for more accurate techniques such as automated probing stations.

In a second step, we present a brief repeatability study conducted on the automated and robotic on-wafer probe station that we developed. The aim is to quantify the probes alignment repeatability on the different measurement structures.

Finally, we use measurements from the automated and robotic station and propagate the measurement uncertainties obtained to the impedance to be measured similarly to the first experiment. A comparison between the manual station and the automated one is then presented.

4.1 On-wafer measurement uncertainties related to probes to pad alignments from manual probing station

4.1.1 Methodology for the determination of residual calibration error terms

4.1.1.1 On-wafer experimental set-up and configuration

In order to determine the measurement uncertainties inherent to the alignments of the probes onto the calibration structures, we used a manual on-wafer probing station. The experimental setup involves a MPS150 conventional on-wafer probe station from Cascade Microtech® equipped with a pair of $100\,\mu m$ pitch GSG Infinity® probes. The VNA used for the S-parameters measurements is an $\mathrm{E8361A}$ (PNA) operating up to $67\,GHz$ from Keysight Technologies®. The intermediate frequency bandwidth (IFBW) is set to $100\,Hz$ and the RF signal source to $-10\,dBm$. The frequency range is set from $50\,MHz$ to $67\,GHz$ with a frequency step of $50\,MHz$ (1340 points). Two $1.85\,mm$ coaxial RF cables from Gore® are used to connect the probes to the VNA. The calibrations are done on the impedance standard substrate (ISS) PN 101-190 C from Form-Factor™. The software Wincal™ is used to perform the LRRM calibration algorithm. Figure 4.1 shows the manual station used.

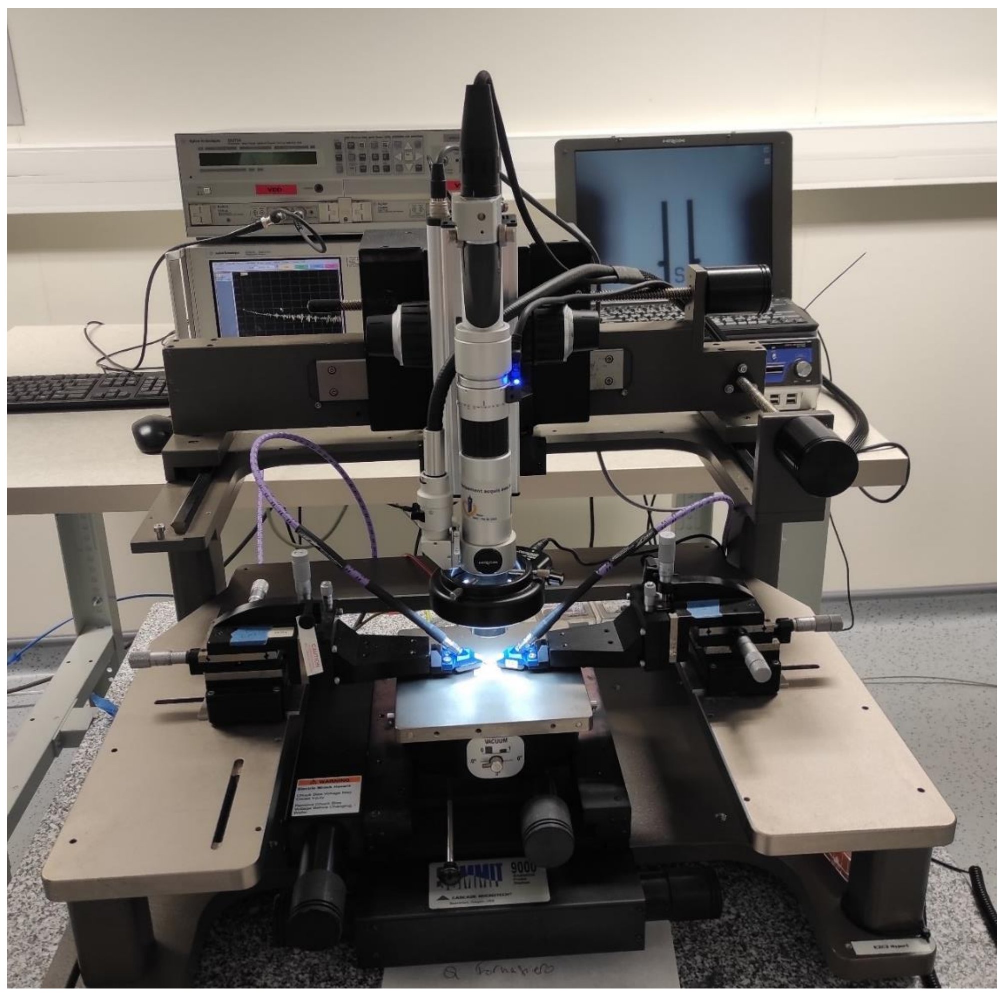

Figure 4.1 Manual probe station in the characterisation platform at the IEMN laboratory.

In chapter two, we presented the 12-error term method for network calibration as well as the LRRM (Line-Reflect-Reflect-Match) algorithm. The software used provides the 12 calibration error terms namely directivity e_{00}, transmission tracking $e_{10}e_{32}$, reflection tracking $e_{10}e_{01}$, source match e_{11}, load match e_{22}, leakage (cross-talk) e_{30} (neglected). Developments in error model throughout the years led to changes in the model presentation. The error terms can be written as follow: directivity E_D, transmission tracking E_T, reflection tracking E_R, source match E_S, load match E_L, leakage (cross-talk) E_X [10].

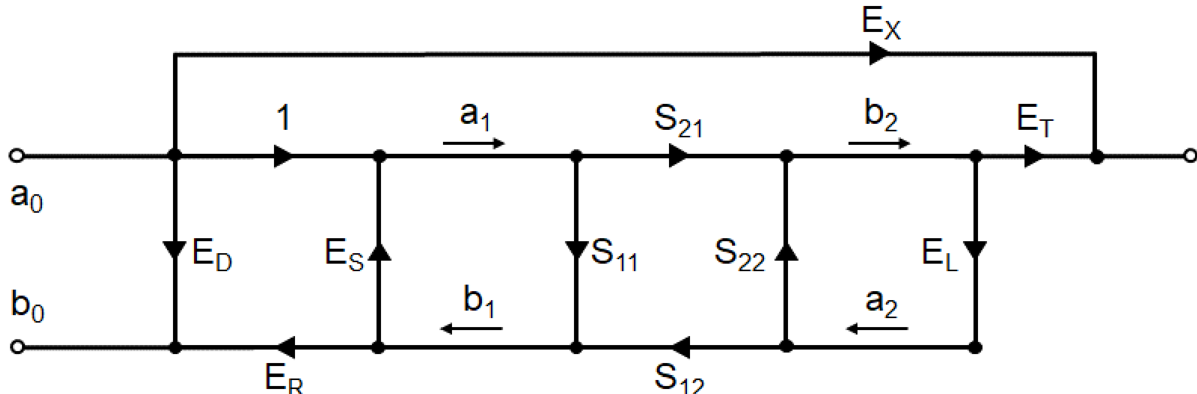

Figure 4.2 12-terms error model in the forward direction represented by the error coefficients ED, ES, ER, EL, ET, and EX [10].

To solve the calibration problem, we start by solving for E_D, E_R *and* E_S using the one-port calibration method at port 1 (same procedure at port 2 for the reverse direction). Then, by connecting the two ports together, we obtain the remaining coefficients in the forward direction (same procedure for the reverse direction. The crosstalk in neglected and equals to 0) [11]:

$$E_L = \frac{S_{11_M} - E_D}{S_{11_M}E_S - (E_D E_S - E_R)} \tag{4.25}$$

$$E_T = S_{21_M}(1 - E_S E_L) \tag{4.26}$$

4.1.1.2 Vector calibration

Two sets of measurements were carried out on the same day in a controlled environment with temperature variations less than $\pm$ 1°, stable ambient hygrometry set to 50 % and anti-vibration building. On the first half of the day, we did a first set of measurements called Z-analysis; on the second half of the day we did the second set of measurements called XYZ-analysis.

The Z-analysis is performed according to the following protocol:

- 10 LRRM calibrations are performed independently
- For each standard, e.g., short, we fixed the alignment of the probes on the X, Y and Z axis. Once the contact is correctly done, we move the probes on the Z axis only using the manual handle of the probing station in order to perform 10 successive measurements of the short standard. We repeat the same procedure for the other standards
- 10 LRRM calibration files are created

The XYZ-analysis is performed as follow:

- 10 LRRM calibrations are performed independently by moving the probes according to the standards on all the axis (displacement in the centimetre range).
- 10 LRRM calibration files are created.

This procedure allows us to study the influence of the manual alignment of the probes in the X, Y and Z directions. From each of the ten calibration files, we compute the 12 calibration error terms using Wincal™.

4.1.1.3 Determination of the residual calibration error terms

There are several techniques in order to determine the residual calibration error terms according to the calibration type or the propagation support [12], [13], [14]. Here, we chose a statistic method that considers successive calibrations of the same calibration standards. Hence, the residual calibration error terms are obtained by computing the complex standard deviation of each one of the error calibration terms (error coefficients). The obtained residual terms are the signatures of (i) mainly the mechanical repeatability of the probe to contact pads, (ii) non-systematic errors occurring between the measurements (instrument drift, environment variations). The residual data are computed for each error term as follows:

$$residual\ error = \sigma = \sqrt{\frac{1}{N-1}\sum_{i=1}^{N}\{(x_i-\bar{x})^2+(y_i-\bar{y})^2\}} \quad (4.27)$$

where x_i and y_i are the real and imaginary component of the ith error term value, $\bar{x}$ and $\bar{y}$ the means values of real and imaginary parts of the error terms respectively, and $N = 10$ the number of measurements. The residual calibration error terms indicate how spread are the values from the mean data. Consequently, the standard deviation must be kept low to ensure the repeatability of the measurements. hence, each residual term is as follow [12]:

- Directivity: δ_1
- Reflection tracking: τ_1
- Transmission tracking: τ_2
- Source match: μ_1
- Load match: μ_2

In addition, to make the link between residual calibration error terms and the measured *S*-parameters of the calibration standards, we compute the standard deviation of the measured *S*-parameters S_{ij_M} of the four calibration standards used for the LRRM calibration, namely short, open, load and thru. All data analysis is done using MATLAB® software.

It has to be mentioned that the method presented is different from the well-known approach developed by D. Rytting [12] in which all sources of uncertainties are considered independently. In particular, systematic and non-systematic (noise, connector repeatability, cable stability, noise drift and stability) errors require a set of specific measurements to identify and quantify each error contribution [15]. In our case, we consider a global approach with the main objective being to quantify the impact of manual positioning (Z and XYZ) directly on the complex impedance to be measured. In the following, a method is proposed to propagate the measurement uncertainty brought by the residual calibration terms on the impedance in a one-port measurement scenario. Indeed, although the method can be generalized to any two-port

network, we focus in the following on the measurement of complex impedance / complex reflection coefficient only.

4.1.2 Experimental set-up and validation

The method presented previously is applied to derive the measurement uncertainties considering the 101-190 C ISS from Form-Factor® in the frequency range 50 $MHz - 67\ GHz$.

Figure 4.3 shows the raw reflection coefficient magnitude of the short, open and load standards considering the XYZ-analysis. Figure 4.4 shows the raw reflection coefficient phase shift of the short, open and load standards considering the XYZ-analysis.

Figure 4.5 shows the raw reflection coefficient magnitude of the short, open and load standards considering the Z-analysis. Figure 4.6 shows the raw reflection coefficient phase shift of the short, open and load standards considering the Z-analysis.

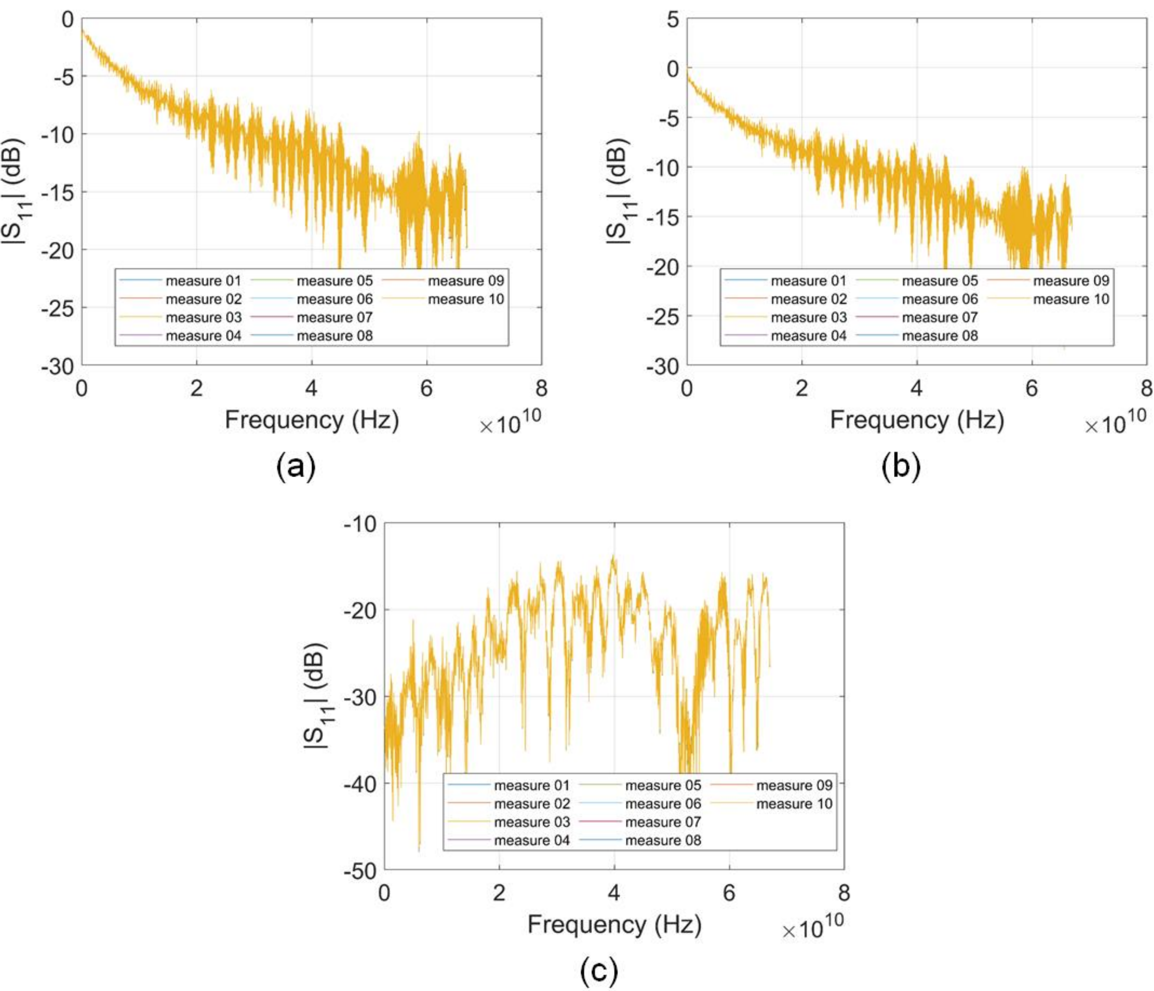

Figure 4.3 Raw reflection coefficient magnitude of the short, open and load standards considering the XYZ-analysis for the 10 measurements.

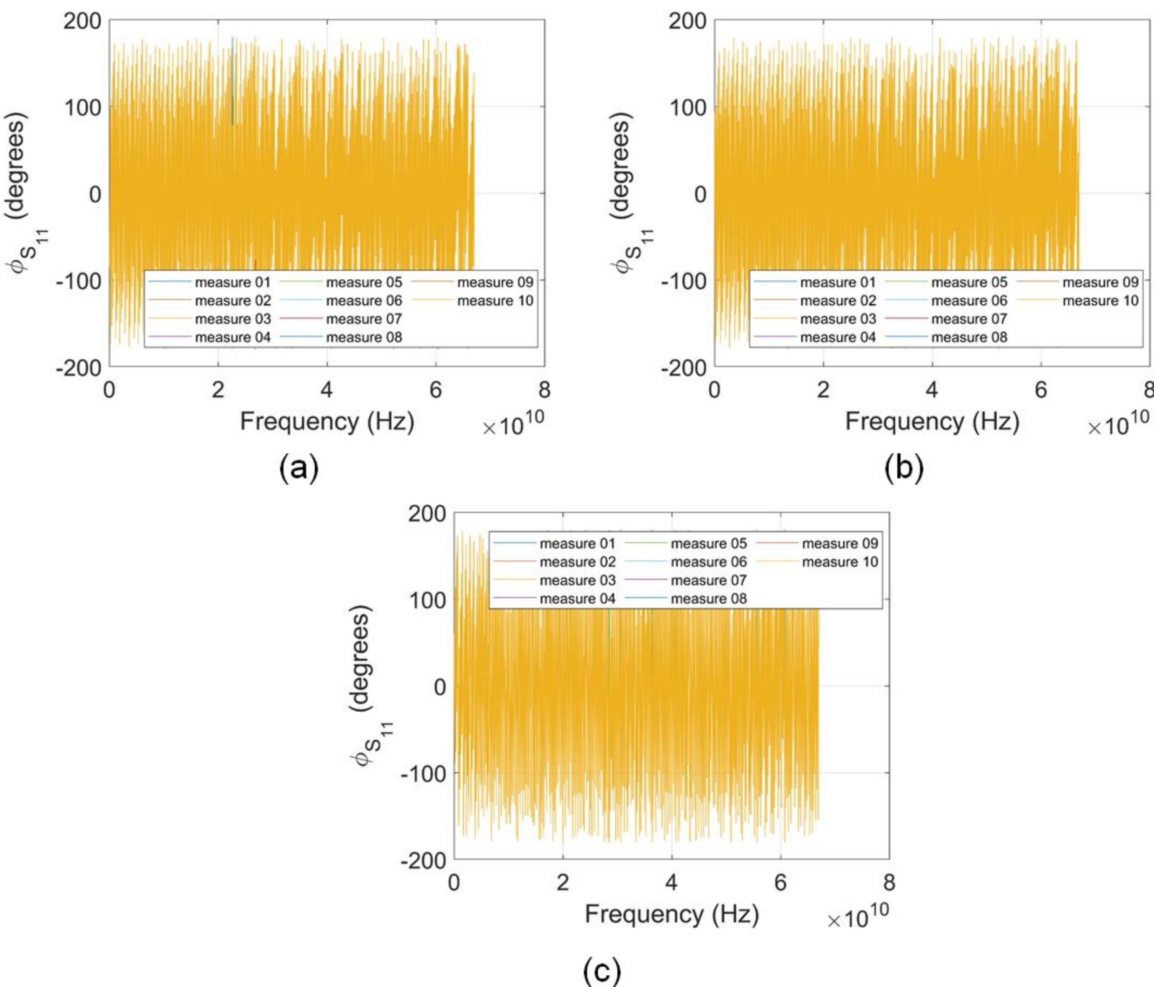

Figure 4.4 Raw reflection coefficient phase shift of the short, open and load standards considering the XYZ-analysis for the 10 measurements.

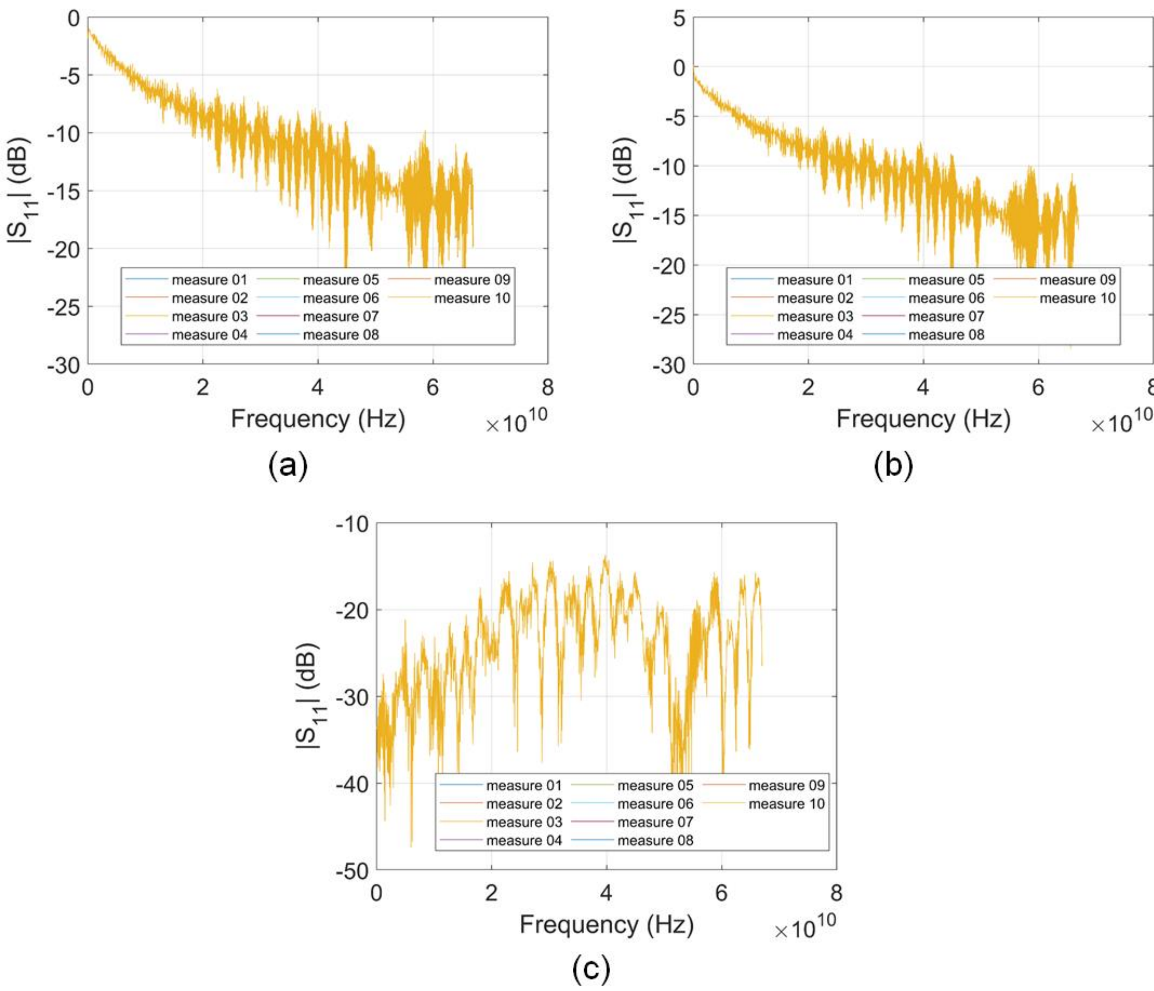

Figure 4.5 Raw reflection coefficient magnitude of the short, open and load standards considering the Z-analysis for the 10 measurements.

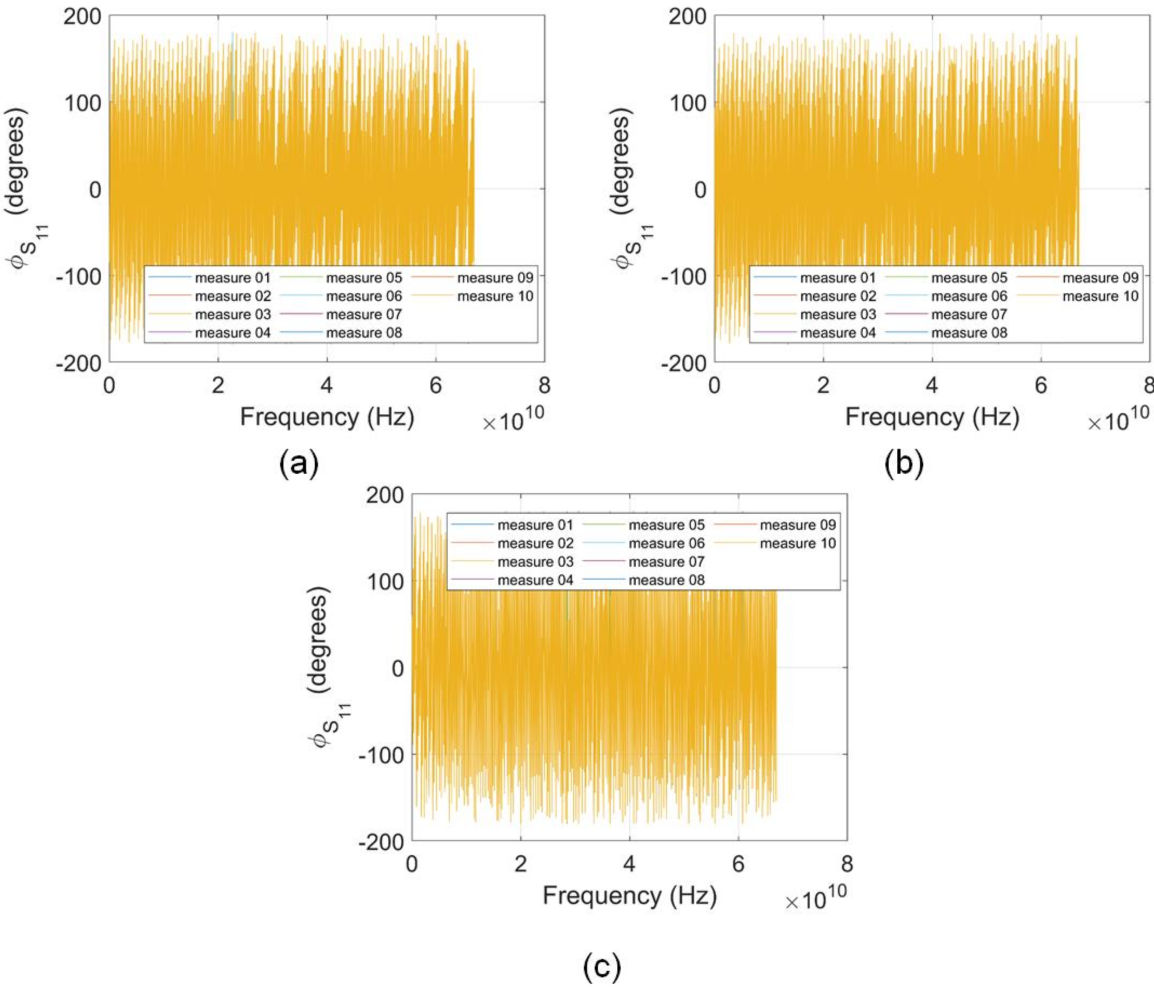

Figure 4.6 Raw reflection coefficient phase shift of the short, open and load standards considering the Z-analysis for the 10 measurements.

4.1.3 Standard deviation computed on microwave signals

Figure 4.7 shows the standard deviation computed from the measured complex reflection coefficients (raw S_{11_M}) on the short, open and load standards, considering 10 calibrations for XYZ-analysis and Z-analysis. From Figure 4.7, we demonstrate that XYZ-analysis results are in degradation of the measurement repeatability in contrast with the Z-analysis for the three calibration standards. We observe that for both methods, the repeatability quality decreases when the frequency rises, up to $20\,GHz$. From 20 to $50\,GHz$, the repeatability of the measurements does not change significantly due to other source of uncertainties (e.g., instrumental drift) that become predominant. Consequently, measurement uncertainties in the lower regime ($<\ 20\,GHz$) can be improved by suitable accurate probing techniques. In the upper frequency regime, complementary strategies to identify and remove sources of uncertainties must be considered.

The individual errors presented in Figure 4.2 and brought by the limited probe to pad repeatability are combined altogether to impact the overall vector calibration discussed in the next sub-section.

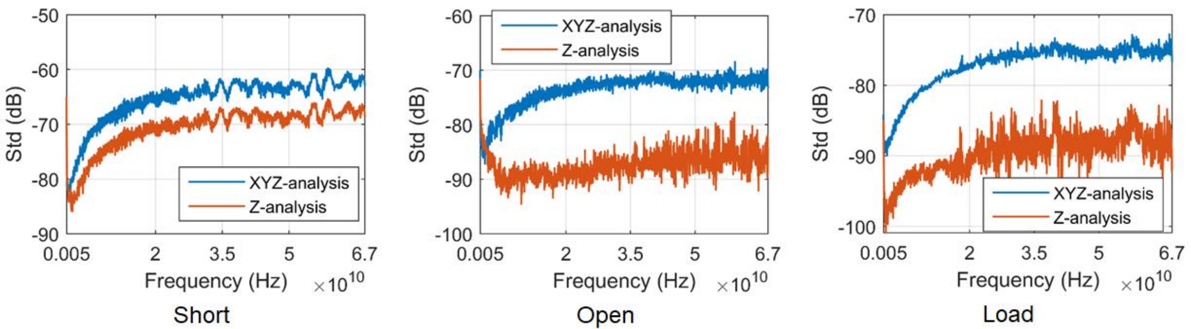

Figure 4.7 Standard deviation (Std) obtained from measured complex reflection coefficient S_{11_M} on the impedance standard substrate (ISS).

4.1.4 Residual calibration error terms

The residual calibration error terms have been computed for both XYZ-analysis and Z-analysis in the range 50 MHz – 67 GHz. Table 4.1 and Table 4.2 present the data obtained for the test frequencies 1, 10, 30 and 60 GHz. The Z-analysis shows, as expected, better results in terms of repeatability. For example, at 10 GHz, the residual directivity error term is increased by a factor around 12 between Z and XYZ-analysis. We are taking three times the value on the residual error obtained (3σ) as is it conventionally used in statistics. Indeed, the 3-sigma rule of thumb states that approximatively 99.7% of the data points in a normally distributed set will fall within 3 standard deviations of the mean.

As a preliminary conclusion, these results provide quantitative data to estimate errors brought by the contact repeatability. In the effort to improve the contact repeatability, NMIs are well recognized to guaranty traceability of S-Parameters measurements [5]. On-going works are clearly oriented towards improving the probe to contact repeatability in the millimetre-wave ($30 - 300$ GHz) up to the regime [16], [17]. As mentioned in the introduction, we focus on the microwave regime (up to 67 GHz) with ultimate objective to address accurate measurements on extreme impedance devices. In this effort, in the following, we study the impact of measurement uncertainties obtained in Table 4.1 and Table 4.2 on the determination of complex impedances.

Table 4.1 3σ standard deviations computed at 1 GHz, 10 GHz, 30 GHz and 60 GHz considering the Z-analysis.

Residual error	1 GHz	10 GHz	30 GHz	60 GHz
	3σ	3σ	3σ	3σ
δ_1	3.7707×10^{-5}	5.9740×10^{-5}	1.3925×10^{-4}	1.4346×10^{-4}
τ_1	2.0059×10^{-4}	1.6715×10^{-4}	2.8929×10^{-4}	3.0141×10^{-4}
τ_2	1.1613×10^{-4}	1.3879×10^{-4}	2.8849×10^{-4}	3.1446×10^{-4}
μ_1	1.3467×10^{-4}	2.4666×10^{-4}	9.7239×10^{-4}	1.7725×10^{-4}
μ_2	1.0131×10^{-4}	2.7117×10^{-4}	9.7285×10^{-4}	1.7873×10^{-4}

Table 4.2 3σ standard deviations computed at 1 GHz, 10 GHz, 30 GHz and 60 GHz considering the XYZ-analysis.

Residual error	1 GHz	10 GHz	30 GHz	60 GHz
	3σ	3σ	3σ	3σ
δ_1	1.4871×10^{-4}	7.4267×10^{-4}	1.3433×10^{-3}	1.3849×10^{-3}
τ_1	3.2338×10^{-3}	2.3201×10^{-3}	2.4030×10^{-3}	2.3857×10^{-3}
τ_2	3.4017×10^{-3}	2.3523×10^{-3}	2.1828×10^{-3}	1.9808×10^{-3}
μ_1	4.0127×10^{-3}	4.0472×10^{-3}	6.3975×10^{-3}	1.3496×10^{-2}
μ_2	3.4688×10^{-3}	4.2423×10^{-3}	6.4681×10^{-3}	1.3530×10^{-2}

4.1.5 Error propagation on complex impedances

In this section, we propose to highlight limitations of conventional on-wafer probe stations to address accurate measurement of extreme impedances such as sub-fF ($10^{-15}\,F$) capacitance values. In particular, we extend the reflection coefficient (S_{11}) uncertainty error model developed by D. Rytting [12] to uncertainty impedance (Z) error model. The reflection coefficient magnitude uncertainty $\Delta|S_{11}|$ and phase-shift uncertainty $\Delta\phi$ can be written as:

$$\Delta|S_{11}| \approx \delta_1 + \tau_1|S_{11}| + \mu_1|S_{11}|^2 \tag{4.28}$$

$$\Delta\phi \approx arcsin\left(\frac{\Delta|S_{11}|}{|S_{11}|}\right) \tag{4.29}$$

Figure 4.8 shows the reflection coefficient magnitude uncertainty as a function of the S_{11} amplitude at 50 GHz for both Z-analysis and XYZ-analysis.

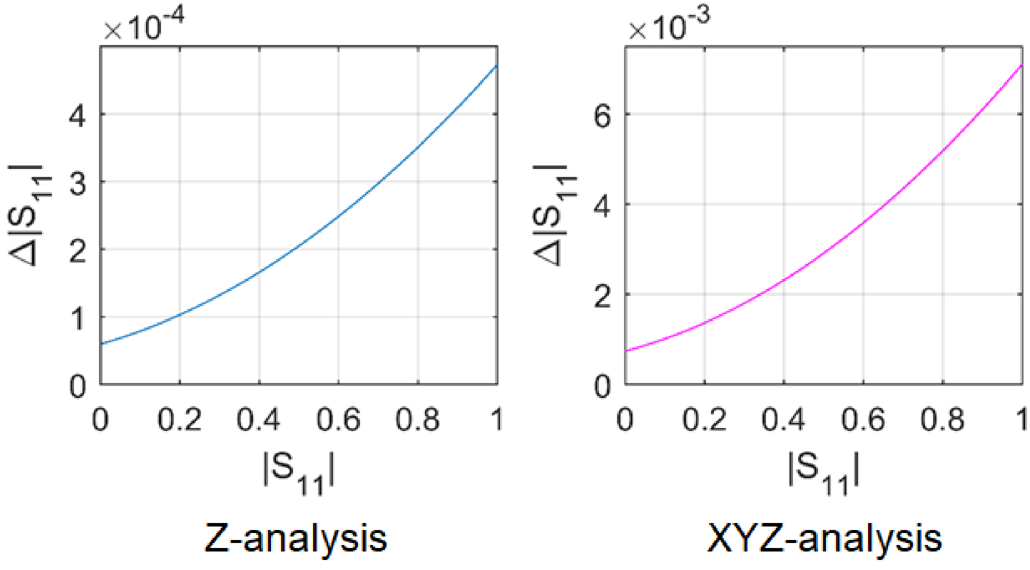

Figure 4.8 Reflection coefficient magnitude uncertainty.

According to (4.28) the amplitude uncertainty increases as a function of S_{11} amplitude, as observed in Figure 4.8. In particular, this implies that measurement of capacitances ($|S_{11}| = 1$) results in relatively large errors. For example, the phase-shift uncertainties computed from (3) at $10\ GHz$ for ($|S_{11}| = 1$) are $0.027°$ and $0.4°$ for Z-analysis and XYZ-analysis respectively. The Z-analysis generates significantly less measurement uncertainties than the XYZ-analysis.

In the following, we extend the work to uncertainty impedance (Z) error modelling. In [12], D. Rytting considers the worst-case uncertainty, where residual calibration error terms are collinear vectors added graphically (to provide maximum $\Delta|S_{11}|$ and $\Delta\phi$). Although this method provides the worst-case uncertainty in terms of complex reflection coefficient, we extend the method by considering a disk error with radius $\Delta|S_{11}|$ to propagate the full disk error on the Z-plane, with:

$$Z = Z_0 \frac{1 + S_{11}}{1 - S_{11}} \ \ with \ \ Z_0 = 50\ \Omega \tag{4.30}$$

and therefore derive the measurement uncertainty in terms of complex impedance. Indeed, we investigate all combination values between reflection coefficient magnitude uncertainty and reflection coefficient phase uncertainty that provide maximum Z-measurement uncertainty.

We consider the S_{11} measurement uncertainty limited by a χ-disk defined by:

$$\underline{\chi} = |\chi| e^{j\phi_\chi} \tag{4.31}$$

with $\in [0\ ;\ \Delta|S_{11}|]\ and\ \phi\chi \in [0\ ; 2\pi]$ (Figure 4.9).

The χ-disk presented in Figure 4.9 delimits the measurement error area on the complex reflection coefficient S_{11}. In the following, we consider a purely capacitive DUT and study the impact of the χ-disk on the determination of the capacitance value. First, we consider the determination of the measurement uncertainty on a capacitance of $320\ fF\ \ [Im(Z) = 50\Omega\ at\ 10\ GHz]$ as follow:

- Compute the complex impedance

$$Z = \frac{1}{jC\omega} \tag{4.32}$$

with $\omega = 2\pi f$ represents the angular frequency,

- Compute the complex reflexion coefficient

$$S_{11} = \frac{Z - Z_0}{Z + Z_0}, \tag{4.33}$$

- Compute the reflection coefficient magnitude uncertainty $\Delta|S_{11}|$ as given previously in (4.28),
- Compute the impedance uncertainty ΔZ using (4.34)

$$\Delta Z = Z_0 \left(\frac{1 + S_{11} + \chi}{1 - S_{11} + \chi} - \frac{1 + S_{11}}{1 - S_{11}} \right), \tag{4.34}$$

- Compute the capacitance uncertainty ΔC using (4.35)

$$\Delta C = C - \frac{1}{\omega \Delta Im(Z) + \frac{1}{C}} \tag{4.35}$$

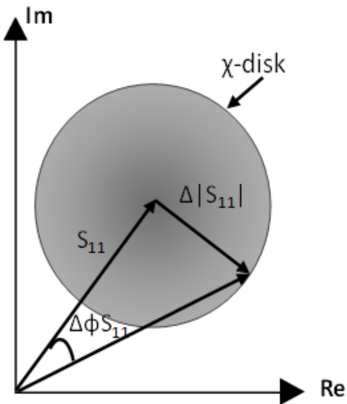

Figure 4.9 Vector representation of the measurement uncertainty on the complex reflection coefficient S_{11}.

Figure 4.10 shows the geometrical propagation of the χ-disk on the imaginary part $\Delta Im(Z)$ of the complex impedance Z considering both Z-analysis and XYZ-analysis. The impact of the repeatability error between the Z-analysis and XYZ-analysis is highlighted with a degradation by one order of magnitude considering XYZ-analysis. These results suggest that fine and repeatable probe to pads positioning is required to address accurate measurements of extreme impedances.

The impact on the determination of capacitance values is discussed in the following. First, we consider capacitance values down to $1\ fF$ and compute the measurement uncertainties $\Delta Im(Z)$ and $\Delta Re(Z)$ at the test frequency $10\ GHz$ (Table 4.3).

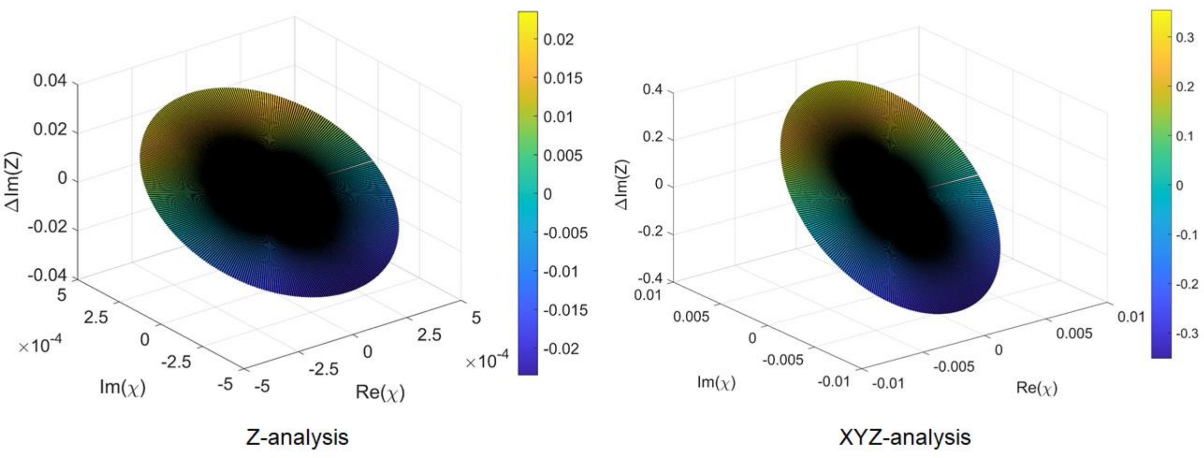

Figure 4.10 Measurement uncertainty ΔIm(Z) computed by propagation of χ-disk on the complex impedance.

According to Table 4.3, the Z-analysis method shows better performances. As an example, for a capacitance value set to $320\ fF$, the relative measurement error introduced by the Z-analysis is 0.047% whereas the XYZ-analysis reaches 0.7%. It is also shown that for a capacitance (perfect imaginary impedance value), we introduce a measurement uncertainty on the real part $\Delta Re(Z)$ of the impedance. Consequently, $\Delta Re(Z)$ represents a series resistor with the capacitor. The RF measured impedance becomes $Z = 0.023\Omega + j(50 \pm 0.023)$ at $10\ GHz$.

Table 4.3 Impedance measurement uncertainty at 10 GHz for Z-analysis and XYZ-analysis.

C(fF)	Δ|S11|		ΔIm(Z) (Ω)		ΔRe(Z) (Ω)	
	Z analysis	XYZ analysis	Z analysis	XYZ analysis	Z analysis	XYZ analysis
320	4.74×10^{-4}	71×10^{-4}	0.023	0.35	0.023	0.35
100	4.74×10^{-4}	71×10^{-4}	0.13	1.95	0.13	1.98
10	4.74×10^{-4}	71×10^{-4}	11.89	1.61×10^{2}	11.98	1.83×10^{2}
1	4.74×10^{-4}	71×10^{-4}	1.39×10^{4}	6.73×10^{4}	1204	6.5×10^{4}

Table 4.4 provides the capacitance measurement uncertainties for the different cases considered. It is clearly shown that conventional on-wafer probe stations are not suitable to measure accurately high impedance devices such as sub-fF capacitors. For example, a capacitance value of 1 fF measured at 10 GHz is characterized with an error around 90 %. The Z-analysis demonstrates that, if the X and Y movements of the probe are theoretically controlled, the error can be reduced to ~7%. In addition, the Z-movement should be improved to foresee measurement of sub-fF capacitances values. In [2], we have tackled the issue of high impedance measurements by considering a two-port measurement configuration that is less insensitive to positioning errors. Although accurate measurements on sub-fF55-nm MOS RF voltage-tunable capacitors have been addressed, the technique is only suitable for one-port devices (configured in two-port measurements) cannot be used for high impedance two-port network characterization.

Table 4.4 Capacitance measurement uncertainties at 10 GHz for Z-analysis and XYZ-analysis.

C(fF)	ΔC (F)		ΔC/C (%)	
	Z analysis	XYZ analysis	Z analysis	XYZ analysis
320	1.51×10^{-16}	2.24×10^{-15}	0.047	0.7
100	8.25×10^{-17}	1.21×10^{-15}	0.082	1
10	7.41×10^{-17}	9.2×10^{-16}	0.74	10
1	7.03×10^{-17}	8.97×10^{-16}	6.53	90

4.2 Robotic-manual measurement for 1-port SOL calibration

At early stage of the development of the automated and robotics probing station, we present results related to manual yet robotic approach for 1-port SOL calibration. Here, we use the manual joystick of the MCS2 in order to make a series of measurements. The joystick provides real-time positions of the positioners in all axis. It also enables the operator to switch between the different mode of the MCS2 (open-loop / closed-loop). Figure 4.11 shows the joystick used and its different functionalities.

The experimental setup involves GSG probes (100 µm pitch probe from FormFactor™) mounted on piezo-electric nanopositionning (translation X, Y, Z and rotation θ) stages from SmarAct®. The impedance standard substrate (ISS) PN 101-190 from Form-Factor®, mounted on a three nanopositioning (X, Y and φ) stage is considered for RF measurements. The RF measurement instrument consists of a compact Streamline 5008A from Keysight Technologies®. The RF source power and the intermediate frequency bandwidth (IFBW) are set to -10 dBm and 100 Hz respectively. The frequency range is set from 50 MHz to 50 GHz with a frequency step of 25 MHz (1999 points). A 30 cm coaxial cable with high phase stability is used to connect the VNA to the probe keeping the overall instrumentation as compact as possible. The software Wincal® is used to perform the SOL calibration and to provide calibration error terms, namely directivity E_D, transmission tracking E_T and source match E_S. Figure 4.12 shows the automated and robotics on-wafer probing station.

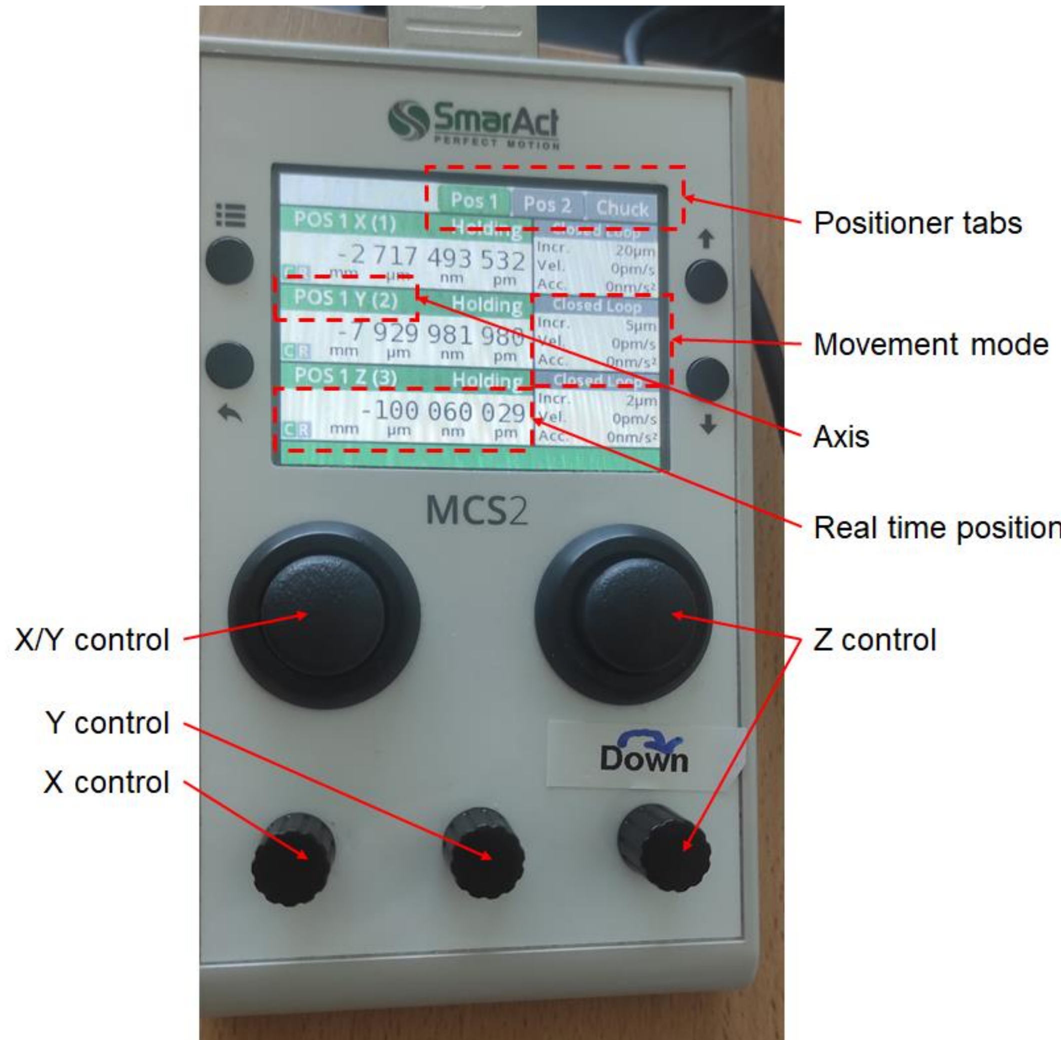

Figure 4.11 MCS2 joystick.

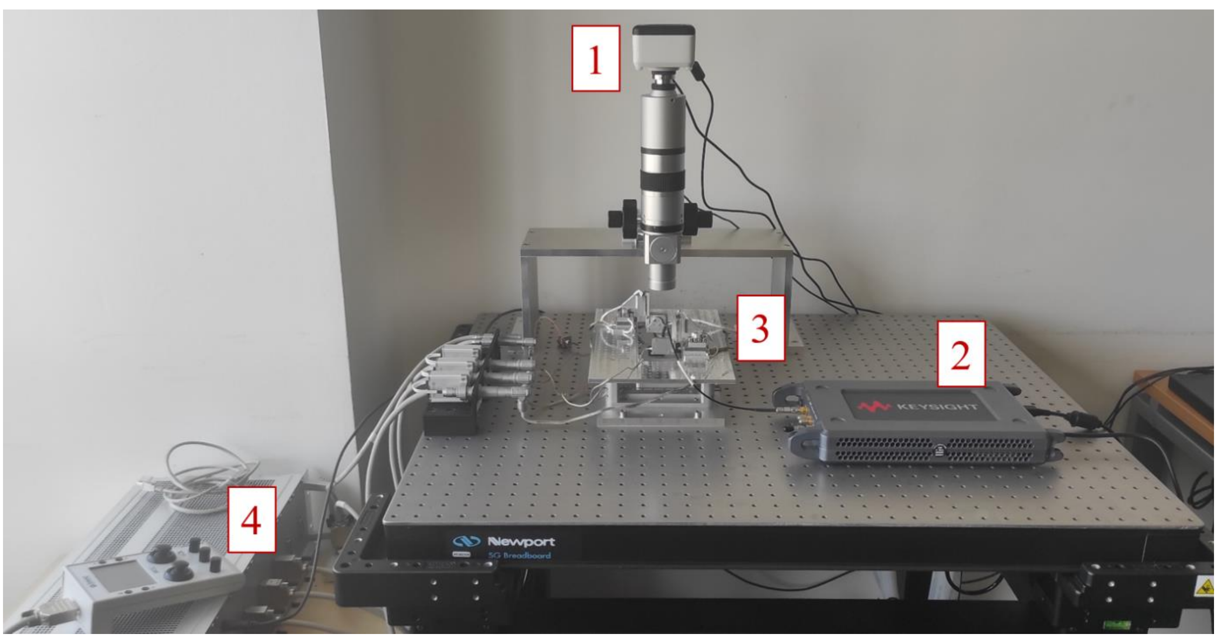

Figure 4.12 Automated and robotics on-wafer probing station. MPI® Camera. (2) VNA. (3) nano-robotic probe station. (4) Controllers.

4.2.1 Measurement protocol

A set of robotic-manual measurements is carried out on the same day according to the following measurement protocol:

- 10 successive SOL calibrations are performed
- For each standard, e.g. short, we fix the alignment of the probes on the X and Y axis
- We realize a first contact moving the probes on the Z axis. Once the contact is established, in particular, the horizontal tilt of the probe is adjusted, we save this position as 0 on the MCS2 joystick
- We perform 10 successive measurements for each standard considering manual approach / retract of the probe with stand-off (distance between probe tips and calibration pads) set to 70 µm. The positioners are used in closed-loop operation with step increment of 1 µm
- The same procedure is repeated for the load standard and the open standard

Note: the open standard used in the study is the true open from the ISS.

This procedure allows us to study the influence of the probe alignment repeatability on the Z axis.

4.2.2 Data analysis

Figure 4.13 shows the absolute Z-position recorded by the stage controller after each “n° of probing”. After each measurement, we perform a new reference to avoid cumulative errors. Each time the probe is moved up and down, the absolute position deviates from the targeted 0-position expected value. It has to be reminded that landing of the probe has not been automated yet and these errors can be reduced by lowering the displacement step and speed.

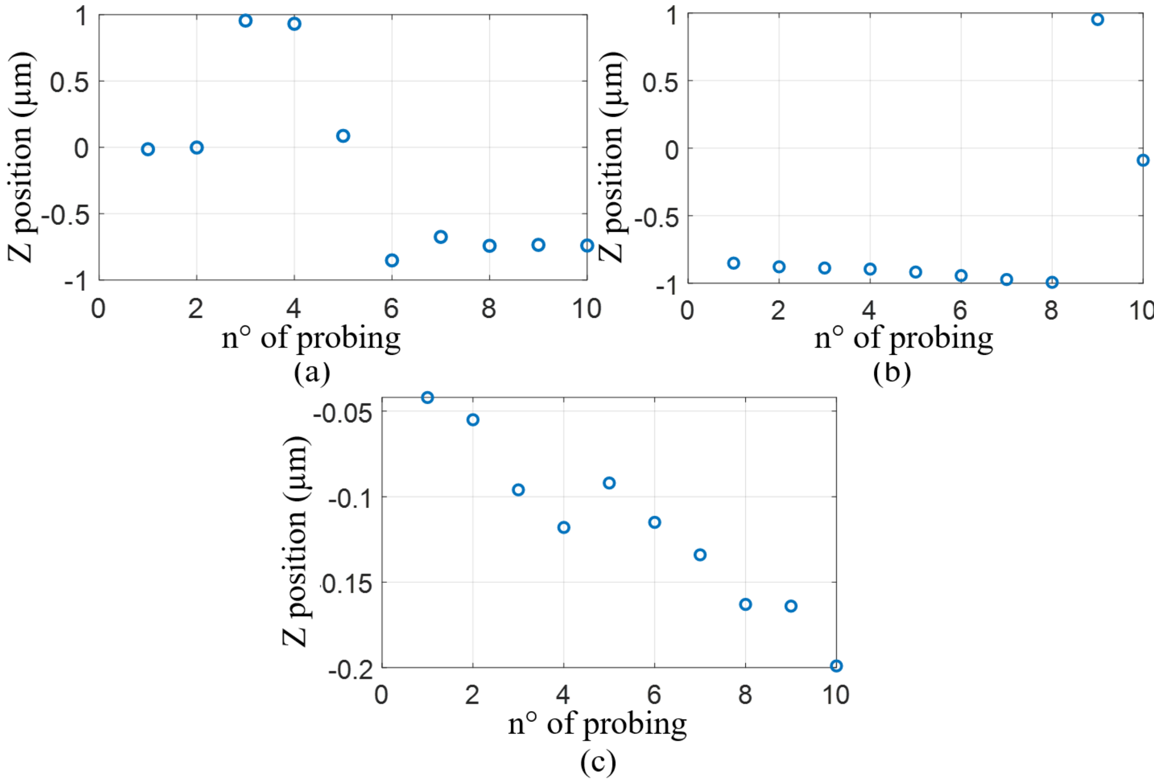

Figure 4.13 Absolute Z-position as a function of "n° of probing" (approach – retract by 70 μm) for (a) short. (b) load. (c) open.

4.2.3 Residual calibration error terms

The residual calibration error terms are computed for the measurement set in the range 50 MHz – 50 GHz.

Figure 4.14 shows the standard deviations calculated for the three error terms, directivity δ_1, reflection tracking τ_1 and source match μ_1. We observe that the repeatability decreases when the frequency rises. From around 30 GHz to 50 GHz, the repeatability of the measurements starts to change less significantly due to other source of uncertainties (e.g., instrumental drift) that become predominant.

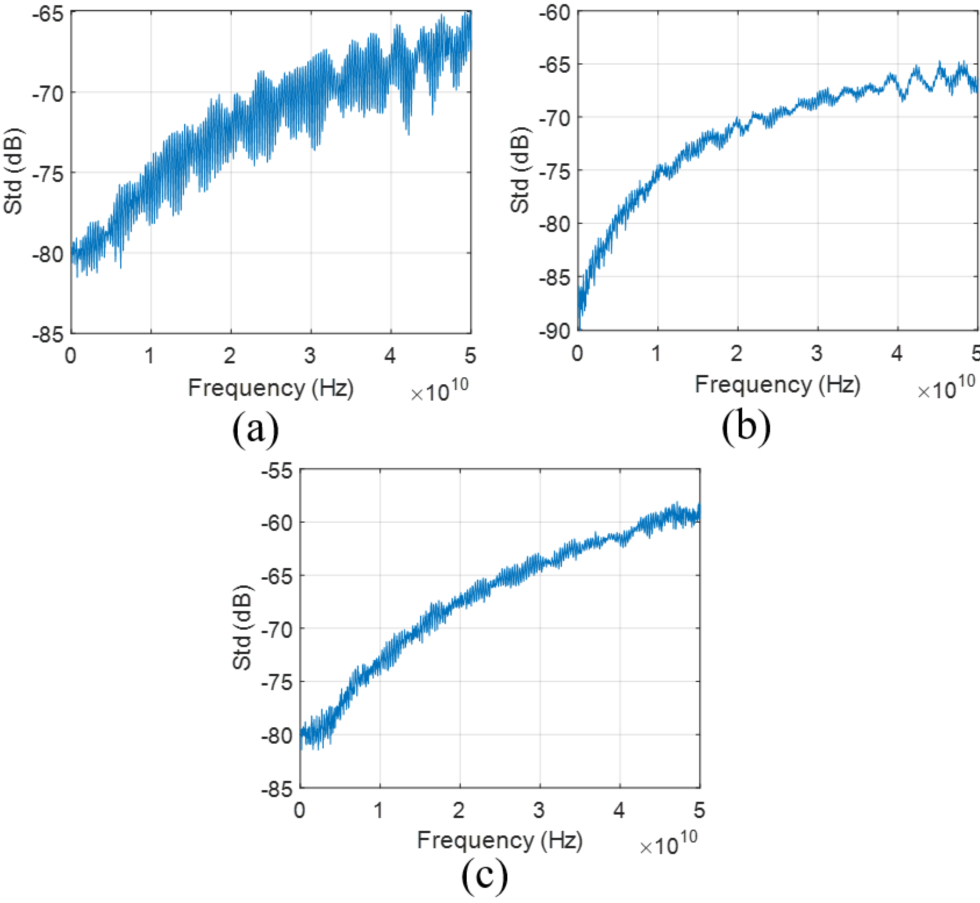

Figure 4.14 Standard deviations calculated for the three error terms (a) directivity δ_1. (b) reflection tracking τ_1. (c) source match μ_1.

We compare the results displayed in Table 4.5 with results from the manual measurements results. As an example, at 10 GHz, the residual directivity for a completely manual probing was 7.43×10^{-4} against 5.31×10^{-4} for the solution proposed. The repeatability was increased by a factor of 1.4. This result is encouraging as of the viability of our system. It is important to note that in this preliminary study, we used a step increment of 1 μm. During mechanical test on the nano-positioners, decreasing the step increment showed a better repeatability.

Table 4.5 3σ standard deviations computed at 1 GHz, 10 GHz, 30 GHz and 50 GHz.

Residual error term	1GHz	10GHz	30GHz	50GHz
	3σ	3σ	3σ	3σ
Directivity δ_1	2.89×10^{-4}	5.31×10^{-4}	1.1×10^{-3}	1.4×10^{-3}
Reflection tracking τ_1	1.82×10^{-4}	5.18×10^{-4}	1.2×10^{-3}	1.4×10^{-3}
Source match μ_1	2.72×10^{-4}	6.21×10^{-4}	2.0×10^{-3}	3.6×10^{-3}

4.2.4 Measurement uncertainty

We investigate the influence of the residual error terms computed from the robotic-manual measurement set by extending the reflection coefficient (S_{11}) uncertainty error model developed by D. Rytting to uncertainty impedance (Z) error model as developed previously.Figure 4.15 shows the reflection coefficient magnitude uncertainties as a function of S_{11} amplitude at 10 GHz for both the robotic-manual approach and the manual probing showed previously. We observe the amplitude uncertainty increases as a function of S_{11} amplitude. The figure also shows that our solution generates less measurement uncertainties than the manual probing counterpart does.

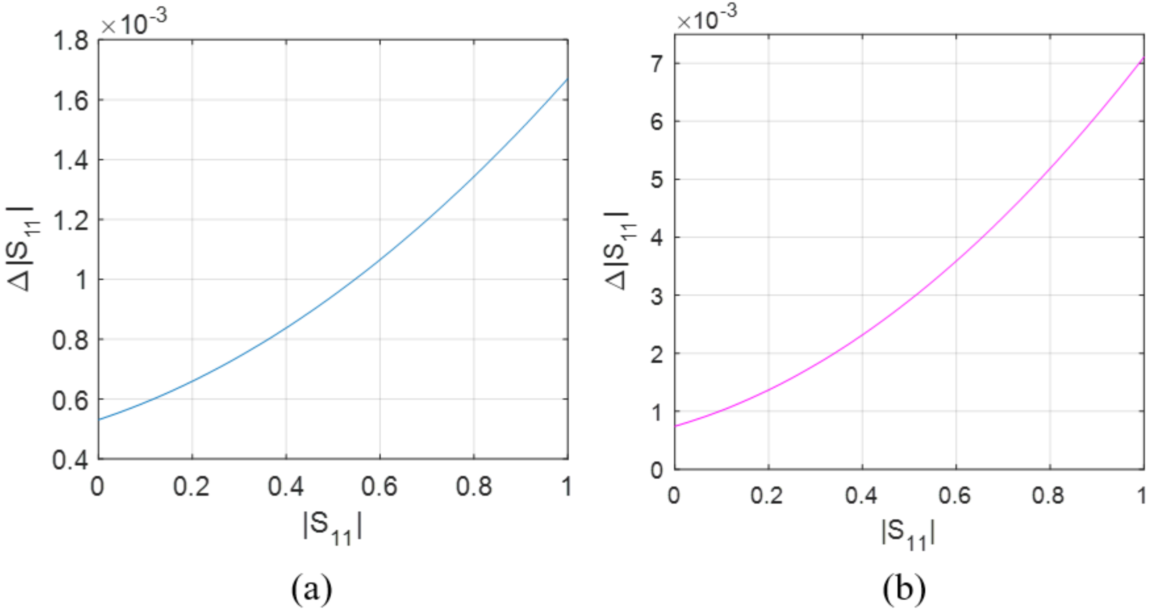

Figure 4.15 Reflection coefficient magnitude uncertainties. (a) robotic-manual approach. (b) conventional probing.

In the following, we propagate the error $|\Delta S_{11}|$ on the corresponding complex impedance. In particular, we focus on reactive devices such as fF capacitances. By considering a capacitance value down to 1 fF, we derive the capacitance measurement uncertainties. Table 4.6 summarizes the results obtained for both manual measurements obtained previously and the proposed method here. Mathematical details regarding the error propagation on complex impedances have been detailed above.

From Table 4.6, it is shown that the conventional probing station is not suitable to measure accurately high impedance devices such as sub-fF capacitance. As an example, a capacitance value of 1 fF measured at 10 GHz is measured with an error around 90%. The approach used in this work, demonstrates that the error can be reduced to 17%. The robotic-manual method for on-wafer calibration demonstrates reduction of the overall measurement uncertainty. As an early stage of the development of the new station, this is a promising result.

Table 4.6 Capacitance measurement uncertainties at 10 GHz.

C(fF)	ΔC (F)		ΔC/C (%)	
	Robotic-manual	Conventional	Robotic-manual	Conventional
320	5.32×10^{-16}	2.24×10^{-15}	0.17	0.7
100	2.90×10^{-16}	1.21×10^{-15}	0.29	1
10	2.52×10^{-16}	9.2×10^{-16}	2.52	10
1	1.73×10^{-16}	8.97×10^{-16}	17.33	90

4.3 Semi-automated measurements for 1-port SOL calibration

The software development involved in the robotics and automated on-wafer probing station went through several development stages. In Chapter 3, we presented the final version that relies of image recognition for the automatic alignment of the probes over the contact pads. Prior to that, other alignment method were tested. Here, we present a semi-automated version of the program.

The instrumental set up is the same as presented previously. A 1-port SOL calibration is done on the ISS in the frequency range 50 MHz – 50 GHz at an IFBW of 100 Hz. The measurement step is 25 MHz (1999 points) and the power is set at -10 dBm. Figure 4.15 shows the Infinity GSG probe’s tips aligned with the alignment structure of the ISS.

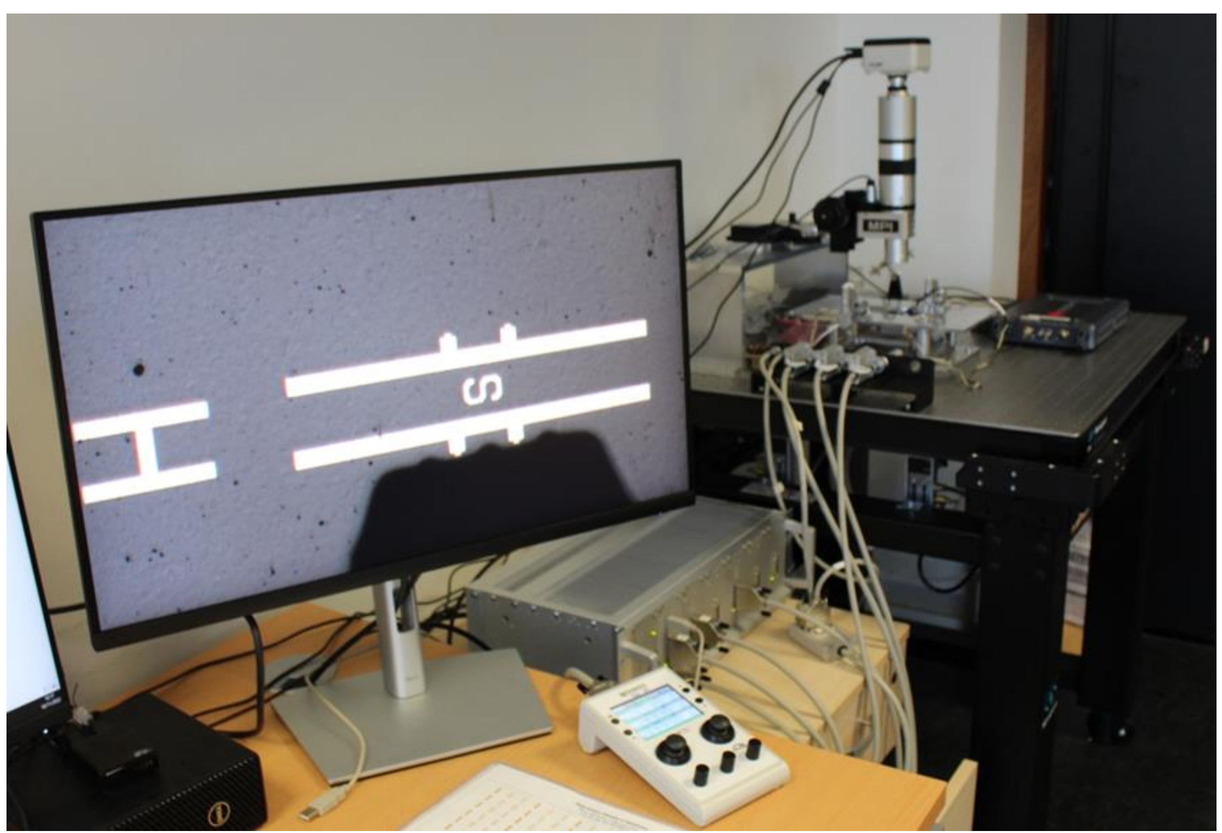

Figure 4.16 Infinity GSG probe’s tips aligned with the alignment structure of the ISS (on screen).

The semi-automated program used was developed in LabVIEW^{TM} and requires: 1- manual adjustments made by the operator, 2-automated re-alignments of the probe in the ISS. The measurement protocol is as follow:

1. Manual adjustments:

- Adjust the probe tilt (by seeing the 3 tips marks on the ISS)
- Adjust the chuck angle making it parallel to the probe
- Adjust the X and Y alignment of the probe according to the alignment structure on the ISS (Figure 4.16)
- Define the contact position
- Define the retract position
- Save the X-axis, Y-axis and Z-axis positions of the probe as reference

2. Semi-Automated calibration procedure

- Align the chuck with the probe according to the 1st standard then save those positions (chuck's positions)
- Go to the contact position (this is done automatically using a move command)
- Measure the reflection coefficient of the 1st standard using Wincal®
- Go to the retract position (this is done automatically using a move command)
- Align the chuck with the probe according to the 2nd standard then save those positions (chuck's positions)
- Go to the contact position (this is done automatically using a move command)
- Measure the reflection coefficient of the 2st standard using Wincal®
- Go to the retract position (this is done automatically using a move command)
- Align the chuck with the probe according to the 3rd standard then save those positions (chuck's positions)
- Go to the contact position (this is done automatically using a move command)
- Measure the reflection coefficient of the 3rd standard using Wincal®
- Go to the retract position (this is done automatically using a move command)
- Save in Wincal® as the 1st calibration then compute the error terms

Now that all positions (probes and chuck for each standard) are known and saved, we can just use move commands in the LabVIEW^{TM} to repeat N times to have N calibrations. For this experiment, we repeated the procedure 5 times. We want to evaluate the uncertainties brought by the semi-automated re-alignment of the probe during the calibration process.

The methodology is the same as used in the manual measurements and the robotic-manual measurements.

Figure 4.17 shows the standard deviations calculated for the three error terms for 5 consecutive measurements. We can make the same observations as before. The measurement uncertainties grow as a function of the frequency up to 20 GHz. Above 20 GHz, the increase is less significant. In the higher frequencies range, other sources of uncertainties become dominant (instrumental uncertainties) and the effect of the probe alignment on the ISS standards is shown less. Figure 4.18 represents the reflection coefficient magnitude uncertainties. We observe similar performances as the robotic-manual approach.

Although results are satisfactory in term of repeatability, we believe that a better degree of reproducibility can be reached. Indeed, the alignment of the probes is still relying on the

operator manual adjustments. Another solution have to be used where very few or no manual operations are required at all.

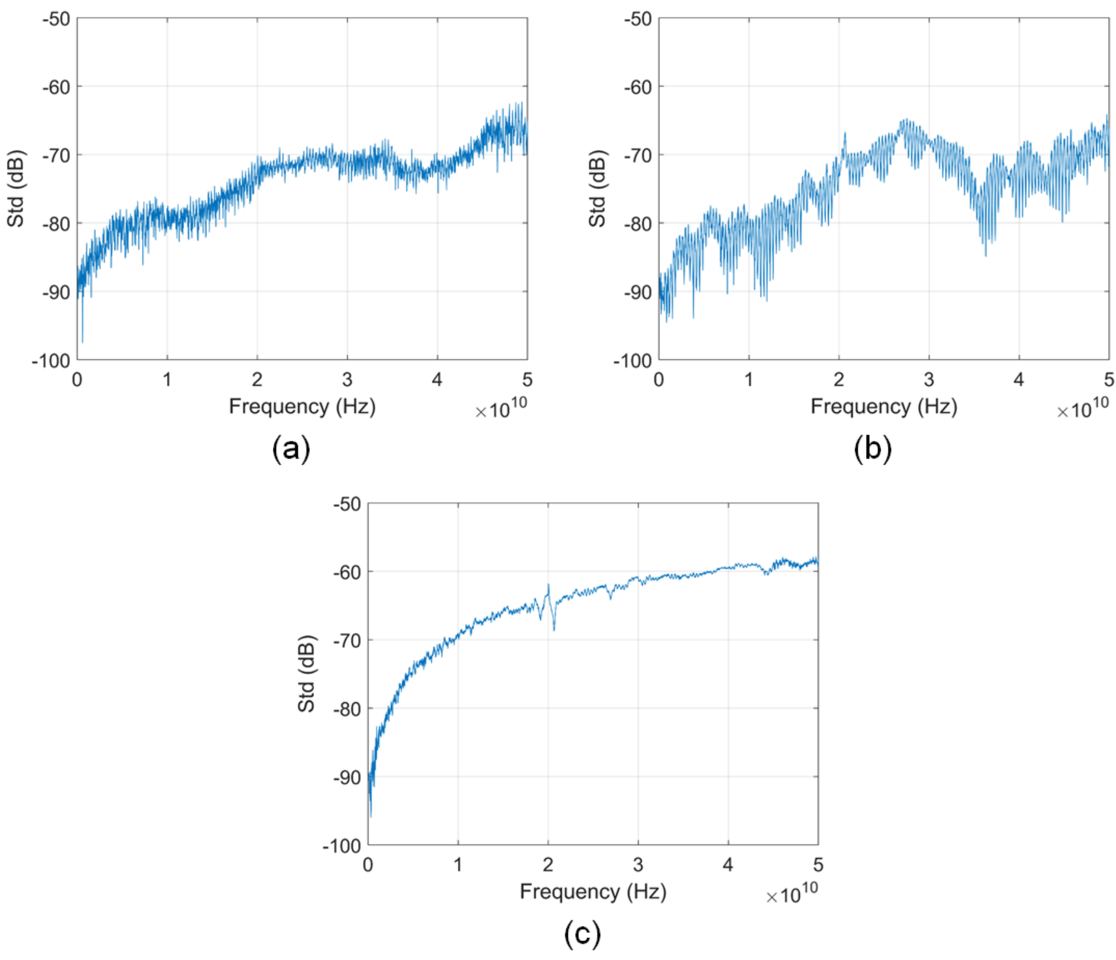

Figure 4.17 Standard deviations calculated for the three error terms (a) directivity δ_1. (b) reflection tracking τ_1. (c) source match μ_1.

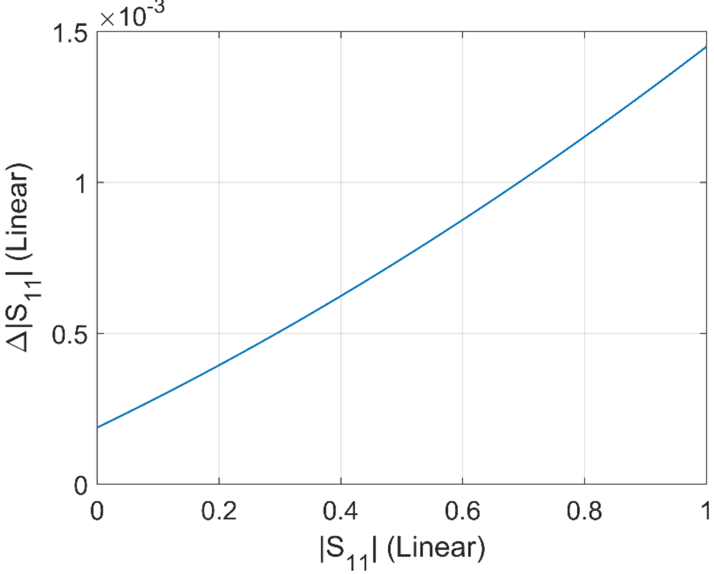

Figure 4.18 Reflection coefficient magnitude uncertainties.

4.4 Approach/retract study for probe-substrate surface contact

One of the main challenges, for on-wafer probing, is to ensure the quality of the contact between the probe and the substrate. Probe manufacturers like FormFactor® usually provide information about the skating and the overtravel that should be respected in order to establish a good and accurate contact as shown in Chapter 1. For example, alignment marks are available on the Impedance Standard Substrate (ISS) to guide the operator while probing. Nevertheless, this step is very operator dependent as it is done manually and can lead to repeatability issues. Before implementing this procedure automatically in the final version of the robotic and automated station, we imagined and investigated a solution that will not rely on the alignment structure and the vision system but on changes on the RF signal measured by the GSG probe. The goal is to first detect when the probe is really close to the surface and when it starts touching it. This can be indicated when there is a sudden change in the measured reflection coefficient. Once the corresponding position is known, we can apply the advised overtravel of the manufacturer.

To this end, we slowly and manually approached the probe to the surface of a calibration standard with the manual joystick of the MCS2 (Figure 4.11). Several displacement steps were used as well as different starting points over the surface. The probe and the positioner used are the same. The positions along the Z-axis were monitored and saved.

Figure 4.19 shows the positions along the Z-axis when approaching a 100 µm Infinity probe on a Short standard of the ISS 101-190C. the starting position is 100 µm above the surface of the ISS. Steps increments of 500 nm were done as regularly as possible. The points 0 to 52 corresponds to probe approaching the surface. From 52 to 54, the probe is establishing the initial contact. From 54 to 62, the probe is skating on the substrate. Finally, point 62 to 65 corresponds to the probe being lifted from the surface. Although the approach/retract was done manually, displacements of the probe are steady. In a similar way, Figure 4.20 shows the positions along the Z-axis of the probe approaching the substrate from 50 µm with a 100 nm step increment.

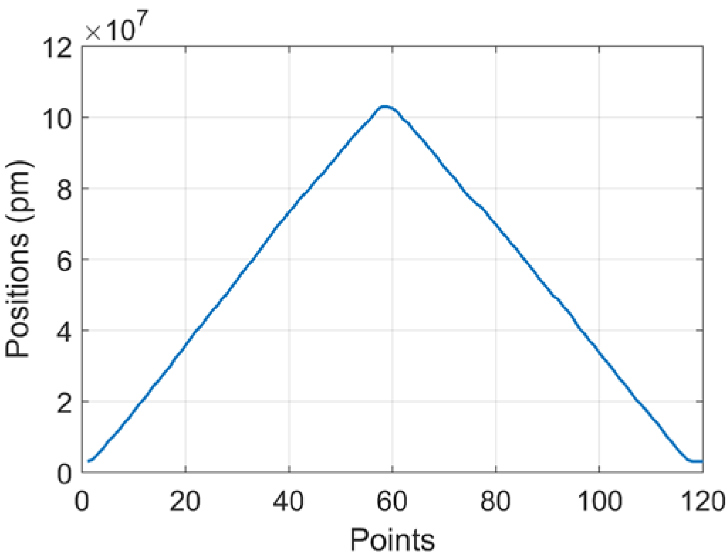

Figure 4.19 Position of the probe along the Z-axis when approaching the probe from 100 µm above the surface with a 500 nm step increment.

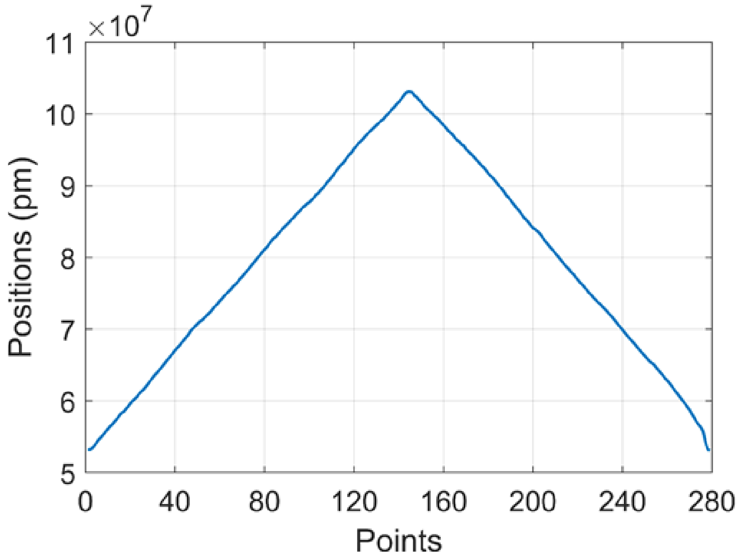

Figure 4.20 Position of the probe along the Z-axis when approaching the probe from 50 µm above the surface with a 100 nm step increment.

Figure 4.21 shows the real part of the measured refection coefficient when approaching from 100 µm with 500 nm step. We observe that when the probe is far from the surface, the signal is small. When the probe gets close to the surface, we can see that the signal start to increase. When the probe touches the surface, we observe a sudden and high increase of the signal. Here, we keep approaching the probe in order to have a good contact. We can see that the signal is completely flat when the probe is correctly in contact with the substrate. We observe a similar but inversed behaviour when retracting the probe from the surface. Figure 4.22 shows the real part of the measured reflection coefficient when approaching from 50 µm with 100 nm step. We observe the same behaviour. No matter the height, we start at or the step increment, we observe the same reflection coefficient signal. Figure 4.23 shows the imaginary part of the measured reflection coefficient for both configuration. We observe the same signal signature during the approach/retract procedure.

Although this solution was not used in the final version of the on-wafer station, results give a good perspective as of using the RF signal measured using the VNA in the probing procedure. We can easily imagine an automated procedure that will use the sudden reflection coefficient shift in value to automatically stop the probes when the contact is good enough.

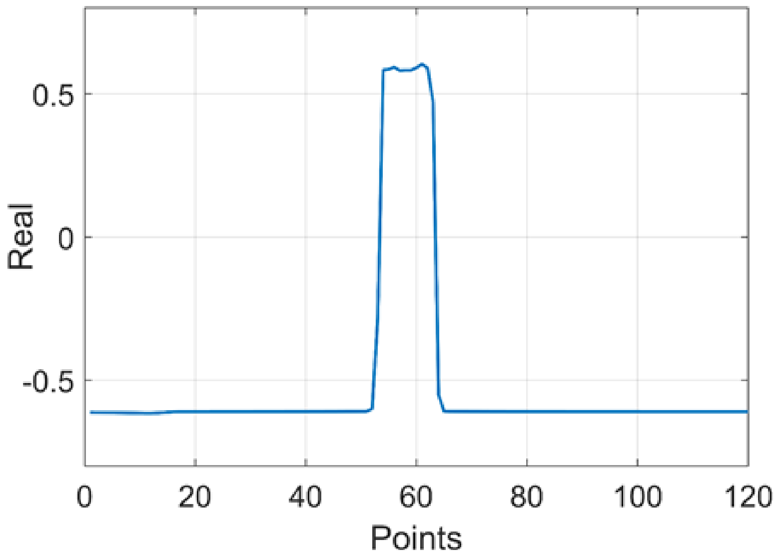

Figure 4.21 Real part of the measured reflection coefficient when approaching from 100 µm with 500 nm step.

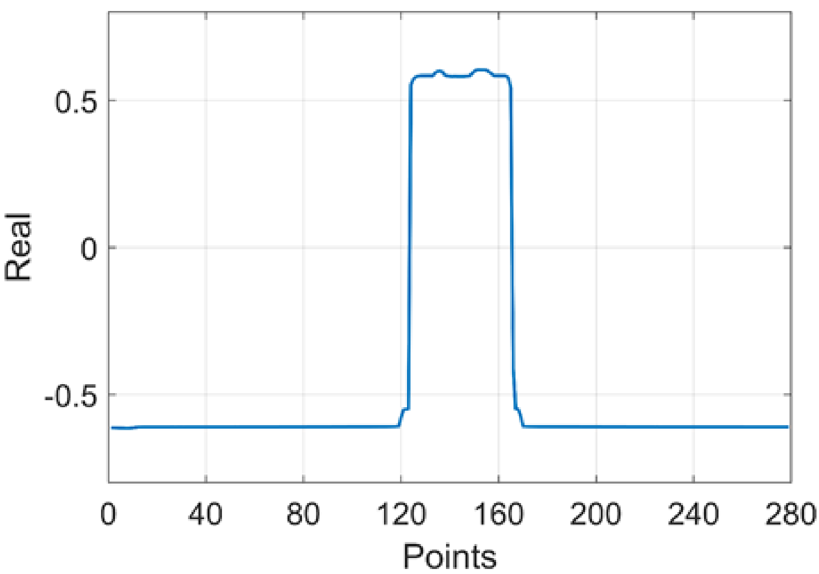

Figure 4.22 Real part of the measured reflection coefficient when approaching from 50 µm with 100 nm step.

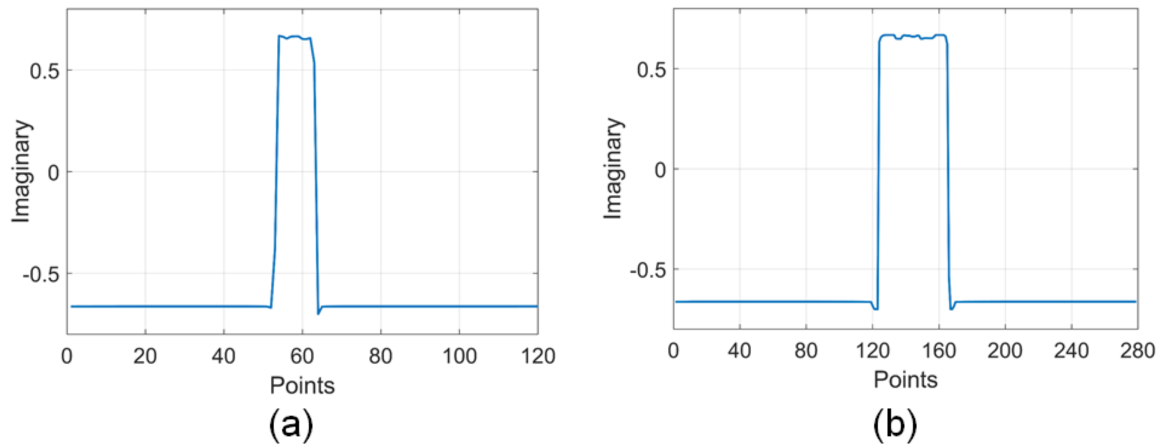

Figure 4.23 Imaginary part of the measured reflection coefficient when approaching from 100 µm with 500 nm step and from 50 µm with 100 nm step.

4.5 Automated measurements for 1-port SOL calibration

In the first section of this chapter, we proved that a conventional manual probing station is limited in term of alignment repeatability. Hence, we developed an automated and robotics probing station equipped with the SmarAct® nano-positioning technology. In this section, we present results of uncertainties propagation to capacitances measurements.

4.5.1 On-wafer experimental set-up and configuration

The experimental set-up used for this experiment was described in details in the third chapter of this manuscript. We will recall the main component here. The set-up consists of a FormFactor™ Infinity 100 μm pitch GSG probe attached to the nano-positioner from SmarAct®. The DUT is the FormFactor™ ISS 101-190 C inserted on the automated and robotic chuck from SmarAct®. RF measurements were done with the Keysight® 5008A Streamline Series USB Vector Network Analyzer. The whole set-up is on the Newport™ M-VIS3036-SG2-325A optical table.

In order to quantify the influence of the probe positioning on the ISS, we conducted two sets of measurement. The first consists of measuring multiple times the same standard without moving the probes. We will refer to this set as "in contact". In the second, we move (in XYZ directions) and reposition the probe before each measurement. We will refer to this set as "in movement". Also, two VNA modes are considered: the sweep mode and the continuous wave (CW) mode. A total of three IFBWs were tested with each mode: 1 Hz, 10 Hz and 100 Hz. Finally, for each configuration, we measured 10 times the Short, Open and Load standards from the ISS. Table 4.7 shows the different measurement configurations. Reducing the IFBW results in a higher resolution measurement. It can also reduce the noise that is integrated onto the measurement and hence improve the accuracy of the measurements. Consequently, we chose to measure at different IFBWs. We also chose to look at measurement results in CW mode in order to determine the influence of environment on the measurements over the duration of the experiment.

Table 4.7 Measurement configurations.

In contact						
	Sweep			CW		
IFBW	1 Hz	10 Hz	100 Hz	1 Hz	10 Hz	100 Hz
Frequency	25 MHz – 50 GHz			1 GHz		
Power	-15 dBm					
In movement						
	Sweep			CW		
IFBW	1 Hz	10 Hz	100 Hz	1 Hz	10 Hz	100 Hz
Frequency	25 MHz – 50 GHz			1 GHz		
Power	-15 dBm					

4.5.2 Automated and robotics alignment

In order to align the probes and the ISS, we developed a proprietary code in LabVIEW™ environment, described superficially in the third chapter. In the following, the measurement procedures are described:

In contact:

- The probes are aligned using the alignment structures of the ISS.
- The chuck is moved allowing the short standard to be seen on screen and under the probes.
- The standard and the probes are aligned and finally the probe is lowered until the final contact position.
- The VNA is triggered and the reflection coefficient of the Short standard at port-1 is saved. This step is done manually.
- Staying in contact, another trigger is sent via the VNA and the reflection coefficient at port-1 is saved once again. This step is repeated 10 times.
- Every step is repeated for both sweep and CW modes at each IFBW.

In movement:

- The probes are aligned using the alignment structure of the ISS.
- The chuck is moved allowing the short standard to be seen on screen and under the probes.
- The standard and the probes are aligned and finally the probe is lowered until the final contact position.
- The VNA is triggered and the reflection coefficient of the Short standard at port-1 is saved. This step is done manually.
- The probes are raised from the surface at 100 μm.
- The probes are moved to the alignment structure of the ISS.
- All the steps are repeated 10 times.
- Every step is repeated for both sweep and CW modes at each IFBW.

Remarks:

- *Same procedure is applied for the Load standard.*
- *Open is measured with probes on air at* $250\ \mu m$ *from the surface. The probes are moved in the same way as the other standard for the "In movement" configuration minus the contact step.*
- *The program is built to operate both probes at the same time. Here, measurements were done on port-1 of the VNA only as a first step.*
- *During the measurements, the VNA was switched between CW mode and Sweep mode and between* $1\ Hz$, $10\ Hz$, *and* $100\ Hz$ *while the probes were still in contact. Indeed, measurement time would have been much longer if each mode was carried out separately. It is important to note that the environment is yet to be controlled in temperature and humidity. Hence, it is preferable to make measurement time as short as possible in order to keep the same measurement environment.*
- *Time step between each measurement is are approximatively 5 min.*

4.5.3 RF measurements results and data interpretation

4.5.3.1 CW Mode

Figure 4.24 shows raw reflection coefficient S_{11} data of 10 successive measurements of the short standard at $1\ Hz$ and $100\ Hz$ measured at $1\ GHz$ for the "In contact – CW" configuration. Figure 4.25 shows the first value of each new measure. We observe that at $1\ Hz$, the magnitude of the complex reflection coefficient S_{11} seems to decrease over each measurement. This suggest that each new trigger of the VNA in CW mode has a direct influence on the measured reflection coefficient S_{11}. Phase-shift of the complex reflection coefficient S_{11} seems to be less influenced by the VNA trigger. The value decreases, but data are still randomly interweaved. At $100\ Hz$, we can still observe a decrease of the first value of each measurement. However, data appear randomly distributed for both magnitude and phase-shift. Table 4.8 shows the maximum difference calculated between the highest and the lowest value for the magnitude and phase shift of the raw reflection coefficient S_{11} for the short standard measure at $1\ GHz$ for the "CW Mode". The "In contact" results shows a relatively small maximum difference over 10 measurements at $1\ Hz$, $10\ Hz$ and $100\ Hz$. These results suggest a good stability of the VNA over the duration of the experiment.

Figure 4.26 shows the raw reflection coefficient S_{11} data of 10 successive measurements of the short standard at $1\ Hz$ and $100\ Hz$ measured at $1\ GHz$ for the "In movement – CW" configuration. Figure 4.27 shows the first value of each measure. At $1\ Hz$, we observe a clear decrease of the measured magnitude and phase-shift of the reflection coefficient S_{11} over the 10 measurements. At $100\ Hz$, the effect is less visible, similarly to the "In contact" configuration. Table 4.8, for the "In movement data", shows that the difference between the highest value and the lowest value in both magnitude and phase-shift is slightly bigger compared to the values obtained when the probes are not moved. Results suggest that the influence of the probes realignment is existent but remains rather small when looking at raw data.

Table 4.9 shows equivalent results calculated for the load standard. Here, the maximum difference of the reflection coefficient S_{11} of the phase-shift is slightly higher when the probes are moved between each measurement. From Table 4.10, which presents results obtained on the open standard, we can make the same conclusion as for the short standard.

Figure 4.28 shows the cumulative complex standard deviation calculated on the different configurations. We observe that the “In contact – 1 Hz” configuration cumulated the lowest errors. We also observe that the “In movement” configuration cumulates the most errors.

Overall, we do not observe a clear correlation between the IFBW used, the measurement set “In contact”/”In movement”) and the maximum difference on the magnitude and the phase shift of the reflection coefficient. We believe the internal noise of the VNA as well as other random uncertainties have the highest impact on the measurements. It also appears that the influence of realignment of the probes is sometimes lost inside the random uncertainties.

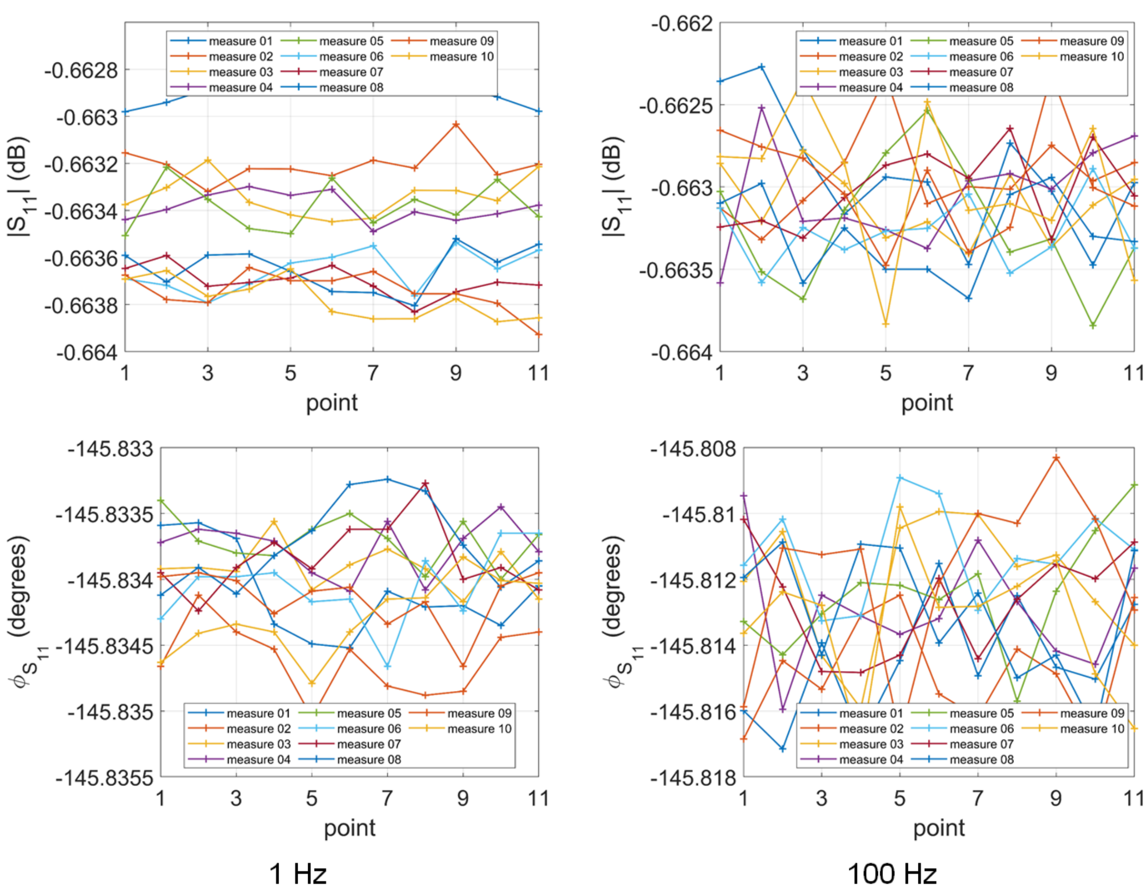

Figure 4.24 “In contact – CW – 1 GHz” raw reflection coefficient S_{11} data of 10 successive measurements of the Short standard at 1 Hz and 100 Hz.

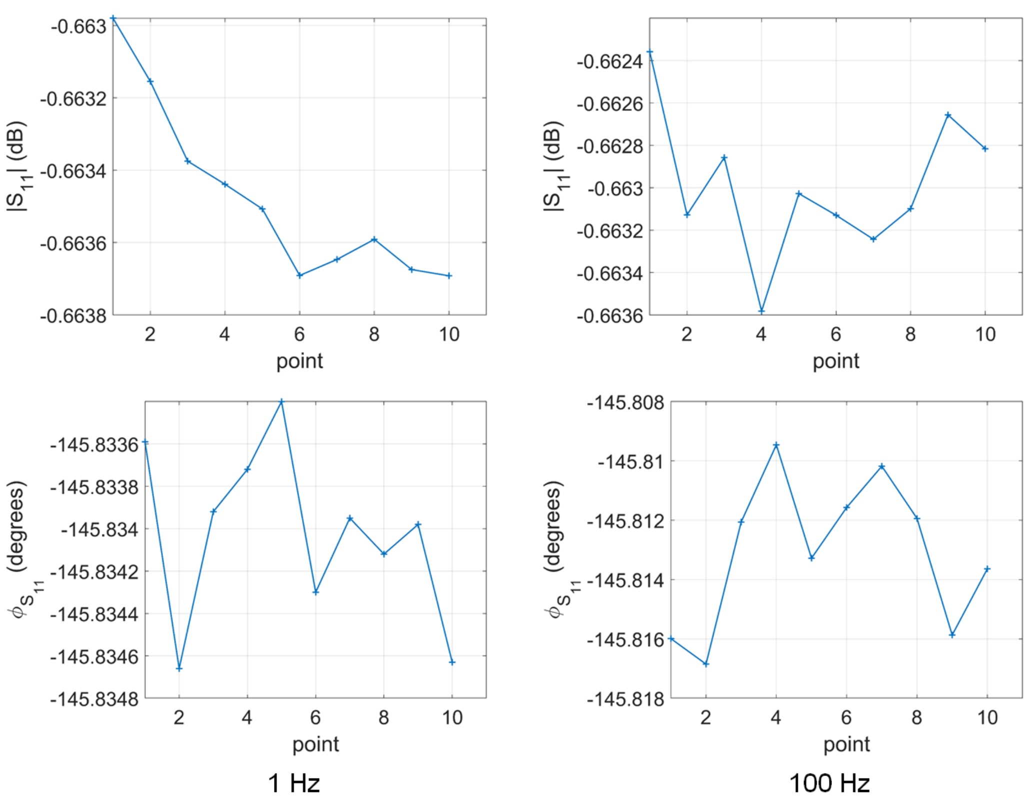

Figure 4.25 “In contact – CW – 1 GHz” First value of the raw reflection coefficient S_{11}.

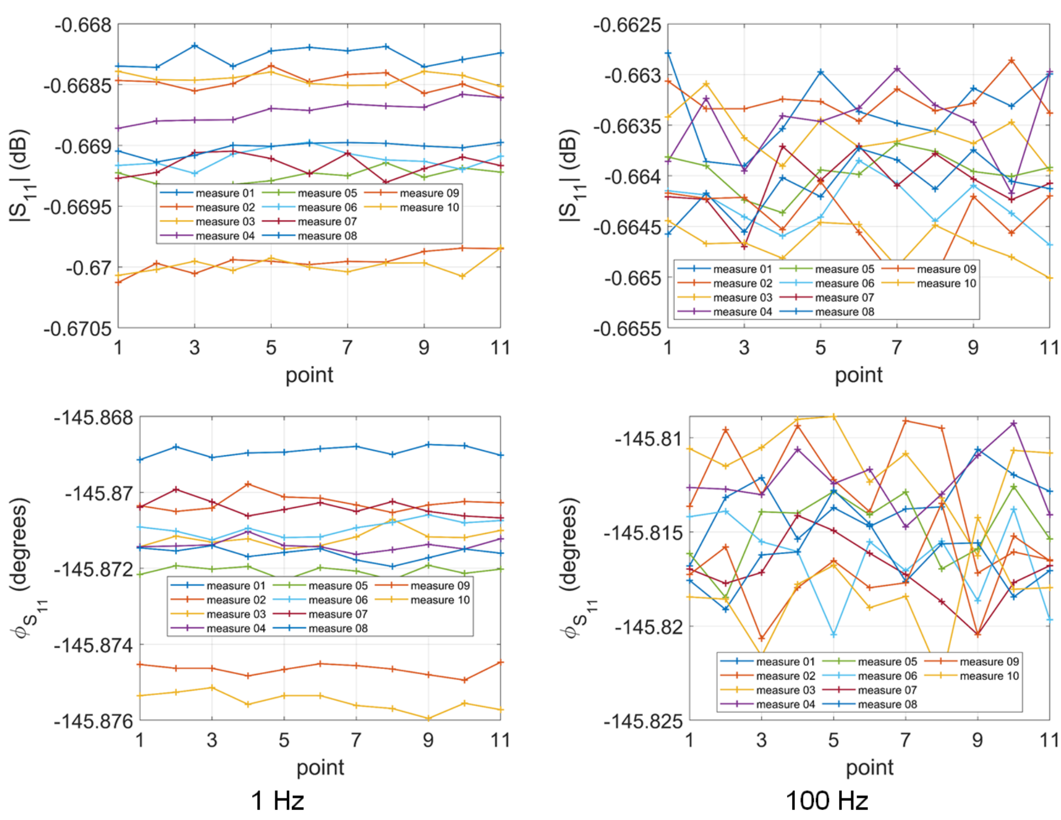

Figure 4.26 “In movement - CW” raw reflection coefficient S_{11} data of 10 successive measurements of the Short standard at 1 Hz, 10 Hz, and 100 Hz.

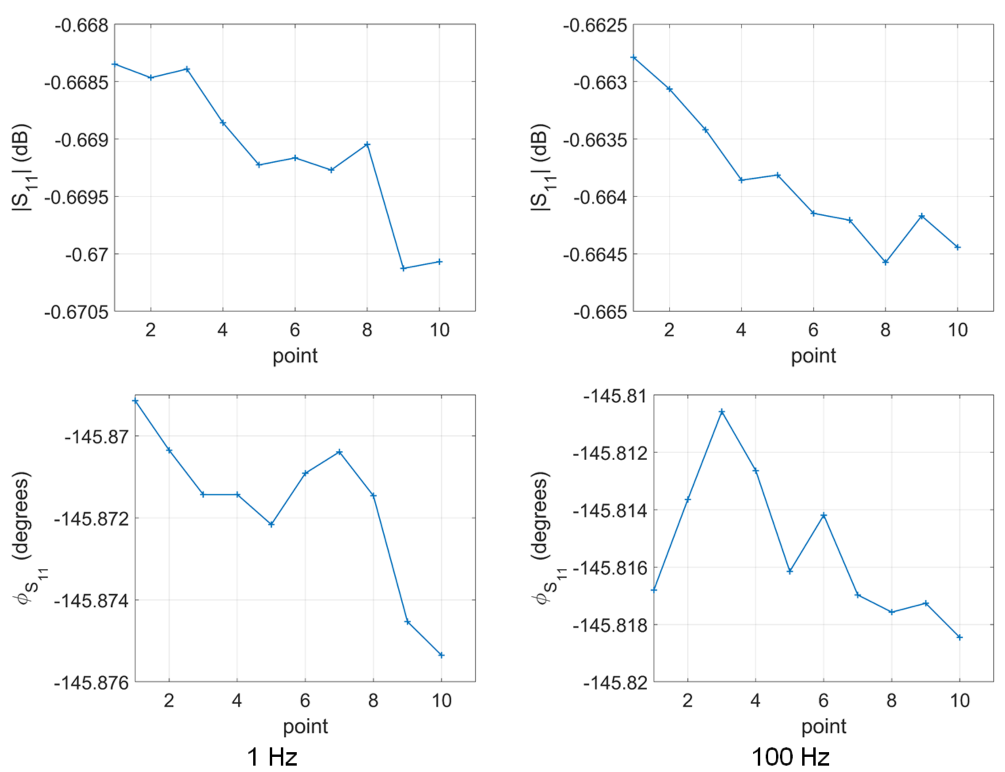

Figure 4.27 "In movement – CW – 1 GHz" First value of the raw reflection coefficient S_{11}.

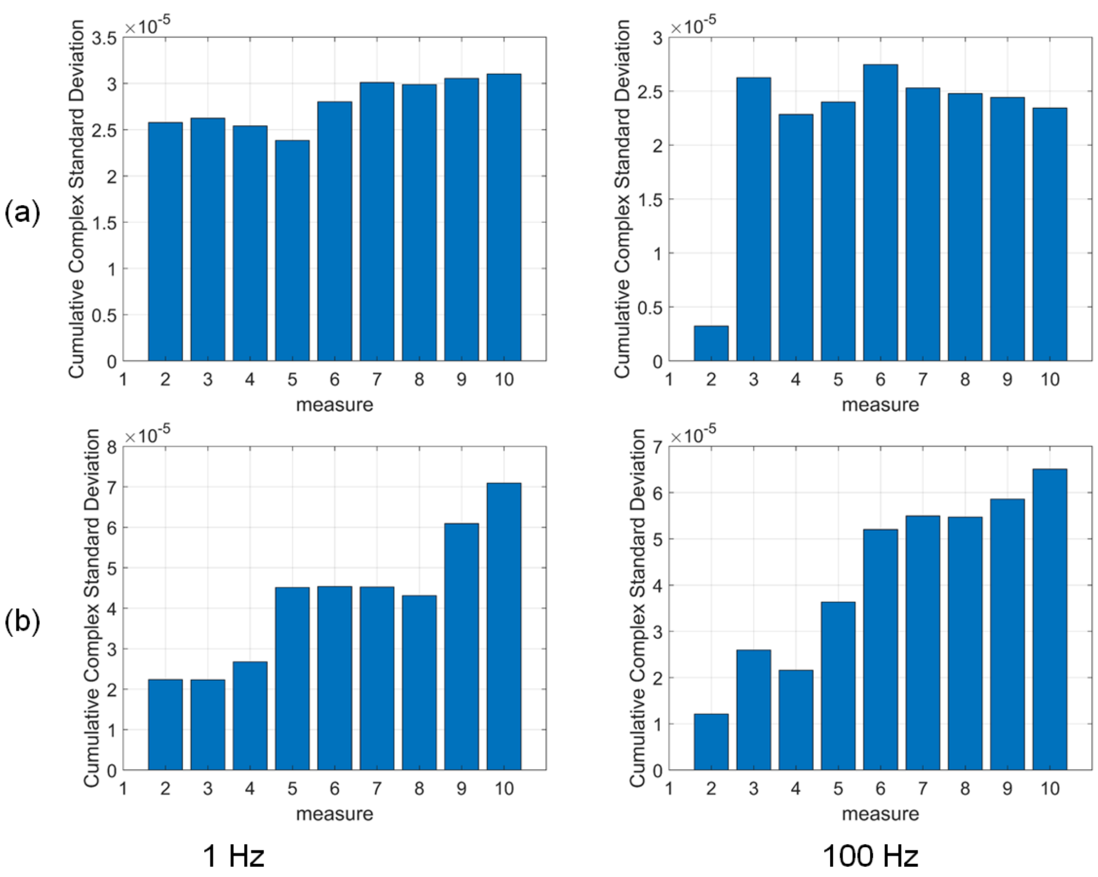

Figure 4.28 Cumulative Complex Standard Deviation for the different configuration. (a) In contact. (b) In movement.

Table 4.8 "CW Mode" Maximum difference calculated between the highest and the lowest value for the magnitude and phase shift of the raw reflection coefficient S_{11} for the Short standard.

In contact - CW			
	1 Hz	10 Hz	100 Hz
Magnitude Max difference (linear)	9.6462×10^{-5}	2.3501×10^{-5}	3.9280×10^{-5}
Phase shift Max difference (degrees)	9.0273×10^{-4}	0.0037	0.0035
In movement - CW			
	1 Hz	10 Hz	100 Hz
Magnitude Max difference (linear)	1.8363×10^{-4}	1.8619×10^{-4}	1.5183×10^{-4}
Phase shift Max difference (degrees)	0.0066	0.0069	0.0072

Table 4.9 "CW Mode" Maximum difference calculated between the highest and the lowest value for the magnitude and phase shift of the raw reflection coefficient S_{11} for the Load standard.

In contact - CW			
	1 Hz	10 Hz	100 Hz
Magnitude Max difference (linear)	1.7415×10^{-5}	1.9646×10^{-5}	2.1352×10^{-5}
Phase shift Max difference (degrees)	0.2956	0.2871	0.2887
In movement - CW			
	1 Hz	10 Hz	100 Hz
Magnitude Max difference (linear)	1.0119×10^{-4}	1.1120×10^{-5}	2.3568×10^{-5}
Phase shift Max difference (degrees)	0.1711	0.1673	0.2202

Table 4.10 “CW Mode” Maximum difference calculated between the highest and the lowest value for the magnitude and phase shift of the raw reflection coefficient S_{11} for the Open standard.

In contact - CW			
	1 Hz	10 Hz	100 Hz
Magnitude Max difference (linear)	1.0402×10^{-4}	9.9752×10^{-5}	1.3281×10^{-4}
Phase shift Max difference (degrees)	0.0027	0.0029	0.0034
In movement - CW			
	1 Hz	10 Hz	100 Hz
Magnitude Max difference (linear)	1.4983×10^{-4}	1.4017×10^{-4}	1.3678×10^{-4}
Phase shift Max difference (degrees)	0.0055	0.0060	0.0062

4.5.3.2 Sweep Mode

Figure 4.29 represents the “In contact – Sweep” and “In movement – Sweep” raw reflection coefficient S_{11} data of the 10 successive measurements of the Load standard at $100\ Hz$. We observe that all 10 measurements are superimposed for both configurations. We also observe that there is no visible difference when the probes are realigned over the load standard and when the probes are kept still. This suggest that the realignment procedure is highly reproducible.

Table 4.11, Table 4.12, and Table 4.13 show results of the “Sweep Mode” maximum difference calculated between the highest and the lowest value for the magnitude and phase shift of the raw reflection coefficient S_{11} for the short, the load, and the open standards respectively at $2.7\ GHz$ and $50\ GHz$. The tables show that the “In movement” configuration generated a bigger difference between the lowest and highest value measured. It also shows that increasing the IFBW or at a higher frequency, the gap is also higher. However, in some cases, those observations are not consistent. This can be attributed to the measurement environment. As stated previously, the environment is not controlled in temperature and humidity. In addition, although the station is on an optical table, this might not be sufficient to cancel all the vibrations of the building, which is suited for sensitive measurements.

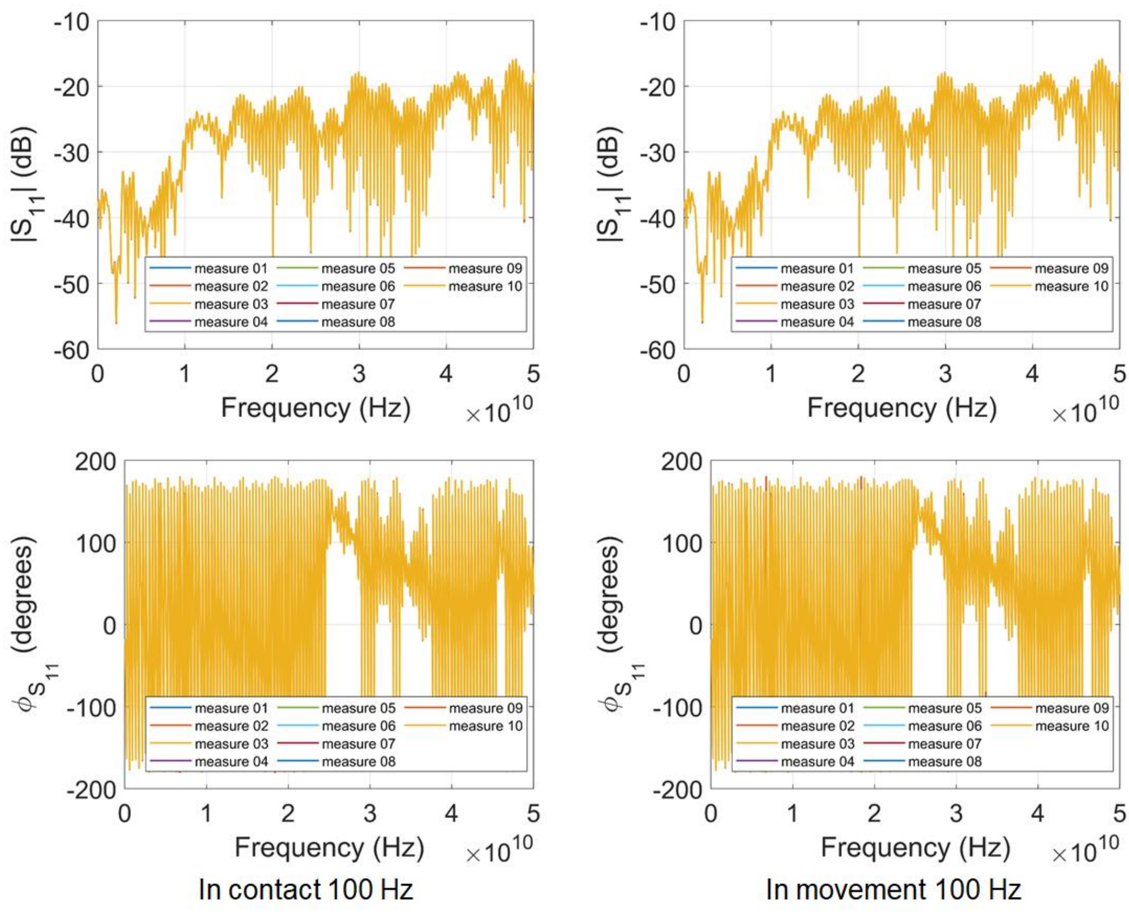

Figure 4.29 "In contact – Sweep" and "In movement – Sweep" raw reflection coefficient S_{11} data of 10 successive measurements of the Load standard at 100 Hz.

Table 4.11 "Sweep Mode" Maximum difference calculated between the highest and the lowest value for the magnitude and phase shift of the raw reflection coefficient S_{11} for the Short standard.

In contact - Sweep						
	1 Hz		10 Hz		100 Hz	
Frequency	2.7 GHz	50 GHz	2.7 GHz	50 GHz	2.7 GHz	50 GHz
Magnitude Max difference (linear)	6.83×10^{-5}	3.46×10^{-4}	1.12×10^{-4}	4.77×10^{-4}	1.05×10^{-4}	5.57×10^{-4}
Phase shift Max difference (°)	0.0067	0.1466	0.0061	0.1199	0.0064	0.1251
In movement - Sweep						
	1 Hz		10 Hz		100 Hz	
Frequency	2.7 GHz	50 GHz	2.7 GHz	50 GHz	2.7GHz	50 GHz
Magnitude Max difference (linear)	1.28×10^{-4}	4.74×10^{-4}	1.31×10^{-4}	5.26×10^{-4}	1.13×10^{-4}	7.19×10^{-4}
Phase shift Max difference (°)	0.0105	0.1340	0.0120	0.1332	0.0141	0.1519

Table 4.12 "Sweep Mode" Maximum difference calculated between the highest and the lowest value for the magnitude and phase shift of the raw reflection coefficient S_{11} for the Load standard.

In contact - Sweep						
	1 Hz		10 Hz		100 Hz	
Frequency	2.7 GHz	50 GHz	2.7 GHz	50 GHz	2.7 GHz	50 GHz
Magnitude Max difference (linear)	1.80×10^{-5}	8.73×10^{-5}	3.38×10^{-5}	8.70×10^{-5}	1.12×10^{-4}	$3.18 \times^{-4}$
Phase shift Max difference (°)	0.5623	0.1508	0.1255	0.1651	0.2605	0.1674
In movement - Sweep						
	1 Hz		10 Hz		100 Hz	
Frequency	2.7 GHz	50 GHz	2.7 GHz	50 GHz	2.7GHz	50 GHz
Magnitude Max difference (linear)	7.62×10^{-6}	7.71×10^{-5}	5.04×10^{-5}	1.03×10^{-4}	4.66×10^{-5}	3.22×10^{-4}
Phase shift Max difference (°)	0.3672	0.0398	0.0705	0.0755	0.4603	0.1958

Table 4.13 “Sweep Mode” Maximum difference calculated between the highest and the lowest value for the magnitude and phase shift of the raw reflection coefficient S_{11} for the Open standard.

In contact - Sweep						
	1 Hz		10 Hz		100 Hz	
Frequency	2.7 GHz	50 GHz	2.7 GHz	50 GHz	2.7 GHz	50 GHz
Magnitude Max difference (linear)	1.68×10^{-4}	6.96×10^{-4}	1.15×10^{-4}	6.32×10^{-4}	1.78×10^{-4}	6.87×10^{-4}
Phase shift Max difference (°)	0.0031	0.1643	0.0095	0.1491	0.0059	0.1343
In movement - Sweep						
	1 Hz		10 Hz		100 Hz	
Frequency	2.7 GHz	50 GHz	2.7 GHz	50 GHz	2.7GHz	50 GHz
Magnitude Max difference (linear)	3.89×10^{-4}	0.0015	7.87×10^{-5}	0.0014	2.79×10^{-4}	0.0015
Phase shift Max difference (°)	0.0201	0.1629	0.0071	0.1497	0.0273	0.1605

4.5.4 Residual calibration error terms

A 1-port SOL calibration was computed for measurements at 1 Hz and 100 Hz using the Sweep data. Wincal™ software was used to compute the SOL calibration algorithm. The first calibration was sent to the VNA and the verification was done and validated by the software. From the obtained error terms, the residual error terms were computed then used to calculate the reflection coefficient magnitude uncertainty. The methodology followed is the same as in the first section of this chapter regarding the manual measurements. Results will be presented in the following.

Figure 4.30 represents the standard deviation of the error terms calculated on 10 successive measurement at 1 Hz and 100 Hz for both “In contact” and “In movement”. We observe that repeatability regarding the three error terms decreases as a function of the frequency. We observe that for both IFBWs (1 Hz and 100 Hz), from 20 GHz, the repeatability of the measurements does not change significantly. The same observation was made when dealing with manual measurements presented in the first section. Indeed, at 20 GHz and above, other source of uncertainties (e.g., instrumental drift) become predominant. The figure also shows that the measurements where the probes were not moved between each of 10 measurement have a better repeatability. However, the difference is not significant. This suggest that the realignment repeatability of the system is robust.

Table 4.14 summarizes the standard deviations computed at $10\ GHz$ considering the "In movement – Sweep & CW – 100 Hz" configurations compared to the manual measurements. As expected, the "In contact" measurements present the best repeatability. For example, the directivity calculated from the automated "In contact" measurements is 6 times better than the directivity obtained from the manual measurements. On the other hand, it is only 1.2 times better than the automated "In movement" measurements. This results confirms the high repeatability of the automated measurements of the station.

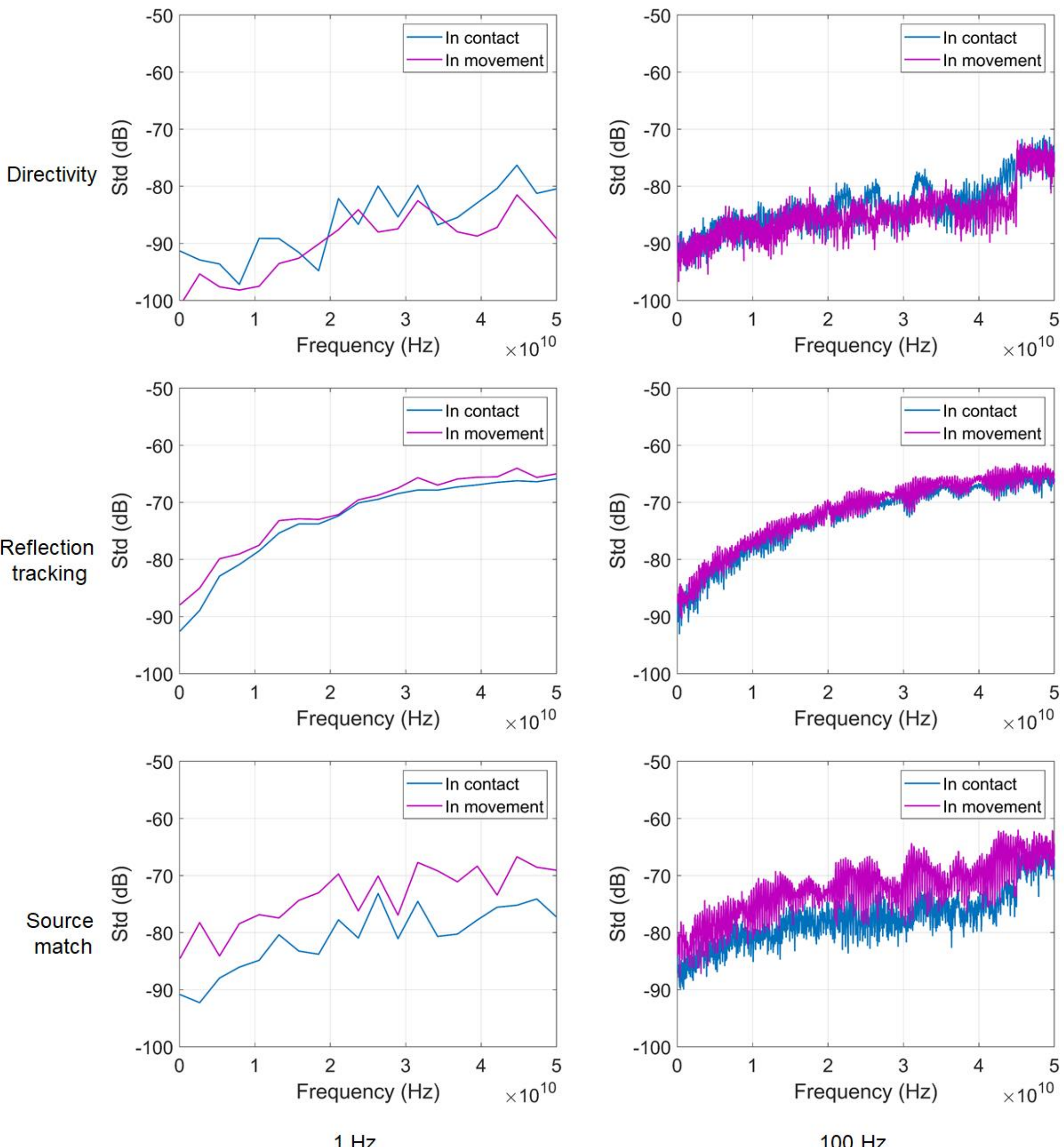

Figure 4.30 Standard deviation of the error terms calculated on 10 successive measurement at 1 Hz and 100 Hz for both measurement sets.

Table 4.14 3σ standard deviations computed at 10 GHz considering the "In contact – Sweep" and "In movement – Sweep" at 100 Hz and the manual measurements.

Residual error	10 GHz		
	$3\,\sigma$		
	Manual	*In contact Automated*	*In movement Automated*
δ_1	7.4267×10^{-4}	1.1703×10^{-4}	1.4900×10^{-4}
τ_1	2.3201×10^{-3}	4.4022×10^{-4}	5.2248×10^{-4}
μ_1	4.0472×10^{-3}	3.1665×10^{-4}	2.6407×10^{-4}

4.5.5 Error propagation on complex impedances

In the following, we propagated the residual errors on the reflection coefficient magnitude as presented previously in the first section. Figure 4.31 shows the reflection coefficient magnitude uncertainty at $1\,Hz$ and $100\,Hz$ for both "In contact" and "In movement" measurement sets. As a reminder, here we are using the data from the Sweep mode only. From Figure 4.31, we see that the uncertainty increases as a function the reflection coefficient magnitude. The two configurations still show close results. At 1 Hz, when $|S_{11}|$ is small, repositioning the probes generates less uncertainties. At $100\,Hz$, repositioning the probes generates slightly less uncertainties. This is explained by the source match term being higher for the "In contact" configuration. From (4.28), we see that the source match term has the biggest influence on the reflection coefficient magnitude uncertainty.

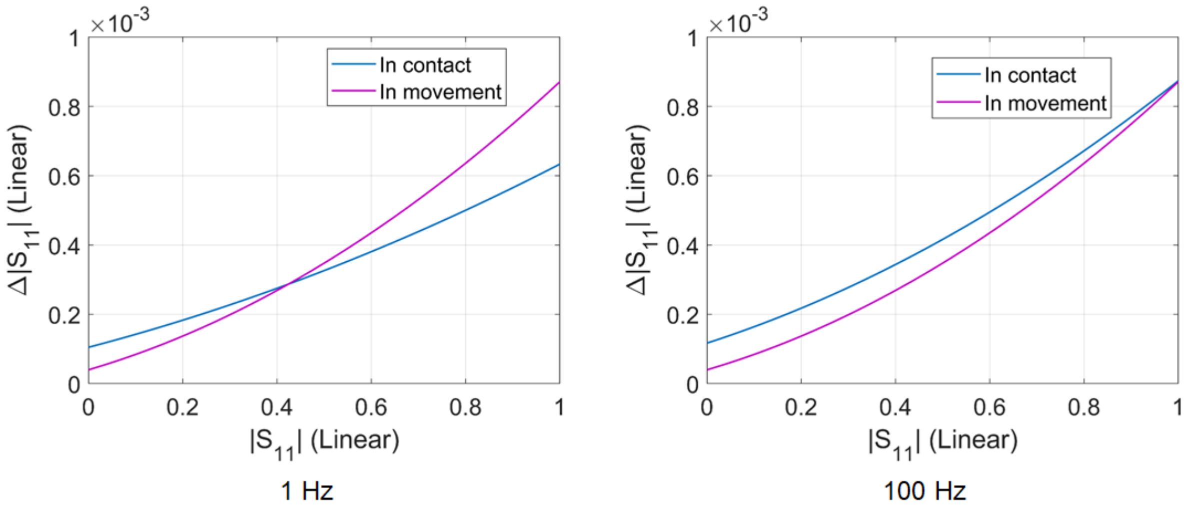

Figure 4.31 Reflection coefficient magnitude uncertainty at 1 Hz and 100 Hz for both measurement sets.

Finally, we can use the residual error terms obtained to calculate the measurement uncertainty of capacitances at 10 GHz. Here again, we use the same methodology as in the first section of this chapter when dealing with measurements conducted on a manual on-wafer probing station.

Table 4.15 and Table 4.16 show the measurement uncertainty and measurement capacitances uncertainties at 10 GHz and at 1 Hz of IFBW for the “In contact” and “In movement” configurations. In both cases, it is also shown that for a capacitance (perfect imaginary impedance value), we introduce a measurement uncertainty on the real part $\Delta Re(Z)$ of the impedance. When repositioning the probes on the calibration standard, we generates less uncertainties. The smaller the capacitance value, the bigger the uncertainties. For example, for $C = 1\ fF$, the capacitance is measured with 8.3 % error for the “In contact” configuration against 10.83 % for the “In movement” configuration. Although a difference exists, it remains quite low. This comforts the previous conclusions made regarding the repeatability of the system.

Table 4.15 “In contact – Sweep – 1 Hz” Measurement uncertainty and measurement capacitances uncertainties on capacitances at 10 GHz.

C(fF)	Δ|S11|	ΔIm(Z) (Ω)	ΔRe(Z) (Ω)	ΔC (F)	ΔC/C (%)
	Automated	Automated	Automated	Automated	Automated
320	6.33×10^{-4}	0.03	0.03	2.02×10^{-16}	0.0632
100	6.33×10^{-4}	0.17	0.18	1.10×10^{-16}	0.1103
10	6.33×10^{-4}	15.87	16.03	9.87×10^{-16}	0.9872
1	6.33×10^{-4}	1.45×10^{3}	1.61×10^{3}	8.37×10^{-17}	8.3753

Table 4.16 “In movement – Sweep – 1 Hz” Measurement uncertainty and measurement capacitances uncertainties on capacitances at 10 GHz.

C(fF)	Δ|S11|	ΔIm(Z) (Ω)	ΔRe(Z) (Ω)	ΔC (F)	ΔC/C (%)
	Automated	Automated	Automated	Automated	Automated
320	8.71×10^{-4}	0.04	0.04	2.78×10^{-16}	0.09
100	8.71×10^{-4}	0.24	0.24	1.51×10^{-16}	0.15
10	8.71×10^{-4}	21.74	22.05	1.35×10^{-16}	1.35
1	8.71×10^{-4}	1.93×10^{3}	2.24×10^{3}	1.08×10^{-16}	10.83

Table 4.17 shows the “In contact” measurement uncertainty and measurement capacitances uncertainties on capacitances at 10 GHz and at an IFBW of 100 Hz. Looking at the relative error introduced in this configuration, it is up to 10.86 %. Here, we observe a clear correlation between the measurement configuration and the impact on the uncertainties introduced on capacitances values. Indeed, it increases when the configuration has more uncertainty parameters (larger IFBW and movement of the probes).

Table 4.17 “In contact – Sweep – 100 Hz” Measurement uncertainty and measurement capacitances uncertainties on capacitances at 10 GHz.

C(fF)	Δ|S11|	ΔIm(Z) (Ω)	ΔRe(Z) (Ω)	ΔC (F)	ΔC/C (%)
	Automated	Automated	Automated	Automated	Automated
320	8.74×10^{-4}	0.04	0.04	2.7869×10^{-16}	0.09
100	8.74×10^{-4}	0.24	0.24	1.5205×10^{-16}	0.15
10	8.4×10^{-4}	21.81	22.12	1.3517×10^{-16}	1.35
1	8.74×10^{-4}	1.94×10^{3}	2.25×10^{3}	1.0864×10^{-16}	10.86

Table 4.18 summarizes results for the “In movement” measurement uncertainty on capacitances at 10 GHz and at 100 Hz compared with manual results measured in the same configuration (details in the first section). We observe that the uncertainties on the real part and the imaginary part of the complex impedance are higher when using a manual probing station. At $C = 1\ fF$, $\Delta Im(Z) = 2.06 \times 10^{3}\Omega$ for the automated station against $\Delta Im(Z) = 1.39 \times 10^{5}\Omega$ for the manual station, making the manual station 67 times worse than the automated one.

Table 4.19 presents the “In movement” measurement capacitances uncertainties on capacitances at 10 GHz and at an IFBW of 100 Hz compared with manual results in the same configuration. We can see that the automated probing station developed here generates less measurement uncertainties. At $C = 1\ fF$, it generates only 11 % errors against almost 90 % for the manual station.

This results proves that the automated and robotic probing station allow to measure extreme impedances devices with significantly less measurement uncertainties than a manual and conventional probing station. Indeed, the misalignment of the probes on the calibration pads can lead to high measurement uncertainties, leading to poor device characterisation.

Table 4.18 “In movement – Sweep – 100 Hz” Measurement uncertainty on capacitances at 10 GHz compared with manual results.

C(fF)	Δ|S11|		ΔIm(Z) (Ω)		ΔRe(Z) (Ω)	
	Automated	XYZ analysis	Automated	XYZ analysis	Automated	XYZ analysis
320	9.35×10^{-4}	71×10^{-4}	0.04	0.35	0.05	0.35
100	9.35×10^{-4}	71×10^{-4}	0.26	1.95	0.26	1.98
10	9.35×10^{-4}	71×10^{-4}	23.32	161.64	23.69	182.86
1	9.35×10^{-4}	71×10^{-4}	2.06×10^{3}	1.39×10^{5}	2.42×10^{3}	6.51×10^{4}

Table 4.19 “In movement – Sweep – 100 Hz” Measurement capacitances uncertainties on capacitances at 10 GHz compared with manual results.

C(fF)	ΔC (F)		ΔC/C (%)	
	Automated	XYZ analysis	Automated	XYZ analysis
320	2.98×10^{-16}	2.25×10^{-15}	0.09	$\mathbf{0.7}$
100	1.63×10^{-16}	1.21×10^{-15}	0.16	$\mathbf{1}$
10	1.44×10^{-16}	9.22×10^{-16}	1.44	$\mathbf{10}$
1	1.14×10^{-16}	8.97×10^{-16}	11.45	$\mathbf{90}$

Table 4.20 gives the uncertainty measured at 1 GHz with an IFBW of 100 Hz in CW and Sweep mode. This gives an idea of the best the system can achieve when the probes are being realigned on the calibration substrate. Indeed, for $C = 1\, fF$ and in CW mode, which allow more precise measurements, we generate 4 % of errors. As a comparison, the sweep mode generates 5 % error.

Table 4.20 “In movement – 100 Hz” Measurement capacitances uncertainties on capacitances at 1 GHz.

At 1 GHz	100 Hz In movement	
	ΔC/C (%)	
C(fF)	CW	Sweep
320	0.03	0.04
1	4.63	5.24

4.6 Conclusion

In this chapter, we investigated the measurement performance of a conventional on-wafer probe system based on mechanical displacements. Two measurement methods have been considered, (i) based on single axis probe displacement Z, (ii) based on three axis probe displacements XYZ. The conducted study demonstrated the measurement performance degradation between the two analysis. In particular, we have proven that controlling the probe alignment in the XY axis improves the measurement repeatability and hence, reduces the impedance measurement uncertainty in the microwave range up to 20 GHz.

We also presented early on-wafer probing procedure, robotic-manual and semi-automated. We proved that both methods reduce the uncertainty measurement brought by misalignments of the probes on calibrations standards. We also presented an approach/retract procedure to automatically detect the initial contact between the probe's tips and the substrate's surface.

Finally, we compared the new automated station to the conventional one. We proved that the method developed which is based on image recognition and automated alignment guarantees a high repeatability. Here, we tested the solution of a calibration substrate and showed that the station generates up to 11 % measurement uncertainties, against 90 % for the manual probing station when dealing with extreme impedance values.

4.7 References

[1] ‘2020IRDS_ES.pdf’.

[2] K. Daffé, G. Dambrine, C. Durand, C. Gaquière, and K. Haddadi, ‘On-Wafer Series-Through Broadband Measurement of Sub-fF55-nm MOS RF Voltage-Tunable Capacitors’, *IEEE Microwave and Wireless Components Letters*, vol. 28, no. 9, pp. 831–833, Sep. 2018, doi: 10.1109/LMWC.2018.2851386.

[3] D. F. Williams, J. Cheron, B. Jamroz, and R. Chamberlin, ‘On-Wafer Transistor Characterization to 750 GHz – the Approach, Results, and Pitfalls’, in *2018 IEEE BiCMOS and Compound Semiconductor Integrated Circuits and Technology Symposium (BCICTS)*, Oct. 2018, pp. 1–5. doi: 10.1109/BCICTS.2018.8550897.

[4] A. Rumiantsev and R. Doerner, ‘RF Probe Technology: History and Selected Topics’, *IEEE Microwave Magazine*, vol. 14, no. 7, pp. 46–58, Nov. 2013, doi: 10.1109/MMM.2013.2280241.

[5] U. Arz *et al.*, ‘Best Practice Guide for Planar S-Parameter Measurements using Vector Network Analysers : EMPIR - 14IND02 PlanarCal’, p. 5952785 bytes, 64 pages, 2019, doi: 10.7795/530.20190424B.

[6] R. G. Clarke, J. Quraishi, and N. M. Ridler, ‘A bilateral comparison of on-wafer S-parameter measurements at millimeter wavelengths’, in *2007 69th ARFTG Conference*, Jun. 2007, pp. 1–7. doi: 10.1109/ARFTG.2007.5456342.

[7] R. Sakamaki and M. Horibe, ‘Realization of Accurate On-Wafer Measurement Using Precision Probing Technique at Millimeter-Wave Frequency’, *IEEE Transactions on Instrumentation and Measurement*, vol. 67, no. 8, pp. 1940–1945, Aug. 2018, doi: 10.1109/TIM.2018.2806058.

[8] K. Daffe *et al.*, ‘On-Wafer Broadband Microwave Measurement of High Impedance Devices-CPW Test Structures with Integrated Metallic Nano-Resistances’, in *2018 48th European Microwave Conference (EuMC)*, Sep. 2018, pp. 25–28. doi: 10.23919/EuMC.2018.8541607.

[9] G. N. Phung *et al.*, ‘Influence of Microwave Probes on Calibrated On-Wafer Measurements’, *IEEE Transactions on Microwave Theory and Techniques*, vol. 67, no. 5, pp. 1892–1900, May 2019, doi: 10.1109/TMTT.2019.2903400.

[10] A. Rumiantsev and N. Ridler, ‘VNA calibration’, *IEEE Microwave*, vol. 9, no. 3, pp. 86–99, Jun. 2008, doi: 10.1109/MMM.2008.919925.

[11] A. Rumiantsev, ‘A Review of VNA Calibration Methods’.

[12] D. Rytting, ‘Network Analyzer Error Models and Calibration Methods’.

[13] J. Stenarson and K. Yhland, ‘Residual error models for the SOLT and SOLR VNA calibration algorithms’, in *2007 69th ARFTG Conference*, Jun. 2007, pp. 1–7. doi: 10.1109/ARFTG.2007.5456330.

[14] G. WÜbbeler, C. Elster, T. Reichel, and R. Judaschke, ‘Determination of the Complex Residual Error Parameters of a Calibrated One-Port Vector Network Analyzer’, *IEEE Transactions on Instrumentation and Measurement*, vol. 58, no. 9, pp. 3238–3244, Sep. 2009, doi: 10.1109/TIM.2009.2017170.

[15] M. Wollensack, J. Hoffmann, J. Ruefenacht, and M. Zeier, ‘VNA Tools II: S-parameter uncertainty calculation’, in *79th ARFTG Microwave Measurement Conference*, Montreal, QC, Canada: IEEE, Jun. 2012, pp. 1–5. doi: 10.1109/ARFTG79.2012.6291183.

[16] F. Mubarak, C. D. Martino, R. Toskovic, G. Rietveld, and M. Spirito, ‘Automated Contacting of On-Wafer Devices for RF Testing’, in *2020 Conference on Precision Electromagnetic Measurements (CPEM)*, Aug. 2020, pp. 1–2. doi: 10.1109/CPEM49742.2020.9191800.

[17] R. Sakamaki and M. Horibe, ‘Precision Adjustment of Probe-Tilt Angle With RF Signal Detection Technique’, *IEEE Transactions on Instrumentation and Measurement*, vol. 69, no. 10, pp. 8500–8505, Oct. 2020, doi: 10.1109/TIM.2020.2991601.

Chapter 5

5. Complementary studies

Table of content

Introduction 145

5.1 Streamline VNA noise characterisation 146

5.1.1 Set-up and material 146

5.1.2 Measurement protocol 146

5.1.3 Measurement set-up 147

5.1.4 Analysis 148

5.2 Extend IQ Six-Port Demodulator RF Bandwidth by 250% Using 157

5.2.1 Fourier Based Modelling 157

5.2.2 Six-port reflectometry 157

5.2.3 The direct problem equation 160

5.2.4 Theoretical and simulation analysis 160

5.2.5 Experimental six-port junction 162

5.2.6 Measurement protocol and Modelling 164

5.2.7 Experimental results 164

5.3 Impedance Standard Substrate EM-Simulation for On-wafer GSG probing 168

5.3.1 Imaging 168

5.3.2 EM modelling 169

5.3.3 Simulation 170

5.3.4 Analysis 171

5.4 Conclusion 174

5.5 References 175

Introduction

In this chapter, we present some complementary studies that were addressed through the years and that aim at enhancing on-wafer measurements of micro- and nano-devices.

First, we present a noise study on two different VNA types, a Streamline and a PNA. The aim is to quantify the best case uncertainty that we can achieve with a compact Streamline VNA in different configurations.

Second, we present a study of the six-port interferometry. Using six-port interferometry could open the door for new S-parameter characterisation that would be integrated to the measurement probes as close as possible. This would considerably decrease measurement uncertainties related the mismatch impedance between the VNA and the DUTs that present extreme impedance compared to the VNA's impedance.

Finally, an early stage Electro-Magnetic (EM) simulation is presented. Understanding the behaviour of the probes and ISS is a key component in improving on-wafer measurements of micro- and nano-devices. An ISS is designed and measurements on a load standard are presented.

5.1 Streamline VNA noise characterisation

In this section, we present a noise measurement study on a Streamline VNA from Keysight, P9375A 300 kHz -26.5 GHz 2-port (demo version), and compare it to noise measurement from a Keysight PNA N5242A 10 MHz-26.5 GHz.

5.1.1 Set-up and material

- Keysight® Streamline 300 kHz to 26.5 GHz 2-port.
- Keysight® PNA N5242A 10 MHz-26.5 GHz.
- GORE® cable E734-60004 MFR 3GW40.
- K type cables provided by Keysight with the demo VNA.
- 2 50 Ω loads provided by Keysight with the demo VNA.
- 2 coaxial short standards.

5.1.2 Measurement protocol

The aim of the measurements performed on the Streamline and the PNA is to determine the intrinsic noise of the two VNAs in several configurations. To this end, the two VNAs were not calibrated and a series of measurement were performed over a defined time range.

The intrinsic noise is inherent to the instrument and is specific to each measurement frequency. It is mainly due to the device heating, which causes thermic drifts. Other noise sources can affect the measurements: vibrations, temperature variations, humidity variations…

Measurement without cables

- 1-port measurements
- No cable is connected to the port 1 of the Streamline and PNA
- We connect a short standard and a load standard successively to the port 1 of the two VNA
- The port 1 is left unconnected to simulate an open standard
- We measure the reflection coefficient and the transmission coefficient

Measurement with cables

- 1-port measurements
- We connect the coaxial cable to the port 1 on the two VNAs
- We connect the short and the load standards to the end of the coaxial cables
- The end of the coaxial cable is left unconnected to simulate an open standard
- we measure the reflection coefficient and the transmission coefficient

Configuration

Table 5.1 summarizes the configurations used for this study. Table 5.2 shows the measurement periods.

Table 5.1 Measurement configurations.

Configurations									
IF Bandwidth	10 Hz			100 Hz			1000 Hz		
Frequency	1GHz	4GHz	10GHz	1GHz	4GHz	10GHz	1GHz	4GHz	10GHz
Time	180 s								

Those configurations are the same for each standard that is measured with and without cables.

Table 5.2 Measurement periods.

	Without cables		With cables	
	Streamline	PNA	Streamline	PNA
CO	08/04/2021	08/04/2021	12/04/2021	12/04/2021
CA	08/04/2021	08/04/2021	12/04/2021	09/04/2021
CC	09/04/2021	09/04/2021	15/04/2021	09/04/2021

Measurement on the open standard are done at the same time on the two VNAs. Indeed, as the port (or the cable's end) is left unconnected, we want to have the same environmental conditions.

5.1.3 Measurement set-up

Figure 5.1 shows the Streamline connected to the coaxial cables. Figure 5.2 shows the PNA connected to the coaxial cables.

Figure 5.1 Keysight Streamline connected to the coaxial cables.

Figure 5.2 Keysight PNA connected to the coaxial cables.

5.1.4 Analysis

As it is impossible to present data from all the configurations without making this document hard to read, we selected a few examples of the results obtained. Figure 5.3 and Figure 5.4 show the reflection coefficient and transmission coefficient measured for a short standard with and without cables respectively with an IFBW of 100 Hz and a measurement frequency of 10 GHz.

In order to have a better understanding of the two VNAs performances, we take a look at the standard deviation. Calculating the standard deviation on a set of data gives information about the dispersion of the elements from their mean. The smaller the standard deviation, the more homogenous the set is.

In our case, we fix a frequency and measure the evolution of the reflection and transmission coefficients over a period of time. Ideally, these coefficients remain stable and constant over time. The standard deviation allows us to know the stability of the device. The lower the standard deviation, the more stable the device is.

The standard deviation values calculated on the measurement related to the Streamline and the PNA are summarized in the tables bellow. We note that, depending on the configuration one of the VNAs performs better. We note the Streamline tends to give better results in transmission and in higher frequencies. Overall, the standard deviation is relatively low, which indicates a good instrumental stability.

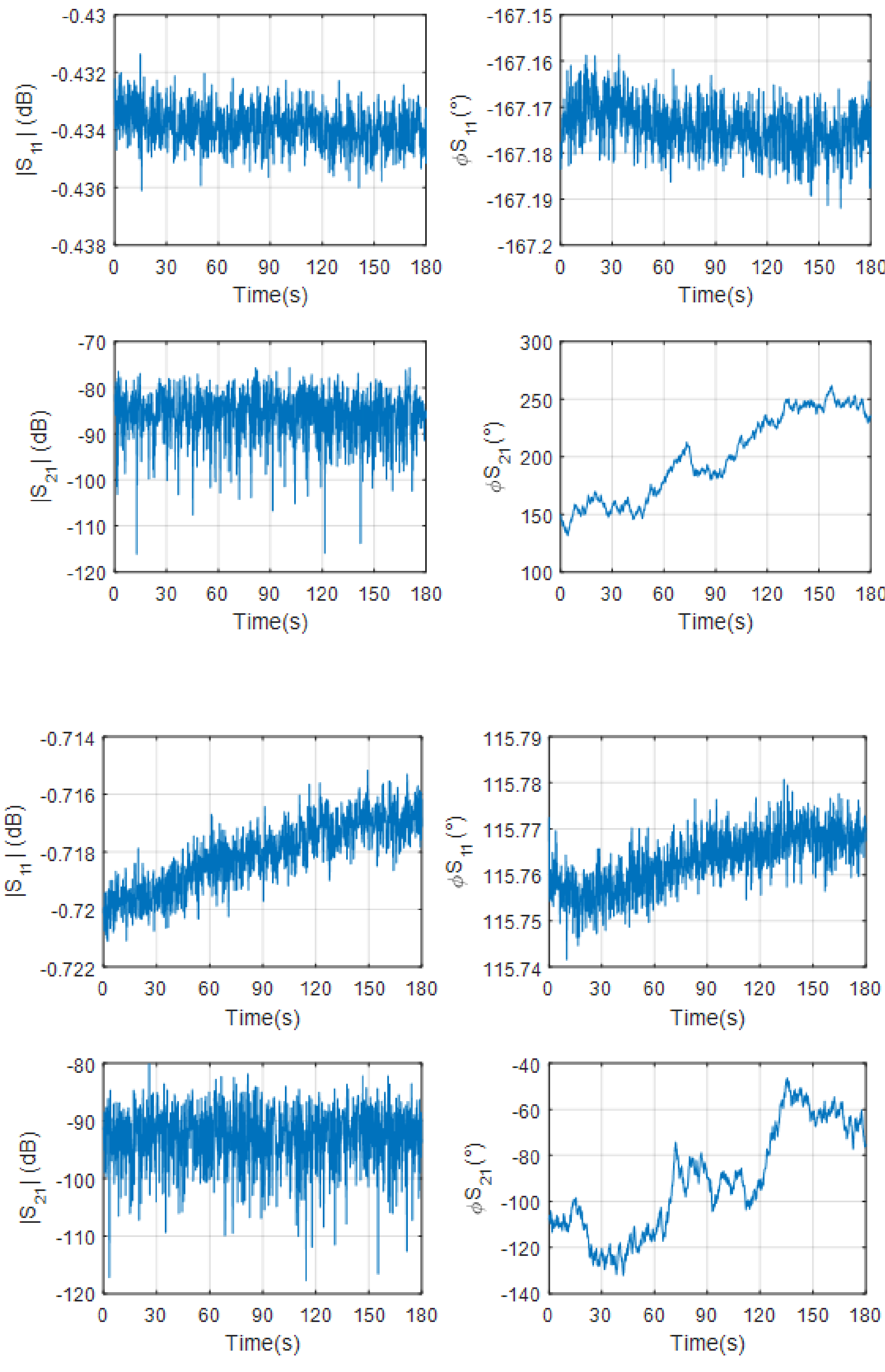

Figure 5.3 Reflection coefficient and transmission coefficient measured for a short standard directly connected to the Streamline (Top 4) and the PNA (Bottom 4) at IFBW of 100 Hz and 10 GHz

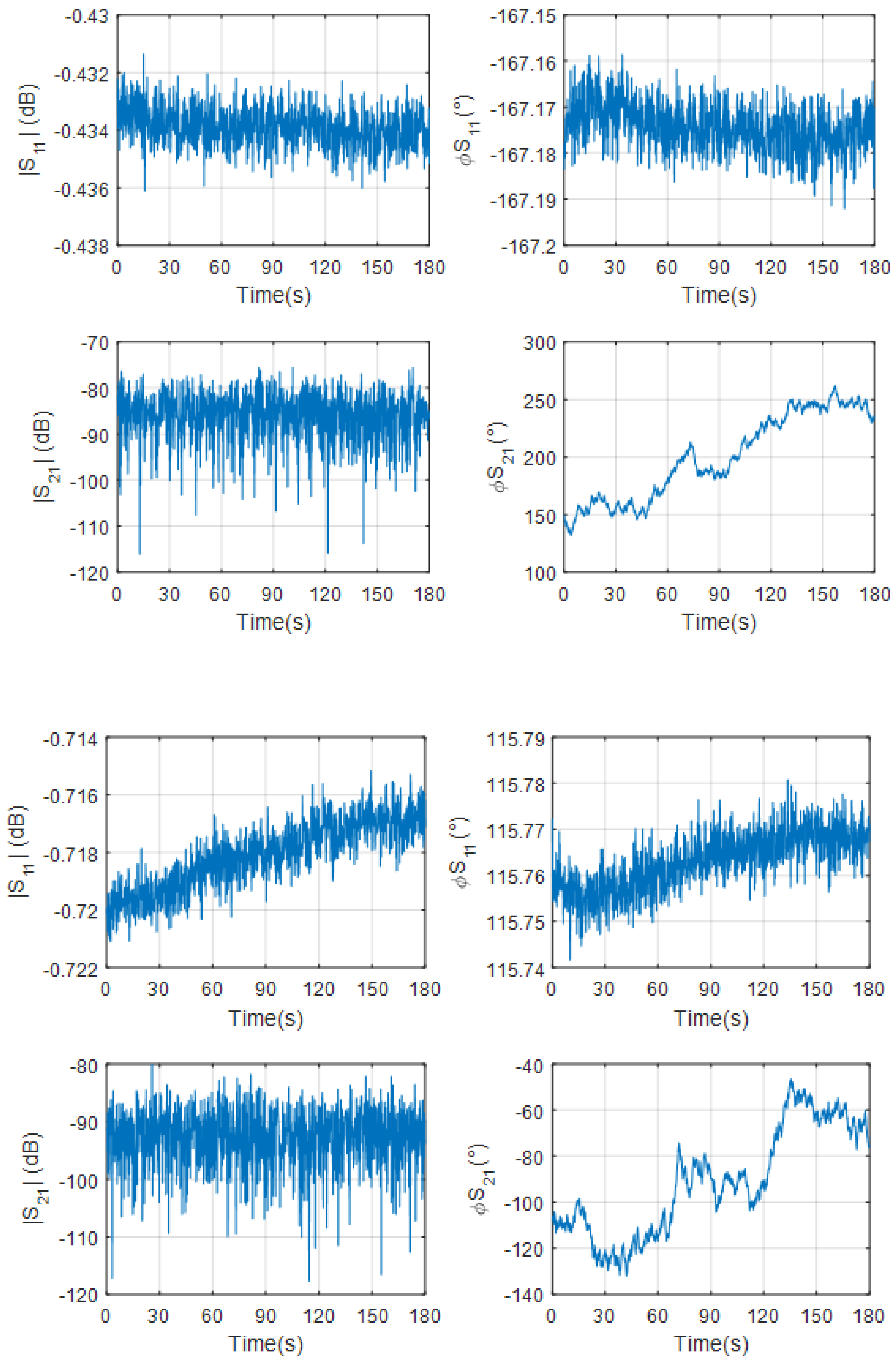

Figure 5.4 Reflection coefficient and transmission coefficient measured for a short standard connected via a cable to the Streamline (Top 4) and the PNA (Bottom 4) at IFBW of 100 Hz and 10 GHz.

Table 5.3 Standard deviation calculated for the load without cables measurement sets.

Load without cable									
Coefficient	S11								
IFBW	10 Hz			100 Hz			1000 Hz		
Frequency	1GHz	4GHz	10GHz	1GHz	4GHz	10GHz	1GHz	4GHz	10GHz
Streamline	0.0377	0.0288	0.0020	0.1114	0.0814	0.0045	0.3318	0.2480	0.0134
PNA	0.0169	0.0204	0.0054	0.0380	0.0598	0.0142	0.1218	0.1923	0.0470
Coefficient	S21								
IFBW	10 Hz			100 Hz			1000 Hz		
Frequency	1GHz	4GHz	10GHz	1GHz	4GHz	10GHz	1GHz	4GHz	10GHz
Streamline	95.6917	95.7375	96.3713	86.1878	85.6184	86.0880	76.4124	76.0473	76.7423
PNA	102.0388	103.4735	103.2592	93.9899	93.5936	93.3114	84.2956	83.5630	83.3083

Table 5.4 Standard deviation calculated for the short without cables measurement sets.

Short without cables									
Coefficient	S11								
IFBW	10 Hz			100 Hz			1000 Hz		
Frequency	1GHz	4GHz	10GHz	1GHz	4GHz	10GHz	1GHz	4GHz	10GHz
Streamline	2.8875 $\times10^{-4}$	2.8731 $\times10^{-4}$	3.0660 $\times10^{-4}$	7.4143 $\times10^{-4}$	7.6112 $\times10^{-4}$	7.0007 $\times10^{-4}$	0.0022	0.0022	0.0020
PNA	7.8119 $\times10^{-4}$	3.2451 $\times10^{-4}$	5.3321 $\times10^{-4}$	5.7419 $\times10^{-4}$	8.7420 $\times10^{-4}$	0.0012	0.0018	0.0019	0.0020
Coefficient	S21								
IFBW	10 Hz			100 Hz			1000 Hz		
Frequency	1GHz	4GHz	10GHz	1GHz	4GHz	10GHz	1GHz	4GHz	10GHz
Streamline	95.9446	95.4767	96.3258	86.3180	85.8247	86.2042	76.7074	75.8123	76.8819
PNA	101.9017	102.9630	102.6405	93.8028	93.5644	93.0636	83.9873	83.6078	82.7935

Table 5.5 Standard deviation calculated for the open without cables measurement sets.

Open without cables									
Coefficient	S11								
IFBW	10 Hz			100 Hz			1000 Hz		
Frequency	1GHz	4GHz	10GHz	1GHz	4GHz	10GHz	1GHz	4GHz	10GHz
Streamline	3.0468×10^{-4}	3.2474×10^{-4}	2.6695×10^{-4}	8.2750×10^{-4}	7.6942×10^{-4}	6.5784×10^{-4}	0.0025	0.0023	0.0019
PNA	2.7089×10^{-4}	3.3433×10^{-4}	3.4624×10^{-4}	6.1499×10^{-4}	6.3307×10^{-4}	6.4141×10^{-4}	0.0023	0.0019	0.0022
Coefficient	S21								
IFBW	10 Hz			100 Hz			1000 Hz		
Frequency	1GHz	4GHz	10GHz	1GHz	4GHz	10GHz	1GHz	4GHz	10GHz
Streamline	94.7370	95.3936	79.3230	84.8560	85.3822	84.5497	75.9174	76.0798	76.6389
PNA	102.6418	100.7868	41.4423	93.7499	93.8645	81.5706	83.8571	83.3441	82.0042

Table 5.6 Standard deviation calculated for the short with cables measurement sets

Short with cables									
Coefficient	S11								
IFBW	10 Hz			100 Hz			1000 Hz		
Frequency	1GHz	4GHz	10GHz	1GHz	4GHz	10GHz	1GHz	4GHz	10GHz
Streamline	3.0654 $\times 10^{-4}$	2.6418 $\times 10^{-4}$	5.2959 $\times 10^{-4}$	8.6379 v	8.4668 $\times 10^{-4}$	0.0011	0.0025	0.0025	0.0030
PNA	9.1665 $\times 10^{-4}$	5.2779 $\times 10^{-4}$	3.1719 $\times 10^{-4}$	6.2541 $\times 10^{-4}$	7.2326 $\times 10^{-4}$	6.5157 $\times 10^{-4}$	0.0017	0.0019	0.0019
Coefficient	S21								
IFBW	10 Hz			100 Hz			1000 Hz		
Frequency	1GHz	4GHz	10GHz	1GHz	4GHz	10GHz	1GHz	4GHz	10GHz
Streamline	94.9454	95.6371	96.1046	84.9956	85.9980	85.9922	75.8167	75.8254	76.4104
PNA	100.4152	93.2843	100.6233	93.9033	92.4632	93.6480	84.0922	83.5910	83.1497

Table 5.7 Standard deviation calculated for the open with cables measurement sets.

Open with cables									
Coefficient	S11								
IFBW	10 Hz			100 Hz			1000 Hz		
Frequency	1GHz	4GHz	10GHz	1GHz	4GHz	10GHz	1GHz	4GHz	10GHz
Streamline	2.5789×10^{-4}	2.8134×10^{-4}	3.7503×10^{-4}	7.6554×10^{-4}	7.7382×10^{-4}	7.8810×10^{-4}	0.0021	0.0023	0.0022
PNA	2.7501×10^{-4}	5.8817×10^{-4}	7.2329×10^{-4}	7.0492×10^{-4}	6.9378×10^{-4}	7.7214×10^{-4}	0.0018	0.0020	0.0021
Coefficient	S21								
IFBW	10 Hz			100 Hz			1000 Hz		
Frequency	1GHz	4GHz	10GHz	1GHz	4GHz	10GHz	1GHz	4GHz	10GHz
Streamline	94.5956	32.6431	76.3221	86.5105	69.8425	83.8206	77.4243	74.5977	76.3440
PNA	101.9413	102.1949	97.0371	93.2465	93.1202	92.9086	84.1976	83.6434	83.2211

Table 5.8 Standard deviation calculated for the Load with cables measurement sets.

Load with cables									
Coefficient	S11								
IFBW	10 Hz			100 Hz			1000 Hz		
Frequency	1GHz	4GHz	10GHz	1GHz	4GHz	10GHz	1GHz	4GHz	10GHz
Streamline	-	-	-	-	-	-	-	-	-
PNA	0.0104	0.0055	0.0111	0.0256	0.0158	0.0161	0.0843	0.0487	0.0429
Coefficient	S21								
IFBW	10 Hz			100 Hz			1000 Hz		
Frequency	1GHz	4GHz	10GHz	1GHz	4GHz	10GHz	1GHz	4GHz	10GHz
Streamline	96.0448	95.4702	96.0555	85.7825	85.6947	86.7823	76.3611	76.2022	76.8953
PNA	101.7496	103.4751	103.2719	93.4645	93.5580	93.3736	84.0195	83.8397	83.1645
The measurements with the load on the Streamline were not properly recorded, which made their exploitation impossible									

5.2 Extend IQ Six-Port Demodulator RF Bandwidth by 250% Using

5.2.1 Fourier Based Modelling

The Six-port technology has been introduced in the 1970's by G. Engen as an elegant solution to measure microwave amplitude and phase-shift passively [1]. Despite a growing interest by the research community and particularly by national metrology institutes (NIMs) to develop a six-port based vector network analyser (VNA), the heterodyne architecture of modern VNAs has supplanted the six-port technology. This failure is mainly attributed to limited dynamic range, poor frequency range of operation and heavy mathematical calibration procedures. Since then, it is well admitted the six-port technology must be thought as low-cost and low-power solution to address peculiar application [2]. Nevertheless, emergent sensing applications requiring low carbon footprint paves the way for revisiting the six-port technology [3], [4], [5], [6], [7], [8]. RF-2S research team at IEMN contributed to the dissemination of the six-port technology in various applications [9], [10], [11], [12], [13], [14], [15].

The recent improvement of signal processing can benefit to the six-port technology for increasing the measurement performance by appropriate modelling taking into account frequency limitations imposed by microstrip or coplanar waveguide (CPW) design.

In this section, we demonstrate an extension considering a low-cost Epoxy printed circuit board (PCB) passive six-port junction designed and optimized at 2.45 GHz. this latter is associated to coaxial HP broadband power detectors. Later in this section, simulation of the ideal six-port junction is run on Keysight Advanced Design System (ADS) software to provide ideal output as a function of the phase-shift between the LO and RF signals. After, experiments considering the microstrip six-port IQ demodulator are performed in the frequency range 500 MHZ – 6 GHz. a modelling based on Fourier analysis is proposed to express the measured DC voltages as a function of I and Q components related to the complex ratio $Z = I + jQ$ between the LO and the RF signals. By introducing second Fourier order terms in the modelling, deviations from the ideal six-port junction are taken into account. The resolution of the inverse problem, i.e. retrieve of the I and Q components from the measured voltages, is exemplary shown to validate the method proposed.

5.2.2 Six-port reflectometry

In [16], author gives the basic notions behind the six-port reflectometry. The six-port technique is based on network analysis and allows complex impedances measurements. The "six-port reflectometry" gets its name from the measurement of a reflection coefficient. The six-port reflectometry relies on power measurement, followed by mathematical analysis of the measured data to obtain the reflection coefficient. Figure 5.5 illustrates the six-port reflectometry technique. The reference RF signal is injected through reference port 1 and powers the six-port network. The DUT is connected to port 2. The reflection coefficient of the DUT is given by:

$$\Gamma = \frac{b_2}{a_2} \tag{5.36}$$

The remaining ports are connected to power detectors P_3 to P_6. Each power detector measures the linear superposition of the a_2 and b_2 waves. It is possible to obtain the reflection coefficient

Γ after a calibration procedure (with known or partially known loads) using the four measured powers P_3, P_4, P_5, and P_6.

The six-port reflectometer based on guided structures as suggested by G. Engen are the most used reflectometers. They consists of directional couplers (90 ° or 180 °) and/or power dividers. Figure 5.6 shows the reflectometer presented by G. Engen [1]. The passive part is made of three 90 ° couplers, one 180 ° coupler and a 6 dB coupler. On the other hand, the double six-port network analyzer measure the four S-parameters S_{ij} of a 2-port network. Initiated in 1977 by C. A. Hoer [17] [18], it consists of a pair of six-port reflectometer, a power divider and a variable phase shifter (Figure 5.7). The RF signal powers simultaneously the six-port networks 1 and 2 through the power divider. Port 1 measure the complex ratio $\Gamma_1 = b_1/a_1$ in the reference plans 1. In the same way, port 2 measures $\Gamma_2 = b_2/a_2$ in the reference plane 2. Γ_1 and Γ_2 translate the two waves propagating in two opposite directions. The relationships between Γ_1 and Γ_2 and the S-parameters are:

$$\Gamma_1 = \frac{b_1}{a_1} = S_{11} + S_{12}\frac{a_2}{a_1} \tag{5.37}$$

$$\Gamma_2 = \frac{b_2}{a_2} = S_{22} + S_{21}\frac{a_1}{a_2} \tag{5.38}$$

By eliminating the ratios a_2/a_1, we can write:

$$\Gamma_2 S_{11} + \Gamma_1 S_{22} - \Delta = \Gamma_1 \Gamma_2 \ with\ \Delta = S_{11}S_{22} - S_{12}S_{21} \tag{5.39}$$

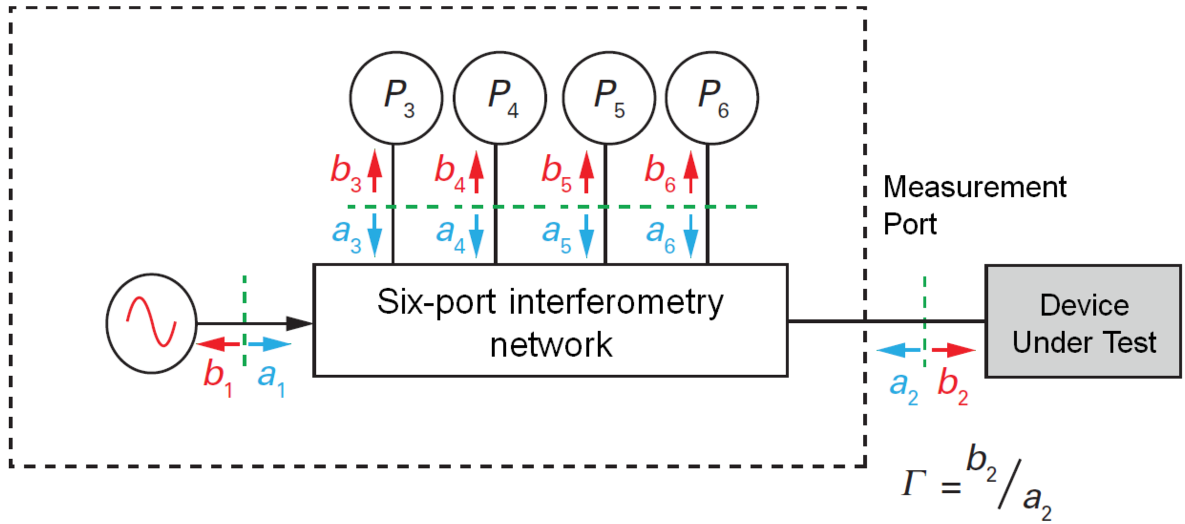

Figure 5.5 Six-port reflectometry technique [16].

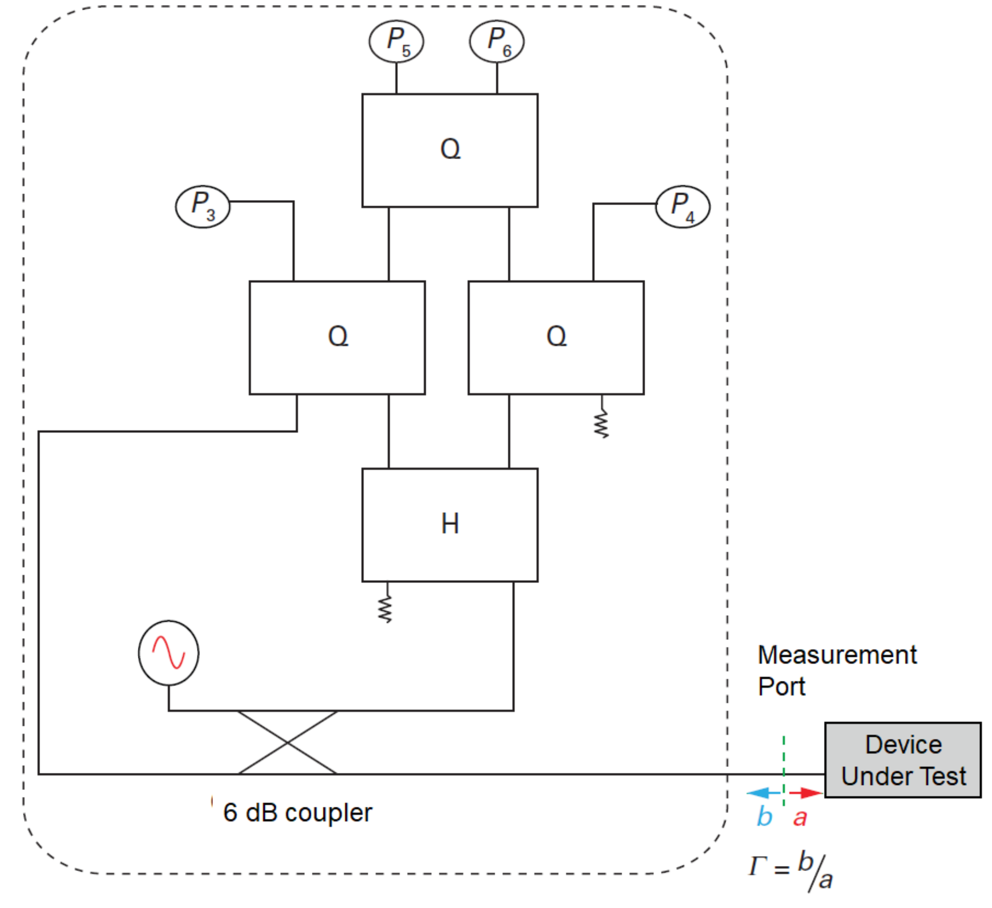

Figure 5.6 Double reactive couplers based six-port reflectometer [16].

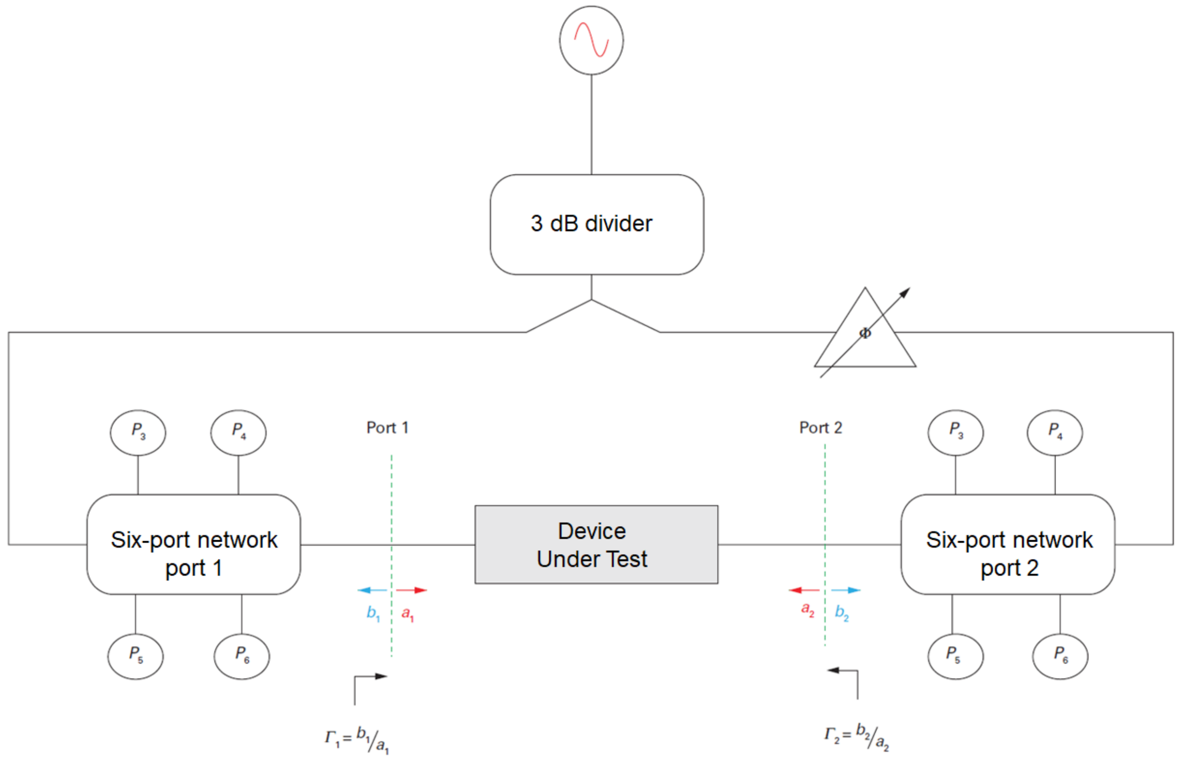

Figure 5.7 Double six-port network analyzer [16].

5.2.3 The direct problem equation

It is possible to express interest variable using the measured powers of the four power detectors of the six-port reflectometer. We can write the measured power of the detectors considered perfectly adapted to the six-port network as:

$$P_i = b_i \times b_i^* = (A_i a_2 + B_i b_2) \times (A_i a_2 + B_i b_2)^* \, for \ i = 3, \dots, 6 \tag{5.40}$$

Considering the magnitudes and phase-shifts of the complex quantities $a_1, b_2, A_i, and \ B_i$, we get:

$$P_i = |A_i|^2|a_2|^2 + |B_i|^2|b_2|^2$$
$$+2|A_i||a_2||B_i||b_2| \cos(arg(A_i) + arg(a_2) - arg(B_i) - arg(b_2)) \tag{5.41}$$
$$for \ i = 3, \dots, 6$$

By introducing the reflection coefficient to be measured, the equation system becomes:

$$P_i = |A_i|^2|b_2|^2 \left(|\Gamma|^2 + \frac{|B_i|^2}{|A_i|^2} + 2\frac{|B_i|}{|A_i|}|\Gamma| \cos(arg(A_i) - arg(B_i) + arg(\Gamma)\right) \tag{5.42}$$
$$for \ i = 3, \dots, 6$$

Which finally gives:

$$P_i = |A_i|^2|b_2|^2(|\Gamma|^2 + |q_i|^2 + 2|q_i||\Gamma| \cos(arg(q_i) - arg(\Gamma))) \, for \ i = 3, \dots, 6 \tag{5.43}$$

The model given in (5.43) does not take into account eventual imperfections of the reflectometer. Hence, we can re-write the four power P_i as a function of the phase shift Φ of Γ for a constant magnitude of Γ as follow:

$$P_i = a_{i0} + a_{i1}|\Gamma|^2 + a_{i2}|\Gamma| \sin(\Phi) + a_{i3}|\Gamma| \cos(\Phi)$$
$$+a_{i4}|\Gamma|^2 \sin(2\Phi) + a_{i5}|\Gamma|^2 \cos(2\Phi) + a_{i6}|\Gamma|^3 \sin(3\Phi) + a_{i7}|\Gamma|^3 \cos(3\Phi) \tag{5.44}$$
$$for \ i = 3, \dots, 6$$

Here, the harmonic distortions of the 2nd order (terms in 2Φ) and 3rd order (terms in 3Φ) are taken into account. The coefficients a_{ij} $(i = 3, \dots, 6 \ and \ i = 0, \dots, 7)$ are complex quantities intrinsic to the six-port reflectometer. More detail about the mathematical development of the six-port formulation can be found in [19].

5.2.4 Theoretical and simulation analysis

The structure used in this work is a microstrip six-port interferometer or a six-port IQ demodulator. It consists of a passive structure built up with a Wilkinson power divider and three hybrid branchline couplers (Figure 5.8). The structure has six ports: two input ports 1 and 2 and four output ports 3, 4, 5, and 6.

The terms $a_1(t)$ and $a_2(t)$ represents the reference incident pseudo-waves (LO and RD signals) given by:

$$a_1(t) = A_1 e^{j(2\pi f t + \phi_1)} \tag{5.45}$$

$$a_2(t) = A_2 e^{j(2\pi f t + \phi_2)} \tag{5.46}$$

Where A_i $(i = 1, 2)$ and $\phi_i (i = 1, 2)$ are the amplitudes and absolute phases of the inputs signals respectively.

The signals $b_i(t)$ $(i = 3, \ldots, 6)$ are the emergent pseudo-waves at remaining output arms. For sake of clarity, the term $e^{j\pi 2 f t}$ is removed in the following expressions:

$$b_3 = \frac{1}{2}\left[a_1 + a_2 e^{-j\frac{\pi}{2}}\right] \tag{5.47}$$

$$b_4 = \frac{1}{2}\left[a_1 e^{-j\frac{\pi}{2}} + a_2\right] \tag{5.48}$$

$$b_5 = \frac{1}{2}\left[a_1 e^{-j\frac{\pi}{2}} + a_2 e^{-j\frac{\pi}{2}}\right] \tag{5.49}$$

$$b_3 = \frac{1}{2}\left[a_1 + a_2 e^{-j\pi}\right] \tag{5.50}$$

The theoretical detected output powers P_i $(i = 3, \ldots, 6)$ are given by:

$$P_3 = b_3 \cdot b_3^* = \frac{1}{4}[A_1^2 + A_2^2 + 2A_1 A_2 \, sin(\Delta\phi)] \tag{5.51}$$

$$P_4 = b_4 \cdot b_4^* = \frac{1}{4}[A_1^2 + A_2^2 - 2A_1 A_2 \, sin(\Delta\phi)] \tag{5.52}$$

$$P_6 = b_5 \cdot b_5^* = \frac{1}{4}[A_1^2 + A_2^2 + 2A_1 A_2 \, cos(\Delta\phi)] \tag{5.53}$$

$$P_6 = b_6 \cdot b_6^* = \frac{1}{4}[A_1^2 + A_2^2 - 2A_1 A_2 \, cos(\Delta\phi)] \tag{5.54}$$

Where $\Delta\phi = \phi_1 - \phi_2$ is the phase shift between the two input LO and RF signals.

The ideal six-port junction has been designed in Keysight ADS software. In Figure 5.9, we present the four detected powers as a function of the phase-shift $\Delta\phi$. Figure 5.9 shows that the output signals are phase-shifted by $\frac{\pi}{2}$ according to (5.51) - (5.54). Although this ADS simulation does not bring any new information, this implementation will be used in future studies to identify the impact of S-parameters of the Wilkinson power divider and hybrid couplers on the simulated output powers. In other words, mismatching, isolation, transmission losses and phase-shifts induced by the microstrip circuitry will be studied separately.

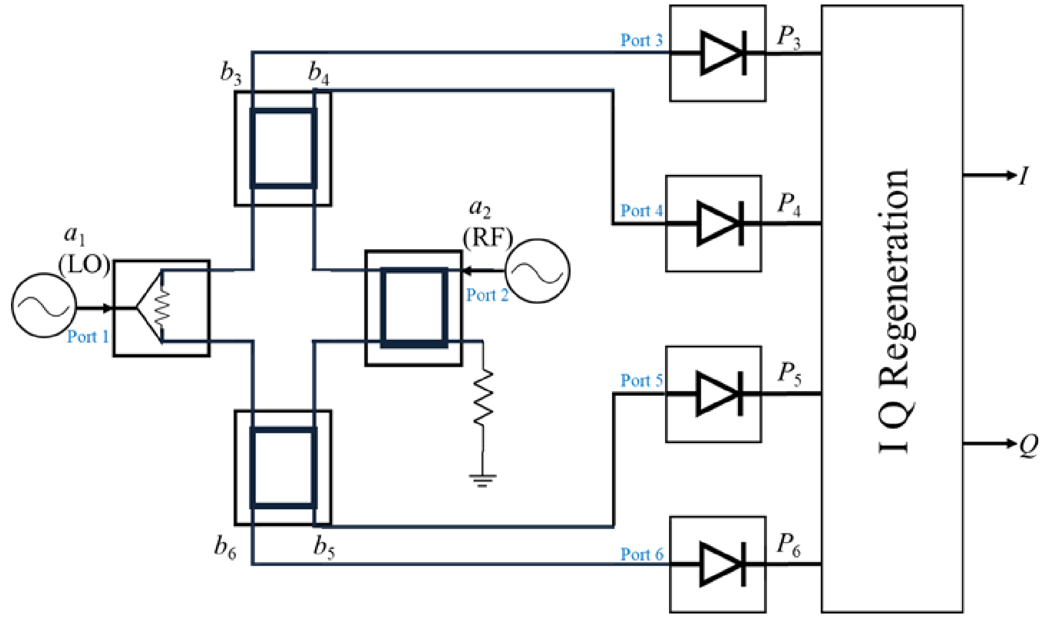

Figure 5.8 Typical six-port IQ demodulator / interferometer comprising a power divider, three hybrid couplers and four power detectors.

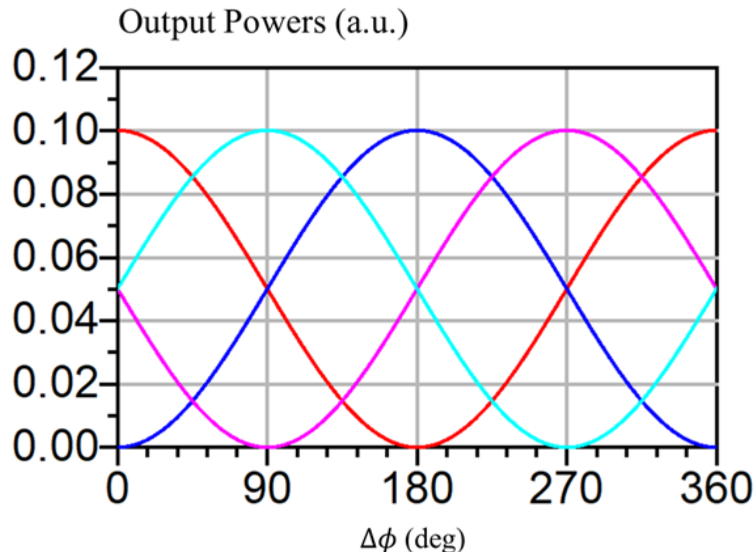

Figure 5.9 Simulated detected powers P_3 to P_6 as a function of the phase-shift $\Delta\phi$ between the LO and the RD signals (_ P_3 _ P_4 _ P_5 _ P_6).

5.2.5 Experimental six-port junction

The experimental set-up is depicted in Figure 5.10. Two externally synchronized frequency synthesizers and a digital scope are used to generate the RF and LO signals and to collect the detected voltages respectively. To set the phase-shift $\Delta\phi$ between the LO and the RF signals, a 1 kHz beat frequency difference between the two input signals is considered. Figure 5.11 shows the six-port ID demodulator realized on microstrip technology at 2.45 GHz. Table 5.9 summarizes the system configuration.

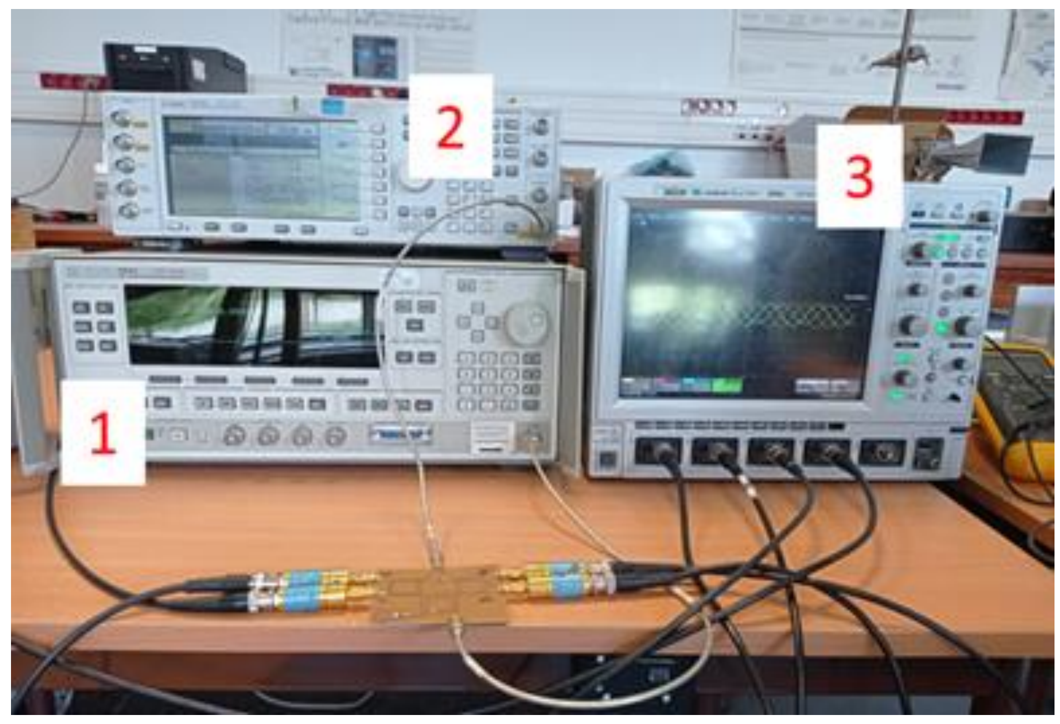

Figure 5.10 Experimental set-up including a six-port IQ demodulator realized on microstrip technology at 2.45 GHz (1. LO signal 2. RF signal 3. Digital score).

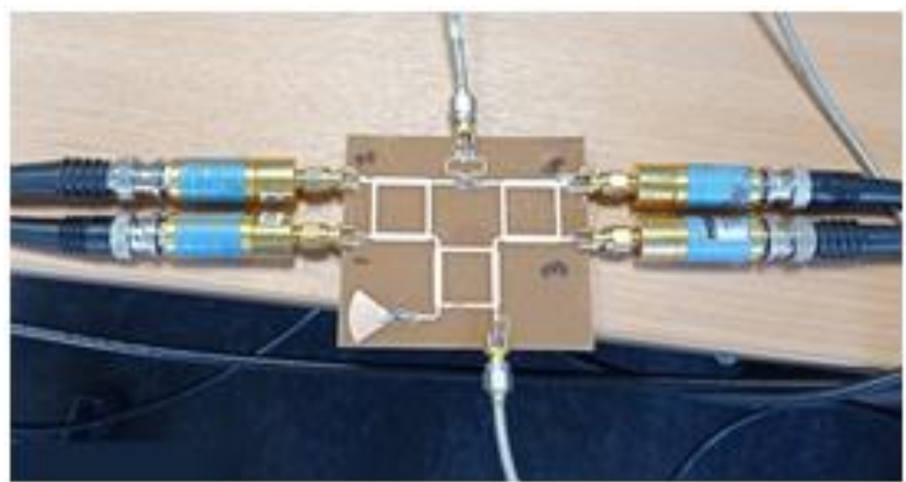

Figure 5.11 The six-port IQ demodulator

Table 5.9 Experimental set-up configuration.

Element	Frequency	Power
LO signal	2.45 GHz	-15 dBm
	6 GHz	
	500 MHz	
RF signal	2.449 999 GHz	- 15 dBm
	5.999 999 GHz	
	499.999 MHz	

5.2.6 Measurement protocol and Modelling

The main objective of this work is to extend digitally the operation frequency range of the six-port demodulator initially designed at 2.45 GHz. As a demonstration, the proposed Fourier analysis is tested at 6 GHz and 500 MHz. The second order Fourier model expressed as a function of the I and Q components is given by:

$$V_1 = a_{10} + a_{11}.I^2 + a_{12}.Q^2 + a_{13}.I + a_{14}.Q + a_{15}.I.Q \quad (5.55)$$

$$V_2 = a_{20} + a_{21}.I^2 + a_{22}.Q^2 + a_{23}.I + a_{24}.Q + a_{25}.I.Q \quad (5.56)$$

$$V_3 = a_{30} + a_{31}.I^2 + a_{32}.Q^2 + a_{33}.I + a_{34}.Q + a_{35}.I.Q \quad (5.57)$$

$$V_4 = a_{40} + a_{41}.I^2 + a_{42}.Q^2 + a_{43}.I + a_{44}.Q + a_{45}.I.Q \quad (5.58)$$

The terms a_{ij} $(i = 1, \ldots, 4 \; and \; j = 0, .., 5)$ are real calibrations coefficients that make the link between the measured data (voltages V_1 to V_4) and the parameters of interest (I and Q). In the following, we describe the method including three different steps. This includes the modelling of the direct problem and the resolution of the inverse problem.

STEP 1: The output voltages of the power detectors $V_1, V_2, V_3 \; and \; V_4$ are recorded as a function of $\Delta\phi$.

STEP 2: The calibration consists to determine the calibration coefficients using the Matlab® Application (APP) Curve Fitting.

STEP 3: A 2D Newton-Raphson algorithm implemented in Matlab® software is used for the determination of the I and Q components from the measured voltages.

To solve the system in (5.55) - (5.58), we need at least two equations. In this work, we use V_1 and V_3. More pairs of equations might give more information such as measurement uncertainty. Another possibility is to consider $(V_1 - V_2)$ and $(V_3 - V_4)$ as commonly found in six-port applications to eliminate the rectified terms. In this work, we do not to compute all possible pairs, the main objective being to prove the validity of our approach. Investigation of the other possibilities and improving the performance of the method will be done in future works.

The equation system is reduced to:

$$a_{10} + a_{11}.I^2 + a_{12}.Q^2 + a_{13}.I + a_{14}.Q + a_{15}.I.Q - V_1 = 0 \quad (5.59)$$

$$a_{30} + a_{31}.I^2 + a_{32}.Q^2 + a_{33}.I + a_{34}.Q + a_{35}.I.Q - V_3 = 0 \quad (5.60)$$

5.2.7 Experimental results

The fours output voltages measured by the digital scope are given in Fig. 4 for the test frequencies 2.45 GHz, 6 GHz and 500 MHz. Figure 5.12(a) shows that the four traces are in quadrature at the test frequency 2.45 GHz. As expected, the measured data are close to their simulation counterparts. At the test frequency 6 GHz, the voltage range becomes smaller, in

accordance with increased propagation losses on the six-port junction (optimized at 2.45 GHz). In addition, the sinusoidal signatures are distorted and are not in quadrature. Same conclusions can be drawn for the test frequency 500 MHz [Figure 5.12(c)]. In addition, the phase-shift between the four curves is drastically reduced due to high guided wavelength of operation at 500 MHz. From the detected voltages, the calibration coefficients are computed according to the STEP 2. The calibration coefficients are summarized in Table 5.10 for the three test frequencies. The determination coefficients R_2 close to 1 demonstrate the performance of the modelling.

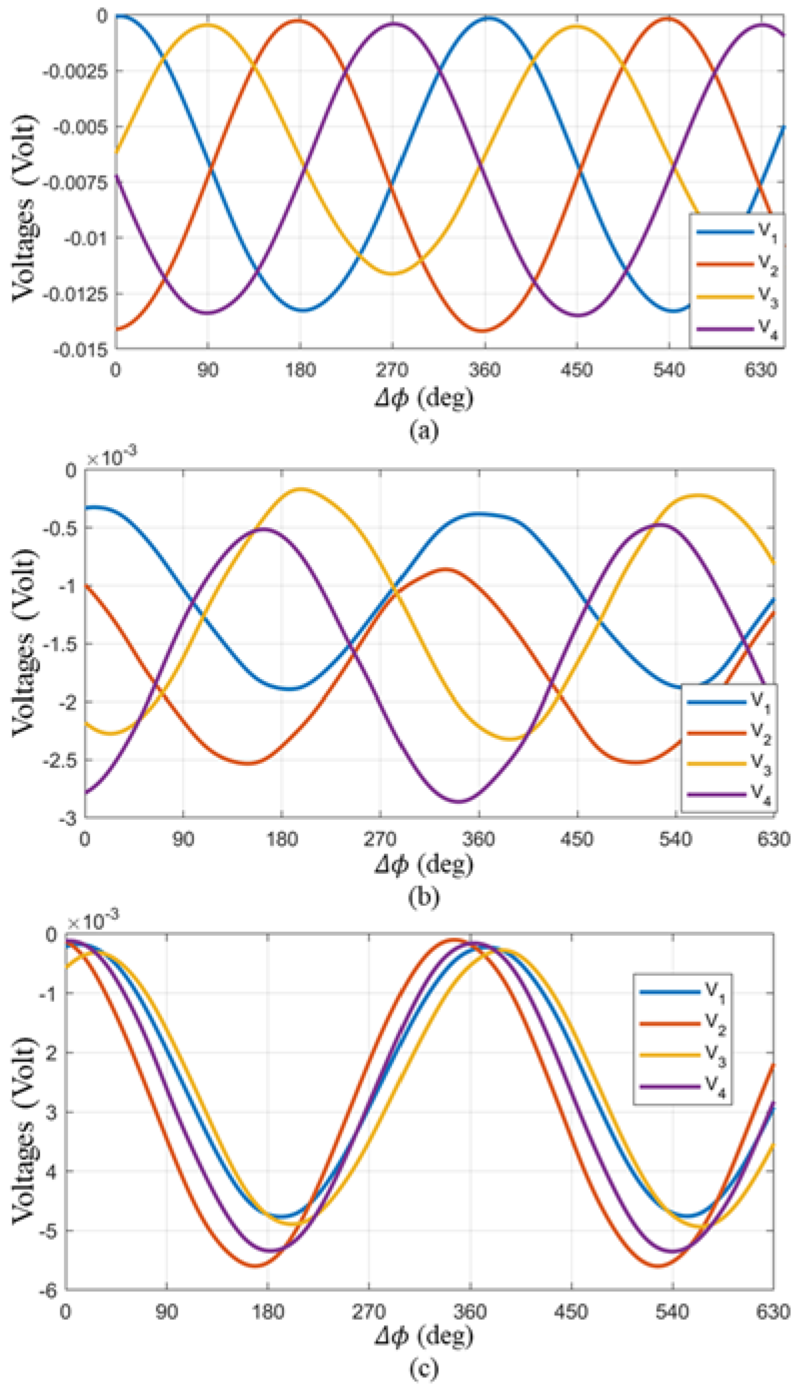

Figure 5.12 Detected voltages as a function of the phase-shift $\Delta\phi$ at different operating frequencies.

Table 5.10 Calibration coefficients at 2.45 GHz, 6 GHz, and 500 MHz.

Coefficient	Parameter	Frequency		
V_1		2.45 GHz	6 GHz	500 MHz
a_{10}	1	-0,0037 V	0.00086 V	-0.0013 V
a_{11}	I^2	-0,0029 V	-0.0019 V	-0.0011 V
a_{12}	Q^2	-0,0033 V	-0.0019 V	-0.001 V
a_{13}	I	0,0065 V	0.0007 V	0.0022 V
a_{14}	Q	0,00047 V	76 µV	0.0004 V
a_{15}	I×Q	0,00012 V	19 µV	31 µV
R^2		1	0.9996	1
Coefficient	Parameter	Frequency		
V_3		2.45 GHz	6 GHz	500 MHz
a_{30}	1	-0,003 V	0.00086 V	-0.0013 V
a_{31}	I^2	-0,002 V	-0.00209 V	-0.0012 V
a_{32}	Q^2	-0,002 V	-0.002 V	-0.0011 V
a_{33}	I	67 µV	-0.0009 V	0.002 V
a_{34}	Q	0,005 V	-0.0003 V	0.0009 V
a_{35}	I×Q	0,0001 V	-16 µV	43 µV
R^2		1	1	0.9998

The 2-D curve fitting model based on the 2nd order Fourier analysis is illustrate graphically in Figure 5.13 for the test frequencies 2.45 and 6 GHz.

Figure 5.13 is instructive as it shows graphically the voltage distortion induced by the frequency of operation. One interesting point concerns the voltage distortion seem even at the optimized frequency 2.45 GHz induced mainly by the deviation from quadratic law of the power detectors. Indeed, a preliminary linearization of the power detectors is usually considered. In this work, we demonstrate that the proposed modelling takes into account the imperfections brought by the power detection as part of the whole calibration process. At this point, we validate the resolution of the direct problem and calibration.

From the calibration coefficients, we can now solve the system given in (5.59) - (5.60) using the Newton-Raphson resolution method and hence address the inverse problem. To present a clear picture in terms of measurement performance, we compute separately the mean and maximum amplitude and phase-shift errors obtained on the determination of the complex impedances (that represent the complex ratio between the RF and LO signals) defined by

$$|Z| = \sqrt{I^2 + Q^2} \tag{5.61}$$

$$\phi_Z = atan\left(\frac{Q}{I}\right) \tag{5.62}$$

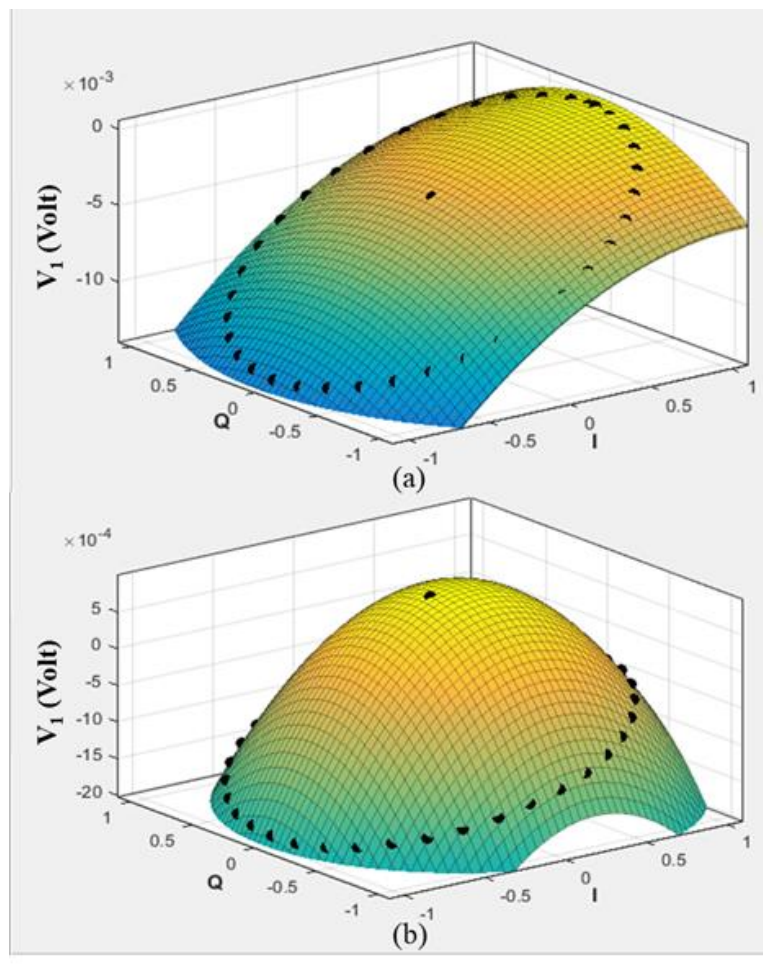

Figure 5.13 Curve fitting based on the 2nd order Fourier analysis for V_1 at (a) 2.45 GHz and (b) 6 GHz.

From Table 5.11, the mean errors in the order of 10^{-8} and 10^{-6} degrees for amplitude and phase-shift respectively demonstrate the performance of the method proposed for the frequencies 2.45 GHz and 500 MHz. For the upper frequency limit, i.e. 6 GHz, the mean errors reach values in the order of 10-4 and 0.2 degrees for amplitude and phase-shift respectively. Whereas the performance still remain good given the limited resource needed to address IQ demodulation, an extension of the modelling at the 3rd order will be investigated in future studies to further reduce the error between measurement and modelling.

Table 5.11 Mean and maximum error on the complex impedance Z.

Frequency	Mean Magnitude Error	Max Magnitude Error
2.45 GHz	9.76e-09	0,341e-07
6 GHz	0,22e-04	6.55e-04
500 MHz	29e-09	0,93e-06
Frequency	Mean Magnitude Error	Max Magnitude Error
2.45 GHz	0,35 µ°	11,78 µ°
6 GHz	0.176 °	0.904 °
500 MHz	79µ °	2,6µ °

5.3 Impedance Standard Substrate EM-Simulation for On-wafer GSG probing

S-parameter measurements and calibration techniques come as a critical step in understanding device behaviour at high frequencies, especially for on-wafer devices with extreme impedances [20], [21]. Electromagnetic simulation plays a significant role in this understanding. Simulation tools allow for virtual analysis of devices behaviour, hence, potentially helping optimize designs and predict technical locks before physical implementation. Authors in [22] and [23] explored some guidelines for the design and characterization of calibration substrates. In this work, we used a scanning electron microscope (SEM) to obtain the physical dimensions of the 101-190 C Impedance Standard Substrate (ISS) from FormFactor™. The ISS was implemented in CST® Studio Suite. Lastly, we simulated the reflection coefficient of a non-perfect 50 Ω load and compared it to actual measurements.

5.3.1 Imaging

In order the accurately characterize and understand the properties of the 101-190 C Impedance Standard Substrate (Figure 5.14), the latter was analysed using a scanning electron microscope (SEM), which allowed for high-resolution imaging and precise measurement of the physical dimensions of the ISS. Figure 5.15 illustrate the different structures found on the ISS. Considering the complexity of the ISS, we decided to initially focus on studying the 50 Ω load structure. The main objective of this analysis was to compare the measured reflection coefficient of the load structure with the simulated values obtained using CST® Studio Suite. This comparative work helped to validate the accuracy and the reliability of the simulation model. It comes as an important step of the main objective, which aims to understand the impact of the geometries of the structures and the radiofrequency probes' alignment on those structures during the calibration process.

Figure 5.16 shows the dimensions of the load's sheet resistance. The dimensions of the sheet resistance are critical parameters that can significantly influence its electrical performances. Therefore, extra care was taken when measuring it. Lastly, we used a profilometer in order to obtain the thickness of the different structures.

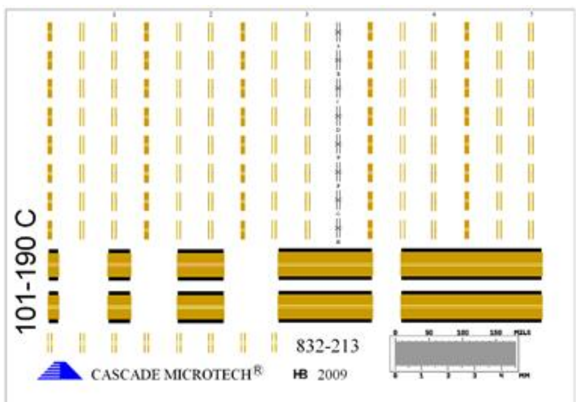

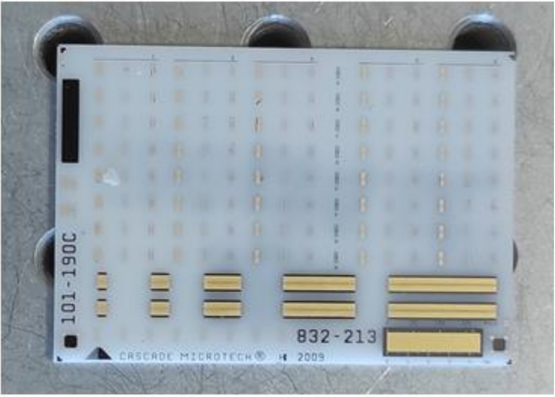

Figure 5.14 101-190 C Impedance Standard Substrate.

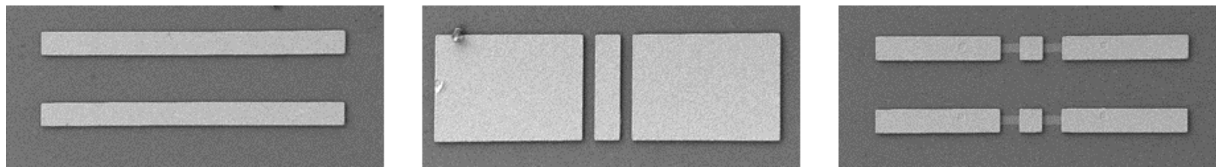

Figure 5.15 SEM images of short (left), thru (middle) and load (right) structures of the 101-190 C Impedance Standard substrate.

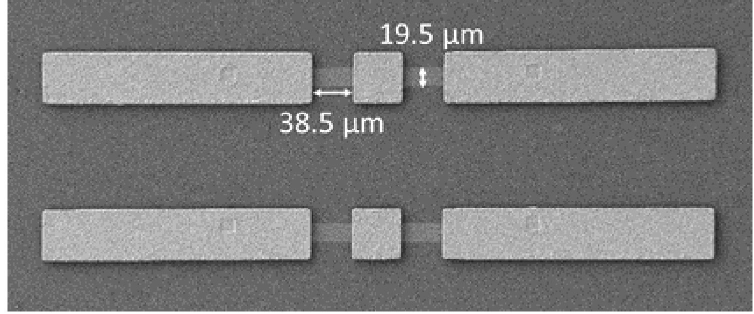

Figure 5.16 Dimensions of the sheet resistance on an ISS load structure.

5.3.2 EM modelling

Here, we describe how the ISS was implemented in the electromagnetic simulation software CST® Studio Suite 2021. As described in the previous section, all the physical dimensions needed to construct the ISS were obtained. Hence, a complete ISS was implemented in the software. Table 5.12 summarizes the materials used for each part of the design as well as the electrical properties of those materials. Figure 5.17 represents the 101-190 C ISS as designed in CST®.

Table 5.12 Material properties of the different part of the ISS.

	Substrate	Resistance	Standards
Material	Alumina	Ohmic sheet	Gold
Epsilon	9.9	--	--
Electrical conductivity [S/m]	--		4.561×10^{7}
Resistance	--	46 Ohm/sq *	--
Thickness	635 µm	--	4.4 µm

**the resistance of the ohmic sheet should be 50 Ω when perfectly flat. However, when representing the ohmic sheet with the dimensions we obtained using the SEM, the simulated response did not match the measured response. In addition, using a voltmeter, we measure a value of 46 Ω for this specific resistance (most of the resistances were 50 Ω). Hence, we defined a 46 Ω ohmic sheet to match the reality.*

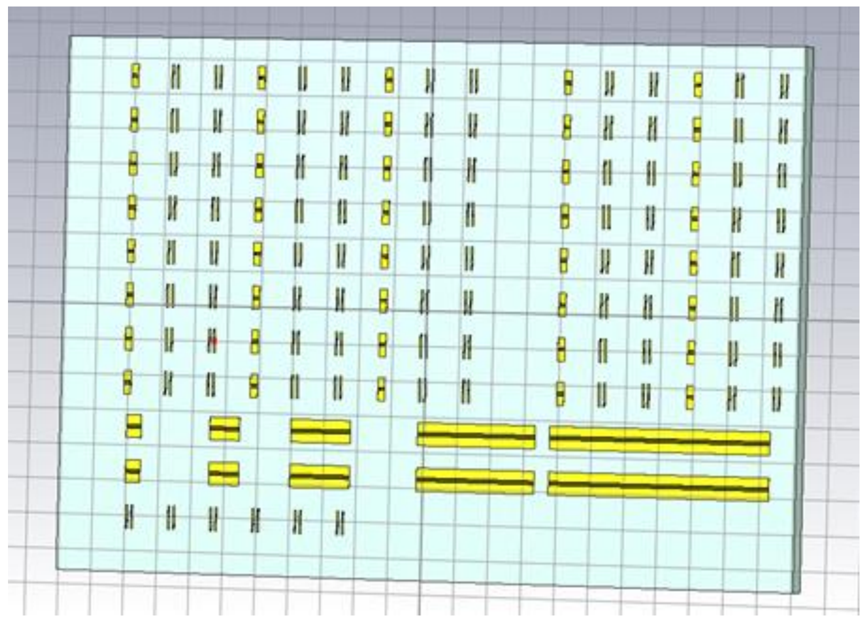

Figure 5.17 The 101-190 Impedance Standard Substrate design in CST Studio Suite.

In order to simplify the simulation and optimize the simulation time, we modelled a portion of interest from the ISS consisting of a 1 cm x 1 cm alumina substrate and the load structure as shown in Figure 5.17. Figure 5.18 illustrate the structure that has been simulated.

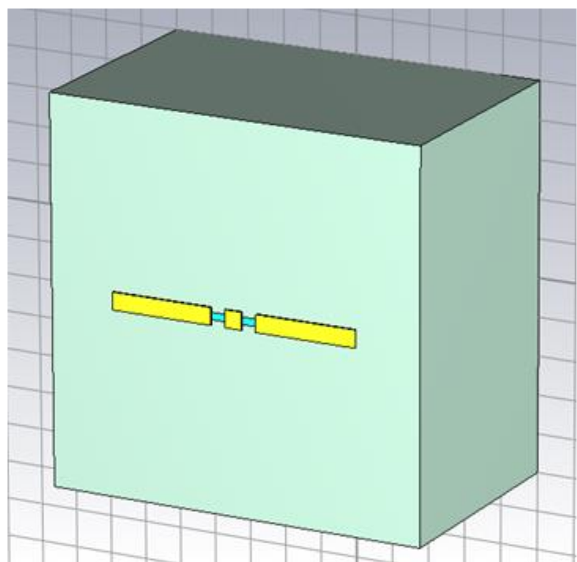

Figure 5.18 Portion of the ISS consisting of a single load structure on alumina substrate.

5.3.3 Simulation

Simulation parameters are summarized in Table 5.13. The waveguide port was defined according to the definitions found in the literature about port definition for ungrounded coplanar lines as shown in Figure 5.19 [24]. Figure 5.20 represents the waveguide port as defined in CST®. Here, we chose to orient the parallel to the structure. We believe it is the best way to represent orientation of the wave transmitted from an on-wafer measurement probe. It has to be noted that the port definition can highly influence the results of the simulation. A port definitions study should be conducted in order to optimise the results. Here, the main objective was to focus on the characterisation of the load structure.

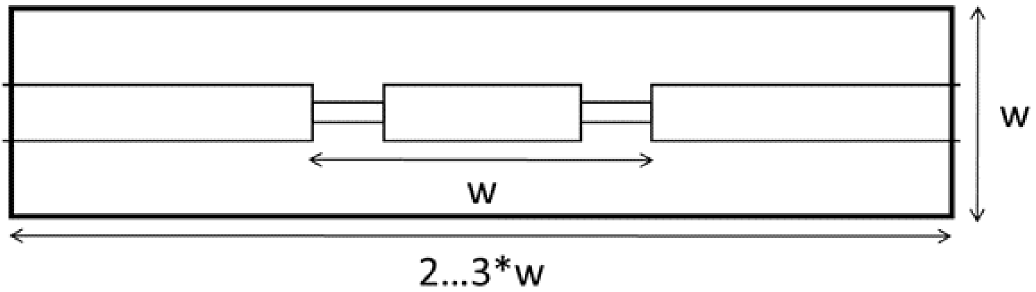

Figure 5.19 Waveguide port definition.

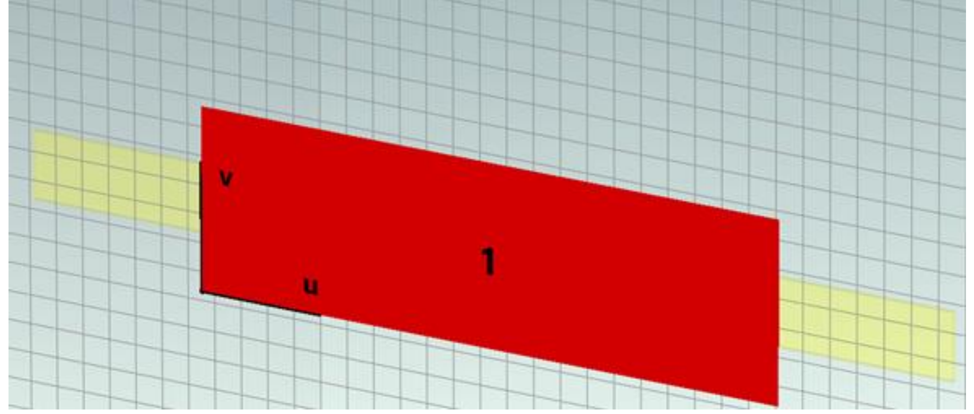

Figure 5.20 The waveguide port as defined in CST®.

Table 5.13 Simulation parameters

Solver	Frequency domain
Frequency	100 kHz – 50 GHz
Adaptive mesh	Enabled

5.3.4 Analysis

Figure 5.21 shows the reflection coefficient of the 50 Ω load obtained from the CST simulation as presented in the previous section. Figure 5.22 shows the reflection coefficient obtained from measuring the load with a vector network analyser. After measuring multiple load, we observed that above 5 GHz, no difference in the measured reflection coefficient was observed, even when comparing loads with very distinct DC resistance values (50 Ω, 62 Ω, 120 Ω). Indeed, as the VNA was not calibrated, at higher frequencies, influence of the instrument, especially the cables, start to be bigger that the response of the measured loads. Hence, comparison was done at lower frequencies. At 5 GHz, the measured reflection coefficient was $-28.33\,dB$ against $-28.39\,dB$ for the simulation. At 2 GHz, we obtain $-28.21\,dB$ and $-29.90\,dB$ for the measured and the simulated reflection coefficient respectively. Although some differences still exist between the measured response and the simulation results, the design provide accurate results overall.

Figure 5.23 shows the electrical and the magnetic fields respectively obtained from the simulation. We can observe the both fields are uniformly and symmetrically distributed throughout the structure. Regarding the electrical field, we can see that the wave if concentrated around the central element of the coplanar line and the resistances on each side

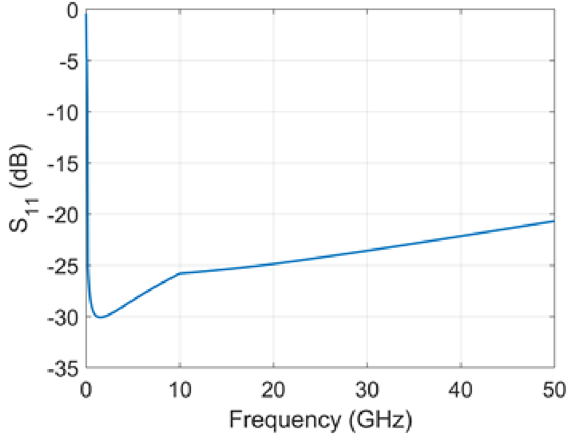

Figure 5.21 Reflection coefficient of the 50 Ω load obtained from the CST simulation.

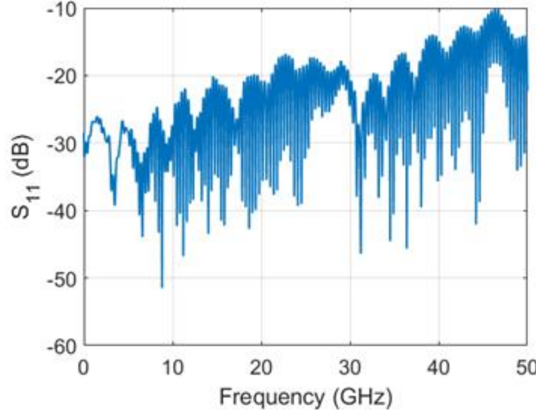

Figure 5.22 Reflection coefficient obtained from measuring the load with a vector network analyser.

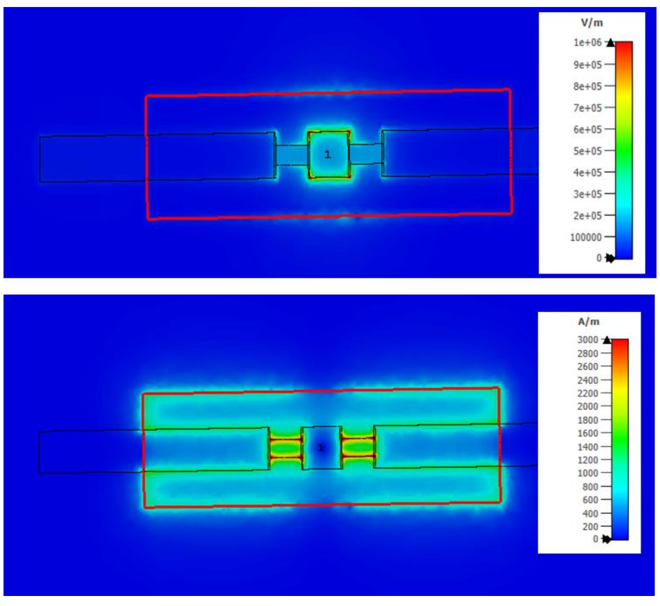

Figure 5.23 Electrical field and magnetic field respectively obtained from a simulated load structure of the 101-190 C ISS.

Multiple conclusions can be drawn from this work. First, it is important to note that results depend highly on the geometry of the resistance and the coplanar line. Here, we defined our resistance as an ohmic sheet. The ohmic sheet is considered perfectly flat. In reality, it may not be the case. Resistances present on the ISS might have a certain thickness. This thickness can change the electrical properties of the load structure. In order to complete this work, the resistance should be analysed using a profilometer in order to obtain its exact thickness and adjust the simulated design accordingly. Another conclusion that can be made from this study is related to the choice of the calibration structures. While calibrating, the calibration structures should be verified through their radiofrequency response and their DC values. As a side work, all loads from the used ISS were measure using a voltmeter. Although almost all the loads had a 50 Ω resistance value or close, some loads did not. This could be caused by deterioration of the ISS.

A future study will be dedicated to designing and simulating an Infinity GSG probe with the ISS. Simulation will help evaluate the influence of the probe positioning on the calibration standards. Indeed, using the reflection coefficient obtained in the simulation, it would be possible to compute a 1-port or a 2-port calibration algorithm. Design of the GSG probe in microstrip line have been realised in CST® using SEM images of the probe (Figure 5.24) However, simulation configuration still need to be correctly chosen in order to obtain accurate results. Figure 5.25 shows the design of the GSG probe in CST®.

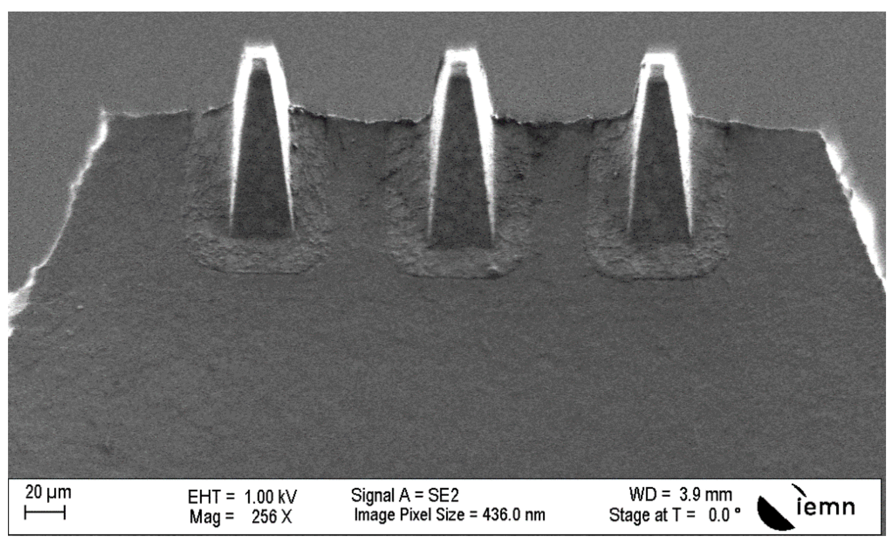

Figure 5.24 SEM picture of the Infinity GSG probe with 100 µm pitch captured at IEMN laboratory.

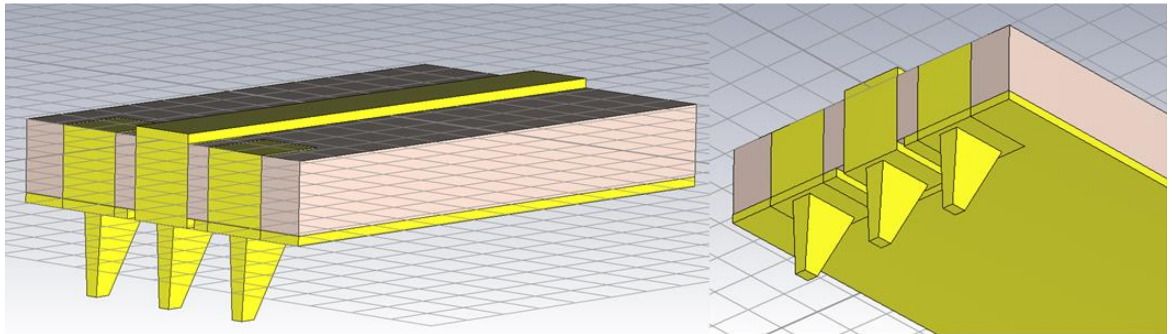

Figure 5.25 CST design of a microstrip line based GSG probe with 100 µm pitch.

5.4 Conclusion

In this chapter, we presented some complementary works that have been performed in order to enhance on-wafer characterization techniques.

We studied the instrumental noise of two types of VNAs, a compact 2-port Streamline and a 2-port PNA. We revealed that each model performs better in certain configurations (IFBW and measurement frequency). In particular, the Streamline appears to perform better in transmission.

A Fourier analysis has been proposed to model the electrical response of the six-port IQ demodulator. By introducing 2nd order Fourier term, imperfections brought by the technology is taken into account mathematically, given the possibility to extend the frequency bandwidth without additional hardware requirement. As a demonstration, a frequency range extension of 250% is exemplary demonstrated considering a low-cost and fully passive six-port IQ demodulator fabricated on standard PCB.

The 101-190 Impedance Standard Substrate (ISS) from FormFactor™ has been designed and simulated in CST® Suite Studio. Electrical properties of a 50 Ω load from the ISS were measured in the direct current (DC) and the radiofrequency (RF) ranges using a voltmeter and a vector network analyser (VNA) respectively. This works come as a preliminary study to improve the on-wafer calibration procedure for precise GSG probing.

5.5 References

[1] G. F. Engen, ‘The Six-Port Reflectometer: An Alternative Network Analyzer’, *IEEE Trans. Microwave Theory Techn.*, vol. 25, no. 12, pp. 1075–1080, Dec. 1977, doi: 10.1109/TMTT.1977.1129277.

[2] K. Haddadi, C. Loyez, S. Lallemand, S. Gong, and A. Koelpin, ‘Status of Six-Port Technology for Wireless Sensing Applications’, in *2018 International Conference on Electromagnetics in Advanced Applications (ICEAA)*, Cartagena des Indias: IEEE, Sep. 2018, pp. 269–271. doi: 10.1109/ICEAA.2018.8520535.

[3] L. Gerardi *et al.*, *A new six-port circuit architecture using only power dividers/combiners*. 2007, p. 44. doi: 10.1109/MWSYM.2007.380213.

[4] B. Boukari, E. Moldovan, S. Affes, K. Wu, R. Bosisio, and S. Tatu, *Six-port FMCW collision avoidance radar sensor configurations*. 2008, p. 000308. doi: 10.1109/CCECE.2008.4564544.

[5] Xinyu Xu, R. G. Bosisio, and K. Wu, ‘A new six-port junction based on substrate integrated waveguide technology’, *IEEE Trans. Microwave Theory Techn.*, vol. 53, no. 7, pp. 2267–2273, Jul. 2005, doi: 10.1109/TMTT.2005.850455.

[6] A. Koelpin, G. Vinci, B. Laemmle, D. Kissinger, and R. Weigel, ‘The Six-Port in Modern Society’, *Microwave Magazine, IEEE*, vol. 11, pp. 35–43, Jan. 2011, doi: 10.1109/MMM.2010.938584.

[7] G. Vinci *et al.*, ‘Six-Port Radar Sensor for Remote Respiration Rate and Heartbeat Vital-Sign Monitoring’, *IEEE Trans. Microwave Theory Techn.*, vol. 61, no. 5, pp. 2093–2100, May 2013, doi: 10.1109/TMTT.2013.2247055.

[8] S. O. Tatu, A. Serban, M. Helaoui, and A. Koelpin, ‘Multiport Technology: The New Rise of an Old Concept’, *IEEE Microwave*, vol. 15, no. 7, pp. S34–S44, Nov. 2014, doi: 10.1109/MMM.2014.2356149.

[9] K. Haddadi, H. El Aabbaoui, B. Gorisse, D. Glay, N. Rolland, and T. Lasri, ‘A Fully InP Monolithic Integrated Millimeter-Wave Reflectometer’, in *2006 European Microwave Conference*, Manchester: IEEE, Sep. 2006, pp. 703–706. doi: 10.1109/EUMC.2006.280998.

[10] K. Haddadi, M. M. Wang, K. Nouri, D. Glay, and T. Lasri, ‘Calibration and performance of two new ultra-wideband four-port-based systems’, *IEEE Transactions on Microwave Theory and Techniques*, vol. 56, pp. 3137–3142, 2008, doi: 10.1109/TMTT.2008.2007138.

[11] K. Haddadi, M. M. Wang, C. Loyez, D. Glay, and T. Lasri, ‘Four-Port Communication Receiver With Digital IQ-Regeneration’, *Microwave and Wireless Components Letters, IEEE*, vol. 20, pp. 58–60, Feb. 2010, doi: 10.1109/LMWC.2009.2035969.

[12] K. Haddadi and T. Lasri, ‘Formulation for Complete and Accurate Calibration of Six-Port Reflectometer’, *IEEE Transactions on Microwave Theory and Techniques - IEEE TRANS MICROWAVE THEORY*, vol. 60, pp. 574–581, Mar. 2012, doi: 10.1109/TMTT.2011.2181861.

[13] K. Haddadi and T. Lasri, ‘V-band two-tone continuous wave radar operating in monostatic/bistatic mode’.

[14] K. Haddadi, M. M. Wang, D. Glay, and T. Lasri, ‘A 60 GHz Six-Port Distance Measurement System with Sub-Millimeter Accuracy’, *Microwave and Wireless Components Letters, IEEE*, vol. 19, pp. 644–646, Nov. 2009, doi: 10.1109/LMWC.2009.2029744.

[15] K. Haddadi, C. Loyez, L. Clavier, D. Pomorski, and S. Lallemand, ‘Six-port reflectometer in WR15 metallic waveguide for free-space sensing applications’, in *2018 IEEE Topical Conference on Wireless Sensors and Sensor Networks (WiSNet)*, Anaheim, CA: IEEE, Jan. 2018, pp. 80–83. doi: 10.1109/WISNET.2018.8311570.

[16] K. Haddadi, ‘Mesure hyperfréquence des propriétés électromagnétiques de matériaux : 300 MHz à 300 GHz’, *Mesures et tests électroniques*, Dec. 2016, doi: 10.51257/a-v1-r1117.

[17] C. A. Hoer, ‘A Network Analyzer Incorporating Two Six-Port Reflectometers’, *IEEE Trans. Microwave Theory Techn.*, vol. 25, no. 12, pp. 1070–1074, Dec. 1977, doi: 10.1109/TMTT.1977.1129276.

[18] C. A. Hoer, ‘Performance of a Dual Six-Port Automatic Network Analyzer’, *IEEE Transactions on Microwave Theory and Techniques*, vol. 27, no. 12, pp. 993–998, Dec. 1979, doi: 10.1109/TMTT.1979.1129779.

[19] K. Haddadi, ‘SYSTEMES A BASE DE SIX-PORT EN GAMMES MICRO-ONDE ET MILLIMETRIQUE ET TECHNIQUES DE CALIBRAGE ASSOCIEES : APPLICATION A L’ANALYSE DE RESEAUX, AUX TELECOMMUNICATIONS ET CONTROLE NON DESTRUCTIF’, 2007.

[20] H. Happy, K. Haddadi, D. Theron, T. Lasri, and G. Dambrine, ‘Measurement Techniques for RF Nanoelectronic Devices: New Equipment to Overcome the Problems of Impedance and Scale Mismatch’, *Microwave Magazine, IEEE*, vol. 15, pp. 30–39, Jan. 2014, doi: 10.1109/MMM.2013.2288710.

[21] K. Daffe, G. Dambrine, F. Von Kleist-Retzow, and K. Haddadi, ‘RF wafer probing with improved contact repeatability using nanometer positioning’, in *2016 87th ARFTG Microwave Measurement Conference (ARFTG)*, San Francisco, CA, USA: IEEE, May 2016, pp. 1–4. doi: 10.1109/ARFTG.2016.7501967.

[22] M. Spirito, U. Arz, G. N. Phung, F. J. Schmückle, W. Heinrich, and R. Lozar, ‘Guidelines for the design of calibration substrates, including the suppression of parasitic modes for frequencies up to and including 325 GHz : EMPIR 14IND02’, p. 2385098 bytes, 31 pages, 2019, doi: 10.7795/530.20190424A.

[23] G. N. Phung and U. ArZ, ‘On the Influence of Metal Chucks in Wideband On-Wafer Measurements’, in *2022 98th ARFTG Microwave Measurement Conference (ARFTG)*, Las Vegas, NV, USA: IEEE, Jan. 2022, pp. 1–4. doi: 10.1109/ARFTG52954.2022.9844119.

[24] ‘Waveguide Port Overview’. Accessed: Oct. 03, 2023. [Online]. Available: https://space.mit.edu/RADIO/CST_online/mergedProjects/3D/special_overview/special_overview_waveguideover.htm

General conclusion

A new generation of on-wafer probe station was presented in this manuscript. The on-wafer station has been developed from scratch completely. This latter is based on piezo-electric nano-positioners to tackle issues related to inaccurate alignments of the RF probes onto the calibration / device substrate.

The hardware development as well as the software development were described. Each component of the station was acquired separately from different manufacturers and had to be studied separately. In term, the different components were brought together to build the station. In particular, we identify three categories: the mechanical part, the instrumentation part, and the software part. The mechanical part consists of the nano-positioners and the part that link it to the RF probes, the camera, the optical table and the optical bridge that links the two. The instrumentation part consists of the VNA, the RF probes and the calibration substrate. Finally, the software consists of the LabVIEWTM program that make the station automated.

Once the development was achieved, the first RF measurements were done. Through a repeatability study of the calibration process, we proved the performances and the automated and robotic on-wafer station. Measurement uncertainties were drastically reduced compared to a manual station.

A lot of perspectives are now opened to follow this work. First, the characterization of RF devices can be achieved in order to evaluate the stations' performances regarding this matter. Indeed, the automation process needs to be extended in order to be able to measure different devices. In particular, additional patterns can be added to the pattern data base in order to recognize more types of contact pads. The aim is to build a "deep learning" program that will handle image recognition of the ISS calibration standards, making stronger especially when faced to unclear patterns (brightness issues, parasitic particles around the standards…). Also, for safety measures (especially the durability of the RF probes and the ISS) the program runs with a relatively slow rate. Some safety features of the program make it slower and can be lifted to speed up the measurement process. Finally, although the VNA automation exists, it has to be fully integrated to the automated calibration process yet. This should be included in the near future.

In the last chapter, we presented EM-simulation of the ISS load standard. First design of a microstrip based GSG probe has also been shown. The goal is to have a complete EM model of the GSG probe and the calibration substrate in order to study the influence of micro- and nano-misplacement of the probes on the calibration substrate.

Beside the on-wafer measurements, the station can host other projects. In particular, the precision of the nano-positioner make it an attractive solution when dealing with applications that require precise and fine displacements. The goal is to offer a tool that would be used by research groups or R&D institutions for on-wafer and/or RF precision applications.

Bibliography

C. Mokhtari, M. Sebbache, V. Avramovic, C. Boyaval, G. Dambrine and K. Haddadi, "Impact of GSG Probe to Pads Contact Repeatability for On-Wafer RF Measurements," *2021 IEEE 7th International Conference on Smart Instrumentation, Measurement and Applications (ICSIMA)*, Bandung, Indonesia, 2021, pp. 241-246.

C. Mokhtari, L. Abassi, M. Sebbache, C. Loyez and K. Haddadi, "Extend IQ Six-Port Demodulator RF Bandwidth by 250% Using Fourier Based Modelling," *2021 IEEE Conference on Antenna Measurements & Applications (CAMA)*, Antibes Juan-les-Pins, France, 2021, pp. 284-288.

Cerine Mokhtari, Mohamed Sebbache, Kamel Haddadi. Mesures hyperfréquences 'On-Wafer' d'impédances extrêmes : Limitations et Solutions. *XXIIèmes Journées Nationales Microondes*, Jun 2022, Limoges, France.

Cerine Mokhtari, L. Abassi, Mohamed Sebbache, Christophe Loyez, Kamel Haddadi. Calibration Six-Port Basée sur une Analyse de Fourier : Extension Record de 250% des Performances Fréquentielles. *XXIIèmes Journées Nationales Microondes*, Jun 2022, Limoges, France.

C. Mokhtari *et al*., "New Generation of On-Wafer Microwave Probe Station for Precision GSG Probing," *2022 24th International Microwave and Radar Conference (MIKON)*, Gdansk, Poland, 2022, pp. 1-4.

C. Mokhtari and K. Haddadi, "Impedance Standard Substrate EM-Simulation for On-Wafer GSG Probing," *2023 IEEE MTT-S International Conference on Numerical Electromagnetic and Multiphysics Modeling and Optimization (NEMO)*, Winnipeg, MB, Canada, 2023, pp. 1-3.

C. Mokhtari *et al*., "Nanorobotics and Automatic On-Wafer Probe Station with Nanometer Positionning Accuracy," *2023 IEEE MTT-S International Conference on Numerical Electromagnetic and Multiphysics Modeling and Optimization (NEMO)*, Winnipeg, MB, Canada, 2023, pp. 22-24.

C. Mokhtari, C. Lenoir, M. Sebbache and K. Haddadi, "Automated and Robotic On-Wafer Probing Station," *2023 IEEE Symposium on Wireless Technology & Applications (ISWTA)*, Kuala Lumpur, Malaysia, 2023, pp. 99-102.

Résumé

Dans le contexte général de l'industrie européenne de la nanoélectronique, il est nécessaire de développer de nouvelles techniques et de nouveaux instruments de caractérisation sous pointes pour la validation précise et fine de circuits destinés à des applications haute fréquence (HF). Pour faire progresser la miniaturisation des dispositifs à haute fréquence, de nouvelles questions métrologiques liées à la caractérisation dimensionnelle et électrique doivent être abordées. Un instrument universel de caractérisation des dispositifs à radiofréquences (RF) consiste en un analyseur de réseau vectoriel (VNA), une station de mesure équipée d’une paire de sondes micro-ondes Ground-Signal-Ground (GSG) alignées manuellement ou automatiquement au moyen d'un microscope ou d'un système de caméra sur des substrats d'étalonnage et des dispositifs sous test (DUT). Les structures de test RF conventionnelles nécessitent des tampons (structures de contact) spécifiques pour s'adapter à la géométrie de la pointe de la sonde. Le positionnement de la sonde sur la structure de test CPW génère des erreurs de mesure de désalignement qui affectent la reproductibilité de la mesure. En outre, les dispositifs présentent des impédances extrêmes par rapport à l'impédance de référence 50 Ω du VNA, ce qui se traduit par une sensibilité et une précision de mesure médiocres.

Pour relever ce défi, une nouvelle station de mesure sous pointe entièrement automatisée et robotisée a été conçue et construite à partir de zéro. Les sondes de mesure ainsi que le porte échantillon accueillant le dispositif sous test sont montés sur des nano-positionneurs piézoélectriques du constructeur SmarAct®. La vision du contact sondes – au – composant sous test est assurée par une caméra microscope haute résolution. Un analyseur de réseau vectoriel Streamline Keysight® a été intégré à la station afin d’obtenir une solution compacte au plus près des sondes et réduire ainsi les erreurs non systématiques inhérentes aux variations de l'environnement. Enfin, un programme de pilotage des sondes et du porte échantillon automatique basé sur la reconnaissance d’image a été développé avec le logiciel LabVIEW™.

Mots clés: mesures hyperfréquences, mesures sous pointes, analyseur de réseaux vectoriel, métrologie haute fréquence, calibration, traçabilité électrique, nano-robotique, automatisation.

Abstract

In the general context of the European nanoelectronics industry, it is necessary to develop new on-wafer characterisation techniques and instruments for precise and accurate validation of circuits designed for high-frequency (HF) applications. To advance the miniaturisation of HF devices, new metrological issues related to dimensional and electrical characterization must be addressed. A universal instrument for the characterization of RF devices consists of a vector network analyzer (VNA), a measurement station equipped with a pair of ground-signal-ground (GSG) microwave probes aligned manually or automatically using a microscope or a camera system on calibration substrates and devices under test (DUT). Conventional RF test structures require contact pads to adapted to the probe tip geometry. The positioning of the probe on the CPW test structure generates misalignment measurement errors that affect the reproducibility of the measurement. In addition, nanodevices have extreme impedances compared to the VNA's characteristic impedance of 50 Ω, resulting in poor measurement sensitivity and accuracy.

To meet this challenge, a new fully automated and robotic on-wafer probing station was designed and built from scratch. The measurement probes as well as the chuck hosting the

device under test are mounted on SmarAct® piezoelectric nanopositioners. The view on the probe-to-DUT contact is provided by a high-resolution microscope camera. A Keysight® Streamline vector network analyzer was integrated into the station to obtain a compact solution close to the probes in order reduce the non-systematic errors inherent in environmental variations. Finally, a program for driving the probes and chuck, based on image recognition, was developed with the LabVIEW™ software.

Keywords: high frequency measurements, on-wafer measurements, vector network analyzer, high frequency metrology, calibration, electrical traceability, nano-robotics, automation.